NON-FLAT FRIEDMANN-LEMAÎTRE-ROBERTSON-WALKER UNIVERSE WITH BARROW HOLOGRAPHIC DARK ENERGY

 Chandra Rekha Mahanta, **Joy Prakash Medhi**[*], **Rajashree Mahanta**

Department of Mathematics, Gauhati University, India

[*]Corresponding Author e-mail: joyprakash@gauhati.ac.in

In this paper, we study a non-flat Friedmann-Lemaître-Robertson-Walker (FLRW) universe filled with cold dark matter and Barrow holographic dark energy. We assume the Hubble horizon as IR cutoff and the scale factor to obey a hybrid expansion law to construct a cosmological model within the framework of General Relativity. The physical and geometrical properties of the model are discussed by studying the evolution of various parameters of cosmological importance. The behaviour of the dark energy equation of state parameter ω_{DE} is also studied for both interacting and non-interacting Barrow holographic dark energy. We observe that the Barrow exponent Δ significantly affects the dark energy equation of state parameter which in turn exhibits the behaviour of quintessence and phantom dark energy. The evolution of the jerk parameter is also studied.

Keywords: *Friedmann-Lemaître-Robertson-Walker universe; Hybrid expansion law; Barrow holographic dark energy; Cold dark matter; Equation of state parameter*

PACS: 95.35.+d, 95.36.+x, 98.80.-k, 98.80.Jk, 98.80.Es, 04.20.Jb

1. INTRODUCTION

According to a number of recent cosmological and astrophysical observations, including Supernovae Type Ia (SN Ia) [1,2], Cosmic Microwave Background (CMB) [3,4], Large Scale Structure (LSS) [5,6], and others the present universe is thought to be dominated by a mysterious physical entity known as dark energy. This indicates that the universe has recently undergone the transition from the matter era with decelerated expansion to the current accelerated expansion phase. Many cosmological observations such as Wilkinson Microwave Anisotropy Probe (WMAP), Baryon Acoustic Oscillation (BAO), Sloan Digital Sky Survey(SDSS), Gravitational Lensing etc. provided strong support to the observed cosmic acceleration. According to Planck Collaboration results, 2018, dark energy contributes about 68.3% of the total energy of the present observable universe. Dark energy permeats all over the space and it has large negative pressure. Since the cosmological constant Λ, introduced by Einstein, is physically comparable to quantum vacuum energy with an equation of state parameter $\omega = -1$, it follows that Λ can be a good contender for dark energy. But the constant Λ is plagued with the fine tuning and cosmic coincidence problems although it fits the observations reasonably well. As an alternative to Λ, a wide range of scenarios with a number of dynamically evolving scaler field models have been considered in the literature to explain the late time cosmic acceleration. Currently, an attempt for probing the true nature of dark energy has been taken in the literature, called holographic dark energy (HDE) [7,8], that originates from the Holographic Principle [9–12]. The fundamental tenet of the Holographic Principle is that, as opposed to scaling with system volume, the number of degrees of freedom that are directly related to entropy of a physical system scales with the system's surrounding surface area. G.'t Hooft [9] first presented it with the goal to explain the thermodynamics of black hole physics. The gravitational entropy inside a closed surface shouldn't always be greater than the particle entropy that travels through the surface's past light-cone, according to a later extension of this idea to the cosmological context made by Fischler and Susskind [12]. In cosmology, a significant implications of the holographic principle is that the entropy of the universe's horizon is directly proportional to its surface area, similar to the Bekenstein-Hawking entropy of a black hole.

Utilizing the black hole entropy expression, one may apply the Holographic Principle to generate holographic dark energy. Consequently, by utilizing different entropies, one can derive multiple varieties of the theory. A new black hole entropy relation, recently suggested by Barrow, indicates that the black hole structure may acquire intricate fractal features due to quantum gravitational processes. Due to its intricate structure, the black-hole entropy equation is distorted and has a limited volume but an infinite (or finite) area [13]. The equation is given by

$$S_B = \left(\frac{A}{A_0}\right)^{1+\frac{\Delta}{2}}$$

(1)

where A_0 is the Planck area and A is the standard horizon area. When $\Delta = 0$, the Barrow exponent Δ corresponds to the standard Bekenstein-Hawking entropy and with $\Delta = 1$, it corresponds to the most complex design. Therefore, the Barrow holographic dark energy (BHDE) is formulated [14] when holographic dark energy is described in accordance with the

general entropy formula given in (1).

Saridakis [15] offered an alternative cosmic arrangement to the Bekenstein-Hawking one by utilizing the Barrow entropy. Srivastava and Sharma [16] investigated the BHDE in a flat Friedmann-Lemaître-Robertson-Walker(FLRW) universe taking the Hubble horizon as the IR cutoff. Srivastava, Kumar and Srivastava [17] also investigated the BHDE model in the background of a flat FLRW universe. Recently many researchers examined the BHDE model in various cosmological and gravitational setups [18–21].

The goal of the current work is to study the evolution of a non-flat Friedmann-Lemaître-Robertson-Walker (FLRW) universe filled with pressureless cold dark matter and Barrow holographic dark energy (BHDE) with Hubble horizon as IR cutoff. We present our work in the following sections of this paper. In section 2, we construct a cosmological model by assuming the scale factor to obey the hybrid expansion law proposed by Akarsu *et al.* [22]. In section 3, we study the properties of the constucted model by examining the geometrical and physical characteristics of a few relevant cosmological parameters. We also study the behaviour of the dark energy equation of state parameter ω_{DE} for both interacting and non-interacting Barrow holographic dark energy. In section 4, we wrap up our paper with a conclusion.

2. THE MODEL

In this section, we consider a non-flat FLRW line element in the form

$$ds^2 = -dt^2 + a^2(t)\left[\frac{dr^2}{1 - kr^2} + r^2 d\Omega^2\right] \tag{2}$$

where $a(t)$ is the scale factor and $k = +1, 0, -1$ corresponds to closed, flat and open spatial curvature respectively and $d\Omega^2 = d\theta^2 + \sin^2\theta d\phi^2$.

Normally, holographic dark energy density given in reference [14] can be obtained in the framework of the holographic model based on the Barrow entropy according to the expression (1)

$$\rho_{DE} = CL^{\Delta-2} \tag{3}$$

with C being a parameter with dimensions $[L]^{-2-\Delta}$ and L is a holographic horizon length. For $\Delta = 0$, equation (3) gives the standard holographic dark energy density $\rho_{DE} = CL^{-2}$, where $C = 3c^2 M_p^2$, c^2 is standard parameter of order one that is present in all holographic dark energy models and M_p, the Planck mass. Taking the IR cutoff ($L = H^{-1}$) as the Hubble horizon, the energy density of BHDE is obtained as

$$\rho_{DE} = CH^{2-\Delta} \tag{4}$$

We consider the universe to be filled with cold dark matter (CDM) and Barrow holographic dark energy (BHDE). Then in natural units, we can write Einstein's field equations as

$$R_{ij} - \frac{1}{2}g_{ij}R = T_{ij} + \bar{T}_{ij} \tag{5}$$

where R_{ij} is the Ricci tensor; R is the Ricci scalar; T_{ij} is the energy-momentum tensor for cold dark matter given by

$$T_{ij} = \rho_m u_i u_j \tag{6}$$

and $\bar{T}_{ij}$ is the energy-momentum tensor for Barrow holographic dark energy given by

$$\bar{T}_{ij} = (\rho_{DE} + p_{DE})u_i u_j + g_{ij}p_{DE} \tag{7}$$

Here, ρ_m is the energy density of cold dark matter, ρ_{DE} and p_{DE} are the energy density and the pressure of the Barrow holographic dark energy respectively.

The Friedmann equations in this case are written as

$$3H^2 + 3\frac{k}{a^2} = \rho_m + \rho_{DE} \tag{8}$$

$$3H^2 + 2\dot{H} + \frac{k}{a^2} = -p_{DE} \tag{9}$$

where $H \equiv \dot{a}/a$ is the Hubble parameter and an over dot denotes differentiation with respect to cosmic time t.

The continuity equation is given by

$$\dot{\rho}_m + \dot{\rho}_{DE} + 3H(\rho_m + \rho_{DE} + p_{DE}) = 0 \tag{10}$$

In view of equation (4), the field equations (8) and (9) constitute a system of non-linear differential equations in three unknowns a, ρ_m and p_{DE}. In order to construct a cosmological model we consider the cosmological scale factor a to obey the hybrid expansion law (HEL) [22]

$$a(t) = a_0 \left(\frac{t}{t_0}\right)^{\alpha} e^{\beta\left(\frac{t}{t_0}-1\right)} \tag{11}$$

where α and β are constants and a_0 and t_0 denote the scale factor and the age of the present universe respectively. The reason for using such scale factor is the fact that it will give the deceleration parameter as a function of cosmic time t. This is amongst the models that describe the transition of the universe from a phase of deceleration to the present phase of acceleration as suggested by the present cosmological observations. Several researchers applied HEL to study behaviour of a number of cosmological models in different gravitational and cosmological backgrounds.

3. PROPERTIES OF THE MODEL

The Hubble parameter $H(t)$, a cosmological parameter that shows the rate of expansion at the epoch t, corresponding to the HEL (11) is obtained as

$$H = \frac{\dot{a}}{a} = \frac{\alpha}{t} + \frac{\beta}{t_0} \tag{12}$$

The deceleration parameter, denoted by q, is a dimensionless measure of the acceleration in the expansion of the universe and is defined by $q = -\frac{a\ddot{a}}{\dot{a}^2} = -\frac{\ddot{a}}{aH^2}$. Thus deceleration parameter q is obtained as

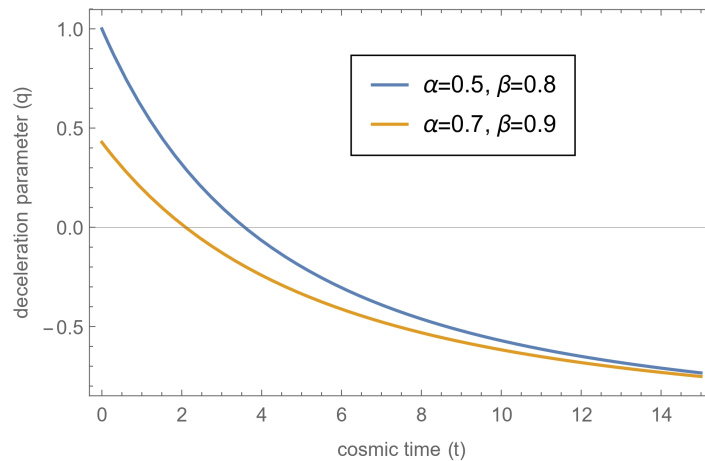$$q = \frac{\alpha}{\left(\alpha + \frac{\beta t}{t_0}\right)^2} - 1 \tag{13}$$

Figure 1. Evolution of deceleration parameter q vs cosmic time t

Figure 1 depicts the evolution of the deceleration parameter (q) for the constructed model against cosmic time (t). With reference to the displayed graph, the outcome reveals that the deceleration parameter (q) attributed a positive value at the initial stage followed by a sharp decrease and subsequently a slow convergence towards the value of negative one. This means that there is a transition from what is referred to as the decelerated phase of the universe which, in cosmological terms, seems to be the initial stage to the phase that is currently an accelerating phase of the universe. The parameters expressing rate of expansion in the earlier epoch have positive values means deceleration while moving toward negative in the later epochs means acceleration. These behaviors are in line with the acquired observational data concerning the validity of the late-time cosmic acceleration.

Using equations (12) in (4) we get the energy density of BHDE as

$$\rho_{DE} = C \left(\frac{\alpha}{t} + \frac{\beta}{t_0}\right)^{2-\Delta} \tag{14}$$

From equations (14),(12) and (8) we obtain the matter energy density as

$$\rho_m = 3\left(\frac{\alpha}{t} + \frac{\beta}{t_0}\right)^2 + 3k\left(a_0\left(\frac{t}{t_0}\right)^\alpha e^{\beta\left(\frac{t}{t_0}-1\right)}\right)^{-2} - C\left(\frac{\alpha}{t} + \frac{\beta}{t_0}\right)^{2-\Delta} \tag{15}$$

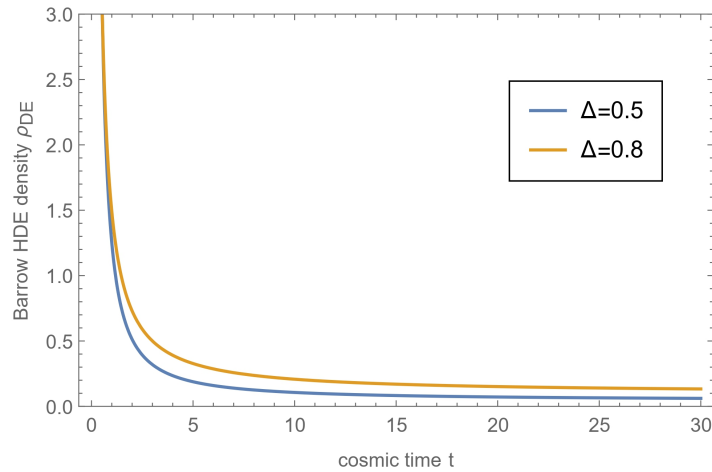For closed ($k = 1$) FLRW universe, equation (15) becomes

$$\rho_m = 3\left(\frac{\alpha}{t} + \frac{\beta}{t_0}\right)^2 + 3\left(a_0\left(\frac{t}{t_0}\right)^\alpha e^{\beta\left(\frac{t}{t_0}-1\right)}\right)^{-2} - C\left(\frac{\alpha}{t} + \frac{\beta}{t_0}\right)^{2-\Delta} \tag{16}$$

Figure 2. Evolution of the Barrow HDE density ρ_{DE} vs cosmic time t for $C = 3$, $t_0 = 13.8$, $\alpha = 0.5$ and $\beta = 0.8$
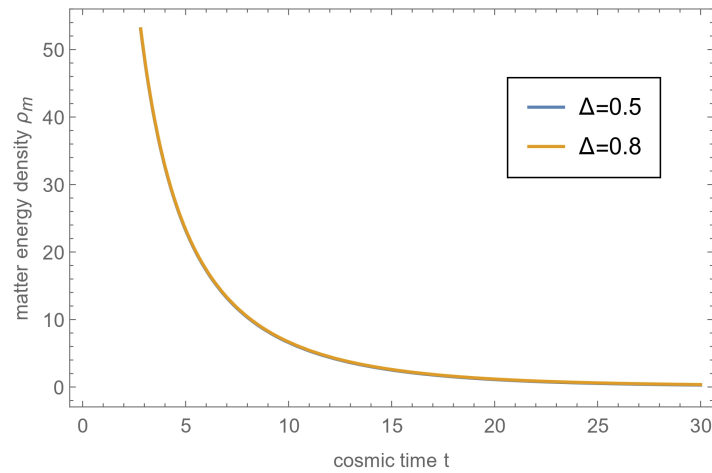

Figure 3. Evolution of the matter energy density ρ_m vs cosmic time t for $C = 3$, $\alpha = 0.5$, $\beta = 0.8$,
$a_0 = 1$ and $t_0 = 13.8$

Figure 2 and Figure 3 clearly indicate that both ρ_{DE} and ρ_m are decreasing functions of the cosmic time t. The decrease in energy densities suggests that the volume of the universe is expanding.

The BHDE density parameter Ω_{DE} and the energy density parameter of matter Ω_m are obtained as

$$\Omega_{DE} = \frac{C}{3\left(\frac{\alpha}{t} + \frac{\beta}{t_0}\right)^\Delta} \tag{17}$$

$$\Omega_m = 1 + \frac{1}{\left(\frac{\alpha}{t} + \frac{\beta}{t_0}\right)^2} \frac{1}{\left(a_0\left(\frac{t}{t_0}\right)^\alpha e^{\beta\left(\frac{t}{t_0}-1\right)}\right)^2} - \frac{C}{3\left(\frac{\alpha}{t} + \frac{\beta}{t_0}\right)^\Delta} \tag{18}$$

Hence the total energy density parameter Ω is obtained as

$$\Omega = \Omega_m + \Omega_{DE} = 1 + \frac{1}{\left(\frac{\alpha}{t} + \frac{\beta}{t_0}\right)^2} \frac{1}{\left(a_0 \left(\frac{t}{t_0}\right)^\alpha e^{\beta\left(\frac{t}{t_0}-1\right)}\right)^2} \tag{19}$$
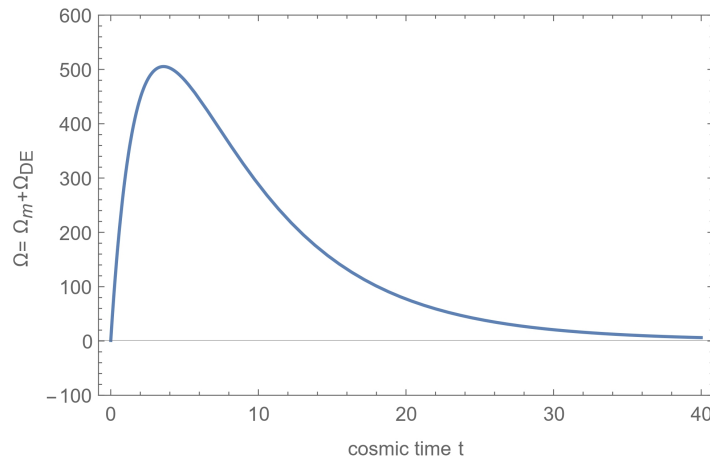

Figure 4. Evolution of the total energy density parameter Ω vs cosmic time t for $\alpha = 0.5$, $\beta = 0.8$, $a_0 = 1$ and $t_0 = 13.8$

Figure 4 represents the evolution of the total energy density parameter Ω as a function of cosmic time t. From the figure we observe that Ω tends to 1. This result is compatible with the observational results. Since our model predicts a flat universe for late times, and the present day universe is very close to flat, so the derived model is also compatible with the observational results.

Now for open ($k = -1$) FLRW universe, the energy density of cold dark matter ρ_m is obtained by using the equation (15) as

$$\rho_m = 3 \left(\frac{\alpha}{t} + \frac{\beta}{t_0}\right)^2 - 3 \left(a_0 \left(\frac{t}{t_0}\right)^\alpha e^{\beta\left(\frac{t}{t_0}-1\right)}\right)^{-2} - C \left(\frac{\alpha}{t} + \frac{\beta}{t_0}\right)^{2-\Delta} \tag{20}$$
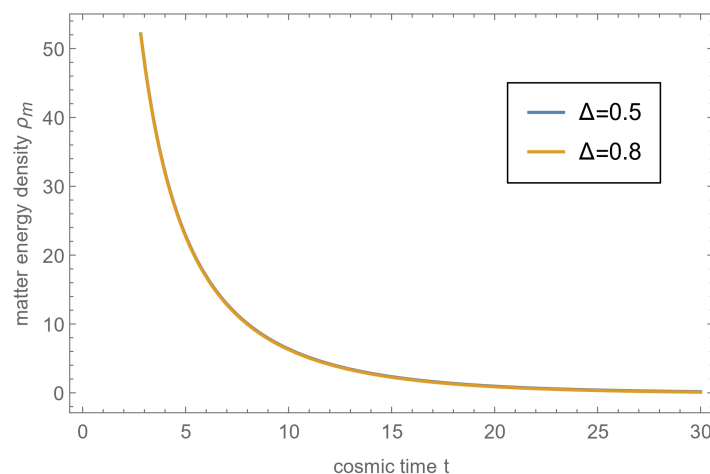

Figure 5. Evolution of the matter energy density ρ_m vs cosmic time t for $C = 3$, $\alpha = 0.5$, $\beta = 0.8$, $a_0 = 1$ and $t_0 = 13.8$

Figure 5 depicts the evolution of the matter energy density ρ_m vs cosmic time t. The graph shows that ρ_m is a decreasing function of cosmic time t, this indicates the expansion of the universe as it evolves.

The BHDE density parameter Ω_{DE} and the energy density parameter of matter Ω_m are obtained as

$$\Omega_{DE} = \frac{C}{3\left(\frac{\alpha}{t} + \frac{\beta}{t_0}\right)^\Delta} \tag{21}$$

$$\Omega_m = 1 - \frac{1}{\left(\frac{\alpha}{t} + \frac{\beta}{t_0}\right)^2} \frac{1}{\left(a_0 \left(\frac{t}{t_0}\right)^\alpha e^{\beta\left(\frac{t}{t_0}-1\right)}\right)^2} - \frac{C}{3\left(\frac{\alpha}{t} + \frac{\beta}{t_0}\right)^\Delta} \tag{22}$$

Hence the total energy density parameter Ω is obtained as

$$\Omega = \Omega_m + \Omega_{DE} = 1 - \frac{1}{\left(\frac{\alpha}{t} + \frac{\beta}{t_0}\right)^2} \frac{1}{\left(a_0 \left(\frac{t}{t_0}\right)^\alpha e^{\beta\left(\frac{t}{t_0}-1\right)}\right)^2} \tag{23}$$
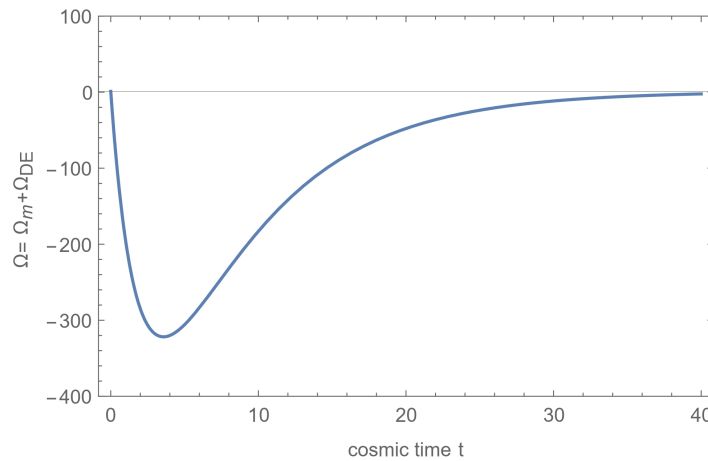

Figure 6. Evolution of the total energy density parameter Ω vs cosmic time t for $\alpha = 0.5$, $\beta = 0.8$, $a_0 = 1$ and $t_0 = 13.8$

From Figure 6, we see that Ω tends to 1. So our model approaches to flat FLRW universe at late times.

Case I: Interacting Barrow HDE

When there is an interaction between dark energy and dark matter, the energy densities do not conserve separately. So, from the continuity equation (10), we have

$$\dot{\rho}_m + 3H\rho_m = Q \tag{24}$$

and

$$\dot{\rho}_{DE} + 3H(\rho_{DE} + p_{DE}) = -Q \tag{25}$$

where Q is the coupling parameter which describes the interaction between dark energy and dark matter. A common choice for the interaction term often takes the form $Q \propto H\rho_m$, $Q \propto H\rho_{DE}$ or a combination of these forms. We consider

$$Q = 3H(\gamma\rho_{DE} + \delta\rho_m) \tag{26}$$

where γ and δ are constants.

Using equations (26), (25), (14) and (12) we get

$$p_{DE} = -C\left(\frac{\alpha}{t} + \frac{\beta}{t_0}\right)^{2-\Delta} - \frac{C(2-\Delta)\left(-\frac{\alpha}{t^2}\right)}{3\left(\frac{\alpha}{t} + \frac{\beta}{t_0}\right)^\Delta} - \frac{\gamma C\left(\frac{\alpha}{t} + \frac{\beta}{t_0}\right)^{2-\Delta} + \delta\rho_m}{3\left(\frac{\alpha}{t} + \frac{\beta}{t_0}\right)} \tag{27}$$

where ρ_m is given by equation (15).

For $k = 1$, using equation (16) in (27), we get

$$
p_{DE} = -C\left(\frac{\alpha}{t} + \frac{\beta}{t_0}\right)^{2-\Delta} - \frac{C(2-\Delta)\left(-\frac{\alpha}{t^2}\right)}{3\left(\frac{\alpha}{t} + \frac{\beta}{t_0}\right)^{\Delta}}
$$

$$
- \frac{\gamma C\left(\frac{\alpha}{t} + \frac{\beta}{t_0}\right)^{2-\Delta} + 3\delta\left(\frac{\alpha}{t} + \frac{\beta}{t_0}\right)^2 + 3\left(a_0\left(\frac{t}{t_0}\right)^{\alpha} e^{\beta\left(\frac{t}{t_0}-1\right)}\right)^{-2} - C\left(\frac{\alpha}{t} + \frac{\beta}{t_0}\right)^{2-\Delta}}{3\left(\frac{\alpha}{t} + \frac{\beta}{t_0}\right)} \tag{28}
$$

Using equations (28) and (14), we get the EoS parameter ω_{DE} as

$$
\omega_{DE} = -1 + \frac{\alpha(2-\Delta)}{3\left(\alpha + \frac{\beta t}{t_0}\right)^2} - \left(\gamma + \frac{3\delta\left(\frac{\alpha}{t} + \frac{\beta}{t_0}\right)^2 + 3\left(a_0\left(\frac{t}{t_0}\right)^{\alpha} e^{\beta\left(\frac{t}{t_0}-1\right)}\right)^{-2} - C\left(\frac{\alpha}{t} + \frac{\beta}{t_0}\right)^{2-\Delta}}{C\left(\frac{\alpha}{t} + \frac{\beta}{t_0}\right)^{2-\Delta}}\right) \tag{29}
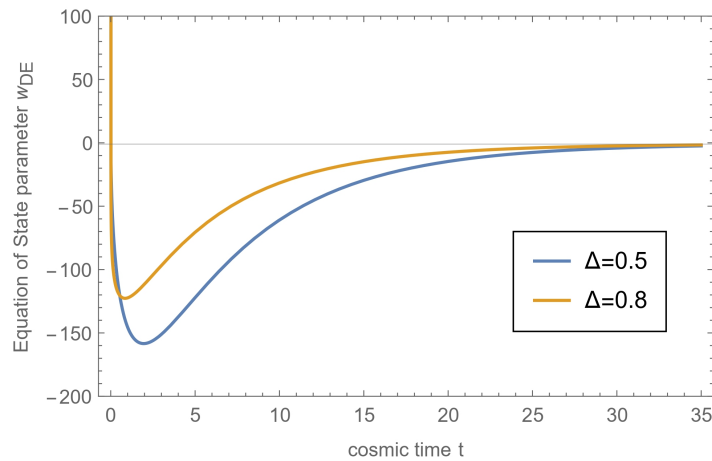$$

Figure 7. Evolution of EoS parameter ω_{DE} vs cosmic time t for $\alpha = 0.5$, $\beta = 0.8$, $t_0 = 13.8$, $\gamma = 1$ and $\delta = -1$.

From figure 7, we observe that ω_{DE} enters a high phantom region in the very early phases of the universe and as time passes it approaches to -1 showing thereby that BHDE behaves like the cosmological constant Λ at late times.

For $k = -1$, using (20) in (27), we get

$$
p_{DE} = -C\left(\frac{\alpha}{t} + \frac{\beta}{t_0}\right)^{2-\Delta} - \frac{C(2-\Delta)\left(-\frac{\alpha}{t^2}\right)}{3\left(\frac{\alpha}{t} + \frac{\beta}{t_0}\right)^{\Delta}}
$$

$$
- \frac{\gamma C\left(\frac{\alpha}{t} + \frac{\beta}{t_0}\right)^{2-\Delta} + 3\delta\left(\frac{\alpha}{t} + \frac{\beta}{t_0}\right)^2 - 3\left(a_0\left(\frac{t}{t_0}\right)^{\alpha} e^{\beta\left(\frac{t}{t_0}-1\right)}\right)^{-2} - C\left(\frac{\alpha}{t} + \frac{\beta}{t_0}\right)^{2-\Delta}}{3\left(\frac{\alpha}{t} + \frac{\beta}{t_0}\right)} \tag{30}
$$

Using equations (30) and (14), the EoS parameter ω_{DE} is obtained as

$$
\omega_{DE} = -1 + \frac{\alpha(2-\Delta)}{3\left(\alpha + \frac{\beta t}{t_0}\right)^2} - \left(\gamma + \frac{3\delta\left(\frac{\alpha}{t} + \frac{\beta}{t_0}\right)^2 - 3\left(a_0\left(\frac{t}{t_0}\right)^{\alpha} e^{\beta\left(\frac{t}{t_0}-1\right)}\right)^{-2} - C\left(\frac{\alpha}{t} + \frac{\beta}{t_0}\right)^{2-\Delta}}{C\left(\frac{\alpha}{t} + \frac{\beta}{t_0}\right)^{2-\Delta}}\right) \tag{31}
$$

From figure 8, we see that for different values of Δ, ω_{DE} gradually decreases and tends to -1 at late times.
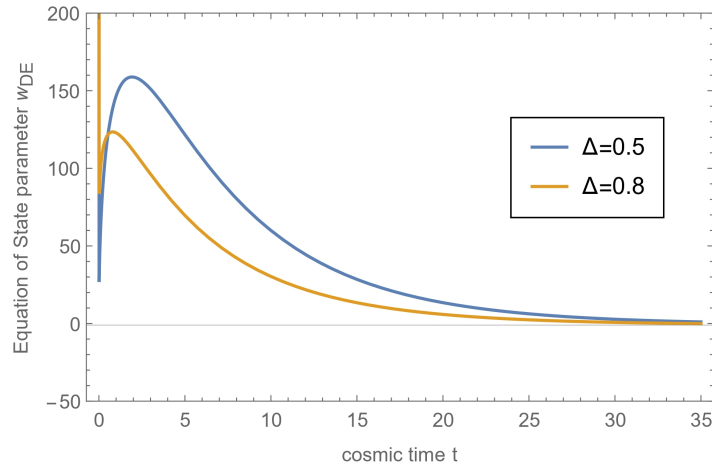
Figure 8. Evolution of EoS parameter ω_{DE} vs cosmic time t for $\alpha = 0.5$, $\beta = 0.8$, $t_0 = 13.8$, $\gamma = 1$ and $\delta = -1$.

Case II: Non-interacting Barrow HDE

If there is no interaction between dark energy and dark matter, the energy densities conserved separately and therefore from equation (10), we have

$$\dot{\rho}_m + 3H\rho_m = 0 \tag{32}$$

and

$$\dot{\rho}_{DE} + 3H(\rho_{DE} + p_{DE}) = 0 \tag{33}$$

From equations (33), (14) and (12), we get

$$p_{DE} = -C\left(\frac{\alpha}{t} + \frac{\beta}{t_0}\right)^{2-\Delta} - \frac{C(2-\Delta)\left(-\frac{\alpha}{t^2}\right)}{3\left(\frac{\alpha}{t} + \frac{\beta}{t_0}\right)^{\Delta}} \tag{34}$$

Using equations (34) and (14), the EoS parameter ω_{DE} is obtained as

$$\omega_{DE} = -1 + \frac{\alpha(2-\Delta)}{3\left(\alpha + \frac{\beta t}{t_0}\right)^2} \tag{35}$$

Since it is independent of the curvature parameter k, therefore, for both closed and open universe, the model represents ΛCDM model when $\omega_{DE} = -1$.
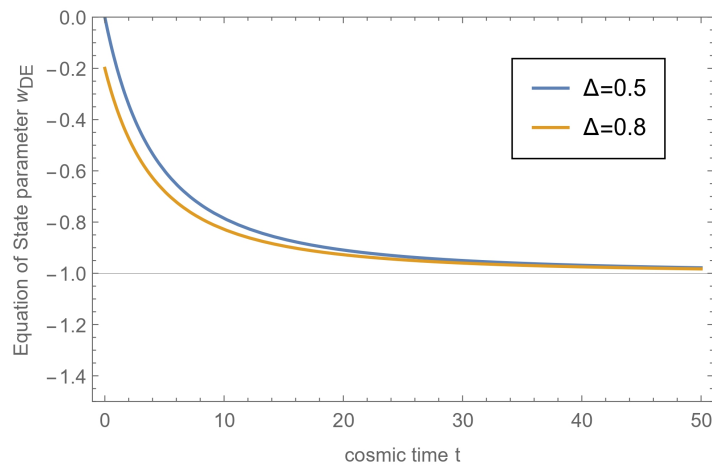

Figure 9. Evolution of EoS parameter ω_{DE} vs cosmic time t for $\alpha = 0.5$, $\beta = 0.8$ and $t_0 = 13.8$

From the figure 9, we observe the quintessence behaviour of BHDE for different values of Δ.

Jerk parameter: The jerk parameter j is a crucial tool for identifying deviations of cosmological model from the ΛCDM model and describing the universe's dynamical evolution. It characterizes models close to ΛCDM through a dimensionless third derivative of the scale factor relative to the cosmic time t. In cosmology it is defined as $j(t) = \frac{1}{aH^3}\frac{d^3a}{dt^3}$ and for our model it is obtained as

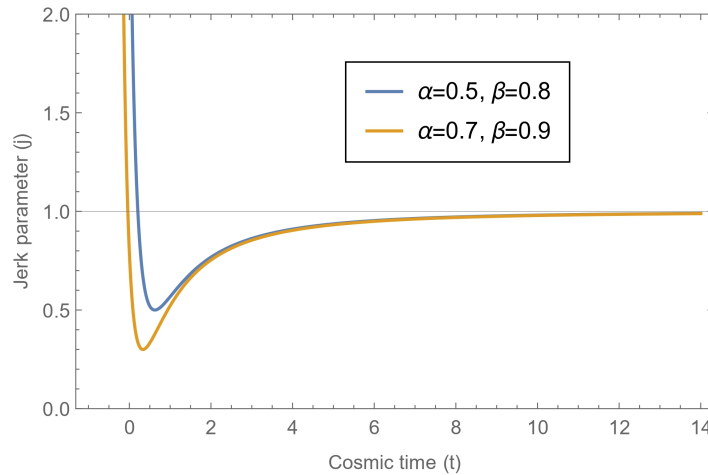$$j = 1 + \frac{(2t_0 - 3\beta t - 3\alpha t_0)\alpha t_0^2}{(\beta t + \alpha t_0)^3} \tag{36}$$

Figure 10. Evolution of jerk parameter j vs cosmic time t for $t_0 = 13.8$

Figure 10 illustrates that the cosmic jerk parameter remains positive throughout the universe's evolution, approaching the value 1 in the later stages.

4. CONCLUSION

In this paper, a non-flat Friedmann-Lemaître-Robertson-Walker (FLRW) universe filled with cold dark matter and Barrow holographic dark energy (BHDE) is studied within the framework of General Relativity. Exact solution of the Einstein field equations are obtained by considering a hybrid expansion law and the physical and geometrical properties of the derived model are studied graphically. We also study the behaviour of the EoS parameter ω_{DE} in two cases: when the BHDE is interacting with CDM and when the BHDE does not interact with CDM. The evolution of the jerk parameter is also studied. We observe that

- The evolution of the deceleration parameter in our model illustrates the universe's transition from its earlier deceleration phase to the current acceleration phase.

- Barrow holographic dark energy density ρ_{DE} and cold dark matter energy density ρ_m decrease with the increase of cosmic time t in both closed ($k = 1$) and open ($k = -1$) universes. This indicates that the universe is expanding.

- The EoS parameter ω_{DE} tends to -1 at late times for both interacting and non-interacting BHDE in a closed ($k = 1$) and open ($k = -1$) universe. However in case of interacting BHDE, ω_{DE} enters into high phantom region before the BHDE behaves like the cosmological constant.

- The Barrow holographic dark energy density parameter Ω_{DE} takes the same value in both closed and open universe. However the energy density parameter of matter Ω_m is different for closed and open universe.

- The total energy density parameter Ω tends to 1 as the universe evolves. This suggests that the universe is approaching towards a flat universe at late times.

- The cosmic jerk parameter remains positive throughout the universe's evolution and approaches 1 in late times. It is consistent with the current observational data.

ORCID

 Chandra Rekha Mahanta, https://orcid.org/0000-0002-8019-8824; **Joy Prakash Medhi**, https://orcid.org/0009-0004-5275-5330; **Rajashree Mahanta**, https://orcid.org/0009-0009-2656-115X

REFERENCES

[1] S. Perlmutter *et al.*, "Measurements of Ω and Λ from 42 high redshift supernovae," Astrophys. J. **517**, 565-586 (1999). https://doi.org/10.1086/307221

[2] A.G. Riess, *et al.*, "Observational evidence from supernovae for an accelerating universe and a cosmological constant," Astron. J. **116**, 1009-1038 (1998). https://doi.org/10.1086/300499

[3] G.F. Smoot, *et al.*, "Structure in the COBE differential microwave radiometer first year maps," Astrophys. J. **396**, L1 (1992). https://repository.hkust.edu.hk/ir/Record/1783.1-81009

[4] C.L. Bennett, *et al.*, "First-Year Wilkinson Microwave Anisotropy Probe (WMAP) Observations: Preliminary Maps and Basic Results," Astrophys. J. Suppl. Ser. **148**, 1-27 (2003). https://doi.org/10.1086/345346

[5] D.N. Spergel, *et al.*, [WMAP Collaboration], "First year Wilkinson Microwave Anisotropy Probe (WMAP) observations: Determination of cosmological parameters," Astrophys. J. Suppl. **148**, 175 (2003). https://doi.org/10.1086/377226

[6] K. Abazajian, *et al.*, "The second data release of the sloan digital sky survey," Astron. J. **128**, 502 (2004). https://dx.doi.org/10.1086/421365

[7] M. Li, "A Model of holographic dark energy," Phys. Lett. B, **603**, 1 (2004). https://doi.org/10.1016/j.physletb.2004.10.014

[8] S. Wang *et al.*, "Holographic dark energy," Phys. Rep. **696**, 1 (2017). https://doi.org/10.1016/j.physrep.2017.06.003

[9] G.'t Hooft, "Dimensional reduction in quantum gravity," arXiv preprint (2009). https://doi.org/10.48550/arXiv.gr-qc/9310026

[10] L. Susskind, "The World as a hologram," J. Math. Phys. **36**, 6377 (1995). hep-th/9409089. https://doi.org/10.1063/1.531249

[11] R. Bousso, "The holographic principle", Rev. Mod. Phys. **74**, 825 (2002). https://doi.org/10.1103/RevModPhys.74.825

[12] W. Fischler, and L. Susskind, "Holography and cosmology," https://doi.org/10.48550/arXiv.hep-th/9806039

[13] J.D. Barrow, "The Area of a Rough Black Hole," Phys. Lett. B, **808**, 135643 (2020). https://doi.org/10.1016/j.physletb.2020.135643

[14] E.N. Saridakis, "Barrow holographic dark energy," Phys. Rev. D, **102**, 123525 (2020). https://doi.org/10.1103/PhysRevD.102.123525

[15] E.N. Saridakis, "Modified cosmology through spacetime thermodynamics and Barrow horizon entropy," Journal of Cosmology and Astroparticle Physics, **07**, 31 (2020). https://dx.doi.org/10.1088/1475-7516/2020/07/031

[16] S. Srivastava, and U. K. Sharma, "Barrow holographic dark energy with Hubble horizon as IR cutoff," Int. J. Geom. Meth. Mod. Phys. **18**, 2150014 (2020). https://doi.org/10.1142/S0219887821500146

[17] M. Srivastava, *et al.*, "Barrow Holographic Dark Energy with Hybrid Expansion Law," Gravitation and Cosmology, **28**, (2022). https://doi.org/10.1134/S020228932201011X

[18] U.K. Sharma, *et al.*, "Barrow agegraphic dark energy," Int. J. Mod. Phys. D, **30**, 2150021 (2021). https://doi.org/10.1142/S0218271821500218

[19] Q. Huang *et al.*, "Dynamical analysis and statefinder of Barrow holographic dark energy," Eur. Phys. J. C, **81**, 686 (2021). https://doi.org/10.1140/epjc/s10052-021-09480-3

[20] A. Sarkar, and S. Chattopadhyay, "The barrow holographic dark energy-based reconstruction of f(R) gravity and cosmology with Nojiri–Odintsov cutoff," Int. J. Geom.Meth. Mod. Phys. **18**, 2150148 (2021). https://doi.org/10.1142/S0219887821501486

[21] P. Adhikary *et al.*, "Barrow Holographic Dark Energy in non-flat Universe," https://doi.org/10.1103/PhysRevD.104.123519

[22] Ö. Akarsu *et al.*, "Cosmology with hybrid expansion law: scalar field reconstruction of cosmic history and observational constraints," JCAP, **01**, 022 (2014). https://doi.org/10.1088/1475-7516/2014/01/022

НЕПЛОСКИЙ ВСЕСВІТ ФРІДМАНА-ЛЕМЕТРА-РОБЕРТСОНА-УОКЕРА З ГОЛОГРАФІЧНОЮ ТЕМНОЮ ЕНЕРГІЄЮ БАРРОУ

Чандра Рекха Маханта, **Джой Пракаш Медхі**, **Раджашрі Маханта**
Факультет математики, Університет Гаухаті, Індія

У цій статті ми вивчаємо неплоский Всесвіт Фрідмана-Леметра-Робертсона-Уокера (FLRW), наповнений холодною темною матерією та голографічною темною енергією Барроу. Ми припускаємо, що горизонт Хаббла є ІЧ-відсіканням, а масштабний коефіцієнт підкоряється гібридному закону розширення для побудови космологічної моделі в рамках загальної теорії відносності. Фізичні та геометричні властивості моделі обговорюються шляхом вивчення еволюції різних параметрів космологічного значення. Поведінка рівняння темної енергії параметра стану ω_{DE} також вивчається як для взаємодіючої, так і для невзаємодіючої голографічної темної енергії Барроу. Ми спостерігаємо, що експонента Барроу Δ суттєво впливає на рівняння темної енергії параметра стану, яке, у свою чергу, демонструє поведінку квінтесенції та фантомної темної енергії. Також вивчається еволюція параметра ривка.

Ключові слова: *Всесвіт Фрідмана-Леметра-Робертсона-Уокера, гібридний закон розширення, голографічна темна енергія Барроу, холодна темна матерія, рівняння параметра стану*

FLRW COSMOLOGICAL MODEL IN F(R,T) GRAVITY

Aroonkumar Beesham[*]

Mangosuthu University of Technology, PO Box 12363, Jacobs 4026, South Africa

[*]Corresponding Author e-mail: abeesham@yahoo.com

In this paper, the Friedmann-Lemaitre-Robertson-Walker cosmological models with a perfect fluid in the f(R,T) theory of gravity are re-discussed. There are several ways to generate solutions. One way is to assume a barotropic equation of state. The other is to use a deceleration parameter that varies linearly with time. An existing solution in the literature is reviewed, where solutions are obtained by assuming, in addition to a barotropic equation of state, a linear varying deceleration parameter. It is pointed out such an assumption leads to an over-determination of the solution. Hence, the feasibility of the solutions is a necessary condition to be satisfied. Only one of the assumptions of an equation of state or of a linearly varying deceleration parameter is sufficient to generate solutions. The proper solutions are given and discussed.

Keywords: *f(R,T) gravity; FLRW models; Linear varying deceleration parameter; Cosmological solutions; Feasibility of solutions*

PACS: 98.80.Jk

1. INTRODUCTION

Recent observations from the anisotropy of the Cosmic Microwave Background (CMB) [1], supernova type Ia (SNeIa) [2], large scale structure [3], baryon acoustic oscillations [4] and weak lensing [5] indicate the phenomenon of the accelerated expansion of the universe at late times. At early times the universe was decelerating, and there was a transition from deceleration to acceleration. There are bacsically two ways to try to explain this. One is that, in general relativity, the matter of the universe contains an exotic component dubbed dark energy which causes a gravitationally repulsive force. Several candidates have been proposed in this direction [6]-[10]. The other way is a modification of general relativity resulting in modified gravity theories which change the Einstein-Hilbert Lagrangian, such as $f(R)$ gravity [11].

Recently, Harko et al. [12] generalized $f(R)$ gravity by introducing an arbitrary function of the Ricci scalar R and the trace T of the energy-momentum tensor. The dependence upon T (in addition to R in the Lagrangian) may be due to quantum effects (conformal anomaly) or to an exotic imperfect fluid. As a result of coupling between matter and geometry, the motion of test particles is non-geodetic, and an extra acceleration is always present. In $f(R,T)$ gravity, where $f(R,T)$ is an arbitrary function of R and T, cosmic acceleration may result not only from the geometrical contribution to the total cosmic energy density, but from the matter content. This theory can be applied to explore several issues of current interest and may lead to some major differences. Houndjo [13] developed the cosmological reconstruction of $f(R,T)$ gravity for $f(R,T) = f_1(R) + f_2(T)$ and discussed the transition of the deceleration matter dominated era to the acceleration one.

Various aspects of the theory have been explored by literally hundreds of authors since Harko et al [12] introduced that theory. We cite a few of the key articles and also recent papers that have a relation to the work that we do in this article. All these articles contain additional references. Akarsu and Dereli [14] studied accelerating universes with a linearly varying deceleration parameter (LVDP). An LVDP in higher dimensions with strange quark matter and domain walls was investigated by Caglar [15]. Bishi et al [16] have applied a quadratic deceleration parameter to $f(R,T)$ gravity, finding bouncing cosmologies. Sofuoglu et al [17] have applied a cubic deceleration parameter to f(R,T) gravity, finding a big-bang singularity at the beginning, and a big rip one in the future.

The LVDP, as well as other variations of it have attracted a lot of interest. Alkaound et al [18] have studied an LVDP in Lyra's geometry, focussing on observational constraints, and future singularities, such as the big rip. Perturbation theory has been used [19] to study the big rip singularity with a LVDP. Ramesh and Umadevi [20] have studied Friedmann-Lemaitre-Robertson Walker (FLRW) solutions in f(R,T) gravity, in which they obtained solutions by assuming, in addition to a barotropic equation of state, a LVDP. In this study, we review this solution, and point out that, firstly, both those assumptions lead to an over-determination of the solution. Only one of them is sufficient to generate a solution. Secondly, each of the assumptions leads to a different solution. The assumption of an equation of state leads to the equivalent solutions in general relativity. Only the second assumption of a linearly varying deceleration parameter alone leads to a solution that exhibits a transition from deceleration to acceleration. Thirdly, there appear to be several errors in the paper, which we correct here.

This paper is organised as follows. In section 2, we give a brief introduction to f(R,T) gravity. Section 3 provides details of the solution by Ramesh and Umadevi [20]. In section 4, we provide the updated solution and in section 5 we give the conclusion.

2. REVIEW OF F(R,T) GRAVITY

The action for $f(R,T)$ gravity is:

$$S = \frac{1}{16\pi} \int f(R,T) \sqrt{-g} \, d^4x + \int L_{\mathrm{m}} \sqrt{-g} \, d^4x \,, \tag{1}$$

where $f(R,T)$ is an arbitrary function of the Ricci scalar R, and of the trace T of the energy-momentum tensor of the matter, T_{ab}. L_m is the matter Lagrangian density, and the energy-momentum tensor of matter is defined as:

$$T_{ab} = -\frac{2}{\sqrt{-g}} \frac{\delta \left(\sqrt{-g} L_m\right)}{\delta g^{ab}} \,, \tag{2}$$

and the trace of T_{ab} by $T = g^{ab} T_{ab}$. By assuming that the Lagrangian density L_{m} of matter depends only on the metric tensor components g_{ab}, and not on its derivatives, we obtain:

$$T_{ab} = g_{ab} L_m - 2 \frac{\partial L_m}{\partial g^{ab}} \,. \tag{3}$$

By varying the action S of the gravitational field with respect to the metric tensor components g^{ab} we get:

$$\delta S = \frac{1}{16\pi} \int \left[f_R(R,T) \, \delta R + f_T(R,T) \frac{\delta T}{\delta g^{ab}} \delta g^{ab} - \frac{1}{2} g_{ab} f(R,T) \, \delta g^{ab} + 16\pi \frac{1}{\sqrt{-g}} \frac{\delta \left(\sqrt{-g} L_{\mathrm{m}}\right)}{\delta g^{ab}} \right] \sqrt{-g} d^4x \,, \tag{4}$$

where we have denoted $\partial f(R,T) / \partial R$ by $f_R(R,T)$ and $\partial f(R,T) / \partial T$ by $f_T(R,T)$. For the variation of the Ricci scalar, we obtain

$$\delta R = \delta \left(g^{ab} R_{ab}\right) = R_{ab} \delta g^{ab} + g^{ab} \left(\nabla_d \delta \Gamma_{ab}^d - \nabla_b \delta \Gamma_{ad}^d\right) \,, \tag{5}$$

where ∇_d is the covariant derivative with respect to the symmetric connection Γ associated with the metric g. The variation of the Christoffel symbols yields

$$\delta \Gamma_{ab}^d = \frac{1}{2} g^{de} \left(\nabla_a \delta g_{be} + \nabla_b \delta g_{ea} - \nabla_e \delta g_{ab}\right) \,, \tag{6}$$

and the variation of the Ricci scalar provides the expression

$$\delta R = R_{ab} \delta g^{ab} + g_{ab} \Box \delta g^{ab} - \nabla_a \nabla_b \delta g^{ab} \,. \tag{7}$$

Therefore, for the variation of the action of the gravitational field we obtain

$$\begin{aligned} \delta S = \ & \frac{1}{16\pi} \int \left[f_R(R,T) R_{ab} \delta g^{ab} + f_R(R,T) g_{ab} \Box \delta g^{ab} - f_R(R,T) \nabla_a \nabla_b \delta g^{ab} \right. \\ & \left. + f_T(R,T) \frac{\delta \left(g^{de} T_{de}\right)}{\delta g^{ab}} \delta g^{ab} - \frac{1}{2} g_{ab} f(R,T) \, \delta g^{ab} + 16\pi \frac{1}{\sqrt{-g}} \frac{\delta \left(\sqrt{-g} L_m\right)}{\delta g^{ab}} \right] \sqrt{-g} d^4x \,. \end{aligned} \tag{8}$$

where $\Box = \nabla^d \nabla_d$. We define the variation of T with respect to the metric tensor as

$$\frac{\delta \left(g^{ef} T_{ef}\right)}{\delta g^{ab}} = T_{ab} + \Theta_{ab} \,, \tag{9}$$

where

$$\Theta_{ab} \equiv g^{de} \frac{\delta T_{de}}{\delta g^{ab}} \,. \tag{10}$$

After partially integrating the second and third terms in Eq. (8), we obtain the field equations of the $f(R,T)$ gravity model as

$$f_R(R,T) R_{ab} - \frac{1}{2} f(R,T) g_{ab} + (g_{ab} \Box - \nabla_a \nabla_b) f_R(R,T) = 8\pi T_{ab} - f_T(R,T) T_{ab} - f_T(R,T) \Theta_{ab} \,. \tag{11}$$

Note that when $f(R,T) \equiv f(R)$, from Eqs. (11) we obtain the field equations of $f(R)$ gravity.

By contracting, Eq. (11) gives the following relation between the Ricci scalar R and the trace T of the stress-energy tensor,

$$f_R(R,T) R + 3 \Box f_R(R,T) - 2f(R,T) = 8\pi T - f_T(R,T) T - f_T(R,T) \Theta \,, \tag{12}$$

where we have denoted $\Theta = \Theta_\mu^{\ \mu}$.

By eliminating the term $\Box f_R(R,T)$ between Eqs. (11) and (12), the gravitational field equations can be written in the form

$$
\begin{aligned}
f_R(R,T)\left(R_{ab} - \frac{1}{3}Rg_{ab}\right) + \frac{1}{6}f(R,T)g_{ab} &= 8\pi\left(T_{ab} - \frac{1}{3}Tg_{ab}\right) - f_T(R,T)\left(T_{ab} - \frac{1}{3}Tg_{ab}\right) \\
&\quad - f_T(R,T)\left(\Theta_{ab} - \frac{1}{3}\Theta g_{ab}\right) + \nabla_a\nabla_b f_R(R,T) .
\end{aligned}
\tag{13}
$$

Taking into account the covariant divergence of Eq. (11), with the use of the following mathematical identity [21]

$$
\nabla^a\left[f_R(R,T)R_{ab} - \frac{1}{2}f(R,T)g_{ab} + (g_{ab}\Box - \nabla_a\nabla_b)f_R(R,T)\right] \equiv 0,
\tag{14}
$$

where $f(R,T)$ is an arbitrary function of the Ricci scalar R and of the trace of the energy-momentum tensor T, we obtain for the divergence of the stress-energy tensor T_{ab}, the equation

$$
\nabla^a T_{ab} = \frac{f_T(R,T)}{8\pi}\left[(T_{ab} + \Theta_{ab})\nabla^a \ln f_T(R,T) + \nabla^a\Theta_{ab}\right] .
\tag{15}
$$

Next we consider the calculation of the tensor Θ_{ab}, once the matter Lagrangian is known. From Eq. (3) we obtain first

$$
\begin{aligned}
\frac{\delta T_{de}}{\delta g^{ab}} &= \frac{\delta g_{de}}{\delta g^{ab}}L_m + g_{de}\frac{\partial L_{\rm m}}{\partial g^{ab}} - 2\frac{\partial^2 L_m}{\partial g^{ab}\partial g^{de}} \\
&= \frac{\delta g_{de}}{\delta g^{ab}}L_{\rm m} + \frac{1}{2}g_{de}g_{ab}L_m - \frac{1}{2}g_{de}T_{ab} - 2\frac{\partial^2 L_m}{\partial g^{ab}\partial g^{de}} .
\end{aligned}
\tag{16}
$$

From the condition $g_{ad}g^{db} = \delta_a^b$, we have

$$
\frac{\delta g_{de}}{\delta g^{ab}} = -g_{df}g_{eh}\delta_{ab}^{fh},
\tag{17}
$$

where $\delta_{ab}^{fh} = \delta g^{fh}/\delta g^{ab}$ is the generalized Kronecker symbol. Therefore for Θ_{ab} we find

$$
\Theta_{ab} = -2T_{ab} + g_{ab}L_{\rm m} - 2g^{de}\frac{\partial^2 L_m}{\partial g^{ab}\partial g^{de}} .
\tag{18}
$$

We take the matter Lagrangian to be given by $L_{\rm m} = p$. Now, there is degeneracy in the choice of the matter Lagrangian in the sense that this choice does not make any difference to the resulting field equations in general relativity. Hence one could also choose $L_m = -\rho$, where ρ is the energy density. [22]. We now indicate briefly how this Lagrangian leads to the energy momentum tensor (Hawking and Ellis [23] give an excellent derivation of this). The fluid current four-vector is defined as $j^a = \rho u^a$, where u^a is the fluid four-velocity. Now it is assumed that this is conserved, i.e., $j^a_{;a} = 0$. Taking the Lagrangian to be $L_m = -\rho$, and varying so that the action is stationary, we get the momentum equation:

$$
(\rho + p)\dot{u}^a = -p_{;b}(g^{ba} + u^a u^b)
\tag{19}
$$

where $\rho = \mu(1 + \epsilon)$, μ is the density, ϵ is the internal energy and the pressure p is given by $p = \mu^2(d\epsilon/d\mu)$. So $\dot{u}^a$ is the acceleration.

We now turn to the form of the energy momentum tensor. The conservation of current may be expressed as:

$$
j^a_{;a} = \frac{1}{\sqrt{-g}}\frac{\partial}{\partial x^a}(\sqrt{-g}j^a)
\tag{20}
$$

or

$$
2\mu\delta\mu = (j^a j^b - j^d j_d g^{ab})\delta g_{ab}
\tag{21}
$$

Now, in general, the Lagrangian L is a scalar function of some fields Ψ^a. The equations of motion can be obtained by the requirement that the action:

$$
I = \int L dv
\tag{22}
$$

be invariant under a variation of the fields in some suitable region. The variation of the fields can be written as an integrand in Δg_{ab} only. Then the integral $\partial I/\partial u$ is:

$$
\frac{1}{2}\int (T^{ab}\delta g_{ab})dv
\tag{23}
$$

where T^{ab} are the components of a symmetric tensor which is taken to be the energy momentum tensor of the fields. Thus, from equations (21)-(23), we get:

$$T^{ab} = \left[\mu(1+\epsilon) + \mu^2 \frac{d\epsilon}{d\mu}\right] u^a u^b + \mu^2 \frac{d\epsilon}{d\mu} g^{ab} \tag{24}$$

or, finally

$$T_{ab} = (\rho + p)u_a u_b + p g_{ab} \tag{25}$$

The four-velocity u_a satisfies the conditions $u_a u^a = -1$ and $u^a \nabla_b u_a = 0$. Then, with the use of Eq. (18), we obtain for the variation of the energy momentum of a perfect fluid the expression

$$\Theta_{ab} = -2T_{ab} + p g_{ab} . \tag{26}$$

As in the case of [20], we take $f(R,T) = R + 2\mathcal{F}(T)$, where $\mathcal{F}(T) = \lambda T$. The gravitational field equations immediately follow from Eq. (11), and are given by

$$R_{ab} - \frac{1}{2}R g_{ab} = 8\pi T_{ab} - 2\mathcal{F}'(T) T_{ab} - 2\mathcal{F}'(T)\Theta_{ab} + \mathcal{F}(T)g_{ab} , \tag{27}$$

where the prime denotes a derivative with respect to the argument.

For the perfect fluid (25), $\Theta_{ab} = -2T_{ab} + p g_{ab}$, and the field equations become

$$R_{ab} - \frac{1}{2}R g_{ab} = 8\pi T_{ab} + 2\mathcal{F}'(T) T_{ab} - 2p\mathcal{F}'(T)g_{ab} + \mathcal{F}(T)g_{ab} . \tag{28}$$

The above equation for $\mathcal{F}(T) = \lambda T$, i.e., $f(R,T) = R + 2\lambda T$, where the trace $T = -\rho + 3p$ finally simplifies as follows:

$$R_{ab} - \frac{1}{2}R g_{ab} = (8\pi + 2\lambda)T_{ab} + \lambda(p - \rho)g_{ab}. \tag{29}$$

3. BRIEF OUTLINE OF THE RAMESH/UMADEVI PAPER

In this section, we briefly outline the paper [20]. The FLRW metric was given by

$$ds^2 = -dt^2 + a^2(t)\left[\frac{dr^2}{1 - kr^2} + r^2(d\theta^2 + \sin^2\theta d\phi^2)\right], \tag{30}$$

where a is the scale factor, (r, θ, ϕ) are the usual spherical coordinates, and k represents the geometrical curvature of the universe, i.e., $k = 0$ implies a flat universe, $k = +1$ is a closed universe, and $k = -1$ is an open universe. For the FLRW metric (30), and the energy–momentum tensor (25), the field equations (29) in $f(R,T)$ gravity have been given as [20]:

$$2\left(\frac{\ddot{a}}{a}\right) + \left(\frac{\dot{a}^2}{a^2}\right) + \frac{k}{a^2} = p(8\pi + 7\lambda) - \lambda p, \tag{31}$$

$$3\left(\frac{\dot{a}^2}{a^2}\right) + 3\frac{k}{a^2} = p(8\pi + 3\lambda) + 5\lambda p. \tag{32}$$

Ramesh and Umadevi then make two assumptions to derive their solutions, viz.,
1. A barotropic equation of state (EoS) of the form

$$p = \epsilon\rho, \ \epsilon = constant \tag{33}$$

where the constant $\epsilon = -1$ to describe DE, $\epsilon = 0$ for pressure-free matter (dust), $\epsilon = 1/3$ for radiation.
2. A linear varying deceleration parameter (LVDP) q of the form [14]

$$q \equiv -\frac{\ddot{a}a}{\dot{a}^2} = -nt + m - 1, \tag{34}$$

where $n \geq 0$ and $m \geq 0$ are constants.

Solving (34), the solutions were given as the three different forms for the scale factor:

$$a = a_0 exp\left[\frac{2}{\sqrt{m^2 - 2c_1 n}}\operatorname{arctanh}\left(\frac{nt - m}{\sqrt{m^2 - 2c_1 n}}\right)\right] \quad \text{for } n > 0 \text{ and } m \geq 0, \tag{35}$$

$$a = a_0(mt + c_2)^{1/m} \quad \text{for } n = 0 \text{ and } m > 0, \tag{36}$$

$$a = a_0 e^{c_1 t} \quad \text{for } n = 0 \text{ and } m = 0, \tag{37}$$

where a_0, a_1, a_2, a_3, c_1, c_2 and c_3 are constants of integration.

It is then stated that by taking $a_0 = 0$ in equation (35), the following solution is obtained:

$$a(t) = exp\left[\frac{2}{m}\text{arctanh}\left(\frac{n}{m}t - 1\right)\right].$$ (38)

The Hubble parameter was given as:

$$H = \frac{\dot{a}}{a} = -\frac{2}{t(nt - 2m)}.$$ (39)

and the energy density as:

$$\rho = \frac{1}{[8\lambda(3\epsilon + 1) + 16\epsilon\lambda]}\left[\frac{24(nt - m + 1)}{(nt^2 - 2mt)^2}\right]$$ (40)

Since they assumed the barotropic equation of state (33) where ϵ is a constant, the pressure is just $p = \epsilon\rho$:

$$p = \frac{\epsilon}{[8\lambda(3\epsilon + 1) + 16\epsilon\lambda]}\left[\frac{24(nt - m + 1)}{(nt^2 - 2mt)^2}\right]$$ (41)

4. REVIEW OF THE SOLUTION IN PREVIOUS SECTION 3

In this section, we first go through the paper [20] as discussed in the previous section, correcting the equations.

- Equations (31) and (32) should read as follows:

$$2\left(\frac{\ddot{a}}{a}\right) + \left(\frac{\dot{a}^2}{a^2}\right) + \frac{k}{a^2} = \lambda\rho - (8\pi + 3\lambda)p,$$ (42)

$$3\left(\frac{\dot{a}^2}{a^2}\right) + 3\frac{k}{a^2} = (8\pi + 3\lambda)\rho - \lambda p.$$ (43)

- Then in the solutions (35), the constants a_1, a_2, a_3 are missing.

- They state that by taking $a_0 = 0$ in equation (35), a solution is obtained. However, if one takes $a_0 = 0$ in equation (35), then one gets $a = 0$.

- In the paragraph just before the conclusion, it is claimed that the energy density ρ us always positive iirrespective of the curvature of the space. However, this is only true if the constants n, m, λ, ϵ are such as to allow positivity - they have to ensure that both numerator and denominator in the equation for the energy density (40) are both positive, or both are negative.

- In their solutions (40) and (41), the "8λ" in the denominators should read "8π".

- We notice that equations (42) and (43) are two equations in the three unknowns a, ρ and p. Hence only one extra condition is necessary to solve these equations. However, in their paper, Ramesh and Umadevi [20] have chosen two conditions, viz., (33) and (34). We now show that any one of them is sufficient to generate solutions, but that only the second condition allows for the transition from an early decelerated universe to a late accelerated one.

Let us start with the first condition of a barotropic equation of state (33), where ϵ is a constant. In this case, equations (42) and (43) can be written as:

$$2\left(\frac{\ddot{a}}{a}\right) + \left(\frac{\dot{a}^2}{a^2}\right) + \frac{k}{a^2} = \lambda\rho - (8\pi + 3\lambda)\epsilon\rho,$$ (44)

$$3\left(\frac{\dot{a}^2}{a^2}\right) + 3\frac{k}{a^2} = (8\pi + 3\lambda)\rho - \lambda\epsilon\rho.$$ (45)

Without loss of generality, we now focus on the case $k = 0$, which can easily be extended to the cases $k = \pm1$. This assumption of the EoS (33) alone is sufficient to obtain a solution since we then have only two unknowns, viz., a and ρ, and two equations. From equations (44) and (45), we obtain the following equation for ρ:

$$[(8\pi + \lambda)^2 - \lambda^2]\rho = -2\lambda\left(\frac{\ddot{a}}{a}\right) + (24\pi + 8\lambda)\left(\frac{\dot{a}^2}{a^2}\right)$$ (46)

It is possible to also write a similar equation for the pressure p alone by eliminating the energy density ρ from equations (42) and (43).The two resulting equations will be sufficient to obtain solutions. The general solutions to these equations are quite complicated, involving hypergeometric functions, so we do not list them here. This is quite unlike general relativity.

We now focus on the second condition of a LVDP (34) alone. This equation alone is enough to find a solution without the additional need for an equation of state. We first note that in the solutions given by [20], viz., (35), (36) and (37), the constants a_1, a_2, a_3 as well as c_3 do not appear. The corrected solutions as given by Akarsu and Dereli [14] to equation (34) are:

$$a = a_1 \, exp \left[\frac{2}{\sqrt{m^2 - 2c_1 n}} \text{arctanh} \left(\frac{nt - m}{\sqrt{m^2 - 2c_1 k}} \right) \right] \quad \text{for } n > 0 \text{ and } m \geq 0, \tag{47}$$

$$a = a_2 (mt + c_2)^{\frac{1}{m}} \quad \text{for } n = 0 \text{ and } m > 0, \tag{48}$$

$$a = a_3 e^{c_3 t} \quad \text{for } n = 0 \text{ and } m = 0, \tag{49}$$

where a_1, a_2, a_3, c_1, c_2 and c_3 are constants of integration. In these solutions, we see the constants a_1, a_2, a_3 as well as c_3, and also that there is no a_0. The last two of the above solutions are for constant q, which have been dealt with previously. The new solution (47), was found by [14]. Only the solution for $k > 0$ and $m > 0$ is discussed further, and the integration constant c_1 has been set equal to . This sets the initial time of the universe as $t_i = 0$. If we need early deceleration and late-time acceleration, we have to choose $n > 0$ and $m > 0$ for compatibility with the observed universe. The condition $n > 0$ corresponds to increasing acceleration ($\dot{q} = -n < 0$). In order to get early deceleration, the condition $m > 0$ must hold, and it can even be $m > 1$. Hence equation (47) is reduced to:

$$a = a_1 \, exp \left[\frac{2}{m} \text{arctanh} \left(\frac{n}{m} t - 1 \right) \right]. \tag{50}$$

We now have to find the energy density and pressure from equations (42) and (43). Let us first find the Hubble parameter $H = \dot{a}/a$. From equation (50), we find the Hubble parameter as:

$$H \equiv \frac{\dot{a}}{a} = -\frac{2}{t(nt - 2m)}. \tag{51}$$

From the above two equations, we find

$$\frac{\ddot{a}}{a} = \frac{4nt - 4m + 4}{2mt - nt^2} \tag{52}$$

From equations (42) and (43), we can derive an expression for the energy density ρ (for $k = 0$):

$$(64\pi^2 + 16\pi\lambda)\rho = (24\pi + 8\lambda)H^2 - 2\lambda(\dot{H} + H^2) \tag{53}$$

and then using equations (50) and (51), we find that:

$$\rho = \frac{96\pi + 24\lambda - 8\lambda nt + 8\lambda m}{(64\pi^2 + 16\pi\lambda)(nt - 2m)^2 t^2} \tag{54}$$

This solution for ρ is a generalisation of the one given by Akarsu and Dereli [14] for the case $k = 0$, and it reduces to that when $\lambda = 0$ (note the system of units we are using corresponds to that used in [20] in which they put only the gravitational constant $G = 1$. In ref [14], the condition $8\pi G = 1$ is used). The pressure may also be determined similarly, as well as for the cases $k = \pm 1$.

Now we determine the equation for the pressure using the LVDP. Again, from equations (50) and (51), we get (for $k = 0$):

$$p = -\frac{64\pi(kt - m + \frac{3}{2}) + 24\lambda - 24m\lambda + 24n\lambda t}{(64\pi^2 + 48\pi\lambda + 8\lambda^2)(nt^2 - 2mt)^2}. \tag{55}$$

The equation of state $\omega = p/\rho$ is given by:

$$\omega = \frac{(64\pi(nt - m + \frac{3}{2}) + 24\lambda - 24m\lambda + 24n\lambda t)(64\pi^2 + 16\pi\lambda)}{(64\pi^2 + 48\pi\lambda + 8\lambda^2)(96\pi + 24\lambda - 8\lambda nt + 8\lambda m)} \tag{56}$$

It can be seen clearly that the pressure (55) is not just a multiple of the energy density (54), as can also be seen from the equation of state (56). If we put $\lambda = 0$, then we recover general relativity, and the corresponding equations as in [14]. They have plotted all these parameters in general relativity, and shown that with a LVDP, it is possible to obtain a transition from deceleration to acceleration. In addition, they have shown that for the values $m = 0.097$ and $n = 1.6$, it is possible to satisfy observational constraints.

5. CONCLUSION

In this work, we have discussed the FLRW solutions in $f(R,T)$ using a linear deceleration parameter. We first began by giving a brief review of the $f(R,T)$ theory of gravity. Then we discussed the paper by Ramesh and Umadevi [20]. Various points from that paper were been clarified. The full solutions to the equations for a linearly varying deceleration parameter as proposed by Akarsu and Dareli were provided and discussed next. We note the following:

- The solutions with a LVDP do not have a barotropic equation of state in general.

- In the above sense, either of the assumptions made is not compatible with the other, and each has to be made separately to generate solutions.

- The solutions in f(R,T) theory provide a transition from deceleration to acceleration.

- The kinematical quantities such as the scale factor, Hubble parameter and deceleration parameter have the same behaviour as that discusssed by Akarsu and Dareli [14].

- f(R,T) offers a wider range of possibilities than general relativity.

- Several investigations have been made with slightly different forms of the LVDP such as linear in different forms of time t, the redshift z, or in the scale factor a [24]. These authors found that these models compare just as well, if not better, than the standard ΛCDM model.

ORCID

Aroonkumar Beesham, https://orcid.org/0000-0001-5350-6396

REFERENCES

[1] C.L. Bennett, *et al*., Astrophys. J. Suppl. **148**, 1 (2003). https://doi.org/10.1086/377253; D.N. Spergel, *et al*., Astrophys. J. Suppl. **148**, 175 (2003). https://doi.org/10.1086/377226; D.N. Spergel, *et al*., Astrophys. J. Suppl. **170**, 377 (2007) https://doi.org/10.1086/513700.

[2] S. Perlmutter, *et al*., Astrophys. J. **483**, 565 (1997). https://doi.org/10.1086/304265; S. Perlmutter, *et al*., Nature, **391**, 51 (1998). https://doi.org/10.1038/34124; S. Perlmutter, *et al*., Astrophys. J. **517**, 565 (1999). https://doi.org/10.1086/307221; A.G. Riess, *et al*., Astrophys. J. **607**, 665 (2004). https://doi.org/10.1086/383612; A.G. Riess, *et al*., Astrophys. J. **659**, 98 (2007). https://doi.org/10.1086/510378

[3] E. Hawkins, *et al*., Mon. Not. Roy. Astron. Soc. **346**, 78 (2003). https://doi.org/10.1046/j.1365-2966.2003.07063.x; M. Tegmark, *et al*., Phys. Rev. **D69**, 103501 (2004). https://doi.org/10.1103/PhysRevD.69.103501; S. Cole, *et al*., Mon. Not. Roy. Astron. Soc. **362**, 505 (2005) https://doi.org/10.1111/j.1365-2966.2005.09318.x.

[4] D.J. Eisentein, *et al*., Astrophys. J. **633**, 560 (2005) https://doi.org/10.1086/466512.

[5] B. Jain, and A. Taylor, Phys. Rev. Lett. **91**, 141302 (2003) https://doi.org/10.1103/PhysRevLett.91.141302.

[6] V. Sahni, and A.A. Starobinsky, Int. J. Mod. Phys. **D9**, 373 (2000). https://doi.org/10.1142/S0218271800000542; V. Sahni, in: *The Physics of the Early Universe. Lecture Notes in Physics*, edited by E. Papantonopoulos (Springer, Berlin, Heidelberg), **653**, 141 (2004). https://doi.org/10.1007/978-3-540-31535-3_5; T. Padmanabhan, Gen. Relativ. Gravit. **40**, 529 (2008). https://doi.org/10.1007/s10714-007-0555-7

[7] R.R. Caldwell, Phys. Lett. B, **545**, 23 (2002). https://doi.org/10.1016/S0370-2693(02)02589-3; S. Nojiri, and S.D. Odintsov, Phys. Lett. B, **562**, 147 (2003). https://doi.org/10.1016/S0370-2693(03)00594-X; S. Nojiri, and S.D. Odintsov, Phys. Lett. B, **565**, 1 (2003). https://doi.org/10.1016/S0370-2693(03)00753-6

[8] B. Feng, X.L. Wamg, and X.M. Zhang, Phys. Lett. B, **607**, 35, (2005). https://doi.org/10.1016/j.physletb.2004.12.071; Z.K. Guo, *et al*., Phys. Lett. B, **608**, 177 (2005) https://doi.org/10.1016/j.physletb.2005.01.017.

[9] A. Kamenshchik, U. Moschella, and V. Pasquier, Phys. Lett. B, **511**, 265 (2001). https://doi.org/10.1016/S0370-2693(01)00571-8; M.C. Bento, O. Bertolami, and A.A. Sen, Phys. Rev. D, **66**, 043507 (2002). https://doi.org/10.1103/PhysRevD.66.043507

[10] T. Padmanabhan, Phys. Rev. D, **66** 021301 (2002). https://doi.org/10.1103/PhysRevD.66.021301; A. Sen, JHEP, **2002**(04), 048 (2002). https://doi.org/10.1088/1126-6708/2002/04/048

[11] S. Nojiri, and S.D. Odintsov, Int. J. Geom. Methods Mod. Phys. **4**, 115 (2007). https://doi.org/10.1142/S0219887807001928; T.P. Sotiriou, and S. Liberati, Ann. Phys. **322**, 935 (2007). https://doi.org/10.1016/j.aop.2006.06.002; T.P. Sotiriou, and V. Faraoni, Rev. Mod. Phys. **82**, 451 (2010). https://doi.org/10.1103/RevModPhys.82.451; A. De Felice, and S. Tsujikawa, Living Rev. Rel. **13**, 3 (2010). https://doi.org/10.12942/lrr-2010-3

[12] T.Harko, F.S.N. Lobo, S. Nojiri, and S.D. Odintsov, Phys. Rev. D, **84**, 024020 (2011). https://doi.org/10.1103/PhysRevD.84.024020

[13] M.J.S. Houndjo, Int. J. Mod. Phys. D, **21**, 1250003 (2012). https://doi.org/10.1142/S0218271812500034

[14] Ö. Akarsu, and T. Dereli, Int. J. Theor. Phys. **51**, 612 (2012). https://doi.org/10.1007/s10773-011-0941-5

[15] D. Çağlar, Mod. Phys. Lett. A, **39**, 2350197 (2024). https://doi.org/10.1142/S0217732323501973

[16] B. Bishi, A. Beesham, and K.L.Z. Mahanta, Zeitschrift für Naturforschung A, **77**, 259 (2022). https://doi.org/10.1515/zna-2021-0192

[17] D. Sofuoğlu, H. Baysal, and R.K. Tiwari, Eur. Phys. J. Plus, **138**, 550 (2023). https://doi.org/10.1140/epjp/s13360-023-04182-z

[18] A. Alkaoud, M.A. Bakry, A. Eid, and M.M. Khader, Mod. Phys. Lett. A, **39**, 2450061 (2024). https://doi.org/10.1142/S0217732324500615

[19] M.A. Bakry, A. Eid, and A. Alkaoud, Pramana, **96**, 108 (2022). https://doi.org/10.1007/s12043-022-02345-8

[20] G. Ramesh, and S. Umadevi, Astrophys. Space Sci. **361**, 2 (2016). https://doi.org/10.1007/s10509-015-2588-9

[21] T. Koivisto, Class. Quant. Grav. **23**, 4289 (2006). https://doi.org/10.1088/0264-9381/23/12/N01

[22] P.H.R.S. Moraes, Eur. Phys. J. C, **79**, 674 (2019). https://doi.org/10.1140/epjc/s10052-019-7195-4

[23] S.W. Hawking, and G.F.R. Ellis, *The large scale structure of spacetime*, (Cambridge University Press, Cambridge, UK., 1973).

[24] Ö. Akarsu, T. Dereli, S. Kumar, and L. Xu, Eur. Phys. J. Plus, **129**, 22 (2014). https://doi.org/10.1140/epjp/i2014-14022-6

КОСМОЛОГІЧНА МОДЕЛЬ FLRW У f(R,T) ГРАВІТАЦІЇ
Арункумар Бішем

Технологічний університет Мангосуту, ПС 12363, Джейкобс, 4026, Південна Африка

У цій статті обговорюються космологічні моделі Фрідмана-Леметра-Робертсона-Уокера з ідеальною рідиною в f(R,T) теорії гравітації. Існує кілька способів створення рішень. Один із способів — припустити баротропне рівняння стану. Інший полягає у використанні параметра уповільнення, який змінюється лінійно з часом. Оглядається існуюче рішення в літературі, де рішення отримані шляхом припущення, на додаток до баротропного рівняння стану, лінійного змінного параметра уповільнення. Зазначається, що таке припущення призводить до надмірної визначеності рішення. Отже, здійсненність рішень є необхідною умовою, яка повинна бути задоволена. Лише одне з припущень рівняння стану або лінійно змінного параметра уповільнення є достатнім для створення рішень. Надаються та обговорюються відповідні рішення.

Ключові слова: *f(R,T) гравітація; моделі FLRW; лінійний змінний параметр уповільнення; космологічні рішення; здійсненність рішень*

NONLINEAR ION-ACOUSTIC SOLITARY WAVES IN A WEAKLY RELATIVISTIC ELECTRON-POSITRON-ION PLASMA WITH RELATIVISTIC ELECTRON AND POSITRON BEAMS

Satyendra Nath Barman[a], **Kingkar Talukdar**[b]*

aB. Borooah College, Guwahati 781007, Assam, India
bDepartment of Mathematics, Gauhati University, Guwahati 781014, Assam, India
*Corresponding author e-mail: kingkartalukdar5@gmail.com

In this investigation, compressive and rarefactive solitons are demonstrated to exist in a plasma model that includes unmagnetized weak-relativistic positive ions, negative ions, electrons, electron beam and positron beam. For these weakly relativistic non-linear ion-acoustic waves in unmagnetized plasma with electron inertia and relativistic beam, the existence of compressive and rarefactive soliton is investigated by deriving the Korteweg-de Vries (KdV) equation. It has been observed that the amplitude and width of compressive and rarefactive solitons vary differently in response to pressure variation and the presence of electron inertia. The research determines the requirements that must be met for the existence of the nonlinear ion-acoustic solitons. The fluid equations of motion governing the one-dimensional plasma serve as the foundation for the analysis. Various relational forms of the strength parameter (ε) are chosen to stretch the space and time variables, leading to a variety of nonlinearities. The findings can have implications not only for astrophysical plasmas but also for inertial confinement fusion plasmas.

Keywords: *Relativistic plasma; Soliton; Ion acoustic wave; Positron Beam; Perturbation theory*
PACS: 52.35.Sb, 52.27.Ny, 52.35.Fp, 41.75.Ht, 52.65.Vv

INTRODUCTION

Kalita, Das and Sarmah [1] have investigated the existence of relativistic compressive solitons of the fast ion acoustic mode in plasmas where the ion beam is drifting perpendicular to the direction of the magnetic field and Q $(= m_b/m_i$, the ratio of the mass of the ion beam to the mass of the ions) is greater than or equal to 1. In these considerations, however, the relativistic Lorentz factor γ is not taken into account by the Poisson's equation or the equation of continuity. Furthermore, some authors, like ElLabany and El-Taibany [2], have studied electronacoustic (EA) solitons without accounting for relativistic effects. Non-relativistic electron acoustic solitary waves were studied by El-Shewy and El-Shamy [3], taking non-thermal electrons into consideration. By using the pseudo potential approach, Alinejad [4] has investigated the characteristics of arbitrary amplitude dust ion acoustic solitary waves in a dusty plasma that contains warm adiabatic, electron following flat-trapped velocity distribution, and arbitrarily (positively or negatively) charged dust immobile dust. The formation of dust ion acoustic solitons in an unmagnetized plasma with the electrons drift velocity through the modified KdV equation has been studied by Das and Karmakar [5]. By resolving the time fractional modified KdV equation, Nazari-Golshan and Nourazar [6] have investigated the nonlinear propagation of small but finite amplitude dust ion-acoustic solitary waves in unmagnetized dusty plasma with trapped electrons and electron solitary waves have been investigated in [13-15] with trapped electrons. Kalita and Das [7] studied both compressive and rarefactive KdV solitons of interesting character in a plasma model consisting of ions and electrons with pressure variations in both the components in the presence of stationary dust. In multispecies plasma model, consisting of negative mobile dusts, non-thermal ions and Boltzmann electrons, dust-ion acoustic solitary waves are studied by Das [8] through reductive perturbative technique by deriving corresponding KdV equation. Different modes of dust ion acoustic waves have been studied theoretically and numerically by Hasnan, Biswas, Habib and Sultana [9] taking into account a four-component magnetised collisional k-nonthermal plasma containing non-inertial k-distributed super thermal electrons, stationary dust grains of opposite charges, and inertial ion fluid. Das [10] investigated the role of streaming speeds of ions and relativistic electrons together with the immobile dust charge to form dust-ion acoustic compressive and rarefactive relativistic solitons in a multispecies plasma model for immobile dusty plasma. Oblique propagation of the quantum electrostatic solitary waves in magnetized relativistic quantum plasma is investigated using the quantum hydrodynamic equations by Soltani, Mohsenpour and Sohbatzadeh [11]. Singh, Kakad, Kakad, Saini [12] studied the evolution of ion acoustic solitary waves (IASWs) in pulsar wind. The study of nonlinear phenomena in their various manifestations is an interesting field of study in many physical contexts [13-16]. Solitons represent a remarkable natural example of nonlinear structure in both magnetised and unmagnetized plasmas [13-16]. Electron solitary wave has been investigated in [16] with resonant electrons. The formation of nonlinear structures like electron acoustic solitons (EAS), ion acoustic solitons (IAS), and double layers [17-20] is being studied by a large number of researchers worldwide. Moreover, space missions such as Solar Anomalous and the Magnetospheric Particle Explorer have demonstrated that relativistic electrons are a threat to the International Space Stations. It may be tried to balance the nonlinear effect by dispersion that leads to solitons in the context of wave particle interactions, in order to avoid warning of the dangers. Space observations with energies greater

than 150 keV confirm the existence of highly relativistic electrons associated with ions in the "Outer zone of the radiation belt" that stretches to distance.

EQUATIONS GOVERNING DYNAMICS OF PLASMA

The fluid equations of motion, governing the collision less dusty plasma in one dimension are:
for positive ions,

$$\frac{\partial n_i}{\partial t} + \frac{\partial (n_i u_i)}{\partial x} = 0 , \tag{1}$$

$$\frac{\partial \gamma_i u_i}{\partial t} + u_i \frac{\partial \gamma_i u_i}{\partial x} = -\frac{\partial \phi}{\partial x}, \tag{2}$$

for negative ions,

$$\frac{\partial n_j}{\partial t} + \frac{\partial (n_j u_j)}{\partial x} = 0, \tag{3}$$

$$\frac{\partial \gamma_j u_j}{\partial t} + u_j \frac{\partial \gamma_j u_j}{\partial x} = \frac{1}{Q'} \frac{\partial \phi}{\partial x}, \tag{4}$$

$$(Q' = \frac{\text{negative ion mass}}{\text{positive ion mass}} = m_j / m_i)$$

for electrons,

$$\frac{\partial n_e}{\partial t} + \frac{\partial (n_e u_e)}{\partial x} = 0 , \tag{5}$$

$$\frac{\partial \gamma_e u_e}{\partial t} + u_e \frac{\partial \gamma_e u_e}{\partial x} = \frac{1}{Q} \frac{\partial \phi}{\partial x} - \frac{1}{Q n_e} \frac{\partial p_e}{\partial x}, \tag{6}$$

$$\frac{\partial p_e}{\partial t} + u_e \frac{\partial p_e}{\partial x} + 3 p_e \frac{\partial \gamma_e u_e}{\partial x} = 0, \tag{7}$$

$$(Q = \frac{\text{electron mass}}{\text{positive ion mass}} = m_e / m_i)$$

for electron beam,

$$\frac{\partial n_b}{\partial t} + \frac{\partial (n_b u_b)}{\partial x} = 0, \tag{8}$$

$$\frac{\partial \gamma_b u_b}{\partial t} + u_b \frac{\partial \gamma_b u_b}{\partial x} = \frac{\partial \phi}{\partial x} - 3\sigma n_b \frac{\partial n_b}{\partial x}, \tag{9}$$

where σ = T_b/T_e = electron beam temperature/electron temperature,
for positron beam,

$$\frac{\partial n_s}{\partial t} + \frac{\partial (n_s u_s)}{\partial x} = 0, \tag{10}$$

$$\frac{\partial \gamma_s u_s}{\partial t} + u_s \frac{\partial \gamma_s u_s}{\partial x} + \frac{1}{\beta} \frac{\partial \phi}{\partial x} = 0. \tag{11}$$

$$(\beta = \frac{\text{positive ion-beam mass}}{\text{positive ion mass}} = m_s / m_i)$$

The basic governing equations are the continuity and the momentum equations of acoustic mode of the plasma. Equations (7) provides the adiabatic response which contributes additional sources of energy to the non-linearity in the usual ion-electron inertial dynamical system. Electron inertia, which is usually neglected, is considered. Again, these equations are to be supplemented by the following Poisson equation for the charge imbalances.

$$\frac{\partial^2 \phi}{\partial x^2} = n_e + n_j - n_i + n_b - n_s, \tag{12}$$

where, $\gamma_a = \{1 - (\frac{u_a}{c})^2\}^{-\frac{1}{2}} = 1 + \frac{u_a^2}{2c^2}, a = i, j, e, b, s$ and c is the speed of light. Here, suffixes *i, j,e,b* and *s* stand for positive ion, negative ion, electron, electron beam and positron beam respectively. In this case, we normalize densities by the equilibrium plasma density n_0; velocities (including c) by the acoustic speed $c_s = (\frac{k_b T_e}{m_i})^{\frac{1}{2}}$; time *t* by the inverse of the characteristic ion plasma frequency $\omega_{pi}^{-1} = (m_i/4\pi n_{e0}e^2)^{1/2}$; the distance *x* by the Debye length $\lambda_{De} = (k_b T_e/4\pi n_{e0}e^2)^{1/2}$; the electron pressure p_e by the characteristic electron pressure $p_{e0} = n_{e0}k_b T_e$; and, the electric potential ϕ by $(\frac{k_b T_e}{e})$, where k_b is the Boltzmann constant and T_e is the characteristic electron temperature.

KdV Equation and its Solution

We use the stretched variables

$$\xi = \varepsilon^{\frac{1}{2}}(x - Vt) \text{ and } \tau = \varepsilon^{\frac{3}{2}}t \tag{13}$$

(where V is the phase velocity) along with the expansions of the flow variables in terms of the smallness parameter ε as $n_k = n_{k0} + \varepsilon n_{k1} + \varepsilon^2 n_{k2} + \varepsilon^3 n_{k3} + ...$, $u_k = u_{k0} + \varepsilon u_{k1} + \varepsilon^2 u_{k2} + \varepsilon^3 u_{k3} + ...$, $p_e = 1 + \varepsilon p_{e1} + \varepsilon^2 p_{e2} + \varepsilon^3 p_{e3} + ...$, $\phi = \varepsilon \phi_1 + \varepsilon^2 \phi_2 + \varepsilon^3 \phi_3 + ...$, (k = i,j,e,b and s), where $n_{e0} = 1$, $n_{b0} = 1$ and $u_{e0} = 1$ to derive the KdV equation from the set of equations (1) to (11).

Using the transformation (13) and the expansions of $n_i, n_j, n_e, n_b, u_i, u_j, u_e, u_b$ and p_e in equations (1) to (11) and equating the coefficient of the first lowest-order of ε we get,

$$n_{i1} = \frac{n_{i0}}{(V-u_{i0})^2\beta_i}\phi_1, \quad u_{i1} = \frac{1}{(V-u_{i0})\beta_i}\phi_1, \quad n_{j1} = \frac{-n_{j0}}{(V-u_{j0})^2Q'\beta_j}\phi_1, \quad u_{j1} = -\frac{1}{(V-u_{j0})Q'\beta_j}\phi_1,$$

$$n_{e1} = \frac{1}{\{3-(V-u_{e0})^2Q\}\beta_e}\phi_1, \quad u_{e1} = \frac{(V-u_{e0})}{\{3-(V-u_{e0})^2Q\}\beta_e}\phi_1, \quad p_{e1} = \frac{3}{\{3-(V-u_{e0})^2Q\}}\phi_1,$$

$$n_{b1} = -\frac{n_{b0}\phi_1}{(V-u_{b0})^2\beta_b-3\sigma n_{b0}}, \quad u_{b1} = -\frac{(V-u_{b0})}{(V-u_{b0})^2\beta_b-3\sigma n_{b0}}\phi_1,$$

$$n_{s1} = \frac{n_{s0}\phi_1}{(V-u_{s0})^2\beta\beta_s}, \quad u_{s1} = \frac{1}{\beta(V-u_{s0})\beta_s}\phi_1,$$

$$\text{with } \beta_i = 1 + \frac{3u_{i0}^2}{2c^2}, \quad \beta_j = 1 + \frac{3u_{j0}^2}{2c^2}, \quad \beta_e = 1 + \frac{3u_{e0}^2}{2c^2}, \quad \beta_b = 1 + \frac{3u_{b0}^2}{2c^2} \text{ and } \beta_s = 1 + \frac{3u_{s0}^2}{2c^2},$$

where $u_{i0}, u_{j0}, u_{e0}, u_{b0}$ and u_{s0} are initial streaming velocities of relativistic positive ions, relativistic negative ions, relativistic electrons, relativistic electron beam and relativistic electron beam respectively.

Using the expansions of $n_{i1}, n_{j1}, n_{e1}, n_{b1}$ and n_{s1} in $n_{e1} + n_{j1} - n_{i1} + n_{b1} - n_{s1} = 0$, the expression of phase velocity V is found as

$$\frac{1}{\{3-(V-u_{e0})^2Q\}\beta_e} - \frac{n_{j0}}{(V-u_{j0})^2Q'\beta_j} - \frac{n_{i0}}{(V-u_{i0})^2\beta_i} - \frac{n_{b0}\phi_1}{(V-u_{b0})^2\beta_b-3\sigma n_{b0}} - \frac{n_{s0}\phi_1}{(V-u_{s0})^2\beta\beta_s} = 0.$$

Eliminating $u_{i2}, u_{j2}, u_{e2}, u_{b2}, u_{s2}$ and p_{e2} from the equations obtained by equating the coefficient of second higher order terms of ε we get the KdV equation as,

$$\frac{\partial\phi_1}{\partial\tau} + p\,\phi_1\frac{\partial\phi_1}{\partial\xi} + q\frac{\partial^3\phi_1}{\partial\xi^3} = 0, \tag{14}$$

where

$$p = \frac{K_1}{K_2}, \quad q = \frac{1}{-K_2},$$

$K_1 = (n_{b0}L_5D_4^2\beta_i^3D_1^4Q'^2\beta_j^3D_2^4\beta_e^3L_1^2 - 2\beta_b n_{b0}D_4^2\beta_i^3D_1^4Q'^2\beta_j^3D_2^4\beta_e^3L_1^2 - 3\sigma n_{b0}^3\beta_i^3D_1^4Q'^2\beta_j^3D_2^4\beta_e^3L_1^2 - 3n_{i0}L_2L_6^3Q'^2\beta_j^3D_2^4\beta_e^3L_1^2 + 3n_{j0}L_3L_6^3\beta_i^3D_1^4\beta_e^3L_1^2 + 3(L_4 - l_7)L_6^3\beta_i^3D_1^4Q'^2\beta_j^3D_2^4)/(L_6^3\beta_i^3D_1^4Q'^2\beta_j^3D_2^4\beta_e^3L_1^2)$

$$K_2 = \frac{-2n_{i0}Q'\beta_jD_2^3\beta_eL_1^2L_6^2 - 2n_{j0}D_1^3\beta_i\beta_eL_1^2L_6^2 - 2QD_3D_1^3\beta_iQ'\beta_jD_2^3L_6^2 - 2n_{b0}\beta_bD_4D_1^3\beta_iQ'\beta_jD_2^3\beta_eL_1^2}{D_1^3\beta_iQ'\beta_jD_2^3\beta_eL_1^2L_6^2}$$

$$\text{and } D_1 = V - u_{i0}, \quad D_2 = V - u_{j0}, \quad D_3 = V - u_{e0}, \quad D_4 = V - u_{b0},$$

$$L_1 = 3 - Q(V - u_{e0})^2, \quad L_2 = \beta_i - \frac{u_{i0}(V-u_{i0})}{c^2}, \quad L_3 = \beta_j - \frac{u_{j0}(V-u_{j0})}{c^2}, \quad L_4 = \beta_e - \frac{u_{e0}(V-u_{e0})}{c^2},$$

$$L_5 = \frac{3u_{b0}(V-u_{b0})}{c^2} - \beta_b, \quad L_6 = 3\sigma n_{b0} - (V - u_{b0})^2\beta_b, \quad L_7 = \frac{\beta_e(1+3\beta_e)}{L_1}$$

We introduce the variable $\eta = \xi - U\tau$, where U is the velocity of the wave in the linear η space, to find a stationary solution of the KdV equation (14). Equation (14) can be integrated using the boundary conditions $\phi_1 = \frac{\partial\phi_1}{\partial\eta} = \frac{\partial^2\phi_1}{\partial\eta^2} = 0$ as $|\eta| \to \infty$, to give

$$\phi_1 = \phi_0\text{sech}^2(\eta/\Delta) \tag{15}$$

where $\phi_0 = (3U/p)$ is the amplitude and $\Delta = (4q/U)^{1/2}$ is the width of the soliton respectively.

RESULTS AND DISCUSSION

Week relativistic effects are incorporated in pursuit of the formation of solitary waves in this plasma model. For nonlinear ion-acoustic solitary waves we have used the reductive perturbation theory to reduce the basic set of equations to KdV equation (14). We have investigated the effects of plasma parameters on the nature of the solitary waves in this model of plasma and displayed their variation graphically in figures 1 to 12. For numerical analysis, some appropriate values of plasma parameters are considered as: $c = 300$, $Q = 0.00054$.
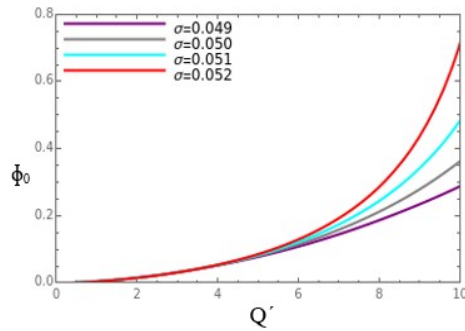
Figure 1. Variation of amplitude with respect to Q′ for different σ and fixed $U = 0.03$, $u_{i0} = 1.17$, $V = 0.74$, $u_{j0} = 0.95$, $n_{i0} = 1.06$, $n_{b0} = 1.06$, $u_{b0} = 0.95$, $n_{j0} = 1.06$, $u_{e0} = 1.22$, $n_{s0} = 1.27$, $u_{s0} = 1.01$
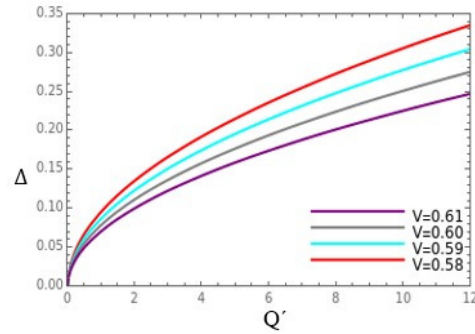
Figure 2. Variation of width with respect to Q′ for different V and fixed $U = 1.01$, $u_{i0} = 1.11$, $u_{j0} = 1.17$, $n_{i0} = 1.22$, $n_{b0} = 1.33$, $u_{b0} = 1.01$, $n_{j0} = 0.79$, $σ = 0.412$, $u_{e0} = 0.74$, $n_{s0} = 1.11$, $u_{s0} = 0.75$

Variation of amplitude with respect to mass ratio is shown in Figure 1. The figure shows that when we increase mass ratio while keeping other parameters mixed the amplitude increases positively. Therefore, we can say that our plasma model has compressive solitons whose amplitude increases as we increase the value of mass ratio. If we increase the value of σ from 0.049 to 0.052 we observe that the soliton amplitude gradually rises. Thus, we can say that we get compressive solitons of higher amplitude for greater values of σ in the comparison of amplitude with respect to mass ratio. Figure 2 shows variation of width with respect to mass ratio. While keeping other parameters fixed as mentioned in Figure 2 we observe that soliton width increases as mass ratio increases. We also observe that soliton width increases when phase velocity increases from 0.58 to 0.61 in the comparison of width with respect to mass ratio.

Figure 3 depicts the amplitude variation with respect to n_{s0}. The figure illustrates how the amplitude increases positively when we increase n_{s0} while maintaining fixed values of other parameters. Therefore, we can conclude that our plasma model has compressive solitons whose amplitude increases as we increase the value of n_{s0}. A gradual increase in the soliton amplitude is observed when the mass ratio is increased from 0.65 to 0.83. Therefore, in the comparison of amplitude with respect to n_{s0}, we can say that for larger values of σ, we obtain compressive solitons of higher amplitude. Figure 4 illustrates how width varies in relation to n_{s0}. Soliton width rises as n_{s0} increases, as shown in Figure 4, while other parameters remain fixed. In the comparison of width with respect to n_{s0}, we also find that soliton width increases when mass ratio increases from 0.15 to 0.43.
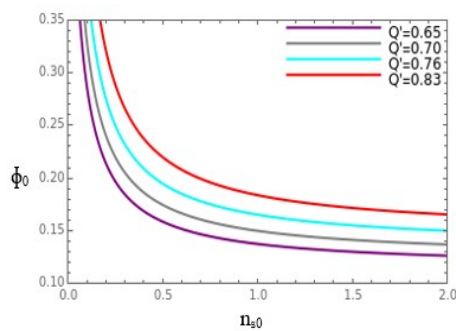

Figure 3. Variation of amplitude with respect to n_{s0} for different Q′ and fixed $U = 0.37$, $u_{i0} = 0.85$, $v = 0.47$, $u_{j0} = 0.9$, $n_{i0} = 0.85$, $n_{b0} = 0.9$, $u_{b0} = 0.42$, $n_{j0} = 0.74$, $σ = 0.047$, $u_{e0} = 0.95$, $u_{s0} = 0.23$
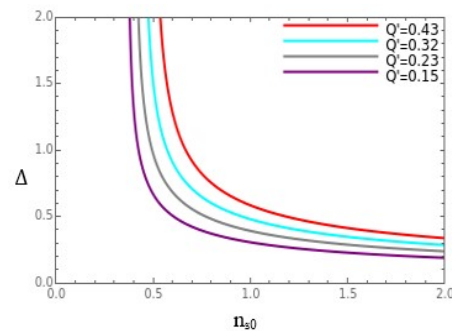
Figure 4. Variation of width with respect to n_{s0} for different Q′ and fixed $U = 1.83$, $u_{i0} = 1.82$, $V = 0.45$, $u_{j0} = 1.43$, $n_{i0} = 1.01$, $n_{b0} = 1.33$, $u_{b0} = 1.64$, $n_{j0} = 0.37$, $σ = 0.071$, $u_{e0} = 1.11$, $u_{s0} = 1.17$

Figure 5 illustrates how the amplitude varies in relation to σ. As we hold other parameters constant, the figure illustrates how the amplitude varies negatively as we increase σ. We can therefore conclude the presence of rarefactive soliton in our plasma model which have increasing amplitude as we increase the value of σ. We find that the soliton amplitude gradually decreases as we increase the mass ratio from 0.87 to 0.94. Therefore, in the comparison of amplitude with respect to σ, we can say that for larger values of mass ratio, we obtain rarefactive solitons of lower amplitude. Figure 6 illustrates how width varies in relation to σ. It is observed that the soliton width increases as σ increases, while other parameters remain fixed as indicated in figure 6. In the comparison of width with respect to σ, we also find that soliton width increases when mass ratio increases from 0.21 to 0.57.
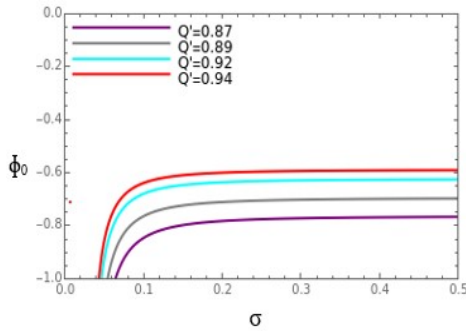
Figure 5. Variation of amplitude with respect to σ for different Q' and fixed $U = 0.9$, $u_{i0} = 1.54$, $V = 1.3$, $u_{j0} = 1.0$, $n_{i0} =1.06$, $n_{b0}= 0.95$, $u_{b0}= 1.43$, $n_{j0}=1.27$, $u_{e0} = 1.06$, $n_{s0}= 0.95$, $u_{s0}= 0.85$
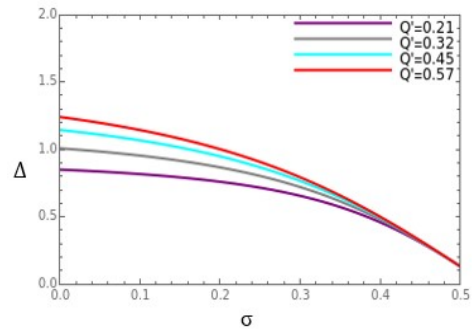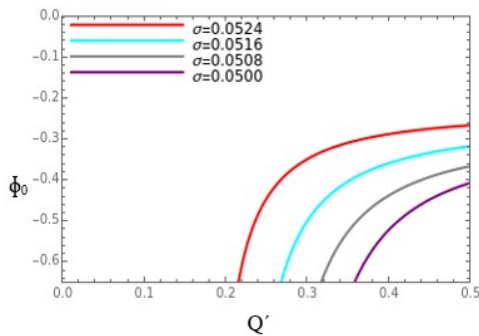

Figure 6. Variation of width with respect to σ for different Q' and fixed $U = 0.85$, $u_{i0} = 0.85$, $v = 2.15$, $u_{j0} = 1.01$, $n_{i0} =1.01$, $n_{b0}= 0.9$, $u_{b0}= 0.95$, $n_{j0}= 1.01$, $n_{s0}= 0.85$, $u_{e0} = 1.11$, $u_{s0}= 1.01$

Figure 7. Variation of amplitude with respect to Q' for different σ and fixed $U = 0.16$, $u_{i0}= 0.9$, $V = 0.7$, $u_{j0} = 1.17$, $n_{i0} =0.79$, $n_{b0}=1.27$, $u_{b0}= 1.17$, $n_{j0}= 1.06$, $\sigma = 0.0524$, $u_{e0} = 1.11$, $n_{s0}= 1.01$, $u_{s0}= 1.11$

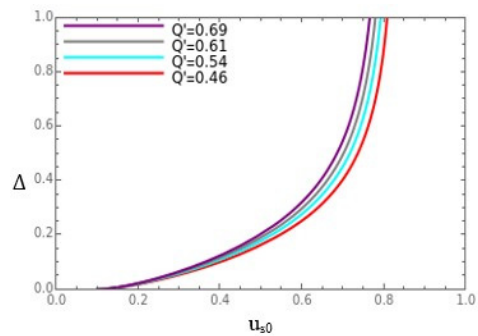**Figure 8.** Variation of width with respect to u_{s0} for different Q' and fixed $U = 1.8$, $u_{i0} = 0.95$, $V = 0.1$, $u_{j0} = 1.49$, $n_{i0} =1.22$, $n_{b0} = 1.27$, $u_{b0}= 0.95$, $n_{j0}= 1.11$, $n_{s0}= 1.43$, $u_{e0} = 1.17$, $\sigma = 0.016$

Figure 7 displays the variation in amplitude in relation to the mass ratio. The graph indicates that the amplitude increases negatively as the mass ratio climbs while the other parameters remain unchanged. As such, we can state the presence of rarefactive solitons in our plasma model whose amplitude increases as we increase the value of mass ratio. The soliton amplitude gradually decreases as we increase the value of σ from 0.0500 to 0.0524. Therefore, when comparing amplitude to mass ratio, we obtain rarefactive solitons with lower amplitudes for higher values of σ. Figure 8 illustrates the variation in width in relation to u_{s0}. We note that soliton width increases as u_{s0} increases while maintaining other parameters fixed, as shown in figure 8. Furthermore, we note that in the comparison of width with respect to u_{s0}, soliton width increases when mass ratio increases from 0.46 to 0.69.

Variation of amplitude with respect to n_{b0} is shown in Figure 9. The figure shows that when we increase n_{b0} while keeping other parameters mixed the amplitude increases positively. Therefore, we can say that our plasma model has compressive solitons whose amplitude increases as we increase the value of n_{b0}. If we increase the value of wave speed from 0.99 to 1.59, we observe that the soliton amplitude gradually rises. Thus, we can say that we get compressive solitons of higher amplitude for greater values of σ in the comparison of amplitude with respect to n_{b0}. Figure 10 shows variation of width with respect to u_{i0}. While keeping other parameters fixed as mentioned in figure 10, we observe that soliton width increases as u_{i0} increases. We also observe that soliton width decreases when u_{j0} increases from 0.53 to 0.74 in the comparison of width with respect to u_{i0}.
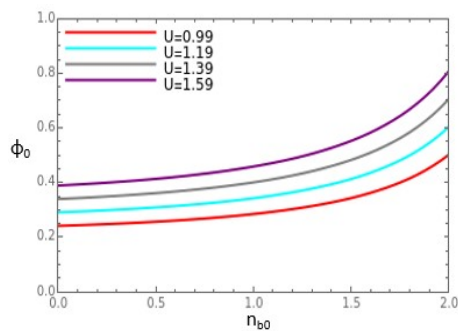

Figure 9. Variation of amplitude with respect to n_{b0} for different U and fixed $u_{i0}=0.62$, $V=0.21$, $u_{j0}=0.39$, $n_{i0}=0.69$, $Q'=0.85$, $n_{s0}=0.53$, $u_{b0}=0.74$, $n_{j0}=0.37$, $\sigma=0.026$, $u_{e0}=0.79$, $u_{s0}=0.53$
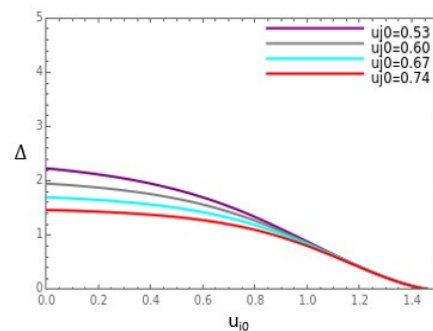

Figure 10. Variation of width with respect to u_{i0} for different u_{j0} and fixed $U=0.21$, $Q'=0.21$, $V=1.49$, $n_{i0}=0.26$, $n_{b0}=0.26$, $u_{b0}=0.26$, $n_{j0}=0.42$, $\sigma=0.018$, $u_{e0}=0.16$, $n_{s0}=0.26$, $u_{s0}=0.37$

Finally, we have observed variation of solitary wave potential φ_1 versus η for four different values of wave speed U as shown in Figure 11 and 12. We found that the wave potential of both compressive (Figure 11) and rarefactive (Figure 12) ion-acoustic soliton increases while the value of wave speed increases.
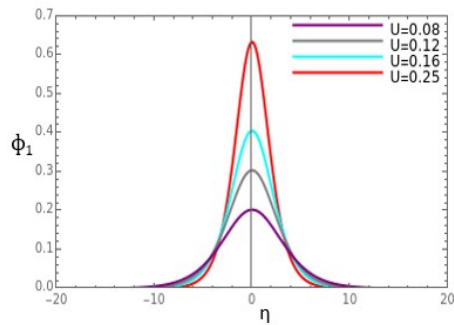

Figure 11. Variation of ϕ_1 with respect to η for different U and fixed $u_{i0} = 4.2$, V = 5.4, $u_{j0} = 0.79$, $n_{i0} = 1.17$, $n_{b0} = 1.59$, $u_{b0} = 1.49$, $n_{j0} = 1.49$, $n_{s0} = 1.43$, $u_{e0} = 1.54$, Q´=0.47, $u_{s0} = 0.47$, $n_{s0} = 0.16$, $\sigma = 0.282$
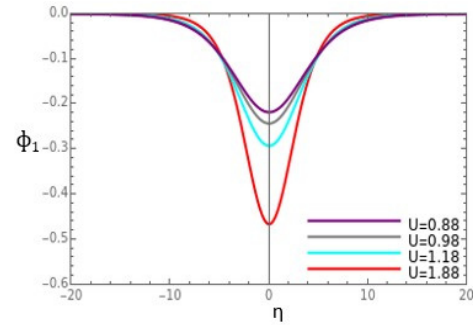
Figure 12. Variation of ϕ_1 with respect to η for different U and fixed $u_{i0} = 0.58$, V = 3.56, $u_{j0} = 0.47$, $n_{i0} = 0.53$, $n_{b0} = 0.58$, $u_{b0} = 0.32$, $n_{j0} = 0.33$, $n_{s0} = 1.43$, $u_{e0} = 0.26$, Q´=0.21, $n_{s0} = 0.42$, $u_{s0} = 0.53$, $\sigma = 0.045$

ORCID
Satyendra Nath Barman, https://orcid.org/0000-0003-1136-8364; **Kingkar Talukdar,** https://orcid.org/0009-0007-5419-134X

REFERENCES

[1]   B.C. Kalita, R. Das, and H.K. Sarmah, "Weakly relativistic solitons in a magnetized ion-beam plasma in presence of electron inertia," Phys. Plasmas, **18**, 012304 (2011). https://doi.org/10.1063/1.3536428

[2]   S.K. El-Labany, and W.F. El-Taibany, "Nonlinear electron-acoustic waves with vortex-like electron distribution and electron beam in a strongly magnetized plasma,"Chaos Solitons Fractals, **33**, 813 (2007). https://doi.org/10.1016/j.chaos.2006.04.039

[3]   E.K. El-Shewy, and E.F. El-Shamy, "Linear and nonlinear properties of electron-acoustic solitary waves with non-thermal electrons," Chaos Solitons Fractals **31**, 1020 (2007). https://doi.org/10.1016/j.chaos.2006.03.104

[4]   H. Alinejad, "Dust ion-acoustic solitary waves in a dusty plasma with arbitrarily charged dust and flat-trapped electrons," Astrophys. Space. Sci. **334**, 331 (2011). https://doi.org/10.1007/s10509-011-0719-5

[5]   R. Das, and K. Karmakar, "Modified Korteweg – de Vries solitons in a dusty plasma with electron inertia and drifting effect of electrons," Can. J. Phys. **91**, 839 (2013). https://doi.org/10.1139/cjp-2012-0360

[6]   A. Nazari-Golshan, and S.S. Nourazar, "Effect of trapped electron on the dust ion acoustic waves in dusty plasma using time fractional modified Korteweg-de Vries equation," Physics of Plasmas, **20**, 103701 (2013). https://doi.org/10.1063/1.4823997

[7]   B.C. Kalita, and S. Das, "Comparative study of dust ion acoustic Korteweg–de Vries and modified Korteweg–de Vries solitons in dusty plasmas with variable temperatures," J. Plasma Phys. **83**, 905830502 (2017). https://doi.org/10.1017/S0022377817000721

[8]   S. Das, "Propagation of dust ion acoustic solitary waves in dusty plasma with Boltzmann electrons," Journal of Physics: Conf. Series, **1290**, 012025 (2019). https://doi.org/10.1088/1742-6596/1290/1/012025

[9]   M.R. Hassan, S. Biswas, K. Habib, and S. Sultana, "Dust–ion-acoustic waves in a κ-nonthermal magnetized collisional dusty plasma with opposite polarity dust," Results in Physics, **33**, 105106 (2022). https://doi.org/10.1016/j.rinp.2021.105106

[10] S. Das, "Weak Relativistic Effect in the Formation of Ion-Acoustic Solitary Waves in Dusty Plasma," IEEE Transactions on Plasma Science, **50**, 2225 (2022). https://doi.org/10.1109/TPS.2022.3181149

[11] H. Soltani, T. Mohsenpour and F. Sohbatzadeh, "Obliquely propagating quantum solitary waves in quantum-magnetized plasma with ultra-relativistic degenerate electrons and positrons," Contributions to Plasma Physics, **59**, e201900038, (2019). https://doi.org/10.1002/ctpp.201900038

[12] K. Singh, A. Kakad, B. Kakad, and N.S. Saini, "Evolution of ion acoustic solitary waves in pulsar wind," Monthly Notices of the Royal Astronomical Society, **500**, 1612 (2021). https://doi.org/10.1093/mnras/staa3379

[13] V. Maslov, and H. Schamel, "Growing electron holes in drifting plasmas," Physics Letters A, **178**(1-2), 171-174 (1993). https://doi.org/10.1016/0375-9601(93)90746-M

[14] H. Schamel, and V.I. Maslov, "Adiabatic growth of electron holes in current-carrying plasmas," Physica Scripta, **T50**, 42 (1994). https://doi.org/10.1088/0031-8949/1994/T50/006

[15] H. Schamel, and V. Maslov, "Langmuir Wave Contraction Caused by Electron Holes," Physica Scripta, **82**, 122 (1999). https://doi.org/10.1238/Physica.Topical.082a00122

[16] V.I. Maslov, "Electron beam excitation of a potential well in a magnetized plasma waveguide," Physics Letters A, **165**(1), 63-68 (1992). https://doi.org/10.1016/0375-9601(92)91055-V

[17] A.F. Tseluyko, V.T. Lazurik, D.L. Ryabchikov, V.I. Maslov, and I.N. Sereda, "Experimental study of radiation in the wavelength range 12.2–15.8 nm from a pulsed high-current plasma diode," Plasma physics reports, **34**(11), 963-968 (2008). https://doi.org/10.1134/S1063780X0811010X

[18] I.V. Borgun, N.A. Azarenkov, A. Hassanein, A.F. Tseluyko, V.I. Maslov, and D.L. Ryabchikov, "Double electric layer influence on dynamic of EUV radiation from plasma of high-current pulse diode in tin vapor," Physics Letters A, **377**(3-4), 307-309 (2013). https://doi.org/10.1016/j.physleta.2012.11.027

[19] A.F. Tseluyko, V.T. Lazuryk, D.V. Ryabchikov, V.I. Maslov, N.A. Azarenkov, I.N. Sereda, D.V. Zinov'ev, *et al*., "Dynamics and directions of extreme ultraviolet radiation from plasma of the high-current pulse diode," Problems of Atomic Science and Technology, (1), 165-167 (2009). https://vant.kipt.kharkov.ua/ARTICLE/VANT_2009_1/article_2009_1_165.pdf

[20] V.I. Maslov, A.P. Fomina, R.I. Kholodov, I.P. Levchuk, S.A. Nikonova, O.P. Novak, and I.N. Onishchenko, "Accelerating field excitation, occurrence and evolution of electron beam near Jupiter," Problems of Atomic Science and Technology, (4), 106-111 (2018). https://vant.kipt.kharkov.ua/ARTICLE/VANT_2018_4/article_2018_4_106.pdf

НЕЛІНІЙНІ ІОННО-АКУСТИЧНІ ОДИНОКІ ХВИЛІ В СЛАБОРЕЛЯТИВІСТСЬКІЙ ЕЛЕКТРОН-ПОЗИТРОН-ІОННІЙ ПЛАЗМІ З РЕЛЯТИВІСТСЬКИМИ ПУЧКАМИ ЕЛЕКТРОНІВ І ПОЗИТРОНІВ

Сатьендра Натх Барман[a], Кінгкар Талукдар[b]
[a]Коледж Б. Боруа, Гувахаті 781007, Ассам, Індія
[b]Департамент математики, Університет Гаухаті, Гувахаті 781014, Ассам, Індія

У цьому дослідженні було продемонстровано існування стискаючих і розріджених солітонів у моделі плазми, яка включає ненамагнічені слабкі релятивістські позитивні іони, негативні іони, електрони, електронний пучок і пучок позитронів. Для цих слабо релятивістських нелінійних іонно-акустичних хвиль у ненамагніченій плазмі з електронною інерцією та релятивістським пучком існування стисливого та розрідженого солітону досліджується шляхом виведення рівняння Кортевега-де Фріза (KdV). Було помічено, що амплітуда та ширина солітонів стиснення та розрідження змінюються по-різному у відповідь на зміну тиску та наявність інерції електронів. Дослідженнями визначено вимоги, які повинні бути виконані для існування нелінійних іонно-акустичних солітонів. Основою для аналізу є рівняння руху рідини, що керують одновимірною плазмою. Різні відносні форми параметра міцності (ε) вибираються для розширення просторових і часових змінних, що призводить до різноманітних нелінійностей. Отримані результати можуть мати наслідки не лише для астрофізичної плазми, але й для термоядерної плазми з інерційним утриманням.

Ключові слова: *релятивістська плазма; солітон; іонна акустична хвиля; пучок позитронів; теорія збурень*

NUMERICAL INVESTIGATION OF THE SQUEEZING FLOW OF TERNARY HYBRID NANOFLUID ($Cu − Al_2O_3 − TiO_2/H_2O$) BETWEEN TWO PARALLEL PLATES IN A DARCY POROUS MEDIUM WITH VISCOUS DISSIPATION AND HEAT SOURCE

 Rubul Bora, Bidyut Boruah*

Department of Mathematics, CNB College, Bokakhat-785612, Assam, India
Corresponding Author e-mail: rubulboracnbc@gmail.com

This work aims to investigate numerically the influence of viscous dissipation and heat source on the magnetohydrodynamics squeezing flow of water-based ternary hybrid nanofluids between two parallel plates in a Darcy porous medium. The nanoparticles Cu, Al_2O_3, and TiO_2 are dispersed in a base fluid H_2O, resulting in the creation of a ternary hybrid nanofluid $Cu − Al_2O_3 − TiO_2/H_2O$. This study examines the deformation of the lower plate as the upper one advances towards it. The numerical results are computed using the 3-stage Lobatto IIIa method, which is specially implemented by Bvp4c in MATLAB. The effects of various parameters are visually illustrated through graphs and quantitatively shown in tables. The absolute skin friction of the ternary hybrid nanofluid is seen to be approximately 5% higher than that of the regular nanofluid at the lower plate and at most 7% higher than that of the nanofluid at the upper plate. The heat transmission rate of the ternary hybrid nanofluid is higher at the upper plate compared to the lower plate.

Keywords: *Thermal radiation; Viscous dissipation; Parallel plate; Heat source; Ternary hybrid nanofluid; Darcy porous medium; bvp*

PACS: 44.05.+e, 44.25.+f, 44.27.+g, 44.40.+a, 47.11.-j, 44.30.+v

1. INTRODUCTION

Ternary hybrid nanofluids consist of three distinct kinds of nanoparticles dispersed in a base fluid. This paper describes a study on a ternary hybrid nanofluid consisting of copper (Cu), aluminum oxide (Al_2O_3), and titanium dioxide (TiO_2) nanoparticles, which are uniformly dispersed in a water-based fluid. This ternary hybrid nanofluid possesses distinctive characteristics that enable it suited for a many different kinds of applications. Introducing copper (Cu) nanoparticles into the nanofluid has been discovered to enhance thermal conductivity, while the inclusion of aluminum oxide (Al_2O_3) and titanium dioxide (TiO_2) nanoparticles has been reported to improve heat transfer efficiency and stability. This nanofluid can be used in a range of applications, including heat exchangers, cooling systems, and electronic devices, to improve heat dissipation and enhance thermal management. Copper nanoparticles exhibit antibacterial properties, while (TiO_2) nanoparticles demonstrate photocatalytic activity against bacteria and other microorganisms. The utilization of the ternary hybrid nanofluid, consisting of $Cu − Al_2O_3 − TiO_2$, has great potential for creating antibacterial coatings on different surfaces, such as textiles, medical equipment, and food packaging. These coatings efficiently hinder bacterial proliferation and help maintain hygiene. Titanium dioxide (TiO_2) nanoparticles possess photocatalytic characteristics, enabling them to effectively catalyze the decomposition of organic pollutants and the sterilization of water. The utilization of the $Cu − Al_2O_3 − TiO_2$, ternary hybrid nanofluid shows promise for implementation in water treatment processes, aiding in the removal of contaminants and improving the overall water quality.

Choi and Eastman [1] were the innovators who first introduced the concept of nanofluids. They claimed that by suspending metallic nanoparticles in conventional heat transfer fluids, a groundbreaking kind of heat transmission fluids might be created. Raees et al. [2] has conducted an investigation of the unsteady squeezing flow of fluid between parallel plates that contains both nanoparticles and gyrotactic microorganisms, one of the plates was moving and the other staying still. Hayat et al. [3] applied the HAM approach to study the magnetohydrodynamic squeezing flow of a nanofluid across a porous stretched surface with thermophoresis effects and Brownian motion. They have taken the lower wall of the channel to be permeable and stretched, while the upper impermeable wall moves in the direction of the lower wall at a prescribed time-dependent velocity. Moreover, Hayat et al. [4] discovered a novel analysis of the magnetohydrodynamic squeezing flow of couple stress nanomaterial between two parallel surfaces. This analysis incorporates the unique characteristics of thermophoresis and Brownian motion, which have not been previously described together with a porous lower surface in the channel. Salehi et al. [5] has conducted research on the magnetohydrodynamic squeezing nanofluid flow of hybrid nanoparticles composed of Fe_3O_4 and MoS_2 that are sandwiched between two infinite parallel plates. They found that as the squeezing and Hartman numbers increased, the velocity profile decreased. Acharya [6] performed research to determine the flow patterns and heat transmission characteristics of hybrid nano liquids in the presence of nonlinear solar radiation. The investigation focused on several solar thermal devices that had Alumina-copper nano ingredients mixed with water as the main fluid. Furthermore, Bio-convective nano liquid flow including gyrotactic microorganisms between two squeezed parallel plates was investigated by Acharya et al. [7] using the classical Runge-Kutta-Fehlberg approach, taking

---

into account the effects of a higher-order chemical reaction and second-order slip. Based on their research, they discovered that the temperature reduces as the squeezing factor and first-order velocity slip parameter increase, but increases as the second-order slip parameter increases. A micro-polar hybrid nanofluid ($GO - Cu/H_2O$) has been investigated by Ikram et al. [8] in the presence of hall current and thermal radiations to look at how it moves and transfers heat between two surfaces in a spinning system. The primary result of their investigation is that increasing the values of the magnetic parameter leads to an increase in the velocity profile and a decrease in the rotational velocity profile. Also, the fractional model of Brinkman type fluid that contains hybrid nanoparticles of TiO_2 and Ag in a base fluid of water within a confined micro-channel has been investigated by Ikram et al. [9]. Khashi'ie et al. [10] investigated the $Cu - Al_2O_3/H_2O$ nanofluid flow between two parallel plates in which a magnetic field and wall mass suction or injection are supplied to the lower plate, allowing the bottom plate to be deformed while the upper plate flows in the opposite direction of the lower plate. The primary finding of their investigation is that an augmentation in the squeezing parameter leads to a degradation of the heat transfer coefficient by 4.28% (upper) and 5.35% (lower), respectively. Yaseen et al. [11] studied the heat transfer properties of the MHD squeezing nanofluid (MoS_2/H_2O) flow and the hybrid nanofluid ($MoS_2 - SiO_2/H_2O - C_2H_6O_2$) flow between two parallel plates, as well as their symmetrical characteristics. In their model, the upper plate is moving downwards towards the lower plate, while the bottom plate is elongating with a constant velocity. A hybrid nanofluid containing Ethylene glycol-water as the base fluid and nanoparticles of TiO_2 and MoS_2 in the presence of dust particles and a magnetic field, flowing over a stretched sheet, was studied by Talebi et al. [12] in terms of its motion and temperature distribution in a porous medium. By considering the effects of thermal radiation and Hall current, Rauf et al. [13] investigated the micropolar tri-hybrid nanofluid($Fe_3O_4 - Al_2O_3 - TiO_2/H_2O$) in a rotating structure between two perpendicular permeable plates. A micro-polar fluid undergoing radiative and magnetohydrodynamic flow across an Al_2O_3 and Cu nanoparticle stretched/shrinking sheet in the presence of viscous dissipation and Joule heating was investigated by Waini et al. [14]. Famakinwa et al. [15] studied how heat radiation and viscous dissipation affect an unstable, incompressible flow of water-hybrid nanoparticles moving between two surfaces that are lined up and have different viscosity. They discovered that there was no apparent alteration in fluid velocity when thermal radiation and viscous dissipation parameters were increased, but that the temperature distribution was reduced. The combined effects of the suction/injection, electromagnetic force, activation energy, chemical reaction, ionized fluid, inertia force and magnetic field that influence the squeezing flow of ternary hybrid nanofluids between parallel plates are investigated numerically by Bilal et al. [16]. Hanif et al. [17] investigated the flow of a hybrid nanofluid based on an aluminum alloy and water across a stretchy horizontal plate with a thermal resistive effect using the Numerical Crank-Nicolson approach. The MHD flow, heat, and mass transfer of the Jeffrey hybrid nanofluid on the squeezing channel via a permeable material in the presence of a chemical reaction and a heat sink/source were studied by Noor and Shafie [18]. Ullah et al. [19] explored the hydrothermal properties of a hybrid nanofluid ($Ag + TiO_2 + H_2O$) in three dimensions in presence of magnetic, thermal, and radiation fluxes between the two vertical plates. Transient free convection of a hybrid nanofluid between two parallel plates in the presence of a magnetic field, a heat source/sink and thermal radiation was explored analytically by Roy and Pop [20]. Moreover, the effect of radiative heat flux on the transient state electro-osmotic squeezing propulsion of a viscous liquid via a porous material between two parallel plates has been investigated by Jayavel et al. [21]. Bhaskar et al. [22] and Maiti and Mukhopadhyay [23] investigated the MHD squeezed flow of casson hybrid nanofluid and unstable nanofluid flow between two parallel plates, respectively, under various effects. Madit et al. [24] studied how a chemical reaction affects the flow of a nanofluid that is squeezed by hydromagnetism between two vertical plates. Khashi'ie et al. [25] carried out investigations into the simultaneous impact of double stratification and buoyancy forces on the flow of nanofluid over a surface that is either shrinking or stretching. It was observed that the heat transfer rate increases by roughly 5.83% to 12.13% when the thermal relaxation parameter is introduced in both shrinking and stretching scenarios. Similarly, Khashi'ie et al. [26] developed numerical solutions and conducts stability analyses for stagnation point flow utilizing hybrid nanofluid in the presence of thermal stratification across a permeable stretching/shrinking cylinder. Nath and Deka [27] studied the effects of thermal and mass stratification on an unsteady MHD nanofluid past a vertical plate that accelerates exponentially with temperature variation in a porous media. Similarly, Nath and Deka [28] conducted a numerical study to examine the combined impacts of thermal and mass stratification on the movement of unstable magnetohydrodynamic nanofluid through an exponentially accelerated vertical plate in a porous media. The unsteady parabolic flow across an infinite vertical plate with exponentially declining temperature and variable mass diffusion in a porous media has been investigated by Nath and Deka [29] with respect to the thermal and mass stratification effect. Nath and Deka [30],[31] performed a numerical investigation on the MHD ternary hybrid nanofluid around a vertically stretching cylinder in a porous medium with thermal stratification. A numerical study was carried out by Krishna [32] to examine the effects of heat absorption and generation on steady free convection flow around a perpendicularly wavy surface. Additionally, Krishna and Vajravelu [33] investigated the chemical reaction, radiation absorption, Hall, and ion slip impacts in the rotating MHD flow of second-grade fluid via a porous media between two vertical plates. In a parallel plate channel with different pressure gradient oscillations, Krishna [34] investigated Hall effects on magnetohydrodynamic rotational flow through a porous media.

Based on the literature review, previous research has not attempted to investigate the squeezing flow of an MHD ternary hybrid nanofluid between two parallel plates in a porous media in presence of viscous dissipation effect. It is assumed that the lower plate has a physically permeable and stretchable shape. The primary aim of this study is to investigate the thermal conductivity characteristics of a ternary hybrid nanofluid composed of $Cu - Al_2O_3 - TiO_2$ particles

suspended in water. This study examines the heat transfer characteristics between two parallel plates, considering the influence of thermal radiation as well as heat sources/sinks. The bvp4c solver in MATLAB is used to transform the non-linear PDEs into ODEs by utilizing the necessary self-similarity variables. The Bvp4c technique employed in this research work to represent the problem is generally acknowledged, as evidenced by its discussion and implementation in MATLAB by Hale and Moore [35]. A visual depiction of the outcomes is presented for many parameters, including $\delta, Ec, Sq, S, \lambda, M, Da, R$ and Q.
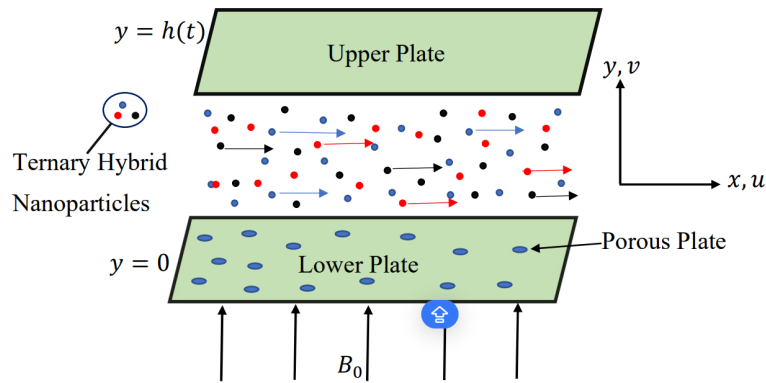
Figure 1. Physical Model and Coordinate System

2. MATHEMATICAL ANALYSIS

Consider a two-dimensional unsteady ternary hybrid nanofluid ($Cu - Al_2O_3 - TiO_2/H_2O$) squeezing flow between two infinite parallel plates in a Darcy porous medium, as illustrated in Fig. 1. The upper plate is positioned at a distance of $y = h(t) = \sqrt{\frac{(1-\alpha t)v_f}{b}}$ from the lower plate. At the same time, the higher plate, with a velocity $V_h = \frac{dh(t)}{dt} = -\frac{\alpha}{2}\sqrt{\frac{v_f}{(1-\alpha t)b}}$, is moving towards the lower plate that is being squeezed. It is assumed that the lower and upper plates are kept at constant temperatures T_1 and T_2, respectively. Additionally, the influence of viscous dissipation, thermal radiation and heat source/sink are taken into consideration in this model; however, the buoyancy effect, which is also known as the gravitational force, is not taken into account. In the meantime, the physical representation for the potential fluid suction or injection includes the porous lower plate, where the wall mass velocity is represented as $v_w = -\frac{V_0}{1-\alpha t}$; for suction, $V_0 > 0$, for injection, $V_0 < 0$, and an impermeable plate corresponds to $V_0 = 0$. Furthermore, the lower plate can be stretched with a linear velocity of $u_w = -\frac{bx}{1-\alpha t}$, where $t < \frac{1}{\alpha}$, and a time-dependent magnetic field is modeled with $B(t) = \frac{B_0}{1-\alpha t}$. In light of these assumptions and with the hybrid nanofluid model that Khashi'ie et al. [10], Famakinwa et al. [15] and Yaseen et al. [11] have proposed, we extended their model to incorporate the ternary hybrid model. Hence, the governing conservation equations are as follows:

$$\frac{\partial u}{\partial x} + \frac{\partial u}{\partial y} = 0 \tag{1}$$

$$\frac{\partial V}{\partial t} + u\frac{\partial V}{\partial x} + v\frac{\partial V}{\partial y} = \frac{\mu_{thnf}}{\rho_{thnf}}\frac{\partial^2 V}{\partial y^2} - \frac{\sigma_{thnf}}{\rho_{thnf}}B(t)^2 V - \frac{\mu_{thnf}}{\rho_{thnf}}\cdot\frac{\phi^* V}{k_p} \tag{2}$$

$$\frac{\partial T}{\partial t} + u\frac{\partial T}{\partial x} + v\frac{\partial T}{\partial y} = \frac{k_{thnf}}{(\rho c_p)_{thnf}}\frac{\partial^2 T}{\partial y^2} - \frac{1}{(\rho c_p)_{thnf}}\frac{\partial q_r}{\partial y} + \frac{Q_0}{(\rho c_p)_{thnf}}(T - T_0) + \frac{\mu_{thnf}}{(\rho c_p)_{thnf}}\left(\frac{\partial u}{\partial y}\right)^2 \tag{3}$$

where $V = \frac{\partial v}{\partial x} - \frac{\partial u}{\partial y}$. The boundary conditions that are associated with the lower and upper plates (Hayat et al. [3] and Khashi'ie et al. [10]) are as follows :

$$u = \lambda\frac{bx}{1-\alpha t} \qquad v = -\frac{V_0}{1-\alpha t} \qquad T = T_1 \qquad \text{at } y = 0 \text{ (lower plate)}$$

$$u = 0 \qquad v = \frac{dh(t)}{dt} \qquad T = T_2 \qquad \text{at } y = h(t) \text{ (upper plate)}$$

Here, u and v represent the velocities in the x and y directions, respectively, while T denotes the temperature of the ternary hybrid nanofluid. In addition, the other symbol signifies the following: ρ represents density, μ represents dynamic viscosity, C_p represents heat capacity, k represents thermal conductivity, $B(t)$ represents magnetic field strength, indicates

porosity of the porous medium, represents permeability of the porous medium, λ is the stretching/shrinking parameter, Q_0 represents heat absorption/generation coefficient, and b denotes the stretching/shrinking rate of the lower plate.

Taking into consideration the Rosseland approximation [36], the value of (q_r) is defined as

$$q_r = -\frac{4\sigma^*}{3k_{thnf}}\left(\frac{\partial T^4}{\partial y}\right)$$

The term "σ^*" represents the Stefan-Boltzmann constant, whereas "k_{thnf}" refers to the mean absorption coefficient. By performing basic calculations with the aforementioned term, Eqn. (3) can be reduced as follows:

$$\frac{\partial T}{\partial t} + u\frac{\partial T}{\partial x} + v\frac{\partial T}{\partial y} = \frac{1}{(\rho c_p)_{thnf}}\left(k_{thnf} + \frac{16\sigma^*T_2^3}{3k}\right)\frac{\partial^2 T}{\partial y^2} + \frac{Q_0}{(\rho c_p)_{thnf}}(T-T_0) + \frac{\mu_{thnf}}{(\rho c_p)_{thnf}}\left(\frac{\partial u}{\partial y}\right)^2$$

The similarity transformation (Ref. Hayat et al. [3]) used in Equations (1)-(3) are as follows

$$u = \frac{bx}{1-\alpha t}f'(\eta), \quad v = -\sqrt{\frac{bv_f}{1-\alpha t}}f'(\eta), \quad \eta = y\sqrt{\frac{b}{(1-\alpha t)v_f}},$$

$$\psi = \sqrt{\frac{bv_f}{1-\alpha t}}xf(\eta), \quad \theta = \frac{T-T_0}{T_2-T_0}$$

and we provide non-dimensional quantities in the following:

$$M = \frac{\sigma_f B_0^2}{b\rho_f}, \quad Da = \frac{k_0 b}{v_f(1-\alpha t)\phi^*}, \quad Ec = \frac{u_w^2}{C_p(T_2-T_0)}, \quad Sq = \frac{\alpha}{b}, \quad S = \frac{V_0}{hb}$$

$$\delta = \frac{T_1-T_0}{T_2-T_0}, \quad Q = \frac{Q_0}{1-\alpha t}, \quad R = \frac{4\sigma^*T_2'^3}{k_f k}, \quad Pr = \frac{(\rho c_p)_f}{k_f}$$

where, M is the magnetic parameter, Da is the Darcy number, Sq is the squeezing parameter, S is the suction/injection parameter, δ is the temperature-ratio parameter, Ec is the Eckert number, Q is the heat source/sink parameter, R is the thermal radiation parameter, Pr is the Prandtl number. Moreover, if $\lambda = 0$, it means the lower plate is not moving, if $\lambda < 0$, it means the lower plate is shrinking, and if $\lambda > 0$, it means the lower plate stretching.

The non-dimensional forms of the transformed equations are given by

$$a_1 a_2 f^{iv} + ff''' - f'f'' - \frac{Sq}{2}(3f'' + \eta f''') - \left(a_2 a_3 M + \frac{a_1 a_2}{Da}\right)f'' = 0 \tag{4}$$

$$\frac{a_4}{Pr}\left(a_5 + \frac{4}{3}R\right)\theta'' + f\theta' - \frac{Sq}{2}\eta\theta' + a_4 Q\theta + a_1 a_4 Ec f''^2 = 0 \tag{5}$$

where,

$$a_1 = \frac{\mu_{thnf}}{\mu_f}, \quad a_2 = \frac{\rho_f}{\rho_{thnf}}, \quad a_3 = \frac{\sigma_{thnf}}{\sigma_f}, \quad a_4 = \frac{(\rho C_p)_f}{(\rho C_p)_{thnf}}, \quad a_5 = \frac{k_{thnf}}{k_f}$$

Here, the symbols $\mu_{thnf}, \rho_{thnf}, (\rho C_p)_{thnf}, \sigma_{thnf}, k_{thnf}$ represent the ternary hybrid nanofluid's coefficient of viscosity, electrical conductivity, heat capacity, density and thermal conductivity, respectively. Also, $\mu_f, \rho_f, (\rho C_p)_f, \sigma_f, k_f$ denote the base fluid's coefficient of viscosity, electrical conductivity, heat capacity, density and thermal conductivity correspondingly. The thermophysical characteristics of the ternary hybrid nanofluid are presented in table 1. Thermo-physical properties of Cu, Al_2O_3 and TiO_2 nanoparticles in pure water are given in table 2.

The transformed boundary conditions are as follows :

$$f(0) = S, \qquad f'(0) = \lambda, \qquad \theta(0) = \delta$$

$$f(1) = \frac{Sq}{2}, \qquad f'(1) = 0, \qquad \theta(1) = 1 \tag{6}$$

where ϕ_1, ϕ_2 and ϕ_3 are volume fraction of Cu(Copper), Al_2O_3 (aluminium oxide) and TiO_2 (titanium oxide) nanoparticles respectively. The suffixes thnf, hnf, nf, f, s1, s2, s3 denote ternary hybrid nanofluid, hybrid nanofluid, nanofluid, base fluid, solid nanoparticles of copper (Cu), aluminum oxide (Al_2O_3), and titanium dioxide (TiO_2) correspondingly.

The skin friction coefficient and local Nusselt number at lower and upper plates are defined by

$$\text{Lower: } C_{f_1}Re_x^{1/2} = \frac{\mu_{thnf}}{\mu_f}f''(0) \quad \text{and} \quad \text{Upper: } C_{f_2}Re_x^{1/2} = \frac{\mu_{thnf}}{\mu_f}f''(1)$$

$$\text{Lower: } Nu_{x_1}Re_x^{-1/2} = -\left(\frac{k_{thnf}}{k_f} + \frac{4}{3}R\right)\theta'(0) \quad \text{and} \quad \text{Upper: } Nu_{x_2}Re_x^{-1/2} = -\left(\frac{k_{thnf}}{k_f} + \frac{4}{3}R\right)\theta'(1)$$

where, $Re_x = \frac{xU_w}{v_f}$ is the local Reynolds Number.

Table 1. The thermo-physical properties of ternary hybrid nanofluid are as follows [31]:

Properties	Ternary Hybrid Nanofluid
Dynamic Viscocity	$\dfrac{\mu_{thnf}}{\mu_f} = \dfrac{1}{(1-\phi_1)^{2.5}(1-\phi_2)^{2.5}(1-\phi_3)^{2.5}}$
Density	$\rho_{thnf} = (1-\phi_3)\left[(1-\phi_2)\left\{(1-\phi_1)\rho_f + \phi_1\rho_{s1}\right\} + \phi_2\rho_{s2}\right] + \phi_3\rho_{s3}$
Electrical Conductivity	$\sigma_{thnf} = \left[\dfrac{(\sigma_{s3}+2\sigma_{hnf})-2\phi_3(\sigma_{hnf}-\sigma_{s3})}{(\sigma_{s3}+2\sigma_{hnf})+\phi_3(\sigma_{hnf}-\sigma_{s3})}\right]\sigma_{hnf}$ $\sigma_{hnf} = \left[\dfrac{(\sigma_{s2}+2\sigma_{nf})-2\phi_2(\sigma_{nf}-\sigma_{s2})}{(\sigma_{s2}+2\sigma_{nf})+\phi_2(\sigma_{nf}-\sigma_{s2})}\right]\sigma_{nf}$ $\sigma_{nf} = \left[\dfrac{(\sigma_{s1}+2\sigma_f)-2\phi_1(\sigma_f-k_{s1})}{(\sigma_{s1}+2\sigma_f)+\phi_1(\sigma_f-\sigma_{s1})}\right]\sigma_f$
Heat Capacity	$(\rho c_p)_{thnf} = (1-\phi_3)\left[(1-\phi_2)\left\{(1-\phi_1)(\rho c_p)_f + \phi_1(\rho c_p)_{s1}\right\} + \phi_2(\rho c_p)_{s2}\right] + \phi_3(\rho c_p)_{s3}$
Thermal Conductivity	$k_{thnf} = \left[\dfrac{(k_{s3}+2k_{hnf})-2\phi_3(k_{hnf}-k_{s3})}{(k_{s3}+2k_{hnf})+\phi_3(k_{hnf}-k_{s3})}\right]k_{hnf}$ $k_{hnf} = \left[\dfrac{(k_{s2}+2k_{nf})-2\phi_2(k_{nf}-k_{s2})}{(k_{s2}+2k_{nf})+\phi_2(k_{nf}-k_{s2})}\right]k_{nf}$ $k_{nf} = \left[\dfrac{(k_{s1}+2k_f)-2\phi_1(k_f-k_{s1})}{(k_{s1}+2k_f)+\phi_1(k_f-k_{s1})}\right]k_f$

Table 2. Thermo-physical Properties of water and nanoparticles [31]

Physical Properties	H_2O (base fluid)	Cu (s1)	Al_2O_3 (s2)	TiO_2 (s3)
$\rho\ (kg/m^3)$	997.1	8933	3970	4250
$C_p\ (J/kgK)$	4179	385	765	686.2
$k\ (W/mK)$	0.613	401	40	8.9538
$\sigma\ (s/m)$	5.5×10^{-6}	59.6×10^6	35×10^6	2.6×10^6

3. METHOD OF SOLUTION

In order to obtain numerical solutions for a system of higher-order nonlinear ordinary differential equations (ODEs) provided by Eqs. (4) and (5) and the boundary conditions, we use the bvp4c solver, built into the computational platform MATLAB. Professionals and researchers have widely employed this technique for solving fluid flow problems. The bvp4c solver, developed by Jacek Kierzenka and Lawrence F. Shampine from Southern Methodist University in Texas, was first presented by Hale and Moore [35]. The bvp4c solver is an algorithm that employs the Lobato IIIA implicit Runge-Kutta technique to provide numerical solutions with fourth-order accuracy. It achieves this by making finite modifications. This method provides the required precision when an estimation is made for the initial mesh points and adjustments to the step size. The investigation conducted by Waini et al. [37] shown that the bvp4c solver produced satisfactory outcomes when compared to both the direct shooting approach and Keller box method. The syntax for using the "bvp4c" solver is as follows: "sol = bvp4c (@OdeBVP, @OdeBC, solinit, options)". Here, we must decrease the higher order derivatives in relation to η. This can be accomplished by introducing the subsequent new variables:

$$f = y(1), \quad f' = y(2), \quad f'' = y(3), \quad f''' = y(4), \quad \theta = y(5), \quad \theta' = y(6)$$

$$\frac{d}{d\eta}\begin{bmatrix}y(1)\\y(2)\\y(3)\\y(4)\\y(5)\\y(6)\end{bmatrix} = \begin{bmatrix}y(2)\\y(3)\\y(4)\\\dfrac{y(2)y(3)-y(1)y(4)+\frac{Sq}{2}(3y(3)+\eta y(4))\left(a_2a_3M+\frac{a_1a_2}{Da}\right)y(3)}{a_1a_2}\\y(6)\\\dfrac{\frac{Sq}{2}\eta y(6)-y(1)y(6)-a_4Qy(5)-a_1a_4Ec\ y(3)^2}{\frac{a_4}{Pr}\left(a_5+\frac{4}{3}R\right)}\end{bmatrix}$$

and boundary condition are expressed as

$$y_0(1) - S, \quad y_0(2) - \lambda, \quad y_0(5) - \delta, \quad y_1(1) - \frac{Sq}{2}, \quad y_1(2), \quad y_1(5) - 1$$

where y_0 is the condition at $\eta = 0$ and y_1 is the condition at $\eta = 1$

4. RESULT AND DISCUSSION

The results are computed by using bvp4c in MATLAB and visually displayed in Figs (2)-(13) for the distribution of skin friction coefficients, velocity, local Nusselt number and temperature on both the upper and bottom plates. The

Prandtl number is set at a constant value of 6.2, indicating the utilisation of water at a temperature of 25°C. The other parameters are constrained within the following ranges: $0 \leq \delta \leq 0.3$ for the temperature-ratio parameter, $0 \leq Sq \leq 1.7$ for the unsteadiness squeezing parameter, $-1.2 \leq S \leq 1.2$ for the suction/injection parameter, $-0.5 \leq \lambda \leq 2$ for the stretching/shrinking parameter, $0 \leq Da \leq 0.1$ for the porous medium parameter and $0 \leq M \leq 6$ for the magnetic parameter, $0 \leq Ec \leq 1$ for the Eckert number, $0 \leq R \leq 3$ for the thermal radiation parameter, $-0.2 \leq Q \leq 0.2$ for the heat source/sink parameter. The comparison of $f''(0)$ for the lower plate and $f''(1)$ for the upper plate with Hayat et al. [3] and Khashi'ie et al. [10] for varying values of M, S when $\lambda = 1, \phi_1 = \phi_2 = \phi_3 = 0$ is presented in Table 3. It can be seen that the results of this study are very similar to those of the two prior investigations.

Table 3. Comparison of $f''(0)$ for lower plate and $f''(1)$ for upper plate when $\lambda = 1, \phi_1 = \phi_2 = \phi_3 = 0$

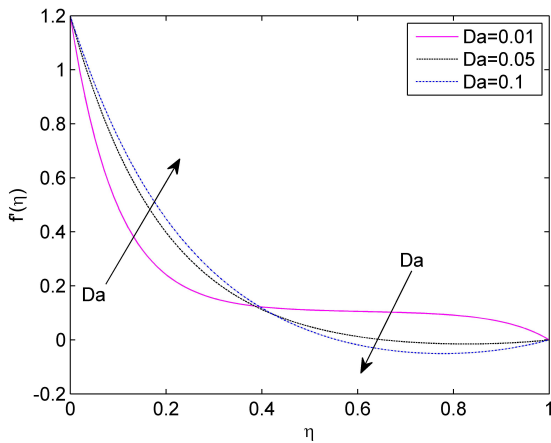| M	S	Present $f''(0)$	Hayat et al. [3] $f''(0)$	Khashi'ie et al.[10] $f''(0)$	Present $f''(1)$	Hayat et al. [3] $f''(1)$	Khashi'ie et al.[10] $f''(1)$
1	0.5	-7.591617	-7.591618	-7.591617	4.739016	4.739017	4.739016
4	0.5	-8.110334	-8.110334	-8.110334	4.820251	4.820251	4.820251
4	0.6	-8.851444	-8.851444	-8.851444	5.391247	5.391248	5.391247
4	1.0	-11.948584	-11.948584	-11.948584	7.593426	7.593426	7.593426

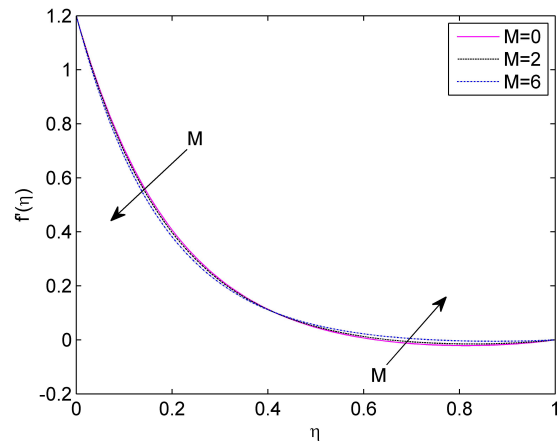**Figure 2.** Effect of Da on $f'(\eta)$

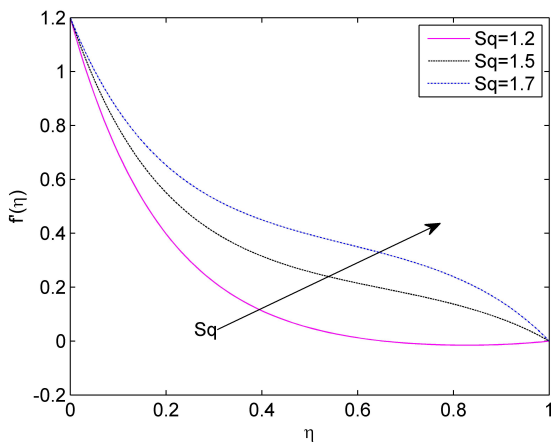**Figure 3.** Effect of M on $f'(\eta)$

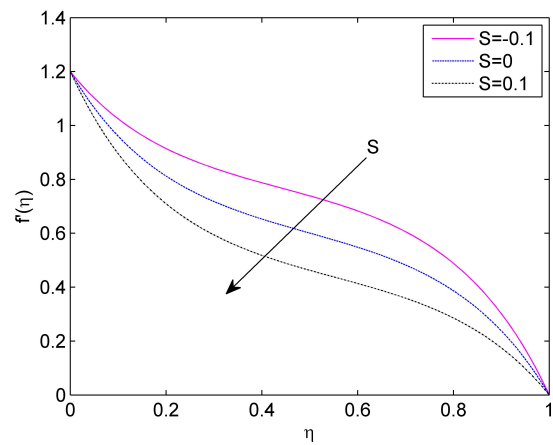**Figure 4.** Effect of Sq on $f'(\eta)$

Figure 5. Effect of S on $f'(\eta)$

The parameters were set at fixed values for the computation of the results: $\delta = 0.1, Sq = 1.2, M = 2, Da = 0.05, S = 0.4, \lambda = 1.2, Ec = 0.5, R = 1, Q = 0.2, \phi_1 = \phi_2 = \phi_3 = 0.01$. The Fig. 2 displays the impact of Darcy number (Da) on velocity profile $f'(\eta)$ of the ternary hybrid nanofluid. In close proximity to the lower plate, the velocity experiences a sudden increase as the Darcy number increases. However, there is a distinct transition point at $\eta \sim 0.5$, beyond which the

velocity exhibits contrasting behaviour. The Darcy number (Da) determines the ratio of the permeability of a medium to its cross-sectional area, while permeability measures the ability of a surface to allow fluid to pass through its membrane. The rising permeability in the surrounding area of the bottom plate hinders the movement of the fluid. Consequently, a rise in the Darcy number (Da) results in velocity profiles that are closer to the upper plate due to greater flow resistance. The impact of the magnetic parameter (M) on the velocity profile is shown in Fig. 3. In close distance to the lower plate, the velocity of the ternary hybrid nanofluid decreases as the magnetic parameter increases. Similarly to Fig 2, Fig. 3 also exhibits a transition point in the vicinity of $\eta \sim 0.5$. Following this transition point, the velocity exhibits opposite behavior. The presence of a powerful magnetic field causes a significant reduction in the movement of liquids. As the magnetic field strength (M) increases, the Lorentz forces become active and cause a decrease in the flow of the liquid. The presence of a magnetic field hinders the flow and ultimately slows down the radial velocity. As seen in Fig. 4, the addition of the unsteadiness squeezing parameter(Sq) improves the velocity distribution $f'(\eta)$ for the ternary hybrid nanofluid. Due to the movement of the upper plate towards the lower plate, the squeezing effect is initiated from the higher plate. It has been observed that the velocity of the fluid increases in tandem with the squeezing parameter (Sq) as it rises higher. Fig. 5 illustrates the effect of the suction/injection parameter(S) on the velocity profile $f'(\eta)$. As seen in the figure, the application of injection results in a higher velocity than suction. Suction/injection is frequently employed as a means to prevent boundary layer separation. In this study, the application of injection results in an observed enhancement in velocity. Therefore, in this study, the injection is more efficient in delaying the separation of the boundary layer. The Fig. 6 demonstrates the impact of the shrinking/stretching parameter(λ) on the velocity profile $f'(\eta)$ for the ternary hybrid nanofluid. The velocity profile $f'(\eta)$ exhibits dual behavior with respect to shrinking/stretching parameter(λ). There is a transition point located close to $\eta \sim 0.3$. The velocity $f'(\eta)$, increases in the surrounding area of the lower plate, but beyond the transition point, the velocity $f'(\eta)$, declines. This outcome suggests that the stretching of the lower plate increases velocity in the surrounding area of the lower plate. However, when the upper plate moves towards the lower plate, the velocity behaves in the opposite way when the parameter(λ) increases.
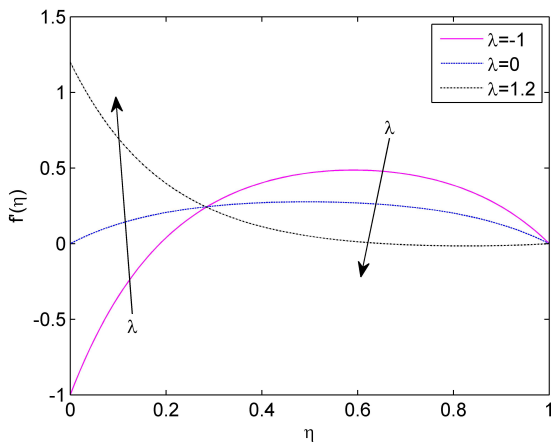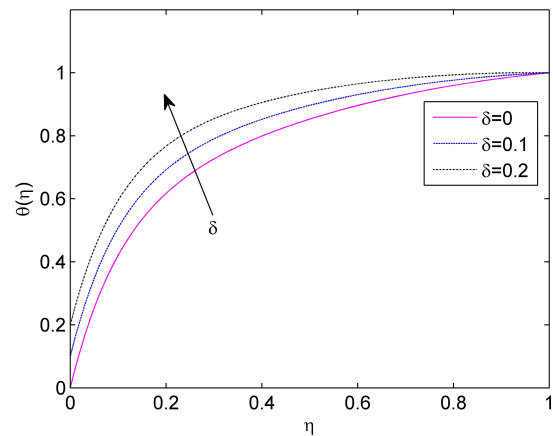

Figure 6. Effect of λ on $f'(\eta)$

Figure 7. Effect of δ on $\theta(\eta)$
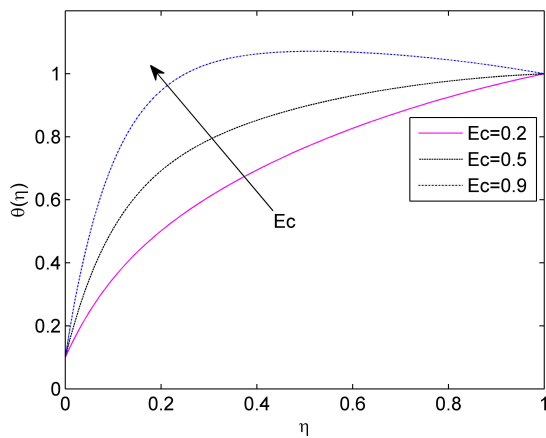

Figure 8. Effect of Ec on $\theta(\eta)$
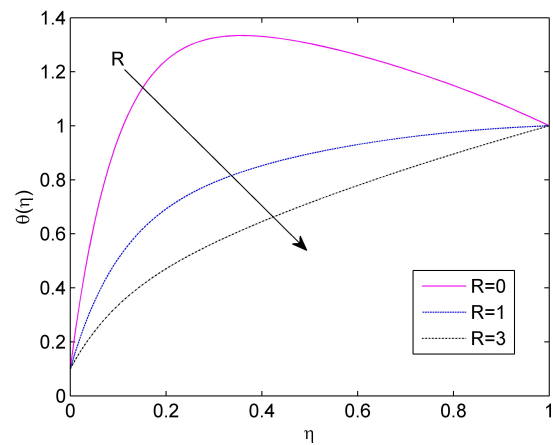

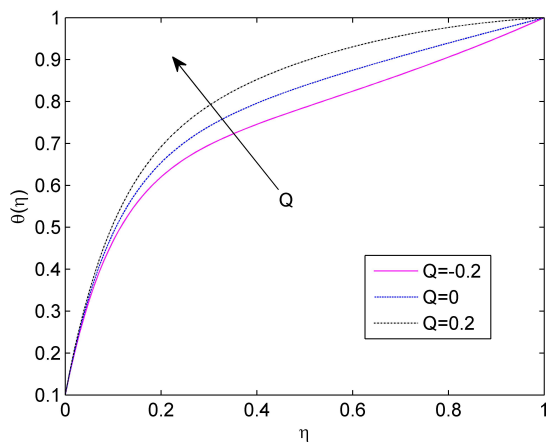**Figure 9.** Effect of R on $\theta(\eta)$

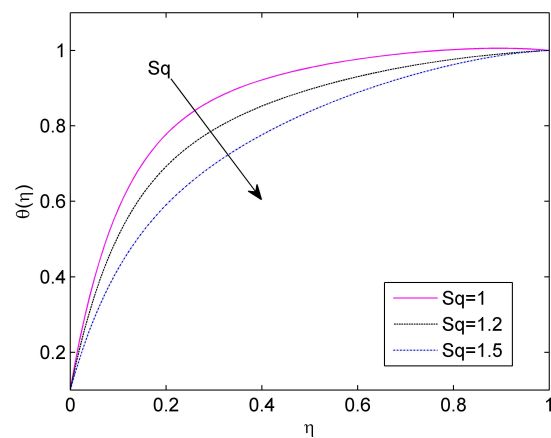**Figure 10.** Effect of Q on $\theta(\eta)$

Figure 11. Effect of Sq on $\theta(\eta)$

The impact of the temperature-ratio parameter(δ) on the temperature profile $\theta(\eta)$ is shown in Fig. 7. The temperature-ratio parameter(δ) is found to increase the temperature of the ternary hybrid nanofluid due to obvious and expected reasons. In Fig 8, it is evident that the temperature of the ternary hybrid nanofluid gets raised by the Eckert number (Ec). The viscous dissipation, which is the process by which the fluid's friction causes its kinetic energy to be converted into thermal energy, becomes more important as the Eckert number(Ec) rises. The dissipation of energy causes the nanofluid to heat up, resulting in an increase in its temperature. The Fig. 9 displays that the temperature $\theta(\eta)$ of the ternary hybrid nanofluid goes down as the thermal radiation(R) goes up. Thermal radiation causes the temperature of the nanofluid to decrease by causing a net loss of energy from the fluid. This loss of energy reduces the kinetic energy of the particles inside the fluid, leading to a lower temperature. Fig. 10 demonstrates the increasing effects of temperature as the heat generation/absorption parameter (Q) increases. Greater values of a parameter (Q) result in an increase in temperature. The parameter (Q) has positive values, indicating the production of heat in the system. Higher values of (Q) correspond to greater amounts of heat being generated. Therefore, as the heat-generation parameter (Q) increases, the temperature also increases. Fig. 11 demonstrates the influence of the squeezing parameter(Sq) on the temperature profile $\theta(\eta)$. It is easy to see from the graph that as the squeezing parameter(Sq) goes up, the temperature goes down. This indicates that when the upper plate moves closer to the lower plates, it limits the spread of heat, resulting in a fall in temperature. Fig. 12 illustrates the fluctuation of the temperature,$\theta(\eta)$ for ternary hybrid nanofluid, in response to changes in the suction/injection parameter(S). An increase in parameter (S) leads to an observed rise in $\theta(\eta)$. The temperature is observed to be higher for the suction value as compared to the injection value. Suction refers to the process of extracting the layers that are detached from the border layer using suction. The fluid layers experience an increase in temperature as they gain momentum through the use of suction.
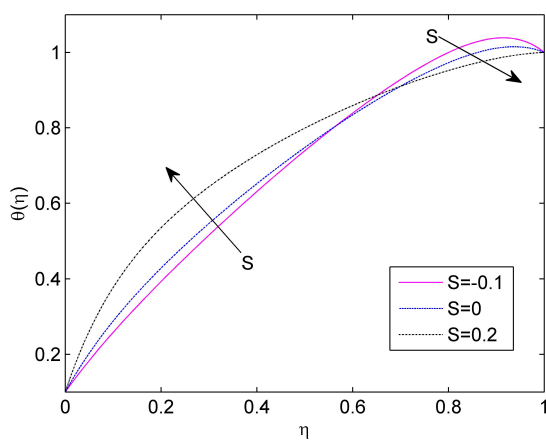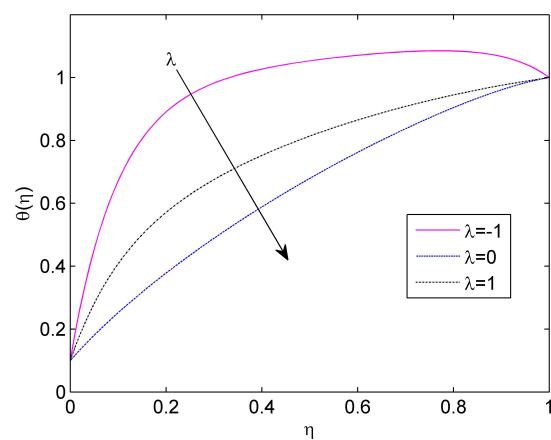

Figure 12. Effect of S on $\theta(\eta)$

Figure 13. Effect of λ on $\theta(\eta)$

The influence of the stretching/shrinking parameter(λ) on the temperature $\theta(\eta)$ is demonstrated in Fig. 13. This model says that $\lambda = 0$ means the lower plate is still, $\lambda < 0$ means it is shrinking, and $\lambda > 0$ means it is stretching. It is observed that the velocity, $\theta(\eta)$, decreases as the values of (λ) increase. The findings suggest that the stretching of the

lower plate decreases the temperature of the flow. In addition, when the degree of shrinkage of the lower plate increases, the temperature increases.

Table 4. Skin-friction and nusselt of $f''(0)$ for upper plate when $\lambda = 1$, $\phi_1 = \phi_2 = 0$

Ec	Sq	M	Da	S	λ	R	Q	$Re_x^{1/2}C_{f_1}$	$Re_x^{1/2}C_{f_2}$	$Re_x^{-1/2}Nu_{x_1}$	$Re_x^{-1/2}Nu_{x_2}$
0.1	1.2	2	0.05	0.4	1.2	1	0.2	-6.9450	0.1994	-5.9341	-0.9706
0.5								-6.9450	0.1994	-14.8166	-0.1527
0.5	1.3	2	0.05	0.4	1.2	1	0.2	-6.5085	-0.2337	-13.4731	-0.2417
	1.5							-5.6312	-1.1046	-11.0875	-0.1442
0.5	1.2	1	0.05	0.4	1.2	1	0.2	-6.8481	0.2282	-14.7150	-0.1391
		1.5						-6.8967	0.2137	-14.7659	-0.1460
0.5	1.2	2	0.07	0.4	1.2	1	0.2	-6.3796	0.3712	-14.2404	-0.0618
			0.1					-5.9207	0.5175	-13.8064	0.0355
0.5	1.2	2	0.05	-0.1	1.2	1	0.2	-2.3816	-4.1070	-4.3122	2.5272
				0.3				-6.0088	-0.6491	-11.7957	-0.3055
0.5	1.2	2	0.05	0.4	-1	1	0.2	8.9081	-3.3656	-21.7764	2.7083
					1			-5.4744	-0.1160	-10.5985	-0.5368
0.5	1.2	2	0.05	0.4	1.2	3	0.2	-6.9450	0.1994	-16.6728	-2.5177
						5		-6.9450	0.1994	-18.9055	-4.9088
0.5	1.2	2	0.05	0.4	1.2	1	-0.2	-6.9450	0.1994	-13.7537	-1.2429
							0	-6.9450	0.1994	-14.2561	-0.7204

Table 4 presents the values of the skin friction coefficients $Re_x^{1/2}C_{f_1}$ and $Re_x^{1/2}C_{f_2}$, as well as the Nusselt numbers $Re_x^{-1/2}Nu_{x_2}$ and $Re_x^{-1/2}Nu_{x_2}$, for various combinations of parameters at the lower and upper plate. The Nusselt numbers express the rates of heat transmission between the upper and bottom plates. An increase in the Eckert number(Ec) leads to a rise in the Nusselt number for the upper plate but decreases for the lower plates. The skin friction coefficient is not influenced by Eckert number(Ec), radiation (R), and heat source (Q) at both plates, as these physical factors are independent of the velocity profile $f'(\eta)$. Increasing the squeezing parameter (Sq) enhances the heat transfer rate at the both plates. However, it reduces the skin friction coefficient at the upper plate and increases it at the lower plate. The magnetic parameter(M) causes a drop in the skin friction coefficient on both the lower and upper plates. Similarly, it leads to an decrease in the Nusselt number on the lower plate and upper plate. Observations indicate that a rise in the Darcy number(Da) leads to an increase in the skin friction coefficient on both the upper and lower plates. Likewise, it results in a increase in the Nusselt number for the both plates. The suction/injection(S) parameter reduces the skin friction coefficient on the bottom plate, but raises it on the top plate. However, the rate of heat transmission reduces at the lower and upper plates. The skin friction coefficient at the upper plate increases as the stretching parameter(λ) is increased, whereas it decreases at the lower plate. in the contrary, the rate of heat transmission increases at the bottom plate while it decreases at the top plate. Radiation(R), causes a drop in the Nusselt number at both the lower and upper plates, while the heat source(Q) results in a fall in the Nusselt number at the lower plate and an increase at the upper plate.

Table 5. Comparison of Skin friction Coefficient for lower plate

ϕ_1	Cu Nanofluid $-Re_x^{1/2}C_{f_1}$	ϕ_2	$Cu-Al_2O_3$ Hybrid Nanofluid $-Re_x^{1/2}C_{f_1}$	Change in Percentage	ϕ_3	$Cu-Al_2O_3-SiO_2$ Ternary Hybrid Nanofluid $-Re_x^{1/2}C_{f_1}$	Change in Percentage
0.01	6.6009	0.01	6.7705	2.56%	0.01	6.9450	5.21%
0.05	7.3976		7.5841	2.52%		7.7750	5.10%
0.1	8.5447		8.7560	2.47%		8.9715	4.99%

Tables 5 and 6 present an analysis of the percentage difference between the nanofluid with hybrid nanofluid and ternary hybrid nanofluid in terms of the absolute skin friction at the top and lower plates, respectively. Moreover, we evaluate the heat transfer rate difference percentage between the nanofluid with hybrid nanofluid and ternary hybrid nanofluid at the upper and lower plates in Tables 7 and 8, respectively. The absolute skin friction of the ternary hybrid nanofluid is seen to be approximately 5% higher than that of the nanofluid at the lower plate and at most 7% higher than that of the nanofluid at the upper plate. Additionally, the rate of heat transmission of the ternary hybrid nanofluid is decreased by 3.61% at the bottom plate. However, the rate of heat transmission of the ternary hybrid nanofluid is increased by at most 209.11% at the upper plate. Observations indicate that the heat transmission rate of the ternary hybrid nanofluid is higher at the upper plate compared to the lower plate.

Table 6. Comparison of Skin friction Coefficient for upper plate

ϕ_1	Cu Nanofluid $-Re_x^{1/2}C_{f_2}$	ϕ_2	$Cu-Al_2O_3$ Hybrid Nanofluid $-Re_x^{1/2}C_{f_2}$	Change in Percentage	ϕ_3	$Cu-Al_2O_3-SiO_2$ Ternary Hybrid Nanofluid $-Re_x^{1/2}C_{f_2}$	Change in Percentage
0.01	0.1906	0.01	0.1950	2.31%	0.01	0.1994	4.62%
0.05	0.1896		0.1949	2.79%		0.2004	5.69%
0.1	0.1966		0.2032	3.35%		0.2103	6.96%

Table 7. Comparison of Local Nusselt number for lower plate

ϕ_1	Cu Nanofluid $-Re_x^{-1/2}Nu_{x_1}$	ϕ_2	$Cu-Al_2O_3$ Hybrid Nanofluid $-Re_x^{-1/2}Nu_{x_1}$	Change in Percentage	ϕ_3	$Cu-Al_2O_3-SiO_2$ Ternary Hybrid Nanofluid $-Re_x^{-1/2}Nu_{x_1}$	Change in Percentage
0.01	15.3716	0.01	15.0910	1.82%	0.01	14.8166	3.61%
0.05	14.3461		14.0945	1.75%		13.8468	3.48%
0.1	13.1438		12.9288	1.63%		12.7149	3.26%

Table 8. Comparison of Local Nusselt number for upper plate

ϕ_1	Cu Nanofluid $-Re_x^{-1/2}Nu_{x_2}$	ϕ_2	$Cu-Al_2O_3$ Hybrid Nanofluid $-Re_x^{-1/2}Nu_{x_2}$	Change in Percentage	ϕ_3	$Cu-Al_2O_3-SiO_2$ Ternary Hybrid Nanofluid $-Re_x^{-1/2}Nu_{x_2}$	Change in Percentage
0.01	0.0494	0.01	0.1029	108.29%	0.01	0.1527	209.11%
0.05	0.2767		0.3306	19.47%		0.3798	37.26%
0.1	0.5622		0.6176	9.85%		0.6665	18.55%

5. CONCLUSION

The present study is a comprehensive examination of the impact of viscous dissipation and thermal radiation on the squeezing flow of a ternary hybrid nanofluid with magnetic field effect between two Parallel Plates, when a heat source/sink is present inside a porous medium. The analysis also takes into account the flow characteristics and their impact on the velocity $f'(\eta)$ and temperature $\theta(\eta)$ profiles, skin friction coefficients, and Nusselt number. The main results of the ongoing study are summarized below:

1. The velocity profile $f'(\eta)$ shows a decrease in pattern when the parameters S and λ on the upper plate and Da on the upper plate are increased. Conversely, it displays an increasing pattern with higher values of Sq and λ on the lower plate, as well as Da on the lower plate.
2. The temperature $\theta(\eta)$ decreases as the values of R, Sq and λ increase, whereas it increases with the increase of δ, Q and Ec.
3. The absolute skin friction of the ternary hybrid nanofluid is seen to be approximately 5% higher than that of the regular nanofluid at the lower plate and at most 7% higher than that of the nanofluid at the upper plate.
4. The ternary hybrid nanofluid demonstrates superior heat transfer efficiency compared to the hybrid nanofluid, while the hybrid nanofluid displays higher heat transfer efficiency than standard nanofluids at the upper plate.
5. The heat transmission rate of the ternary hybrid nanofluid is higher at the upper plate compared to the lower plate.

The future potential of ternary hybrid nanofluids, which consist of copper (Cu), aluminum oxide (Al_2O_3), and titanium dioxide (TiO_2), is significant in multiple scientific and technical fields. Ternary hybrid nanofluids provide the possibility of greatly enhancing heat transfer efficiency in various applications, such as radiators, heat exchangers and cooling devices. Improved heat transfer properties might be beneficial for use in geothermal power extraction, solar energy systems and high-temperature operations.

ORCID

 Rubul Bora, https://orcid.org/0000-0002-3164-2255; **Bidyut Boruah**, https://orcid.org/0009-0004-4978-1343

REFERENCES

[1] S.U.S. Choi, and J.A. Eastman, *Enhancing thermal conductivity of fluids with nanoparticles*, (Argonne National Lab., Argonne, IL, United States, 1995).

[2] A. Raees, H. Xu, and S.-J. Liao, "Unsteady mixed nano-bioconvection flow in a horizontal channel with its upper plate expanding or contracting," International Journal of Heat and Mass Transfer, **86**, 174-182 (2015). https://doi.org/10.1016/j.ijheatmasstransfer.2015.03.003

[3] T. Hayat, T. Muhammad, A. Qayyum, A. Alsaedi, and M. Mustafa, "On squeezing flow of nanofluid in the presence of magnetic field effects," Journal of Molecular Liquids, **213**, 179-185 (2016). https://doi.org/10.1016/j.molliq.2015.11.003

[4] T. Hayat, R. Sajjad, A. Alsaedi, T. Muhammad, and R. Ellahi, "On squeezed flow of couple stress nanofluid between two parallel plates," Results in physics, **7**, 553-561 (2017). https://doi.org/10.1016/j.rinp.2016.12.038

[5] S. Salehi, A. Nori, Kh. Hosseinzadeh, and D.D. Ganji, "Hydrothermal analysis of MHD squeezing mixture fluid suspended by hybrid nanoparticles between two parallel plates," Case Studies in Thermal Engineering, **21**, 100650 (2020). https://doi.org/10.1016/j.csite.2020.100650

[6] N. Acharya, "On the flow patterns and thermal behaviour of hybrid nanofluid flow inside a microchannel in presence of radiative solar energy," Journal of Thermal Analysis and Calorimetry, **141**(4), 1425-1442 (2020). https://doi.org/10.1007/s10973-019-09111-w

[7] N. Acharya, R. Bag, and P.K. Kundu, "Unsteady bioconvective squeezing flow with higher-order chemical reaction and second-order slip effects," Heat Transfer, **50**(6), 5538-5562 (2021). https://doi.org/10.1002/htj.22137

[8] S. Islam, A. Khan, W. Deebani, E. Bonyah, N.A. Alreshidi, and Z. Shah, "Influences of Hall current and radiation on MHD micropolar non-newtonian hybrid nanofluid flow between two surfaces," AIP Advances, **10**(5), 055015 (2020). https://doi.org/10.1063/1.5145298

[9] M.D. Ikram, M.I. Asjad, A. Akgül, and D. Baleanu, "Effects of hybrid nanofluid on novel fractional model of heat transfer flow between two parallel plates," Alexandria Engineering Journal, **60**(4), 3593-3604 (2021). https://doi.org/10.1016/j.aej.2021.01.054

[10] N.S. Khashi'ie, I. Waini, N.Md. Arifin, and I. Pop, "Unsteady squeezing flow of Cu-Al$_2$O$_3$/water hybrid nanofluid in a horizontal channel with magnetic field," Scientific reports, **11**(1), 14128 (2021). https://doi.org/10.1038/s41598-021-93644-4

[11] M. Yaseen, S.K. Rawat, A. Shafiq, M. Kumar, and K. Nonlaopon, "Analysis of heat transfer of mono and hybrid nanofluid flow between two parallel plates in a Darcy porous medium with thermal radiation and heat generation/absorption," Symmetry, **14**(9), 1943 (2022). https://doi.org/10.3390/sym14091943

[12] H.T. Rostami, M.F. Najafabadi, Kh. Hosseinzadeh, and D.D. Ganji, "Investigation of mixture-based dusty hybrid nanofluid flow in porous media affected by magnetic field using RBF method," International Journal of Ambient Energy, **43**(1), 6425-6435 (2022). https://doi.org/10.1080/01430750.2021.2023041

[13] A.R. Faisal, N.A. Shah, and T. Botmart, "Hall current and morphological effects on mhd micropolar non-newtonian tri-hybrid nanofluid flow between two parallel surfaces," Scientific Reports, **12**(1), 16608 (2022). https://doi.org/10.1038/s41598-022-19625-3

[14] I. Waini, A. Ishak, and I. Pop. "Radiative and magnetohydrodynamic micropolar hybrid nanofluid flow over a shrinking sheet with joule heating and viscous dissipation effects," Neural Computing and Applications, **34**(5), 3783-3794 (2022). https://doi.org/10.1007/s00521-021-06640-0

[15] O.A. Famakinwa, O.K. Koriko, and K.S. Adegbie, "Effects of viscous dissipation and thermal radiation on time dependent incompressible squeezing flow of CuO-Al$_2$O$_3$/water hybrid nanofluid between two parallel plates with variable viscosity," Journal of Computational Mathematics and Data Science, **5**, 100062 (2022). https://doi.org/10.1016/j.jcmds.2022.100062

[16] M. Bilal, A. El-Sayed Ahmed, R.A. El-Nabulsi, N.A. Ahammad, K.A.M. Alharbi, M.A. Elkotb, W. Anukool, and A.S.A. Zedan, "Numerical analysis of an unsteady, electroviscous, ternary hybrid nanofluid flow with chemical reaction and activation energy across parallel plates," Micromachines, **13**(6), 874 (2022). https://doi.org/10.3390/mi13060874

[17] H. Hanif, W. Jamshed, M.R. Eid, R. Ibrahim, S. Shafie, A.A. Raezah, S.M. El Din, *et al.*, "Numerical Crank-Nicolson methodology analysis for hybridity aluminium alloy nanofluid flowing based-water via stretchable horizontal plate with thermal resistive effect," Case Studies in Thermal Engineering, **42**, 102707 (2023). https://doi.org/10.1016/j.csite.2023.102707

[18] N.A.M. Noor, and S. Shafie, "Magnetohydrodynamics squeeze flow of sodium alginate-based Jeffrey hybrid nanofluid with heat sink or source," Case Studies in Thermal Engineering, **49**, 103303 (2023). https://doi.org/10.1016/j.csite.2023.103303

[19] A. Ullah, N. Fatima, K.A.M. Alharbi, S. Elattar, and W. Khan, "A numerical analysis of the hybrid nanofluid (Ag+TiO$_2$+water) flow in the presence of heat and radiation fluxes," Energies, **16**(3), 1220 (2023). https://doi.org/10.3390/en16031220

[20] N.C. Roy, and I. Pop, "Analytical investigation of transient free convection and heat transfer of a hybrid nanofluid between two vertical parallel plates," Physics of Fluids, **34**(7), 072005 (2022). https://doi.org/10.1063/5.0096694

[21] P. Jayavel, R. Katta, and R.K. Lodhi, "Numerical analysis of electromagnetic squeezing flow through a parallel porous medium plate with impact of suction/injection," Waves in Random and Complex Media, 1-24, (2022). https://doi.org/10.1080/17455030.2022.2088890

[22] K. Bhaskar, K. Sharma, and K. Bhaskar. "MHD squeezed radiative flow of Casson hybrid nanofluid between parallel plates with joule heating," International Journal of Applied and Computational Mathematics, **10**(2), 80 (2024). https://doi.org/10.1007/s40819-024-01720-w

[23] H. Maiti, and S. Mukhopadhyay, "Squeezing unsteady nanofluid flow among two parallel plates with first-order chemical reaction and velocity slip," Heat Transfer, **53**(4), 1790-1815 (2024). https://doi.org/10.1002/htj.23015

[24] B.M. Madit, J.K. Kwanza, and P.R. Kiogora, "Hydromagnetic squeezing nanofluid flow between two vertical plates in presence of a chemical reaction," Journal of Applied Mathematics and Physics, **12**(1), 126-146 (2024). https://doi.org/10.4236/jamp.2024.121011

[25] N.S. Khashi'ie, N.Md. Arifin, E.H. Hafidzuddin, and N. Wahi, "Dual stratified nanofluid flow past a permeable shrinking/stretching sheet using a non-fourier energy model," Applied sciences, **9**(10), 2124 (2019). https://doi.org/10.3390/app9102124

[26] N.S. Khashi'ie, E.H. Hafidzuddin, N.Md. Arifin, and N. Wahi, "Stagnation point flow of hybrid nanofluid over a permeable vertical stretching/shrinking cylinder with thermal stratification effect," CFD Letters, **12**(2), 80-94 (2020). https://www.akademiabaru.com/submit/index.php/cfdl/article/view/3215/2247

[27] R.S. Nath, and R.K. Deka, "Theoretical Study of Thermal and Mass Stratification Effects on MHD Nanofluid Past an Exponentially Accelerated Vertical Plate in a Porous Medium in Presence of Heat Source, Thermal Radiation and Chemical Reaction," International Journal of Applied and Computational Mathematics, 10(2), 92 (2024). https://doi.org/10.1007/s40819-024-01721-9

[28] R.S. Nath, and R.K. Deka, "Thermal and mass stratification effects on MHD nanofluid past an exponentially accelerated vertical plate through a porous medium with thermal radiation and heat source," International Journal of Modern Physics B, 2550045, (2024). https://doi.org/10.1142/S0217979225500456

[29] R.S. Nath, and R.K. Deka, "Thermal and mass stratification effects on unsteady parabolic flow past an infinite vertical plate with exponential decaying temperature and variable mass diffusion in porous medium," ZAMM-Journal of Applied Mathematics and Mechanics/Zeitschrift für Angewandte Mathematik und Mechanik, e202300475 (2024). https://doi.org/10.1002/zamm.202300475

[30] R.S. Nath, and R.K. Deka, "A Numerical Study on the MHD Ternary Hybrid Nanofluid (Cu-Al_2O_3-TiO_2/H_2O) in presence of Thermal Stratification and Radiation across a Vertically Stretching Cylinder in a Porous Medium," East European Journal of Physics, (1), 232-242 (2024). https://doi.org/10.26565/2312-4334-2024-1-19

[31] R.S. Nath, and R.K. Deka, "A Numerical Investigation of the MHD Ternary Hybrid Nanofluid (Cu-Al_2O_3-TiO_2/H_2O) Past a Vertically Stretching Cylinder in a Porous Medium with Thermal Stratification," Journal of Advanced Research in Fluid Mechanics and Thermal Sciences, **116**(1), 78-96 (2024). https://doi.org/10.37934/arfmts.116.1.7896

[32] M.V. Krishna, "Numerical investigation on steady natural convective flow past a perpendicular wavy surface with heat absorption/generation," International Communications in Heat and Mass Transfer, 139, 106517 (2022). https://doi.org/10.1016/j.icheatmasstransfer.2022.106517

[33] M.V. Krishna, and K. Vajravelu, "Rotating MHD flow of second grade fluid through porous medium between two vertical plates with chemical reaction, radiation absorption, Hall, and ion slip impacts," Biomass Conversion and Biorefinery, **14**(7), 8745-8759 (2024). https://doi.org/10.1007/s13399-022-02802-9

[34] M.V. Krishna, "Hall effects on magnetohydrodynamic rotating flow through porous medium in a parallel plate channel with various oscillations of pressure gradient," Heat Transfer, **52**(1), 236-266 (2023). https://doi.org/10.1002/htj.22693

[35] N. Hale, and D. Moore, *A sixth-order extension to the MATLAB package bvp4c of J. Kierzenka and L. Shampine*, (Oxford University Computing Laboratory, 2008).

[36] S. Rosseland, *Astrophysik und atom-theoretische Grundlagen*, (Springer-Verlag; Berlin, 1931).

[37] I. Waini, A. Ishak, and I. Pop, "Mixed convection flow over an exponentially stretching/shrinking vertical surface in a hybrid nanofluid," Alexandria Engineering Journal, **59**(3), 1881-1891 (2020). https://doi.org/10.1016/j.aej.2020.05.030

ЧИСЕЛЬНЕ ДОСЛІДЖЕННЯ СТИСКАЮЧОГО ПОТОКУ ПОТРІЙНОЇ ГІБРИДНОЇ НАНОРІДИНИ
($Cu - Al_2O_3 - TiO_2/H_2O$) МІЖ ДВОМА ПАРАЛЕЛЬНИМИ ПЛАСТИНАМИ В ПОРИСТОМУ
СЕРЕДОВИЩІ ДАРСІ З В'ЯЗКОЮ ДИСИПАЦІЄЮ ТА ДЖЕРЕЛОМ ТЕПЛА
Рубул Бора, Бідют Боруа
Факультет математики, коледж CNB, Бокахат-785612, Ассам, Індія

Ця робота спрямована на чисельне дослідження впливу в'язкої дисипації та джерела тепла на магнітогідродинамічний стискаючий потік потрійних гібридних нанофлюїдів на водній основі між двома паралельними пластинами в пористому середовищі Дарсі. Наночастинки Cu, Al_2O_3 і TiO_2 диспергуються в базовій рідині H_2O, що призводить до створення потрійної гібридної нанорідини $Cu - Al_2O_3 - TiO_2/H_2O$. У цьому дослідженні вивчається деформація нижньої пластини, коли верхня просувається до неї. Чисельні результати обчислюються за допомогою 3-етапного методу Лобатто IIIa, який спеціально реалізовано Bvp4c у MATLAB. Вплив різних параметрів візуально проілюстровано за допомогою графіків і кількісно показано в таблицях. Вважається, що абсолютне поверхневе тертя потрійної гібридної нанорідини приблизно на 5% вище, ніж у звичайної нанорідини на нижній пластині, і щонайбільше на 7% вище, ніж у нанорідини на верхній пластині. Швидкість теплопередачі потрійної гібридної нанофлюїду вища на верхній пластині порівняно з нижньою.

Ключові слова: *теплове випромінювання; в'язке розсіювання; паралельна пластина; джерело тепла; потрійний гібридний нанофлюїд; пористе середовище Дарсі; bvp*

THERMAL PERFORMANCE OF NANOFLUID FLOW ALONG AN ISOTHERMAL VERTICAL PLATE WITH VELOCITY, THERMAL, AND CONCENTRATION SLIP BOUNDARY CONDITIONS EMPLOYING BUONGIORNO'S REVISED NON-HOMOGENEOUS MODEL

Sujit Mishra, Aditya Kumar Pati, Ashok Misra*, Saroj Kumar Mishra

Centurion University of Technology and Management, Paralakhemundi, Odisha, India
*Corresponding author e-mail: amisra1972@gmail.com

This study examines the natural convection of a steady laminar nanofluid flow past an isothermal vertical plate with slip boundary conditions. A review of existing literature reveals no prior research that has explored the combined effects of thermophoresis, Brownian diffusion, and particle electrification while considering slip boundary conditions in nanofluid flow. Buongiorno's revised four-equation non-homogeneous model, incorporating mechanisms for thermophoresis, Brownian diffusion and particle electrification, is utilized to address this gap. The model employs velocity, thermal, and concentration slip boundary conditions to investigate enhancing the nanofluid's thermal conductivity. The resulting local similar equations are tackled using MATLAB's bvp4c package. The study discusses the influence of key parameters, such as thermophoresis, Brownian motion, and electrification, on temperature, velocity, and concentration distributions, as well as on heat, mass transfer and skin friction coefficients. The findings of the simulation are consistent with previous studies, showing that an improvement in the electrification parameter rises the heat transfer coefficient, while thermophoresis and Brownian motion parameters have the opposite effect. Additionally, mass transfer coefficient values increase with higher Brownian motion and electrification parameters while reducing with the thermophoresis parameter. This physical model has potential applications in heat exchangers using nanofluids and in cooling plate-shaped products during manufacturing processes. The novelty of this study lies in the analysis of Brownian diffusion, thermophoresis, and particle electrification mechanisms in nanofluid flow under slip boundary conditions.

Keywords: *Thermal Conductivity; Nanofluid; Velocity Slip Boundary Condition; Thermal Slip Boundary Condition; Concentration Slip Boundary Condition*
PACS: 44.20.+b, 44.25.+f, 47.10.ad, 47.55.pb, 47.15.Cb

1. INTRODUCTION:

Nanofluids have gained widespread use across numerous industrial applications due to the remarkable chemical and physical properties of nanoscale particles. These nanofluids are sophisticated composite materials composed of solid nanoparticles, typically between 1 and 100 nm in size, dispersed within a liquid medium. The use of nanofluids instead of traditional base fluids to enhance heat transfer rates has garnered significant attention from researchers worldwide, highlighting the distinct advantages of nanofluids over conventional fluids. Nanofluids, which consist of nanoparticles suspended in a base fluid, have been recognized as effective coolants for improving heat transfer performance in various applications. These applications include paper manufacturing, electronic devices, nuclear reactors, power generation, air conditioning systems, domestic refrigerators, and the automotive industry. By leveraging the unique properties of nanofluids, these industries can achieve more efficient thermal management, leading to better performance and energy savings.

The concept of "nanofluids" was first coined by Choi [1], marking a pivotal breakthrough in the study of fluid dynamics at the nanoscale. Subsequent research demonstrated that even a minimal addition of nanoparticles can dramatically improve the thermal conductivity of fluids. Buongiorno [2] further advanced the field by investigating the convective transport phenomena in nanofluids, providing valuable insights into their distinctive flow behaviors. Buongiorno observed that the improvement in the thermal performance of nanofluids is primarily driven by the slip mechanisms of Brownian motion and thermophoresis. Since then, numerous studies, including those by Kuznetsov and Nield [3], Gasmi et al. [4], Ebrahem et al. [5], Kinyanjui et al. [6], Ahmed et al. [7], Biswal et al. [8], Khairul et al. [9], Sobamowo et al. [10], Sobamowo [11], Sobamowo [12], and Aziz and Khan [13] have explored the behavior of natural convection considering different types of nanofluid flow along a vertical plate employing a homogeneous model.

Based on the literature reviewed (Kuznetsov and Nield [3], Mojtabi et al. [14], Abu-Nada et al. [15], Probstein [16], Tyndall [17], Bird et al. [18], Pakravan and Yaghoubi [19]), the slip boundary condition for velocity, temperature, and solute has generally been overlooked. In systems like emulsions, foams, gels, and slurries, the non-homogeneous properties of fluid at solid boundaries often result in "apparent wall slip." This phenomenon happens when the fluid's viscosity near the boundary decreases, leading to the formation of a thin layer with a steep velocity gradient, often described as a "slipping layer." Comprehensive studies on wall slip in shrinking sheets by Makinde et al. [20] reveal that true slip involves a velocity discontinuity at the wall. In contrast, for the other systems discussed, true slip is absent. Instead, "apparent slip" occurs, which is caused by a region with a steeper velocity gradient near the wall. In such cases,

the no-slip condition fails to accurately represent the physical situation, making slip conditions a more suitable choice. Similarly, the no-slip condition is also inadequate for non-Newtonian fluids and nanofluids. During processes like annealing and thinning, the final product's quality is heavily influenced by the heat transfer rate at the continuously stretching surface. Both the stretching kinematics and the concurrent heating or cooling are crucial factors in determining the final product's quality. Therefore, incorporating slip boundary conditions for concentration, temperature, and velocity is essential.

In recent years, several investigations (Pati et al. [21-26], Panda et al. [27], Pattnaik et al. [28]) have explored the electrification of nanoparticles within nanofluid flows under various physical conditions. In all the previously mentioned studies on nanofluid dynamics involving the electrified nanoparticles, the slip boundary conditions have been overlooked.

Based on the past literature, this study aims to investigate the impacts of thermophoresis, Brownian diffusion, and particle electrification on the transfer of heat and mass within the natural convective boundary layer nanofluid flow along an isothermal vertical plate with slip boundary conditions. This study takes into account various boundary conditions, including velocity, thermal, and concentration slip conditions. Buongiorno's revised four-equation non-homogeneous model is employed in the present investigation. This particular approach to modeling the flow of nanofluids concerning heat and mass transport phenomena has not been explored in previous research literature.

2. MATHEMATICAL FORMULATION

An analysis is conducted on a nanofluid's laminar steady boundary layer flow over an isothermal vertical plate. The orientation of the plate is aligned with the vertical axis. It is assumed that both the concentration C_w and temperature T_w of the plate remain invariant. The free stream parameters of C and T defined as C_∞ and T_∞, respectively. The physical representation of the system is illustrated in Fig. 1.
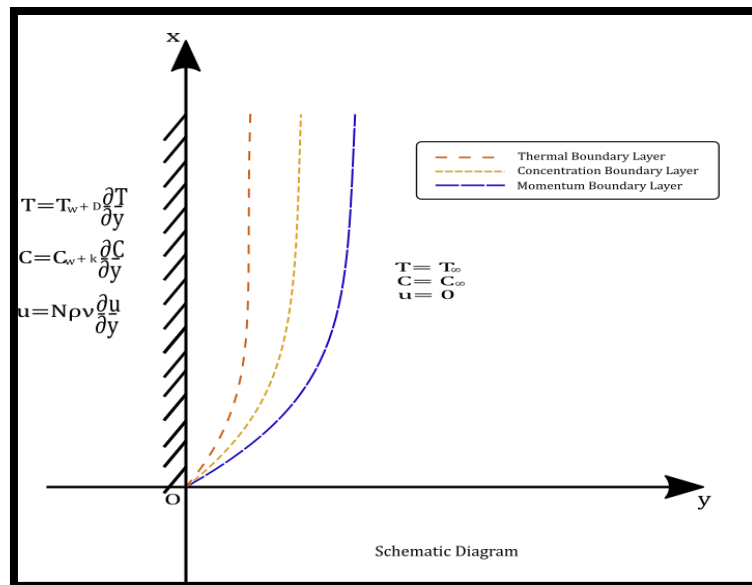

Figure 1. Coordinate system and physical model

Based on the assumptions outlined earlier and applying boundary layer simplifications according to Pati et al. [22], the governing equations for the flow field in a two-dimensional Cartesian coordinate system can be derived and are given as follows.

$$\frac{\partial u}{\partial x} + \frac{\partial v}{\partial y} = 0, \tag{1}$$

$$\rho_{nf}\left[u\frac{\partial u}{\partial x} + v\frac{\partial u}{\partial y}\right] = -\frac{\partial p}{\partial x} + \mu_{nf}\left[\frac{\partial^2 u}{\partial y^2}\right] - \rho_{nf}\ g + C\left(\frac{q}{m}\right)E_x, \tag{2}$$

$$\left[u\frac{\partial T}{\partial x} + v\frac{\partial T}{\partial y}\right] = \frac{k_{nf}}{(\rho c)_{nf}}\frac{\partial^2 T}{\partial y^2} + \frac{c_s D_B}{(\rho c)_{nf}}\frac{\partial C}{\partial y}\frac{\partial T}{\partial y} + \frac{\rho_s c_s}{(\rho c)_{nf}}\frac{D_T}{T_\infty}\frac{\partial T}{\partial y}\frac{\partial T}{\partial y} + \left(\frac{q}{m}\right)\frac{c_s C}{F(\rho c)_{nf}}\left(E_x\frac{\partial T}{\partial x} + E_y\frac{\partial T}{\partial y}\right), \tag{3}$$

$$u\frac{\partial C}{\partial x} + v\frac{\partial C}{\partial y} = D_B\frac{\partial^2 C}{\partial y^2} + \frac{\rho_s D_T}{T_\infty}\frac{\partial^2 T}{\partial y^2} + \left(\frac{q}{m}\right)\frac{1}{F}\left[\frac{\partial(CE_x)}{\partial x} + \frac{\partial(CE_y)}{\partial y}\right]. \tag{4}$$

The electric field (E-field) is defined by the following equation.

$$\frac{\partial E_x}{\partial x} + \frac{\partial E_y}{\partial y} = \frac{\rho_s}{\epsilon_0}\frac{q}{m}. \tag{5}$$

According to the Oberbeck-Boussinesq Approximation, the equation of motion in the x-direction, represented by Equation (2), is expressed as follows:

$$\rho_{nf}\left[u\frac{\partial u}{\partial x} + v\frac{\partial u}{\partial y}\right] = \mu_{nf}\left[\frac{\partial^2 u}{\partial y^2}\right] + \beta_{f\infty}\rho_{f\infty}(T - T_\infty)(1 - C_\infty)g - (C - C_\infty)(\rho_s - \rho_{f\infty})g + (C - C_\infty)\left(\frac{q}{m}\right)E_x. \quad (6)$$

The relevant slip boundary conditions for this study are defined by

$$\left.\begin{array}{l} y = 0, u = U + N\rho v\frac{\partial u}{\partial y}, v = 0, T = T_W + D\frac{\partial T}{\partial y}, C = C_W + K\frac{\partial C}{\partial y} \\ y \to \infty, u = 0, v = 0, T = T_\infty, C = C_\infty \end{array}\right\}. \quad (7)$$

Based on Soo [29], by disregarding the variation of the electric field in the x-direction, the transverse electric field can be expressed as

$$\frac{\partial E_y}{\partial y} = \frac{\rho_s}{\epsilon_0}\frac{q}{m}.$$

Introducing the stream function and scale analysis of the governing equation (1) are satisfied following Kuznetsov and Nield [3].

$$u = \frac{\partial \psi}{\partial y}, v = -\frac{\partial \psi}{\partial x}, s(\eta) = \frac{C - C_\infty}{C_w - C_\infty},$$

$$\psi = \alpha_f(Ra)^{\frac{1}{4}}f(\eta), \theta(\eta) = \frac{T - T_\infty}{T_w - T_\infty},$$

where, $\eta = \frac{y}{x}(Ra)^{\frac{1}{4}}$, is the local similarity variable and $Ra_x = \frac{(T_w - T_\infty)(1 - C_\infty)\beta_f gx^3}{v_f \alpha_f}$, is the local Rayleigh number, we get,

$$u = \frac{\partial \psi}{\partial y} = \frac{\alpha_f(Ra_x)^{\frac{1}{2}}}{x}f', v = -\frac{\partial \psi}{\partial x} = -\frac{\alpha_f(Ra_x)^{\frac{1}{4}}}{4x}[3f - \eta f']$$

The equations (2), (3), (4) converted into non-dimensional equations (8), (9), (10) as follows:
Momentum equation:

$$f''' + \frac{\varphi_1}{4Pr}[3ff'' - 2(f')^2] + \varphi_1\varphi_2\frac{M\,Sc\,N_b}{PrN_F}s + \frac{1}{\varphi_5}(\theta - Nrs) = 0. \quad (8)$$

Energy equation:

$$\theta'' + \frac{3}{4}\frac{1}{\varphi_3\varphi_4}f\theta' + \frac{1}{\varphi_4}Pr\,N_b s'\theta' + \frac{1}{\varphi_4}Pr\,N_t(\theta')^2 + \frac{1}{\varphi_4}Sc\,N_b\left[\frac{N_F}{N_{Re}} - \frac{1}{4}M\right](s + Nc)\eta\theta' = 0. \quad (9)$$

Concentration equation:

$$s'' + \frac{3}{4}\frac{Sc}{Pr}fs' + \frac{N_t}{N_b}\theta'' - \frac{1}{4}\frac{M\,Sc}{Pr}\eta s' + \frac{N_F Sc}{PrN_{Re}}(\eta s' + s + Nc) = 0. \quad (10)$$

Similarly, the slip boundary conditions in equation (7) converted into non-dimensional form as follows:

$$\left.\begin{array}{l} \eta = 0; f = 0; f' = Af'', \theta = 1 + \chi\theta'; s = 1 + \gamma s' \\ \eta \to \infty; f' = 0; \theta = 0; s = 0 \end{array}\right\} \quad (11)$$

where,

$$\gamma = K\frac{1}{x}(Ra_x)^{\frac{1}{4}}; \chi = D\frac{(Ra_x)^{\frac{1}{4}}}{x}; A = N\mu\frac{(Ra_x)^{\frac{1}{4}}}{x};$$

$$M = \left(\frac{q}{m}\right)\frac{1}{F\left(\frac{\alpha_f(Ra_x)^{\frac{1}{2}}}{x}\right)}E_x, N_F = \frac{\left(\frac{\alpha_f(Ra_x)^{\frac{1}{2}}}{x}\right)}{Fx}, \frac{1}{N_{Re}} = \left(\frac{q}{m}\right)^2\frac{\rho_s}{\epsilon_0}\frac{x^2}{\left(\frac{\alpha_f(Ra_x)^{\frac{1}{2}}}{x}\right)^2}, Nr = \frac{(\rho_s - \rho_f)(C_w - C_\infty)}{(1 - C_\infty)\rho_f\beta_f(T_w - T_\infty)};$$

$$Pr = \frac{v_f}{\alpha_f}, Sc = \frac{v_f}{D_B}, N_b = \frac{(\rho c)_s D_B(C_w - C_\infty)}{(\rho c)_f v_f}, N_t = \frac{(\rho c)_s D_T(T_w - T_\infty)}{(\rho c)_f v_f T_\infty}, N_c = \frac{C_\infty}{(C_w - C_\infty)}.$$

This investigation considers a copper water nanofluid which contains 1% of copper nanoparticles. Table-1 provides the thermophysical properties of copper-water nanofluid as outlined by Oztop and Abunada [30], while Table-2 lists the corresponding thermophysical constants.

Table 1. Thermophysical properties

Property	copper	water
$c_p (J/kgK)$	0.385	4.179
$\rho (kg/m^3)$	8933	997.1
$k (W/mK)$	401	0.613

Table 2. Thermophysical constants

φ_1	$(1 - C_\infty)^{2.5} \left[C_\infty \dfrac{\rho_s}{\rho_f} + (1 - C_\infty) \right]$
φ_2	$\dfrac{c_f}{c_s} \dfrac{1}{\left[C_\infty \dfrac{\rho_s}{\rho_f} + (1 - C_\infty) \right]}$
φ_3	$\dfrac{1}{C_\infty \tau + (1 - C_\infty)}$
φ_4	$\dfrac{2k_f + k_s - 2C_\infty(k_f - k_s)}{2k_f + k_s + C_\infty(k_f - k_s)}$
φ_5	$\dfrac{1}{(1 - C_\infty)^{2.5}}$

The local skin friction C_{fx}, local Sherwood number Sh_x for mass transfer purpose and local Nusselt number Nu_x for heat transfer purpose are given as

$$\frac{(Ra_x)^{\frac{1}{4}}}{Pr} C_{fx} = (f'')_{\eta=0}; \quad \frac{1}{(Ra_x)^{\frac{1}{4}}} Nu_x = -(\theta')_{\eta=0}; \quad \frac{1}{(Ra_x)^{\frac{1}{4}}} Sh_x = -(s')_{\eta=0},$$

where ($'$) indicates derivative with respect to η and $(f'')_{\eta=0}, -(\theta')_{\eta=0}$, and $-(s')_{\eta=0}$ denotes the dimensionless skin friction coefficient, Nusselt number and Sherwood number, respectively.

3. METHOD OF SOLUTION

It has been observed that Pohlhausen-Kuiken-Bejan problems (Bejan [31]) for conventional heat transfer fluids have one non-dimension parameter Pr. However, the non-dimensional equations of the present problem contain nine independent dimensionless parameters, such as Pr, N_b, N_t, N_{Re}, M, Nr, Sc, N_F, Sc. Thus, input selective values are required to solve the problem. Additionally, the processing time for each of these input parameters is quite brief. Since the physical domain extends infinitely while the computational domain is limited, it is essential to select an optimal finite value for η_∞. Since the needed initial value $f''(0), -\theta'(0), -s'(0)$, which are not defined for the present problem. Hence, some initial guesses are used at the starting point, as well as some finite values of η_∞, for a specific range of physical parameters. The solution process is iteratively applied with different values of η_∞ until the successive values of $f''(0), -\theta'(0), -s'(0)$ differ by a specified precision. The final η_∞ value obtained is considered the most suitable for that set of parameters. This approach is known as the shooting method.

To address the system of local similarity equations (8)-(10) with the boundary conditions (11) using the shooting method, the MATLAB built-in function bvp4c, which utilizes the collocation technique (as described by Shampine and Kierzenka [32]), is employed to produce numerical results for the specified physical parameters. The variations of the computational values of $(f'')_{\eta=0}, -(\theta')_{\eta=0}$ and $-(s')_{\eta=0}$ with different values of M, N_b and N_t, are presented in tabular form. Similarly, the variations of the non-dimensional temperature profile $\theta(\eta)$, non-dimensional velocity profile $f'(\eta)$ and dimensionless concentration distribution of nanoparticles $s(\eta)$ are depicted in Figures 2 to 10.

4. COMPARISON AND VALIDATION

The resultant quantitative data have been contrasted with those computed by Narahari et al. [33], in conjunction with the pertinent values for the particular context of regular fluid outlined in Table 3. The present outcomes exhibit a notable alignment with the prior findings.

Table 3. Comparison of present results with existing literature

Pr	Narahari et al. [33]	Present analysis
1	0.401	0.4010
10	0.459	0.4649
100	0.473	0.4900
1000	0.474	0.4985

5. RESULTS AND DISCUSSION

In this subsection, the impact of M, N_t, and N_b on $f'(\eta)$, $\theta(\eta)$ and $s(\eta)$ against η, illustrated and examined with the help of graphical analysis. Further, the impact of these parameters on $f''(0), -\theta'(0), -s'(0)$ are presented in Tabular form. Additionally, the contour plots are presented to explore the combined effects of M, N_t, and N_b on $f''(0), -\theta'(0), -s'(0)$.

5.1 Influence of electrification parameter M on $f'(\eta)$, $\theta(\eta)$ and $s(\eta)$ with slip boundary conditions

Figures 1 and 2 show that as the parameter M increases, the value of $f'(\eta)$ rises while $\theta(\eta)$ falls throughout the boundary layer. This effect is attributed to the Lorentz force, which results from the electric field acting as an accelerating force that reduces frictional resistance. Consequently, the decrease in frictional resistance leads to a lower temperature in the boundary layer, as no extra thermal energy is produced. Figure 3 depicts the changes in the non-dimensional particle concentration profile $s(\eta)$, illustrating that the concentration decreases with increasing M because the particles are carried away by the fluid moving from the plate. This observed trend suggests that elevated parameter values facilitate particle transport, resulting in a more homogeneous distribution throughout the flow. Figures 2-4 illustrate the variation of $f'(\eta)$, $\theta(\eta)$ and $s(\eta)$ with M while keeping other parameters constant ($A = \chi = \gamma = N_t = N_b = N_F = Nc = Nr = 0.1, Sc = N_{Re} = 2.0$, and $Pr = 6.2$).
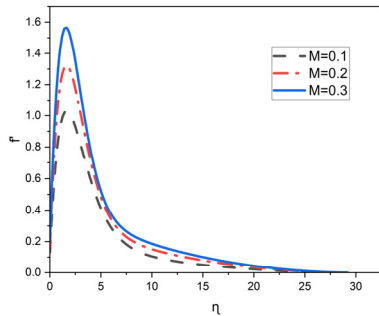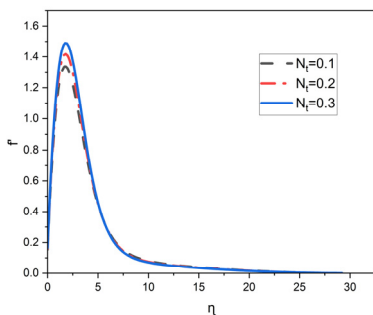

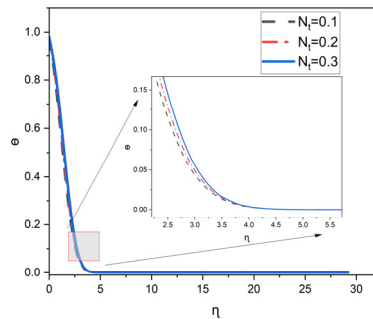**Figure 2.** Impact of M on $f'(\eta)$ **Figure 3.** Impact of M on $\theta(\eta)$ **Figure 4.** Impact of M on $s(\eta)$
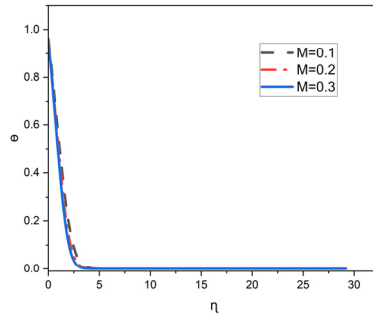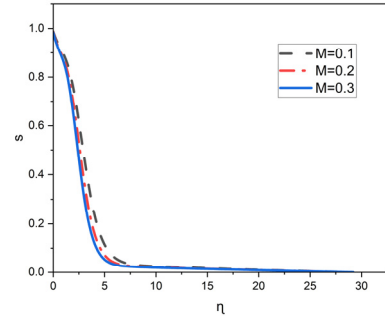
5.2 Influence of thermophoresis parameter N_t on $f'(\eta)$, $\theta(\eta)$ and $s(\eta)$ with slip boundary conditions

Figures 5, 6, and 7 show how the thermophoresis parameter N_t affects on $f'(\eta)$, $\theta(\eta)$, and $s(\eta)$. It is noted that with higher values of N_t, all $f'(\eta)$, $\theta(\eta)$ and $s(\eta)$ profile increases. This is because the increased thermophoresis force causes hot nanoparticles to move faster from the plate region towards the fluid region, thereby raising the dimensionless velocity profiles as well as temperature and concentration profiles. This behaviour is crucial for optimizing the efficiency of thermal systems, as it allows for better heat transfer and enhanced performance in applications such as cooling and energy conversion. Figures 5-7 illustrates the variation of $f'(\eta)$, $\theta(\eta)$ and $s(\eta)$ with N_t while keeping other parameters constant ($A = \chi = \gamma = M = N_b = N_F = Nc = Nr = 0.1, Sc = N_{Re} = 2.0$, and $Pr = 6.2$).

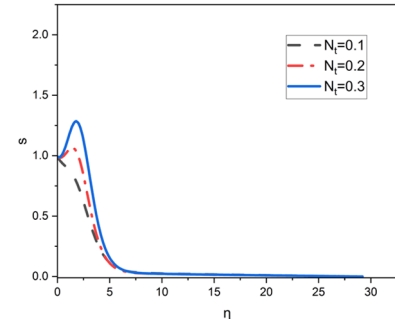**Figure 5.** Impact of N_t on $f'(\eta)$ **Figure 6.** Impact of N_t on $\theta(\eta)$ **Figure 7.** Impact of N_t on $s(\eta)$

5.3. Influence of Brownian motion parameter N_b on $f'(\eta)$, $\theta(\eta)$ and $s(\eta)$ with slip boundary conditions

Brownian motion describes the erratic movement of minute particles suspended in a fluid. This unpredictable motion increases the frequency of collisions between nanoparticles and fluid molecules, leading to the transformation of the molecules' kinetic energy into heat. Smaller particles experience more intense Brownian motion, leading to higher values in N_b. In contrast, larger particles exhibit weaker Brownian motion, resulting in lower values in N_b.
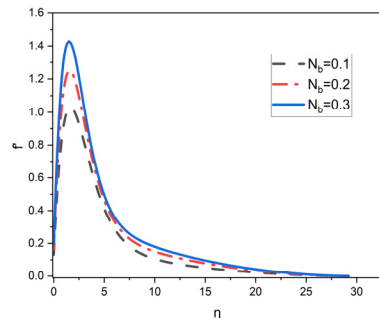

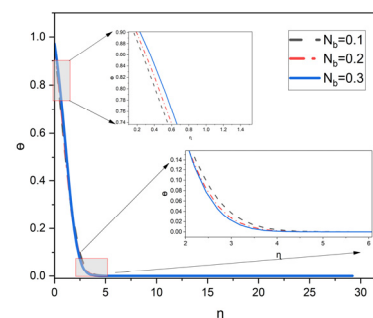
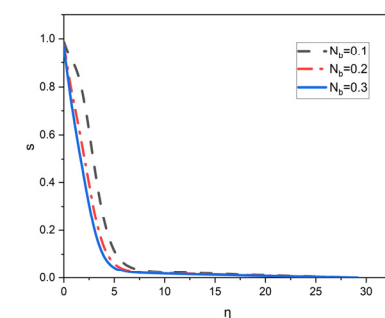**Figure 8.** Impact of N_b on $f'(\eta)$ **Figure 9.** Impact of N_b on $\theta(\eta)$ **Figure 10.** Impact of N_b on $s(\eta)$

Figures 8, 9, and 10 depict the impact of N_b on $f'(\eta), \theta(\eta)$, and $s(\eta)$ profiles. It is observed that the profiles of $f'(\eta)$ show an upward trend, while the $s(\eta)$ shows a downward trend as the values increase for N_b. The profile of $\theta(\eta)$ demonstrates a dual characteristic with the N_b. The temperature distribution increases near the surface of the plate but decreases away from it. As the values in N_b increase, the movement of nanoparticles becomes more pronounced. Consequently, their activity becomes more dynamic, resulting in more frequent collisions within the system. This increased activity promotes a uniform distribution of nanoparticles within the medium, ultimately influencing the system's thermal conductivity and overall performance. Figures 8-10 illustrates the variation of $f'(\eta), \theta(\eta)$ and $s(\eta)$ with N_b while keeping other parameters constant ($A = \chi = \gamma = M = N_t = N_F = Nc = Nr = 0.1, Sc = N_{Re} = 2.0,$ and $Pr = 6.2$).

5.4. Influence of $M, N_t,$ and N_b on the non-dimensional skin friction, heat and mass transfer coefficients with slip boundary conditions

Table 4 illustrates the influences of M, N_t, and N_b on $f''(0)$, $-\theta'(0)$ and $-s'(0)$. The values of $f''(0)$ enhances with larger values of all the three parameters $M, N_t,$ and N_b. Values of $-\theta'(0)$ rises as M increases and reduces with higher values of N_t, and N_b. However, $-s'(0)$ improves with M and N_b, but reduces with higher values of N_t.

Table 4. Effects of $M, N_t,$ and N_b on $f''(0), -\theta'(0)$ and $-s'(0)$ when $Sc = N_{Re} = 2.0, Pr = 6.2, A = \chi = \gamma = Nr = Nc = N_F = 0.1$.

M	N_t	N_b	$f''(0)$	$-\theta'(0)$	$-s'(0)$
0.1	0.1	0.1	1.30966	0.37392	0.12734
0.2	0.1	0.1	1.68596	0.41169	0.15141
0.3	0.1	0.1	2.03417	0.44147	0.16622.
0.1	0.1	0.1	1.30966	0.37392	0.12734
0.1	0.2	0.1	1.53577	0.34208	0.07440
0.1	0.3	0.1	1.77814	0.28933	0.07335
0.1	0.1	0.1	1.30966	0.37392	0.12734
0.1	0.1	0.2	1.63950	0.32896	0.27441
0.1	0.1	0.3	1.93596	0.27784	0.33639

5.5. Combined effects of M and N_t on the non-dimensional skin friction, heat and mass transfer coefficients with slip boundary conditions

Combined effects of M and N_t on $f''(0)$, $-\theta'(0)$ and $-s'(0)$ are graphically examined in Figs. 11, 12 and 13, respectively. It is analyzed that all $f''(0)$, $-\theta'(0)$ and $-s'(0)$ are improves with M for different values of N_t. However, only $f''(0)$ increases, whereas both $-\theta'(0)$ and $-s'(0)$ decreases with N_t for varied values of M.
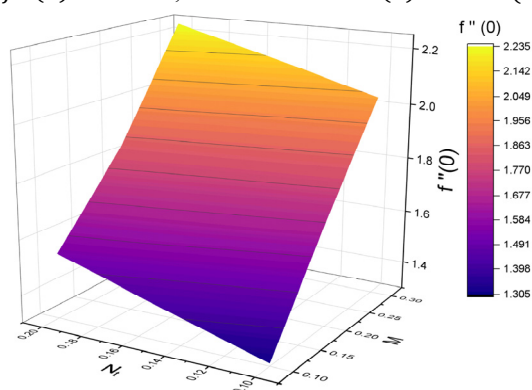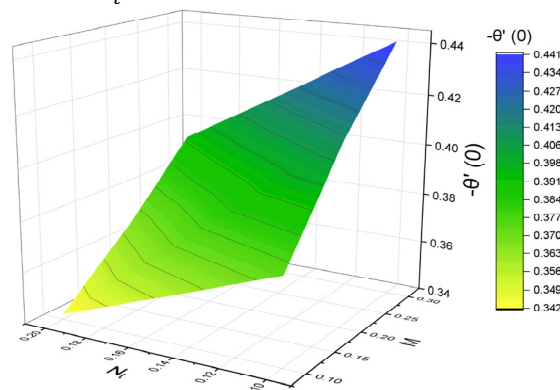

Figure 11. Combined effects of M and N_t on $f''(0)$

Figure 12. Combined effects of M and N_t on $-\theta'(0)$
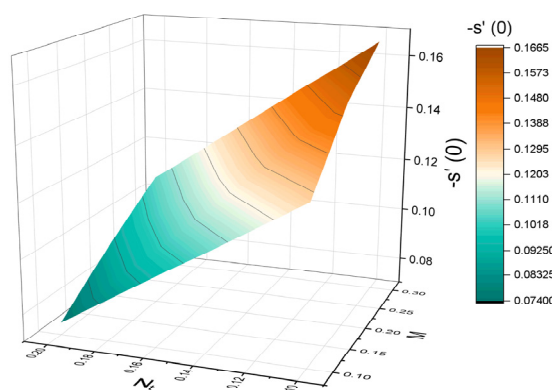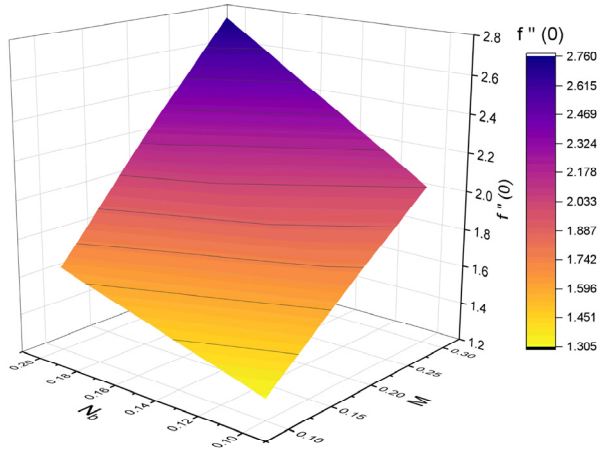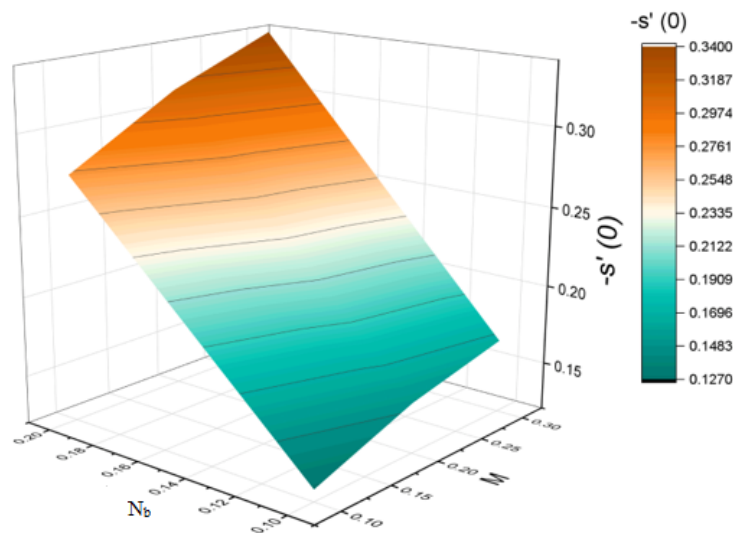

Figure 13. Combined effects of M and N_t on $-s'(0)$

5.6. Combined effects of M and N_b on the non-dimensional skin friction, heat and mass transfer coefficents with slip boundary conditions

Combined effects of M and N_b on $f''(0)$, $-\theta'(0)$ and $-s'(0)$ are graphically explored in Figs. 14, 15 and 16, respectively. It is observed that all the values of $f''(0)$, $-\theta'(0)$ and $-s'(0)$ are enhanced with M for different values of N_b. Additionally, it is noticed that both $f''(0)$ and $-s'(0)$ rises while $-\theta'(0)$ reduces with N_b for varied values of M.

Figure 14. Combined effects of M and N_b on $f''(0)$
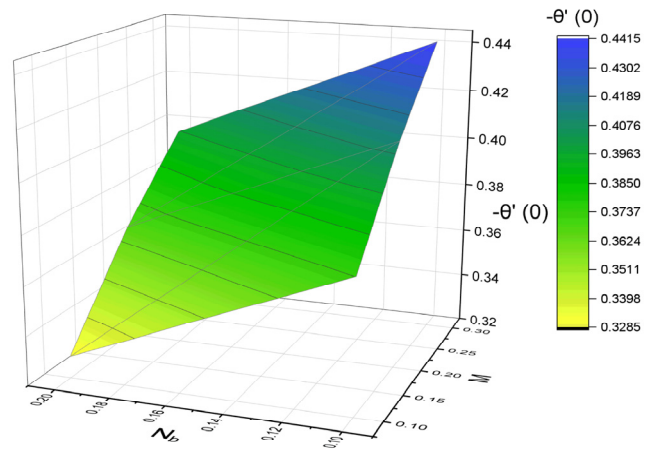
Figure 15. Combined effects of M and N_b on $-\theta'(0)$

Figure 16. Combined effects of M and N_b on $-s'(0)$

6. CONCLUSIONS

The study successfully examined the steady laminar flow of natural convective Copper-water nanofluid moving along an isothermal vertical plate while considering slip boundary conditions. The outcomes, illustrated and discussed through the figures, reveal a notable impact of control parameters, such as M, N_t and N_b on the non-dimensional temperature, concentration and velocity profiles. In addition, a comprehensive quantitative analysis was conducted on the skin friction, heat transfer, and mass transfer rates of copper-water nanofluid, with a focus on Brownian diffusion, electrification, and thermophoresis mechanisms under slip boundary conditions. This analysis was meticulously presented through detailed tables and contour surface graphs. These visual representations illustrate the impacts of these mechanisms on the reduced skin friction coefficient, heat transfer rate, and mass transfer rate, providing a clear understanding of how each factor influences these parameters. The main findings are as follows:

i. The shooting method implemented in MATLAB's bvp4c effectively addressed the local similarity equations, incorporating velocity, thermal, and concentration slip boundary conditions, ensuring accurate and reliable results.

ii. Dimensionless skin friction coefficient improves with higher values of all the three parameters M, N_t and N_b. Reduced Nusselt number enhances with only M. However, reduced Sherwood number rises with both M and N_b.

iii. An improved understanding of the interplay between electric fields, thermophoresis, and Brownian motion using copper water nanofluids can lead to developing more efficient cooling systems for compact and smart heat exchanger devices.

The findings of this study provide valuable insights into the behavior of electrified nanofluids with velocity, thermal, and concentration slip boundary conditions that can be applied to enhance thermal management in various engineering applications.

Nomenclature

A	Velocity slip parameter	N_t	Thermophoresis parameter
χ	Temperature slip parameter	Nr	Buoyancy ratio
γ	Concentration slip parameter	Nc	Concentration ratio
N	Velocity slip factor	N_F	Momentum transfer number
D	Thermal slip factor	N_{Re}	Electric Reynolds number
K	Concentration slip factor	Sc	Schmidt number
U, C, T	Local velocity, concentration & temperature	β_f	Volumetric thermal expansion coefficient
C_∞, T_∞	Free stream concentration & temperature	F	Momentum transfer time constant between the fluid and nanoparticles
C_w, T_w	Wall Surface concentration & temperature	ϵ_0	Permittivity
u, v	Velocity Component in direction x, y	ρ_s	Density of solid particles
E_x, E_y	Electric Intensity Component in direction x, y	ρ_f	Density of base fluid
g	Gravitational acceleration	ρ_{nf}	Density of nanofluid
D_T	Thermophoretic diffusion coefficient	μ_f	Viscosity of base fluid
D_B	Brownian diffusion coefficient	μ_{nf}	Viscosity of nanofluid
m	Mass of the nanoparticle	k_s	Thermal conductivity of solid particles
q	Charge of the nanoparticle	k_f	Thermal conductivity of base fluid
p	Pressure	k_{nf}	Thermal conductivity of nanofluid
Pr	Prandtl number	c_s	Specific heat capacity of solid particles
M	Electrification parameter	c_f	Specific heat capacity of base fluid
N_b	Brownian motion parameter	c_{nf}	Specific heat capacity of nanofluid

ORCID

Sujit Mishra, https://orcid.org/0000-0003-0106-7234; **Aditya Kumar Pati,** https://orcid.org/0000-0003-0966-5773
Ashok Misra, https://orcid.org/0000-0002-1148-1378; **Saroj Kumar Mishra,** https://orcid.org/0009-0005-2217-2764

REFERENCES

[1] S.U.S. Choi, Z.G. Zhang, W. Yu, F.E. Lockwood, and E.A. Grulke, "Anomalously thermal conductivity enhancement in nanotube suspensions," Applied Physics Letters, **79**, 2252-2254 (2001). https://doi.org/10.1063/1.1408272

[2] J. Buongiorno, "Convective transport in nanofluids," ASME J. Heat Transf. **128**, 240-250 (2006). https://doi.org/10.1115/1.2150834

[3] A.V. Kuznetsov, and D.A. Nield, "Natural convective boundary-layer flow of a nanofluid past a vertical plate," Int. J. Thermal Sci. **49**, 243-247 (2010). https://doi.org/10.1016/j.ijthermalsci.2009.07.015

[4] H. Gasmi, U. Khan, A. Zaib, A. Ishak, S.M. Eldin, and Z. Raizah, "Analysis of Mixed Convection on Two-Phase Nanofluid Flow Past a Vertical Plate in Brinkman-Extended Darcy Porous Medium with Nield Conditions," Mathematics, **10**(20), 3918 (2022). https://doi.org/10.3390/math10203918

[5] E.A. Algehyne, M. Areshi, A. Saeed, M. Bilal, W. Kumam, and P. Kumam, "Numerical simulation of bioconvective Darcy Forchhemier nanofluid flow with energy transition over a permeable vertical plate," Scientific Reports, **12**, 3228 (2022). https://doi.org/10.1038/s41598-022-07254-9

[6] J.K. Kigio, M.W. Nduku, and O.A. Samuel, "Analysis of Volume Fraction and Convective Heat Transfer on MHD Casson Nanofluid over a Vertical Plate," Fluid Mechanics, **7**(1), (2021). https://doi.org/10.11648/J.FM.20210701.11

[7] N. Ahmed, N.A. Shah, B. Ahmad, S.I. Shah, S. Ulhaq, M.R. Gorji, "Transient MHD Convective Flow of Fractional Nanofluid between Vertical Plates," Applied and Computational Mechanics, **5**(4), 592-602 (2019). https://doi.org/10.22055/JACM.2018.26947.1364

[8] U. Biswal, S. Chakraverty, and B.K. Ojha, "Natural convection of nanofluid flow between two vertical flat plates with imprecise parameter," Coupled systems mechanics, **9**(3), 219-235 (2020). https://doi.org/10.12989/CSM.2020.9.3.219

[9] M.K.A. Mohamed, H.R. Ong, M.Z. Salleh, and B. Widodo, "Mixed convection boundary layer flow of engine oil nanofluid on a vertical flat plate with viscous dissipation," Journal of Automotive Technology, **1**(1), 29–38 (2019). https://www.journal.dhuautomotive.edu.my/autojournal/article/view/7/6

[10] G. Sobamowo, and A.A. Yinusa, "Insight into the Boundary Layer Flows of Free Convection and Heat Transfer of Nanofluids over a Vertical Plate using Multi-Step Differential Transformation Method," Iranian Journal of Mechanical Engineering Transactions of the ISME, (2019).

[11] G. Sobamowo, "Free Convection Flow and Heat Transfer of Nanofluids of Different Shapes of Nano-Sized Particles over a Vertical Plate at Low and High Prandtl Numbers," Journal of Applied and Computational Mechanics, **5**(1), 13-39 (2019). https://doi.org/10.22055/JACM.2018.24529.1196

[12] G. Sobamowo, "Combined Effects of Thermal Radiation and Nanoparticles on Free Convection Flow and Heat Transfer of Casson Fluid over a Vertical Plate," International Journal of Chemical Engineering, (2018). https://doi.org/10.1155/2018/7305973

[13] A. Aziz, and W.A. Khan, "Natural convective boundary layer flow of a nanofluid past a convectively heated vertical plate," International Journal of Thermal Sciences, **52**, 83-90 (2012). https://doi.org/10.1016/j.ijthermalsci.2011.10.001

[14] Mojtabi, M.C. Charrier-Mojtabi, "Double-diffusive convection in porous media," in: *Handbook of Porous Media*, edited by K. Vafai, (Dekker, New York, 2000).

[15] E. Abu-Nada, Z. Masoud, H.F. Oztop, and A. Campo, "Effect of nanofluid variable properties on natural convection in enclosures," Int. J. Therm. Sci. **49**, 479-491 (2010). https://doi.org/10.1016/j.ijthermalsci.2009.09.002

[16] R.F. Probstein, *Physicochemical Hydrodynamics*, second ed., (Wiley Interscience, Hoboken, New Jersey, 2003)

[17] J. Tyndall, "On dust and disease," Proc. R. Inst. **6**, 1-14 (1870).

[18] R.B. Bird, W.E. Stewart, and E.N. Lightfoot, *Transport Phenomena*, second ed. (Wiley, New York, 1960).

[19] H.A. Pakravan, and M. Yaghoubi, "Combined thermophoresis, Brownian motion and Dufour effects on natural convection of nanofluids," Int. J. Therm. Sci. **50**, 394-402 (2011). https://doi.org/10.1016/j.ijthermalsci.2010.03.007

[20] O.D. Makinde, W.A. Khan, Z.H. Khan, "Buoyancy effects on MHD stagnation point flow and heat transfer of a nanofluid past a convectively heated stretching/shrinking sheet," International Journal of Heat and Mass Transfer, **62**, 526-533 (2013). http://dx.doi.org/10.1016%2Fj.ijheatmasstransfer.2013.03.049

[21] A.K. Pati, A. Misra, and S.K. Mishra, "Effect of electrification of nanoparticles on heat and mass transfer in boundary layer flow of a copper water nanofluid over a stretching cylinder with viscous dissipation," JP journal of heat and mass transfer, **17**(1), 97-117 (2019). http://dx.doi.org/10.17654/HM017010097

[22] A.K. Pati, A. Misra, S.K. Mishra, S. Mishra, R. Sahu, and S. Panda, "Computational modelling of heat and mass transfer optimization in copper water nanofluid flow with nanoparticle ionization," JP Journal of Heat and Mass Transfer, **31**, 1-18 (2023). https://doi.org/10.17654/0973576323001

[23] A.K. Pati, A. Misra, and S.K. Mishra, "Heat and mass transfer analysis on natural convective boundary layer flow of a Cu-water nanofluid past a vertical Flat plate with electrification of nanoparticles," Advances and Applications in Fluid Mechanics, **23**(1), 1-15 (2019). http://dx.doi.org/10.17654/FM023010001

[24] A.K. Pati, S. Mishra, A. Misra, and S.K. Mishra, "Heat and Mass Transport Aspects of Nanofluid Flow towards a Vertical Flat Surface influenced by Electrified Nanoparticles and Electric Reynolds Number," East European Journal of Physics, (2), 234-241 (2024). https://doi.org/10.26565/2312-4334-2024-2-22

[25] A.K. Pati, A. Misra, and S.K. Mishra, "Effect of electrification of nanoparticles on natural convective boundary layer flow and heat transfer of a Cu-Water nanofluid past a vertical flat plate," International Journal of Engineering, Science and Mathematics, **6**(8), 1254-1264 (2017). https://www.ijmra.us/project%20doc/2017/IJESM_DECEMBER2017_Special_Issue/4553_pdf.pdf

[26] A.K. Pati, A. Misra, and S.K. Mishra, "Modeling electrification of nanoparticles in free convective nanofluid flow," TEST Engineering and Management, (83), 17663-17669 (2020). http://testmagzine.biz/index.php/testmagzine/article/view/6854/5299

[27] S. Panda, A. Misra, S.K. Mishra, A.K. Pati, and K.K. Pradhan, "Flow and Heat Transfer Analysis of H2O-Al2O3 Nanofluid Over a Stretching Surface with Electrified Nanoparticles and Viscous Dissipation," Advances in Dynamical Systems and Applications, **16**(2), 1533-1545 (2021).

[28] R. Pattnaik, A. Misra, S.K. Mishra, K. Kumar, S.P. Pradhan, and A.K. Pati, "Thermal Performance Analysis of Nanofluid Past an Exponentially Stretching Surface Due to the Electrification Effect of Nanoparticles," International Journal of Difference Equations (IJDE), **16**(2), 189-203 (2021). https://www.ripublication.com/ijde21/v16n2p02.pdf

[29] S.L. Soo, "Effect of electrification on the dynamics of a particulate system," Industrial and Engineering Chemistry Fundamentals **3**, 75-80 (1964). https://doi.org/10.1021/i160009a013

[30] H.F. Oztop, and E. Abu-Nada, "Numerical study of natural convection in partially heated rectangular enclosures filled with nanofluids," International Journal of Heat Fluid Flow, **29**, 1326-1336 (2008). https://doi.org/10.1016/j.ijheatfluidflow.2008.04.009

[31] Adrian Bejan, *Convection Heat Transfer*, (John Wiley and Sons, 2013).

[32] J. Kierzenka, and L.F. Shampine, "A BVP Solver based on residual control and the MATLAB PSE," ACM Trans. Math. Softw. **27**(3), 299–316 (2001).

[33] M. Narahari, S. Akilu and A. Jaafar, *Free convection flow of a nanofluid past an isothermal inclined plate*, in: *Applied Mechanics and Materials*, vol. 390, (Trans Tech Publications Ltd. 2013).

ТЕПЛОВІ ХАРАКТЕРИСТИКИ ПОТОКУ НАНОРІДИНИ ВЗДОВЖ ІЗОТЕРМІЧНОЇ ВЕРТИКАЛЬНОЇ ПЛАСТИНИ З ГРАНИЧНИМИ УМОВАМИ ШВИДКОСТІ, ТЕПЛОВОГО ТА КОНЦЕНТРАЦІЙНОГО КОВЗАННЯ ЗА ВИКОРИСТАННЯ ПЕРЕГЛЯНУТОЇ НЕОДНОРІДНОЇ МОДЕЛІ БУОНДЖОРНО

Суджит Мішра, Адітя Кумар Паті, Ашок Місра, Сародж Кумар Мішра

Університет технології та менеджменту Центуріон, Паралахемунді, Одіша, Індія

У цій роботі досліджується природна конвекція постійного ламінарного потоку нанофлюїду повз ізотермічну вертикальну пластину з граничними умовами ковзання. Огляд існуючої літератури не виявив жодних попередніх досліджень, які б досліджували комбіновані ефекти термофорезу, броунівської дифузії та електризації частинок при розгляді граничних умов ковзання в потоці нанорідин. Переглянута неоднорідна модель із чотирьох рівнянь Буонджорно, що включає механізми термофорезу, броунівської дифузії та електризації частинок, використовується для усунення цієї прогалини. Модель використовує граничні умови швидкості, тепла та концентраційного ковзання для дослідження підвищення теплопровідності нанофлюїду. Отримані локальні аналогічні рівняння обробляються за допомогою пакета bvp4c MATLAB. У дослідженні обговорюється вплив ключових параметрів, таких як термофорез, броунівський рух і електризація, на температуру, швидкість і розподіл концентрації, а також на тепло-, масообмін і коефіцієнти тертя шкіри. Результати моделювання узгоджуються з попередніми дослідженнями, показуючи, що покращення параметра електризації підвищує коефіцієнт теплопередачі, тоді як параметри термофорезу та броунівського руху мають протилежний ефект. Крім того, значення коефіцієнта масопередачі збільшуються з вищими параметрами броунівського руху та електризації, одночасно зменшуючись із параметром термофорезу. Ця фізична модель має потенційне застосування в теплообмінниках з використанням нанофлюїдів і в охолодженні пластинчастих продуктів під час виробничих процесів. Новизна цього дослідження полягає в аналізі механізмів броунівської дифузії, термофорезу та електризації частинок у потоці нанофлюїдів за граничних умов ковзання.

Ключові слова: *теплопровідність; нанофлюїд; гранична умова швидкісного ковзання; граничний стан термічного ковзання; гранична умова концентраційного ковзання*

IMPACT OF ANISOTROPIC PERMEABILITY ON MICROPOLAR FLUID DYNAMICS AND HEAT TRANSFER IN POROUS CHANNELS

R. Vijaya Sree[a, b], **V. K. Narla**[b*]

ACE Engineering College, Ghatkesar Mandal, Medchal District, Telangana, 501301, India
GITAM Deemed to be University, Department of Mathematics, Hyderabad, 502329, India
*Corresponding Author e-mail: vnarla@gitam.edu

The current study explores the fluid dynamics and heat transfer characteristics of micropolar fluids within a channel filled with anisotropic porous media. The governing equations for the fluid flow, microrotation, and temperature profiles are numerically solved using Spectral Quasi-Linearization Method (SQLM). The research examines the influence of various key parameters such as the anisotropic permeability ratio, anisotropic angle, Darcy number, Reynolds number, Brinkman number, Prandtl number, and coupling number. Key findings indicate that the anisotropic permeability ratio and anisotropic angle significantly affect fluid flow and heat distribution, with increased anisotropy leading to enhanced microrotation and temperature, albeit with reduced velocity at the channel center. Higher Darcy numbers result in less restricted flow, increasing velocity and reducing microrotation effects, while increasing the coupling number contributes to a more uniform temperature profile. These results provide significant insights into the optimization of heat transfer and flow control in engineering applications that involve micropolar fluids in porous media.

Keywords: *Micropolar fluid; Anisotropic porous media; Anisotropic permeability; Microrotation; Heat transfer; Spectral Quasi-Linearization method*

PACS: 47.50.-d; 47.56.+r; 44.30.+v; 44.15.+a; 02.70.Hm

1. INTRODUCTION

The advent of the micropolar fluid theory occurred in recent decades due to the necessity to model a fluid with rotating micro-components. Micropolar fluids are fluids that display a correlation between the rotational dynamics of particles and the overall velocity structure at a large scale. Suspension of hard particles in a viscous medium forms these fluids. Liquid Crystals, magnetic fluids(ferrofluids), blood, and lubricants with additives are examples of micropolar fluids. Other industrial applications, including biological structures, lubricant fluids, and polymer solutions, utilise micropolar fluids. Micropolar fluids theory has been extensively investigated by researchers worldwide. Eringen [1] revolutionised the micropolar fluid framework and polymer solutions which make use of these fluids. He derived the micropolar fluid flow governing equations and boundary conditions and implemented them in analysis of channel flow, taking into account the thermodynamic limitations. Researchers have investigated the kinetics of both natural and combined convection flows of micropolar fluids on flat and cylindrical surfaces [2]–[5]. Mirzaaghaian et al. [6] analysed the flow characteristics of a micropolar fluid and the dynamics of heat transfer in a porous conduit. To solve nonlinear equations the Differential Transformation Method (DTM) [7]–[11] was utilised. In this study, the influencing factors were the Peclet number, Reynolds number, and the micro-rotation/angular velocity. The findings showed that while the temperature and concentration fields will only slightly alter, the stream function will be greatly altered by varying the Reynolds number. An analysis was conducted by Mabood et al. [12] to investigate the flow and heat transfer properties of a micropolar fluid across a stretchable sheet in a porous media. The flow was exposed to a magnetic field, thermodiffusion, and variable heat sources in their work and solutions were obtained for the resultant equations. A comparison of outcomes with earlier research revealed very good agreement. The research revealed that the distribution of velocity decreased as the parameter for the magnetic field increased, despite the fact that the thermal and concentration distribution were elevated.

Extensive research conducted globally on the use of micropolar and nanofluid fluids has shown promising results for various industrial processes and scientific research oriented applications, including heat exchangers, combined propulsion systems, and medical procedures. Many researchers [13]–[18] have conducted an in-depth review of the fundamental principles governing micropolar fluid flow in porous conduits. The behaviour of micropolar fluid in a conduit confined by two parallel permeable walls was analysed by Jalili et al. [19]. The fluid flow was considered two-dimensional, and steady. It was observed that with the exception of the dimensionless microrotation profile, all of the mentioned dimensionless parameters have increasing average values when the values of coupling number increase. Moreover, temperature distribution is the most significant parameter that can be affected by Peclet number for heat diffusion. The solution for this problem shows that the averages of the dimensionless parameters reduce if the ratio of micropolar-inertia density is increased along channel, with the exception of the non-dimensional flow function characteristics. Under the presumptions of heat radiation and reaction rate coefficients, Shamsuddin et al. [20] analysed the dynamics of a micropolar

fluid flow through a conduit considering both combined and non-linear heat transfer. It was shown how the temperature, concentration, and dimensionless velocity of micropolar fluid reached their peak values near the channel's centre. The dynamics of mass and heat tranfer in micropolar fluids are determined by their thermal and solution properties.

Abdalbagi [21] examined the dynamics of a micropolar fluid flow and characteristics of heat transfer in a porous conduit, applying the method of iterative linearization. This study showed that fluid flow, mass transport, microrotation and heat transfer are all positively impacted by increasing coupling and spin-gradient viscosity parameters. Conversely, these profiles exhibit a decline as micro-inertia density increases. While an increased Peclet number indicates optimised heat transfer by convection and mass transfer, higher Reynolds numbers reduce the distributions of velocity, microrotation, and temperature. Micropolar fluid framework, which is applicable to non-Newtonian fluids, accounts for microrotation and also couple stresses. The research explores how the magnetic force field slows down the flow of fluid, while channel permeability increases velocity. Heat radiation enhances the temperature distribution, impacting heat transfer. The findings have practical significance in the domains of engineering like temperature control systems, and MHD generators, where these conditions are frequently encountered. A study by Shah et al. [22] provided a description of the fluid flow dynamics and heat transfer of blood-infused gold micropolar nanofluids in a porous conduit. The channel contained thermal radiation whether the walls were in motion or rest. Blood was considered as the base fluid, and microgold was thought to be the polar nanofluid. The study conducted by Ahmad et al. [23] investigated the problem of mass and heat transfer in a micropolar fluid flow within a porous conduit using a Quasi-linearization approach. At fluid temperatures above a certain threshold, the concurrent phenomena of heat radiation buildup, absorption heat, heat exchange, and Brownian flow were observed. When it comes to magnetic parameters and materials, supportive engineering forces like velocity, skin friction, and heat exchange have proven to be beneficial. However, the transfer rate of mass showed an opposite response. Akbarzadeh et al. [24] analysed the flow of a nanofluid which was considered laminar and forced convective heat transport within a wavy channel. In their study, it was demonstrated that if the aspect ratio of the conduit is increased, the average Nusselt number becomes more sensitive to the Reynolds number and also to the aspect ratio of the channel. The gradient of the temperature on the left sheet will decrease as the motion parameter increases. However, the gradient exhibits a positive correlation with Lorentz forces. The effects of thermal radiation and also thermo-diffusion on Williamson model nanofluid along a porous and stretchable surface were examined by Rashidi, and Bhatti [25]. Their findings showed that the fluid's magnitude increases with large porosity and Williamson fluid parameters. On the other hand, the gradient on the left sheet increases as Lorentz forces do. In a transverse magnetic force field presence, Rashidi et al. [26] examined the exchange of heat for a nanofluid flow along a stretchable sheet while considering buoyancy effects, and heat radiation into account. It has been noticed that nanofluid's velocity rises when the buoyancy factor is increased while the distribution of temperature decreases. Assuming the fluid is incompressible and steady, Takhar et al. [27] analysed the problem of axisymmetric flow of micropolar fluid and heat transfer between two permeable discs. A finite analysis method was employed to solve the flow governing equations, which describes the velocity, temperature and also microrotation. Quantitative simulations have been conducted to determine the axial, radial, microrotation velocities, temperature, couple stress coefficient, skin friction, and heat transfer rate on the discs, for varying values of injection Reynolds number and micropolar parameter.

The empirical study conducted by Pathak et al. [28] examined the flow and heat transfer properties of micropolar fluids along a stretchable sheet in a Darcy porous media. The flow governing system of equations, which are nonlinear, were solved by the authors using a quasi-uniform mesh in conjunction with a nonstandard finite difference approach. Validation of the results was achieved by a comparison with those computed using the RK method of order four. The results indicate that the boundary layer thickness was reduced with an increase in the values of the Reynolds number, micropolar parameter, and injection/suction parameter. Additionally, a rise in the Prandtl number, heat index parameter, and the micropolar and injection/suction parameters enhances microrotation, indicating a more pronounced effect of the micropolar characteristics on the dynamics of fluid flow and heat transfer. In their study, Cutis [29] examined the phenomenon of a creeping flow in an incompressible, micropolar fluid bounded over a permeable shell. Empirical evidence demonstrated that when hydraulic resistivity is low and the sphere is completely porous, efficient circulation occurs between the porous area and the surrounding fluid. This finding can be utilised for efficient drug delivery by using a fully porous sphere with outstanding permeability as the carrier for the drug.

Recent progress has centered on creating effective numerical techniques to address the complex, nonlinear differential equations that control fluid flow dynamics. The Spectral Quasi-Linearization Method (SQLM) is one such technique, combining quasilinearization with spectral methods to achieve high accuracy in linearizing and solving nonlinear terms. This method is effectively used for investigating boundary layer flows over stretching/shrinking sheets in non-Darcy porous media and other fluid flow applications. Srinivasacharya et al. [30] have examined the process of production of entropy and heat exchange in a micro-polar fluid flow inside an annular region subjected to a magnetic field. The two geometry walls in this study, one acting as suction and the other as injection, have the same velocity. The solution was obtained using a spectral Chebyshev collocation method. These findings demonstrate that the interior cylinder exhibited the greatest entropy production, whereas the exterior cylinder displayed the lowest entropy production. Alharbey et al. [31] employed Structural Equation Modelling (SQLM) to investigate the dynamics of a micropolar fluid along a horizontal plate within a non-Darcy porous media. Similarity variables in SQLM convert flow-governing equations into ODE, resulting in numerical solutions with rapid convergence. Entropy production decreases with Reynolds and Brinkman numbers, while velocity profiles increase with material parameters, demonstrating the method's resilience and effectiveness in complex fluid dynamics applications.

Majority of the studies reported in the literature focused on the study of micropolar fluid flow with regard to stretching sheets or within porous conduits. This work presents a mathematical model for the analysis of flow and heat transfer phenomena in a micropolar fluid in between a channel with parallel and permeable walls, saturated with anisotropic porous media. The momentum and energy equations, together with the boundary conditions, are initially transformed into a non-dimensional form by similarity transformation. Subsequently, a numerical solution is obtained using the Spectral Quasi-Linearization Method (SQLM). A systematic investigation is conducted to examine the influence of several key parameters, including the anisotropic permeability ratio, anisotropic angle, Darcy number, Reynolds number, Brinkmann number, Prandtl number, and coupling number on the velocity, microrotation, and temperature distributions within the boundary layer.

2. MATHEMATICAL FORMULATION OF THE PROBLEM

Consider a 2-D channel filled with anisotropic porous media, where the flow of a steady, laminar, incompressible micropolar fluid is observed. This work assumes that the channel walls are permeable, enabling the steady flow of fluid into or out of the channel at a constant velocity of v_0. The X-axis is aligned parallel to the surface of the channel walls, while the Y-axis exhibits a perpendicular orientation to them. Moreover, the channel walls are situated at $y = \pm h$ and the temperatures near the boundaries are represented as T_1 and T_2, respectively (see Figure 1). As the porous media is considered anisotropic the permeability matrix which is a second-order tensor $\mathbb{K}$, is given by [32]

$$\mathbb{K} = \begin{bmatrix} k_2 \cos^2 \phi + k_1 \sin^2 \phi & (k_2 - k_1) \sin \phi \cos \phi \\ (k_2 - k_1) \sin \phi \cos \phi & k_2 \sin^2 \phi + k_1 \cos^2 \phi \end{bmatrix}. \tag{1}$$

k_1 and k_2 are the vertical and horizontal permeabilities which are assumed constant. ϕ is the anisotropic angle formed by the intersection of the main axis and the horizontal permeability k_2. The governing equations for micropolar fluid with
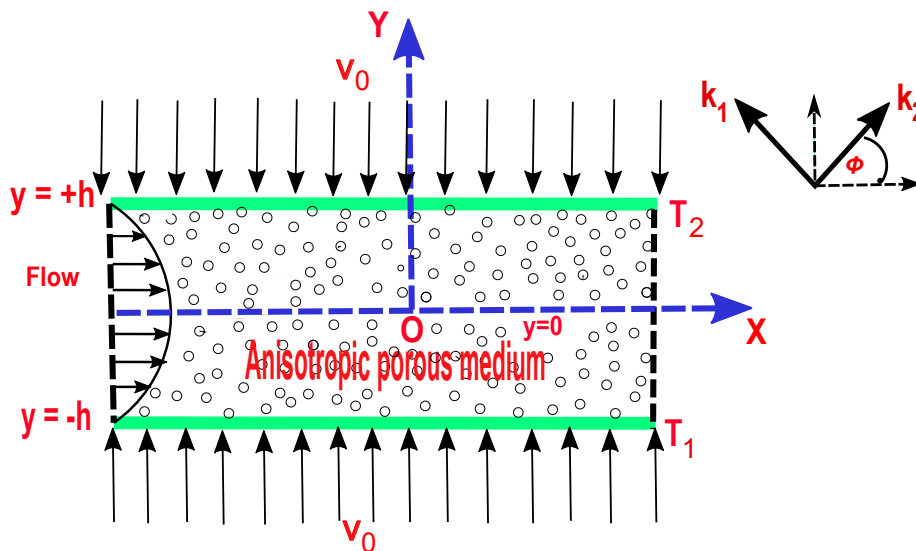

Figure 1. A physical interpretation of micropolar fluid flow problem.

anisotropic porous permeability are stated below, taking into account the aforementioned factors:

$$\frac{\partial u}{\partial x} + \frac{\partial v}{\partial y} = 0, \tag{2}$$

$$\rho \left[u \frac{\partial u}{\partial x} + v \frac{\partial u}{\partial y} \right] = -\frac{\partial p}{\partial x} + (\mu + \kappa) \left[\frac{\partial^2 u}{\partial x^2} + \frac{\partial^2 u}{\partial y^2} \right] + \kappa \frac{\partial W}{\partial y}$$
$$- \frac{\mu + \kappa}{k_1 k_2} \left[(k_1 \cos^2(\phi) + k_2 \sin^2(\phi))u + (\frac{1}{2}(k_1 - k_2) \sin(2\phi))v \right], \tag{3}$$

$$\rho \left[u \frac{\partial v}{\partial x} + v \frac{\partial v}{\partial y} \right] = -\frac{\partial p}{\partial y} + (\mu + \kappa) \left[\frac{\partial^2 v}{\partial x^2} + \frac{\partial^2 v}{\partial y^2} \right] - \kappa \frac{\partial W}{\partial x}$$
$$- \frac{\mu + \kappa}{k_1 k_2} \left[(\frac{1}{2}(k_1 - k_2) \sin 2(\phi))u + (k_1 \sin^2(\phi) + k_2 \cos^2(\phi))v \right], \tag{4}$$

$$\rho j \left[u \frac{\partial W}{\partial x} + v \frac{\partial W}{\partial y} \right] = -\kappa \left[2W + \frac{\partial u}{\partial y} - \frac{\partial v}{\partial x} \right] + \gamma \left[\frac{\partial^2 W}{\partial x^2} + \frac{\partial^2 W}{\partial y^2} \right], \tag{5}$$

$$(\rho c_p) \left[u \frac{\partial T}{\partial x} + v \frac{\partial T}{\partial y} \right] = K_f \left[\frac{\partial^2 T}{\partial x^2} + \frac{\partial^2 T}{\partial y^2} \right] + \frac{\kappa}{2} \left[\frac{\partial v}{\partial x} - \frac{\partial u}{\partial y} - 2W \right]^2 + \gamma \left[\left(\frac{\partial W}{\partial x} \right)^2 + \left(\frac{\partial W}{\partial y} \right)^2 \right]$$
$$+ (2\mu + \kappa) \left[(\frac{\partial u}{\partial x})^2 + (\frac{\partial v}{\partial y})^2 + \frac{1}{2}(\frac{\partial u}{\partial y} + \frac{\partial v}{\partial x})^2 \right] \tag{6}$$
$$+ \frac{\mu + \kappa}{k_1 k_2} \left[(k_1 \cos^2(\phi) + k_2 \sin^2(\phi))u^2 + (k_1 - k_2) \sin 2(\phi)uv + (k_2 \cos^2(\phi) + k_1 \sin^2(\phi))v^2 \right].$$

Mathematical formulations for boundary conditions of a micropolar fluid flow problem are as below:

$$u = 0, \ v = -v_0, \ W = 0, \ T = T_1, \ \text{at} \ y = -h,$$
$$u = 0, \ v = v_0, \ W = 0, \ T = T_2, \ \text{at} \ y = +h. \tag{7}$$

The variables u and v in the equations above represent the dimensional components of fluid velocity in X and Y coordinate directions. Furthermore, the variables considered are: p denotes pressure, T denotes temperature, W denotes microrotation velocity, κ denotes vortex viscosity, γ denotes spin-gradient viscosity, j denotes micro-inertia density, ρ denotes the effective density of the micropolar fluid, μ denotes effective dynamic viscosity of micropolar fluid, c_p denotes specific heat of micropolar fluid, and K_f denotes the thermal conductivity of micropolar fluid.
Following dimensionless parameters are introduced:

$$\xi = \frac{x}{h}, \ \eta = \frac{y}{h}, \ u = -\frac{v_0 x}{h} f'(\eta), \ W = \frac{v_0 x}{h^2} g(\eta), \ v = v_0 f(\eta), \ \theta = \frac{(T - T_1)}{(T_2 - T_1)} = \theta_1(\eta) + \xi^2 \theta_2(\eta). \tag{8}$$

In these equations, v_0 is the cross-flow transpiration velocity, which remains constant. $v_0 < 0$ stands for suction and $v_0 > 0$ for injection. After substituting the above into the flow governing equations (3)- (6) and after the pressure gradient is removed, and upon equating the coefficients of ξ^0, ξ, and ξ^2 we get:

$$\left(\frac{1}{1-N} \right) f^{iv} - \frac{N}{1-N} g'' + Re[f'f'' - ff'''] - \frac{1}{(1-N)Da} [K \cos^2 \phi + \sin^2 \phi] f'' = 0, \tag{9}$$

$$\left(\frac{2-N}{m^2} \right) g'' - 2g + Re \ a_j \left(\frac{1-N}{N} \right) (f'g - fg') + f'' = 0, \tag{10}$$

$$\theta_1'' + 2\theta_2 - Pr \ Re[f\theta_1'] + \frac{N(2-N)}{1-N} \frac{Br}{m^2} g^2 + \frac{Br}{Da} [\cos^2 \phi + K \sin^2 \phi] f^2$$
$$+ 2 \left(\frac{2-N}{1-N} \right) Br f'^2 = 0, \tag{11}$$

$$\theta_2'' + \frac{Br}{2} \left(\frac{N}{1-N} \right) [f''^2 + 4g^2 - 4f''g] + \frac{Br}{m^2} g'^2 \left(\frac{N(2-N)}{1-N} \right) + 2Pr \ Re \ \theta_2 f' - Pr \ Re f \theta_2'$$
$$+ \frac{Br}{2} \left(\frac{2-N}{1-N} \right) f''^2 + \frac{Br}{(1-N)Da} [K \cos^2 \phi + \sin^2 \phi] f'^2 = 0. \tag{12}$$

The boundary conditions are:

$$f(\eta) = -1, \ f'(\eta) = 0, \ g(\eta) = 0, \ \theta_1(\eta) = 0, \ \theta_2(\eta) = 0 \ \text{at} \ \eta = -1,$$
$$f(\eta) = 1, \ f'(\eta) = 0, \ g(\eta) = 0, \ \theta_1(\eta) = 1, \ \theta_2(\eta) = 0, \ \text{at} \ \eta = 1. \tag{13}$$

Here Br represents Brinkman number, Pr represents Prandtl number, Re represents Reynolds number, Da represents Darcy number, N represents coupling number, a_j represents micro-inertia parameter, m^2 represents micropolar parameter, K represents anisotropic permeability ratio. These parameters are defined as below:

$$Br = \frac{\mu v_0^2}{K_f(T_2 - T_1)}, \ Pr = \frac{\mu c_p}{K_f}, \ Re = \frac{\rho v_0 h}{\mu}, \ Da = \frac{k_1}{h^2},$$
$$N = \frac{\kappa}{(\kappa + \mu)}, \ a_j = \frac{j}{h^2}, \ m^2 = \frac{(\kappa + 2\mu)h^2 \kappa}{(\kappa + \mu)\gamma}, \ K = \frac{k_1}{k_2}. \tag{14}$$

3. METHOD OF SOLUTION

A numerical solution was obtained for the non-linear equations (9) - (12) by applying the Spectral Quasi-Linearization approach, while considering the boundary conditions in equation (13). This iterative approach combines a spectral framework with a Quasi-linearization method for solving nonlinear differential equations. Bellman and Kalaba [33] developed the Quasilinearization Method (QLM) as an extension of the Newton-Raphson method, specifically designed to address nonlinear boundary value problems. On applying the above procedure, the linear equations are obtained as:

$$e_{1,r} f_{r+1}^{iv} + e_{2,r} f_{r+1}''' + e_{3,r} f_{r+1}'' + e_{4,r} f_{r+1}' + e_{5,r} f_{r+1} + e_{6,r} g_{r+1}'' = S_1, \tag{15}$$

$$f_{r+1}'' + e_{7,r} f_{r+1}' + e_{8,r} f_{r+1} + e_{9,r} g_{r+1}'' + e_{10,r} g_{r+1}' + e_{11,r} g_{r+1} = S_2, \tag{16}$$

$$e_{12,r} f_{r+1}' + e_{13,r} f_{r+1} + e_{14,r} g_{r+1} + (\theta_1)_{r+1}'' + e_{15,r} (\theta_1)_{r+1}' + e_{16,r} (\theta_2)_{r+1} = S_3, \tag{17}$$

$$e_{17,r} f_{r+1}'' + e_{18,r} f_{r+1}' + e_{19,r} f_{r+1} + e_{20,r} g_{r+1}' + e_{21,r} g_{r+1} + (\theta_2)_{r+1}'' + e_{22,r} (\theta_2)_{r+1}' + e_{23,r} (\theta_2)_{r+1} = S_4. \tag{18}$$

The obtained boundary conditions are :

$$\begin{aligned} f_{r+1} = -1, \ f_{r+1}' = 0, \ g_{r+1} = 0, \ (\theta_1)_{r+1} = 0, \ (\theta_2)_{r+1} = 0 \ \text{at} \ \eta = -1, \\ f_{r+1} = 1, \ f_{r+1}' = 0, \ g_{r+1} = 0, (\theta_1)_{r+1} = 1, \ (\theta_2)_{r+1} = 0, \ \text{at} \ \eta = 1. \end{aligned} \tag{19}$$

The coefficients obtained are as follows:

$$e_{1,r} = \frac{1}{1-N}, \quad e_{2,r} = -Re f_r, \quad e_{3,r} = -\frac{1}{(1-N)Da}[K\cos^2\phi + \sin^2\phi] + Re f'_r, \quad e_{4,r} = Re f''_r,$$

$$e_{5,r} = -Re f'''_r, \quad e_{6,r} = -\frac{N}{1-N}, \quad e_{7,r} = Re \, a_j(\frac{1-N}{N})g_r, \quad e_{8,r} = -Re \, a_j(\frac{1-N}{N})g'_r, \quad e_{9,r} = \frac{2-N}{m^2},$$

$$e_{10,r} = -Re \, a_j(\frac{1-N}{N})f_r, \quad e_{11,r} = Re \, a_j(\frac{1-N}{N})f'_r - 2, \quad e_{12,r} = 4(\frac{2-N}{1-N})Br \, f'_r,$$

$$e_{13,r} = -Pr \, Re(\theta_1')_r + 2\frac{Br}{(1-N)Da}[\cos^2\phi + K\sin^2\phi] \, f_r, \quad e_{14,r} = \frac{2N(2-N)}{1-N}\frac{Br}{m^2} g_r, \quad e_{15,r} = -PrRe f_r,$$

$$e_{16,r} = 2, \quad e_{17,r} = \frac{N}{1-N}Br(f'')_r - \frac{2N}{1-N}Br \, g_r + \frac{2-N}{1-N}Br(f'_r),$$

$$e_{18,r} = 2Pr \, Re(\theta_2)_r + \frac{2Br}{(1-N)Da}[K\cos^2\phi + \sin^2\phi]f'_r, \quad e_{19,r} = -PrRe(\theta_2')_r, \quad e_{20,r} = \frac{2N(2-N)}{1-N}\frac{Br}{m^2}g'_r,$$

$$e_{21,r} = \frac{4N}{1-N}Br \, g_r - \frac{2N}{1-N}Br(f'')_r, \quad e_{22,r} = -Pr \, Re f_r, \quad e_{23,r} = 2Pr \, Re f'_r,$$

$$S_1 = Re[f'_r f''_r - f_r f'''_r], \quad S_2 = Re \, a_j(\frac{1-N}{N})[f'_r g_r - f_r g'_r],$$

$$S_3 = -Pr \, Re(f)_r(\theta_1')_r + \frac{N(2-N)}{1-N}\frac{Br}{m^2}(g)_r^2 + \frac{Br}{(1-N)Da}[\cos^2\phi + K\sin^2\phi](f)_r^2 + \frac{2(2-N)}{1-N}Br(f')_r^2,$$

$$S_4 = \frac{1}{2}(\frac{N}{1-N})Br[(f'')_r^2 + 4(g)_r^2 - 4(f'')_r g_r] + \frac{N(2-N)}{1-N}\frac{Br}{m^2}(g')_r^2 + 2PrRe(f')_r - PrRe(f)_r(\theta_2')_r$$

$$+ \frac{1}{2}(\frac{2-N}{1-N})Br(f''^2)_r + \frac{Br}{(1-N)Da}[K\cos^2\phi + \sin^2\phi](f')_r^2.$$

To solve the linearised equations (15)-(18), a Chebyshev spectral collocation approach [34, 35] is used. Chebyshev interpolating polynomials are used to estimate the unknown functions. These polynomials are collocated at the Gauss-Lobatto points, which are defined as $\zeta_j = \cos(\pi j/M)$, where $j = 1, 2, \cdots M$ of collocation points. The derivatives of $f(\eta)$, $g(\eta)$, $\theta_1(\eta)$, and $\theta_2(\eta)$ are determined by using the differential matrix $\mathbf{D}$ to calculate Chebyshev polynomials from the collocation nodes. At the collocation nodes, the derivatives of f_{r+1}, g_{r+1}, $(\theta_1)_{r+1}$, and $(\theta_2)_{r+1}$ are represented as:

$$\frac{\partial^P f_{r+1}}{\partial \eta^P} = \left(\frac{2}{L}\right)^P \sum_{i=0}^M D_{M,i}^p f_{r+1}(\eta_i) = \mathbf{D}^P F,$$

$$\frac{\partial^P g_{r+1}}{\partial \eta^P} = \left(\frac{2}{L}\right)^P \sum_{i=0}^M D_{M,i}^p g_{r+1}(\eta_i) = \mathbf{D}^P G,$$

$$\frac{\partial^P (\theta_1)_{r+1}}{\partial \eta^P} = \left(\frac{2}{L}\right)^P \sum_{i=0}^M D_{M,i}^p (\theta_1)_{r+1}(\eta_i) = \mathbf{D}^P \Theta_1, \tag{20}$$

$$\frac{\partial^P (\theta_2)_{r+1}}{\partial \eta^P} = \left(\frac{2}{L}\right)^P \sum_{i=0}^M D_{M,i}^p (\theta_2)_{r+1}(\eta_i) = \mathbf{D}^P \Theta_2.$$

Where $\mathbf{D}$ is Chebyshev differentiation matrix which is scaled by $L/2$ and is of order $(M+1) \times (M+1)$ with derivative of order p. On substituting the equation (20) into equations (15) - (18), we obtain

$$[e_{1,r}\mathbf{D}^4 + e_{2,r}\mathbf{D}^3 + e_{3,r}\mathbf{D}^2 + e_{4,r}\mathbf{D} + e_{5,r}I]f_{r+1} + e_{6,r}\mathbf{D}^2 g_{r+1} = S_1, \tag{21}$$

$$[\mathbf{D}^2 + e_{7,r}\mathbf{D} + e_{8,r}I]f_{r+1} + [e_{9,r}\mathbf{D}^2 + e_{10,r}\mathbf{D} + e_{11,r}I]g_{r+1} = S_2, \tag{22}$$

$$[e_{12,r}\mathbf{D} + e_{13,r}I]f_{r+1} + [e_{14,r}I]g_{r+1} + [\mathbf{D}^2 + e_{15,r}\mathbf{D}](\theta_1)_{r+1} + [e_{16,r}I](\theta_2)_{r+1} = S_3, \tag{23}$$

$$[e_{17,r}\mathbf{D}^2 + e_{18,r}\mathbf{D} + e_{19,r}I]f_{r+1} + [e_{20,r}\mathbf{D} + e_{21,r}I]g_{r+1} + [\mathbf{D}^2 + e_{22,r}\mathbf{D} + e_{23,r}I](\theta_2)_{r+1} = S_4. \tag{24}$$

On applying the spectral method to boundary conditions we get:

$$f_{r+1}(\zeta_0) = 1, \quad \sum_{k=0}^{M} \mathbf{D}_{M,k}f_{r+1}(\zeta_0) = 0,$$

$$f_{r+1}(\zeta_M) = -1, \quad \sum_{k=0}^{M} \mathbf{D}_{M,k}f_{r+1}(\zeta_M) = 0,$$

$$g_{r+1}(\xi_0) = 0, \; g_{r+1}(\zeta_M) = 0, \tag{25}$$

$$(\theta_1)_{r+1}(\zeta_0) = 1, \quad (\theta_1)_{r+1}(\zeta_M) = 0,$$

$$(\theta_2)_{r+1}(\zeta_0) = 0, \, (\theta_2)_{r+1}(\zeta_M) = 0.$$

The matrix form of the aforementioned equation system is written as

$$\begin{bmatrix} \mathbf{A}_{11} & \mathbf{A}_{12} & \mathbf{A}_{13} & \mathbf{A}_{14} \\ \mathbf{A}_{21} & \mathbf{A}_{22} & \mathbf{A}_{23} & \mathbf{A}_{24} \\ \mathbf{A}_{31} & \mathbf{A}_{32} & \mathbf{A}_{33} & \mathbf{A}_{34} \\ \mathbf{A}_{41} & \mathbf{A}_{42} & \mathbf{A}_{43} & \mathbf{A}_{44} \end{bmatrix} \times \begin{bmatrix} F_{r+1} \\ G_{r+1} \\ \Theta_{1r+1} \\ \Theta_{2r+1} \end{bmatrix} = \begin{bmatrix} S_1 \\ S_2 \\ S_3 \\ S_4 \end{bmatrix}, \tag{26}$$

Boundary conditions are placed on separate matrices as follows:

$$\mathbf{A}_{11} = \begin{bmatrix} 1 & 0 & \cdots & 0 & 0 \\ \mathbf{D}_{1,0} & \mathbf{D}_{1,1} & \cdots & \mathbf{D}_{1,M-1} & \mathbf{D}_{1,M} \\ & & A_{11} & & \\ \mathbf{D}_{M-1,0} & \mathbf{D}_{M-1,1} & \cdots & \mathbf{D}_{M-1,M-1} & \mathbf{D}_{M-1,M} \\ 0 & 0 & \cdots & 0 & 1 \end{bmatrix}, \quad \mathbf{A}_{12} = \begin{bmatrix} 0 & 0 & \cdots & 0 & 0 \\ 0 & 0 & \cdots & 0 & 0 \\ & & A_{12} & & \\ 0 & 0 & \cdots & 0 & 0 \\ 0 & 0 & \cdots & 0 & 0 \end{bmatrix},$$

$$\mathbf{A}_{13} = \begin{bmatrix} 0 & 0 & \cdots & 0 & 0 \\ 0 & 0 & \cdots & 0 & 0 \\ & & A_{13} & & \\ 0 & 0 & \cdots & 0 & 0 \\ 0 & 0 & \cdots & 0 & 0 \end{bmatrix}, \quad \mathbf{A}_{14} = \begin{bmatrix} 0 & 0 & \cdots & 0 & 0 \\ 0 & 0 & \cdots & 0 & 0 \\ & & A_{14} & & \\ 0 & 0 & \cdots & 0 & 0 \\ 0 & 0 & \cdots & 0 & 0 \end{bmatrix}, \quad \mathbf{A}_{21} = \begin{bmatrix} 0 & 0 & \cdots & 0 & 0 \\ & & A_{21} & & \\ 0 & 0 & \cdots & 0 & 0 \end{bmatrix},$$

$$\mathbf{A}_{22} = \begin{bmatrix} 1 & 0 & \cdots & 0 & 0 \\ & & A_{22} & & \\ 0 & 0 & \cdots & 0 & 1 \end{bmatrix}, \quad \mathbf{A}_{23} = \begin{bmatrix} 0 & 0 & \cdots & 0 & 0 \\ & & A_{23} & & \\ 0 & 0 & \cdots & 0 & 0 \end{bmatrix}, \quad \mathbf{A}_{24} = \begin{bmatrix} 0 & 0 & \cdots & 0 & 0 \\ & & A_{24} & & \\ 0 & 0 & \cdots & 0 & 0 \end{bmatrix},$$

$$\mathbf{A}_{31} = \begin{bmatrix} 0 & 0 & \cdots & 0 & 0 \\ & & A_{31} & & \\ 0 & 0 & \cdots & 0 & 0 \end{bmatrix}, \quad \mathbf{A}_{32} = \begin{bmatrix} 0 & 0 & \cdots & 0 & 0 \\ & & A_{32} & & \\ 0 & 0 & \cdots & 0 & 0 \end{bmatrix}, \quad \mathbf{A}_{33} = \begin{bmatrix} 1 & 0 & \cdots & 0 & 0 \\ & & A_{33} & & \\ 0 & 0 & \cdots & 0 & 1 \end{bmatrix},$$

$$\mathbf{A}_{34} = \begin{bmatrix} 0 & 0 & \cdots & 0 & 0 \\ & & A_{34} & & \\ 0 & 0 & \cdots & 0 & 0 \end{bmatrix}, \quad \mathbf{A}_{41} = \begin{bmatrix} 0 & 0 & \cdots & 0 & 0 \\ & & A_{41} & & \\ 0 & 0 & \cdots & 0 & 0 \end{bmatrix}, \quad \mathbf{A}_{42} = \begin{bmatrix} 0 & 0 & \cdots & 0 & 0 \\ & & A_{42} & & \\ 0 & 0 & \cdots & 0 & 0 \end{bmatrix},$$

$$\mathbf{A}_{43} = \begin{bmatrix} 0 & 0 & \cdots & 0 & 0 \\ \hline & & A_{43} & & \\ \hline 0 & 0 & \cdots & 0 & 0 \end{bmatrix}, \quad \mathbf{A}_{44} = \begin{bmatrix} 1 & 0 & \cdots & 0 & 0 \\ \hline & & A_{44} & & \\ \hline 0 & 0 & \cdots & 0 & 1 \end{bmatrix}, \quad \mathbf{F}_{r+1} = \begin{bmatrix} f_{r+1,0} \\ f_{r+1,1} \\ \vdots \\ f_{r+1,M-1} \\ f_{r+1,M} \end{bmatrix},$$

$$\mathbf{G}_{r+1} = \begin{bmatrix} g_{r+1,0} \\ \vdots \\ g_{r+1,M} \end{bmatrix}, \quad \mathbf{\Theta_1}_{r+1} = \begin{bmatrix} \theta_{1r+1,0} \\ \vdots \\ \theta_{1r+1,M} \end{bmatrix}, \quad \mathbf{\Theta_2}_{r+1} = \begin{bmatrix} \theta_{2r+1,0} \\ \vdots \\ \theta_{2r+1,M} \end{bmatrix}, \quad S_1 = \begin{bmatrix} 1 \\ 0 \\ \mathbf{s_1} \\ 0 \\ -1 \end{bmatrix},$$

$$S_2 = \begin{bmatrix} 0 \\ \mathbf{s_2} \\ 0 \end{bmatrix}, \quad S_3 = \begin{bmatrix} 1 \\ \mathbf{s_3} \\ 0 \end{bmatrix}, \quad S_4 = \begin{bmatrix} 0 \\ \mathbf{s_4} \\ 0 \end{bmatrix}.$$

where

$A_{11} = [\text{diag}(\mathbf{e}_{1,r}) \quad \text{diag}(\mathbf{e}_{2,r}) \quad \text{diag}(\mathbf{e}_{3,r}) \quad \text{diag}(\mathbf{e}_{4,r}) \quad \text{diag}(\mathbf{e}_{5,r})][\mathbf{D}^4 \quad \mathbf{D}^3 \quad \mathbf{D}^2 \quad \mathbf{D} \quad I]^T,$

$A_{12} = [\text{diag}(\mathbf{e}_{6,r})][\mathbf{D}^2]^T, \quad A_{13} = 0, \quad A_{14} = 0,$

$A_{21} = [1 \quad \text{diag}(\mathbf{e}_{7,r}) \quad \text{diag}(\mathbf{e}_{8,r})][D^2 \quad \mathbf{D} \quad I]^T,$

$A_{22} = [\text{diag}(\mathbf{e}_{9,r}) \quad \text{diag}(\mathbf{e}_{10,r}) \quad \text{diag}(\mathbf{e}_{11,r})][\mathbf{D}^2 \quad \mathbf{D} \quad I]^T, \quad A_{23} = 0,$

$A_{24} = 0, \quad A_{31} = [\text{diag}(\mathbf{e}_{12,r}) \quad \text{diag}(\mathbf{e}_{13,r})][D \quad I]^T, \quad A_{32} = [\text{diag}(\mathbf{e}_{13,r})][I]^T,$

$A_{33} = [\text{diag}(\mathbf{e}_{14,r}) \quad \text{diag}(\mathbf{e}_{15,r})][\mathbf{D}^2 \quad D]^T, \quad A_{34} = [\text{diag}(\mathbf{e}_{16,r})][I]^T,$

$A_{41} = [\text{diag}(\mathbf{e}_{17,r}) \quad \text{diag}(\mathbf{e}_{18,r}) \quad \text{diag}(\mathbf{e}_{19,r})][\mathbf{D}^2 \quad \mathbf{D} \quad I]^T,$

$A_{42} = [\text{diag}(\mathbf{e}_{20,r}) \quad \text{diag}(\mathbf{e}_{21,r})][\mathbf{D} \quad I]^T, \quad A_{43} = 0,$

$A_{44} = [1 \quad \text{diag}(\mathbf{e}_{22,r}), \quad \text{diag}(\mathbf{e}_{23,r})][D^2 \quad D \quad I].$

Here, $\mathbf{e}$, $\mathbf{I}$, and $\mathbf{0}$ represent the diagonal, unit, and null matrices, respectively which are of order $(M+1) \times (M+1)$.
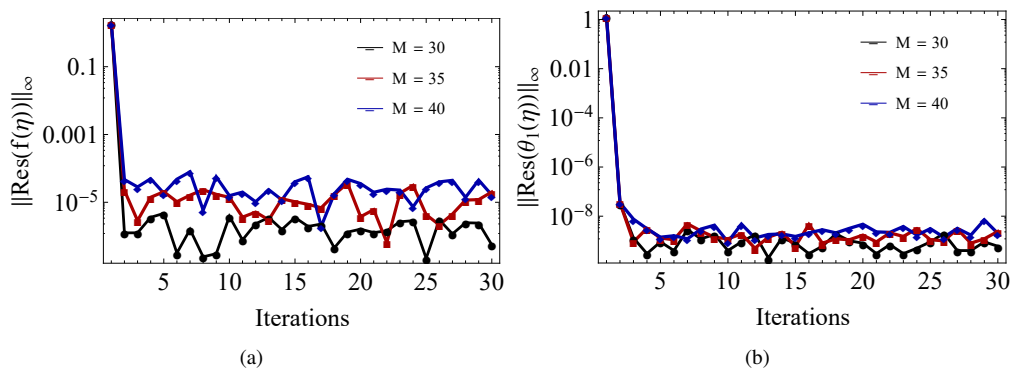

Figure 2. Influence of iterations on (a) $\|\text{Res}(f(\eta))\|_\infty$ and (b) $\|\text{Res}(\theta_1)\|_\infty$
for collocation points when $a_j = 1$, $m = 2$ $\phi = \pi/4$, $Re = 0.4$, $N = 0.4$, $Pr = 0.7$, $Br = 0.2$, $Da = 0.01$, $K = 0.5$.

4. CONVERGENCE ANALYSIS AND RESULTS

Convergence analysis entails demonstrating that the iterative procedure converges to an exact solution for the nonlinear differential equations (9) and (11), by taking the boundary conditions (13) into account. The calculation of residual errors is performed to guarantee the precision of the numerical results. Inaccuracies measure the extent of discrepancy between the numerical solution and the precise original solution. These errors quantify the degree of deviation experienced by the numerical solution from the original solution. For equations (9) and (11), the residual errors are obtained as follows:

$$\text{Res}(f) = \left(\frac{1}{1-N}\right)f^{iv} - \frac{N}{1-N}g'' + Re[f'f'' - ff'''] - \frac{1}{(1-N)Da}[K\cos^2\phi + \sin^2\phi]f'', \tag{27}$$

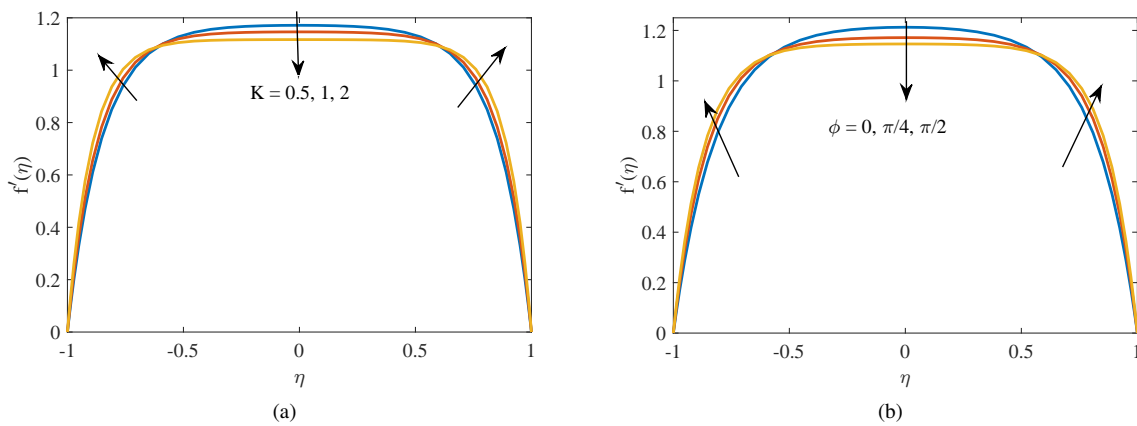**Figure 3.** Axial velocity profile for different values of (a) Anisotropic permeability ratio K (b) Anisotropic angle ϕ for $aj = 1$, $m = 2$, $Re = 0.4$, $N = 0.4$, $Pr = 0.7$, $Br = 0.2$, $Da = 0.01$, $K = 0.5$, $\phi = \pi/4$.

$$\text{Res}(\theta_1) = \theta_1'' + 2\theta_2 - Pr\,Re\,[f\theta_1'] + \frac{N(2-N)}{1-N}\frac{Br}{m^2}g^2 + \frac{Br}{(1-N)Da}[\cos^2\phi + K\sin^2\phi]f^2 + 2\left(\frac{2-N}{1-N}\right)Brf'^2. \quad (28)$$

The infinite norms of (27) and (28) are represented as $\|\text{Res}(f)\|_\infty$, and $\|\text{Res}(\theta_1)\|_\infty$ respectively which indicate the largest absolute value of the error over the whole domain. Increasing the values of M(number of collocation points), affects the accuracy of the solution generated by SQLM, as illustrated in Figure (2). The residual error in f over 30 iterations for different collocation points ($M = 30$, 35, 40) is displayed in figure 2(a). The optimal accuracy is achieved with collocation points between 30 and 40, with residual errors around 10^{-6}. The residual error in θ_1 over 30 iterations is depicted in figure 2(b). Furthermore, the convergence becomes increasingly evident after the fifth iteration, as the residual error norms fall in between 10^{-9} to 10^{-10}. Effects of various key parameters on micropolar fluid flow and heat transfer characteristics are investigated. These parameters include Darcy number, Reynolds number, Prandtl number, Brinkman number, anisotropic ratio, anisotropic angle, and the coupling number.

Figures in (3) and (4), depict the axial velocity distribution $f'(\eta)$ against the dimensionless distance η. In figure 3(a),
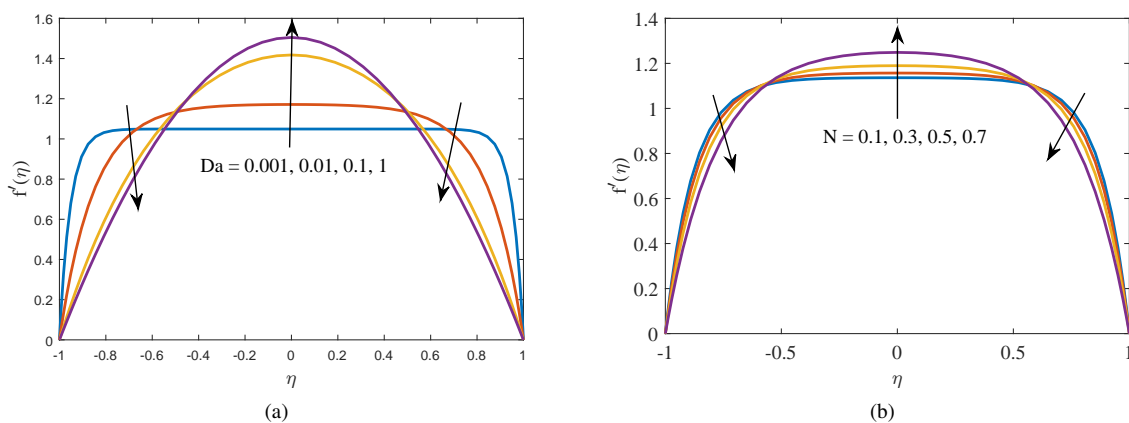

Figure 4. Axial velocity profile for different values of (a) Darcy number Da (b) Coupling number N for $aj = 1$, $m = 2$, $Re = 0.4$, $Pr = 0.7$, $Br = 0.2$, $Da = 0.01$, $K = 0.5$, $\phi = \pi/4$.

it is evident that the velocity rises near the vicinity of the boundaries as the values of permeability ratio K are increased. Whereas near the centre line, a decline can be noted, and maximum velocity is attained at the centre. This is due to the fact that the value of $k = k_1/k_2$ increases which implies the horizontal permeability decreases and so the velocity at the walls. Figure 3(b) depicts the variation of velocity with an anisotropic angle. Optimal velocity is attained when $\phi = 0$, while the lowest velocity is seen when $\phi = \frac{\pi}{2}$. This behaviour is consistent with the concept that when the value of K is less than or equal to 1 and keeps Da or k_1 constant, a value of $\phi = 0$ indicates a higher horizontal permeability k_2. Conversely, if the value of K is greater than 1, the behaviour will be the opposite. The value of $\phi = 0$ is equivalent to
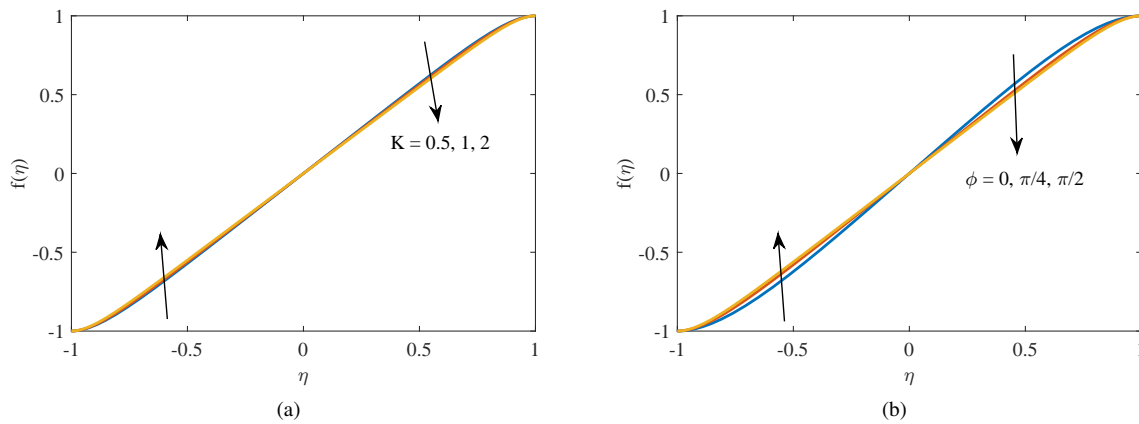
Figure 5. Transverse velocity profile for different values of (a) Anisotropic permeability ratio K (b) Anisotropic angle ϕ for $aj = 1$, $m = 3$, $Re = 0.2$, $N = 0.2$, $Pr = 0.7$, $Br = 0.2$, $Da = 0.01$, $K = 0.2$, $\phi = \pi/4$.

k_2 the horizontal permeability, resulting in a reduction in permeability along the flow direction. The velocity exhibits an upward trend in the vicinity of the walls and a downward trend at the centre as the angle increases. The graph in figure 4(a) illustrates a reduction in the velocity at boundaries and an increase at the centre of channel as the values of Da are raised. As Da increases from 0.001 to 1, the velocity profile shifts from uniform to parabolic, indicating less restricted fluid flow and increased velocity near the center. In the graph of figure 4(b), it can be observed that the velocity distribution is decreasing near the boundaries, whereas it is increasing at the centre. With increasing N, the influence of microrotations becomes more pronounced, leading to a flatter, more uniform velocity distribution across the channel. Figures (5)-(6), depict the transverse velocity profile $f(\eta)$ against the dimensionless distance η. Figure 5(a) illustrates that the transverse velocity rises at the lower boundary and reduces at the upper boundary, as the value of K is increased. Maximum velocity is attained at the upper wall. For a constant Da (constant k_1), an increase in K results in a decrease in k_2, the horizontal permeability. As k_2 diminishes, the shear resistance in the horizontal direction escalates, consequently enhancing the energy dissipation attributed to internal friction within the flow. This energy dissipation influences the overall decrease in fluid momentum and, indirectly, the transverse velocity as well. In figure 5(b), the velocity is seen rising near the lower boundary and decreasing towards upper boundary with an increase in ϕ. Elevating anisotropic angle ϕ causes the permeability of the porous media to align with the transverse direction. This alignment reduces resistance and induces redistributing of the fluid flow, so enhancing the transverse velocity component near the lower wall and a decrease at the upper wall. Figures in 6(a) and 6(b) show the effect of Da and N on the transverse velocity. The velocity
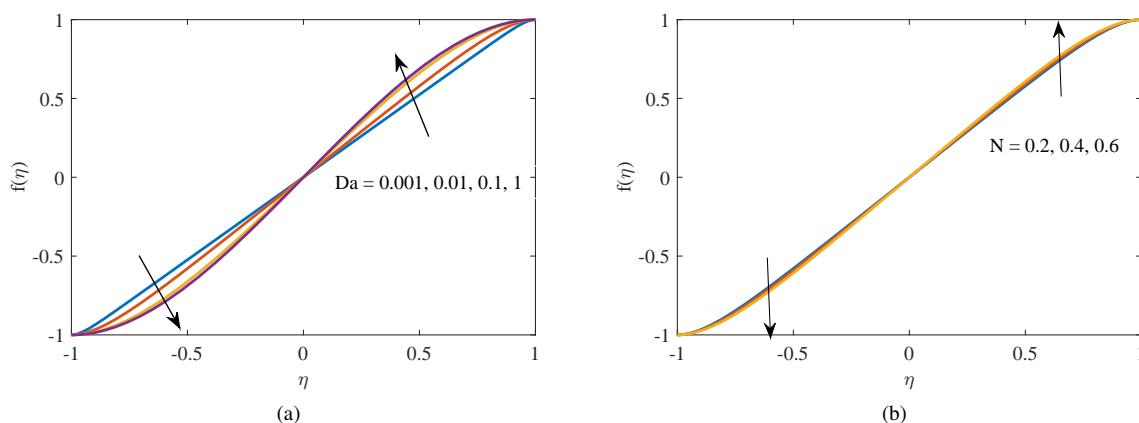

Figure 6. Transverse velocity profile for different values of (a) Darcy number Da (b) Coupling number N for $aj = 1$, $m = 3$, $Re = 0.2$, $N = 0.2$, $Pr = 0.7$, $Br = 0.2$, $Da = 0.01$, $K = 0.2$, $\phi = \pi/4$.

is observed to reduce near the lower boundary and rises from the centre towards the upper wall as values of Da and N are increased. This is expected because a higher Darcy number typically implies a more permeable medium, allowing fluid to move more freely. As N increases, the velocity profiles are almost overlapping with a slight shift upward. This

overlap suggests that variations in the coupling number have a relatively small impact on the transverse velocity. The
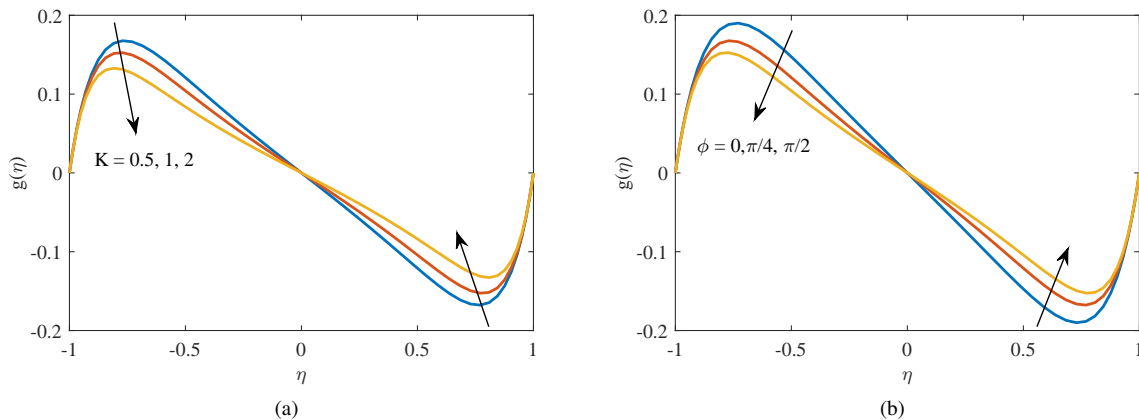

(a)   (b)

Figure 7. Microrotation profile for different values of (a) Anisotropic permeability ratio K (b) Aisotropic angle ϕ for $aj = 1$, $m = 2$, $Re = 0.2$, $N = 0.2$, $Pr = 0.7$, $Br = 0.2$, $Da = 0.01$, $K = 0.5$, $\phi = \pi/4$.

microrotation profile in figure 7(a) shows a wave-like pattern with distinct peaks and troughs. The amplitude of these oscillations, especially at the centre of the channel, can be seen to decrease. This is due to the dampening effects of rotation in the fluid as the anisotropic permeability K increases. Figure 7(b) demonstrates that increasing the anisotropic angle also reduces microrotation, affecting the rotational dynamics in the fluid. In figure 8(a), as Da increases, an increase in microrotation near the vicinity of lower wall is observed, which declines towards the upper wall. A higher Darcy number, corresponding to more permeable media, reduces microrotation effects. Understanding this relationship is crucial for accurately modelling fluid behaviour in micropolar systems, especially in industrial and biomedical applications where porous media play a significant role. Figure 8(b) demonstrates that increasing the values of coupling number N leads
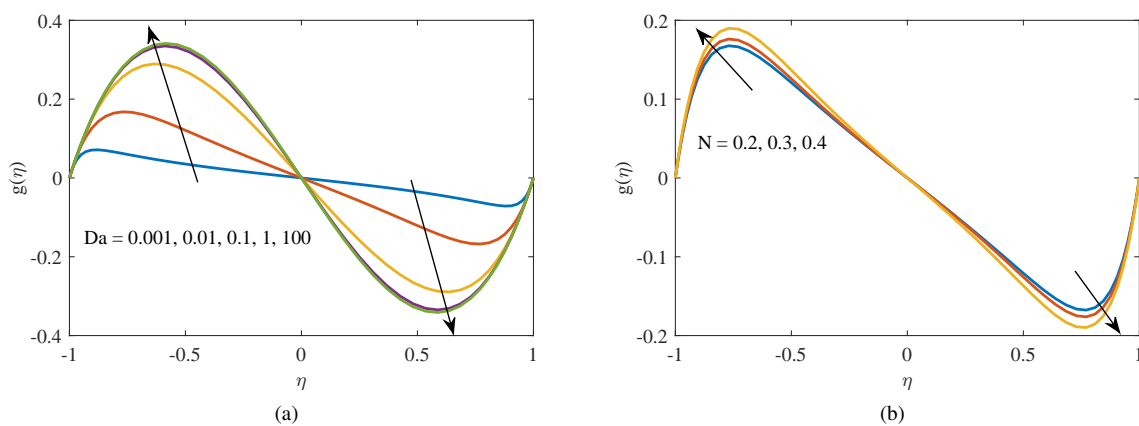

(a)   (b)

Figure 8. Microrotation profile for different values of (a) Darcy number Da (b) Coupling number N for $aj = 1$, $m = 2$, $Re = 0.2$, $N = 0.2$, $Pr = 0.7$, $Br = 0.2$, $Da = 0.01$, $K = 0.5$, $\phi = \pi/4$.

to reduction in microrotation located near the upper channel wall. This phenomenon occurs because an increase in the coupling number leads to a decrease in the thickness of the boundary layer. Furthermore, the microrotation is unimpeded by the microelements distributed over the metal plate. The microrotation profile in the boundary layer thickness is not hindered by the microelements that are dispersed away from the plate. Therefore, the distribution of microrotation is an increasing function of the coupling number till $\eta = 0$ and opposite from $\eta = 0$ to $\eta = 1$. Figures in (9) depict the reverse trend for increasing the values of Re, Pr, and Br. Figures in (10)- (12) depict the variation of temperature profile against the non-dimensional distance η. It can be seen from figure 10(a) the flatter curve is a result of increased permeability, which raises K values and results in a more uniform temperature distribution. Figure 10(b) shows that the temperature is decreasing when the anisotropic angle ϕ is increased. A wider and more uniform temperature distribution is indicated by the peak temperature's slight decrease with increasing anisotropic angle. According to this, better heat diffusion throughout
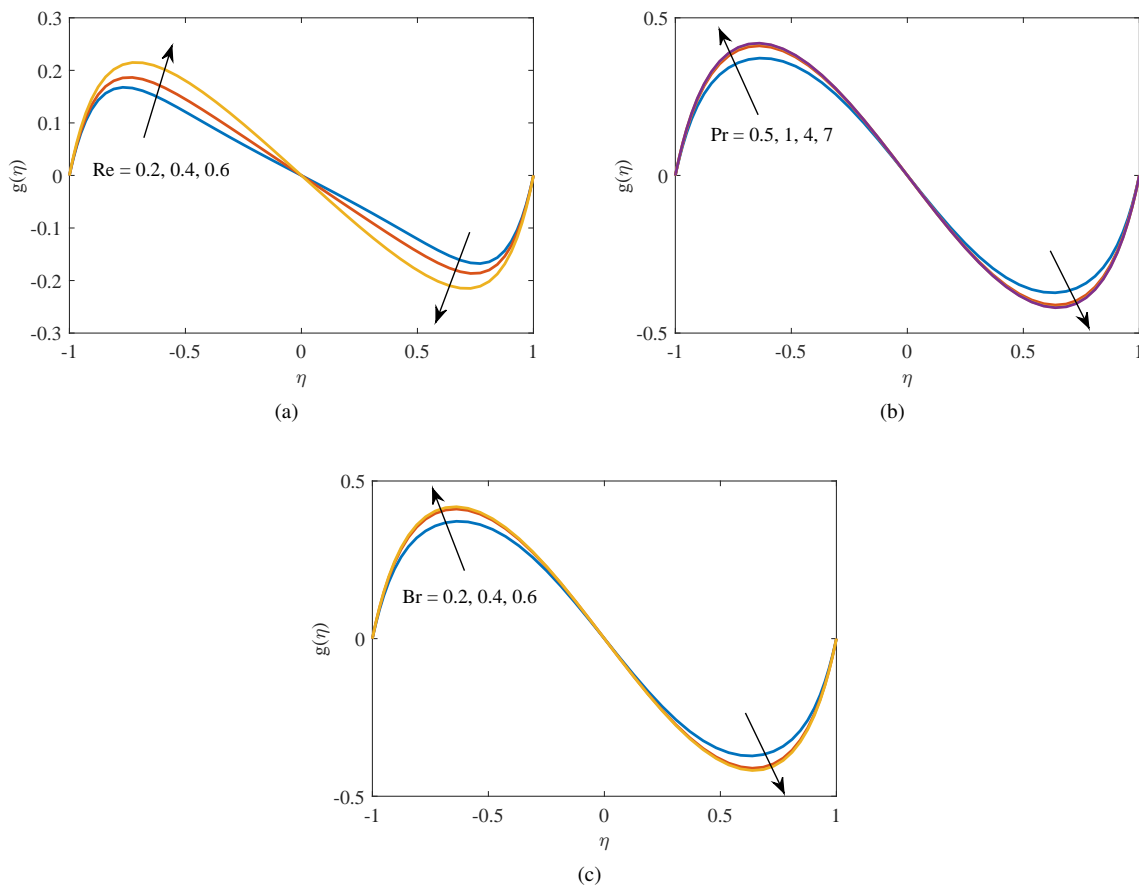
Figure 9. Microrotation profile for different values of (a) Reynold's number Re (b) Prandtl number Pr (c) Brinkman number Br, for $aj = 1$, $m = 2.4$, $Re = 0.75$, $N = 0.2$, $Pr = 0.7$, $Br = 0.2$, $Da = 0.01$, $K = 0.5$, $\phi = \pi/4$.
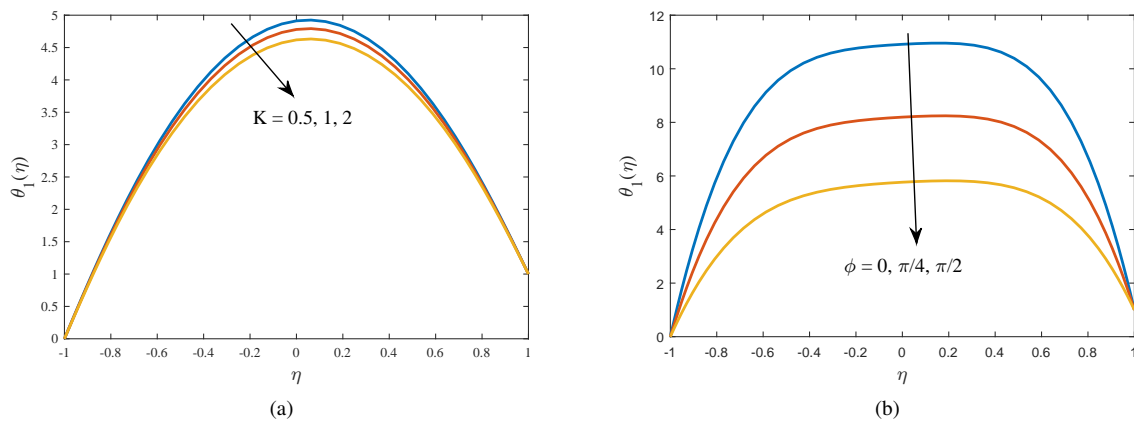

Figure 10. Temperature profile for different values of (a) Anisotropic permeability ratio K (b) Anisotropic angle ϕ for $aj = 1$, $m = 2$, $Re = 0.4$, $N = 0.4$, $Pr = 0.7$, $Br = 0.2$, $Da = 0.01$, $K = 0.5$, $\phi = \pi/4$.

the fluid is produced by larger anisotropic angles. The temperature reaches its maximum at the center of the wall and for $\phi = 0$. Figure 11(a) shows that higher Da values typically correspond to more permeable media, allowing for more efficient heat transfer. Figure 11(b) illustrates that higher values of N indicate more significant coupling effects, which enhance thermal diffusion, leading to a more uniform temperature profile. As Re increases, in figure 12(a), we observe that the temperature profile peaks near the center and reduces towards the boundaries. This indicates higher Reynold's
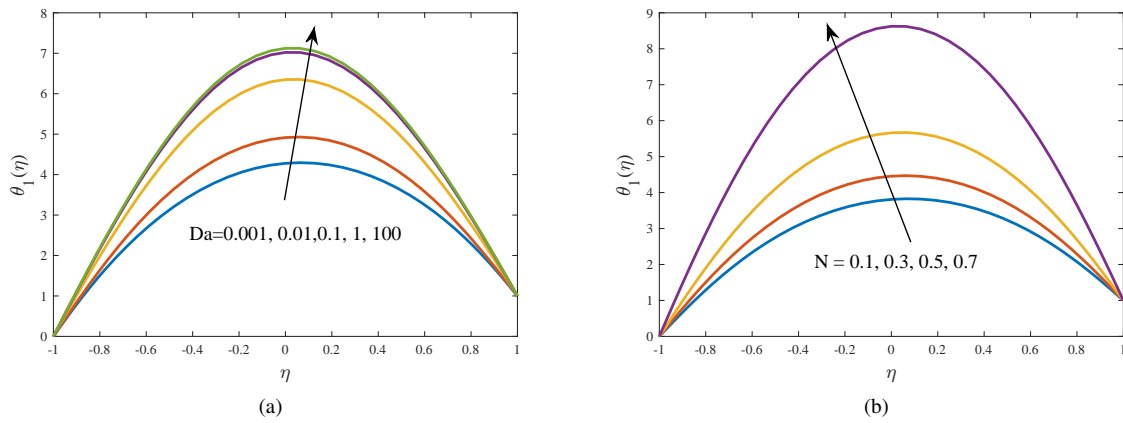
Figure 11. Temperature profile for different values of (a) Darcy number Da (b) Coupling number N for $aj = 1$, $m = 2$, $Re = 0.4$, $N = 0.4$, $Pr = 0.7$, $Br = 0.95$, $Da = 0.01$, $K = 0.5$, $\phi = \pi/4$.
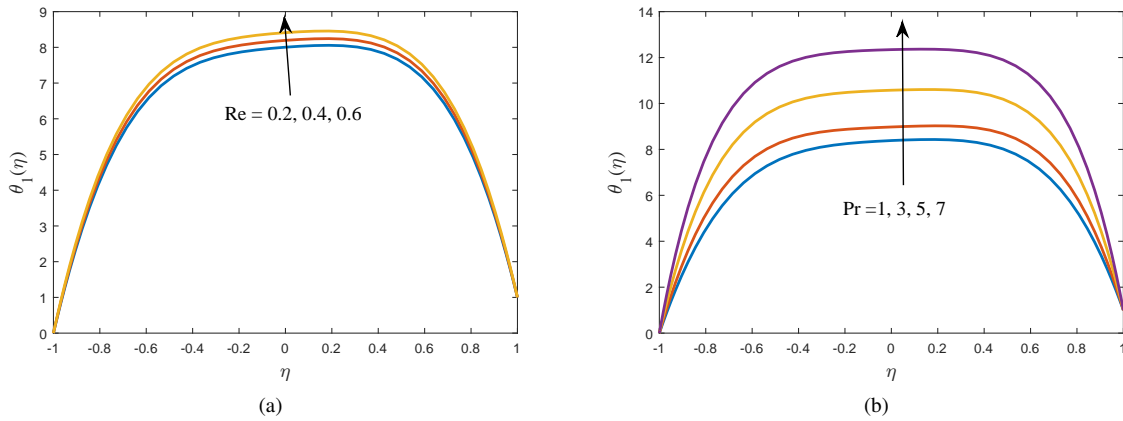

Figure 12. Temperature profile for different values of (a) Reynold's number Re (b) Prandtl number Pr for $aj = 1$, $m = 2$, $Re = 0.4$, $N = 0.4$, $Pr = 0.7$, $Br = 0.2$, $Da = 0.01$, $K = 0.5$, $\phi = \pi/4$.
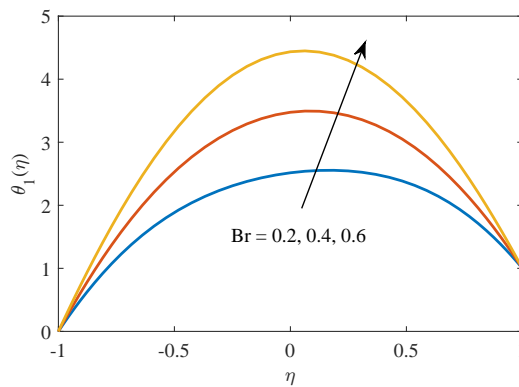

Figure 13. Temperature profile for different values of Brikman number Br for $aj = 1$, $m = 2$, $Re = 0.4$, $N = 0.4$, $Pr = 0.7$, $Da = 0.1$, $K = 0.5$, $\phi = \pi/4$.

number leads to more uniform temperature distribution, resulting in enhanced heat transfer. Higher Re corresponds to higher flow rates or lower viscosity due to which the temperature gradient becomes less steep. Figure 12(b) illustrates

that the temperature peaks near $\eta = 0$ and decreases towards the boundaries as the value of Pr increases. Greater Prandtl number Pr values result in decreased thermal diffusion and more pronounced temperature gradients, which results in more localised changes near the center. Figure (13) shows that increasing the value of Brinkman number Br, results in a higher temperature peak, indicating that viscous dissipation effects become more significant.

5. CONCLUSIONS

The present work introduces a mathematical model that describes the dynamics of fluid flow and the heat transfer of a micropolar fluid within a conduit that is saturated with anisotropic porous media. The numerical solutions are obtained using a Spectral Quasi-Linearization Method (SQLM). An in-house developed MATLAB program is used to generate graphs that depict the impacts of some important physical parameters identified in the review. The results obtained are summarized as follows:

- Anisotropic permeability ratio and angle significantly impact the fluid flow and heat characteristics. As K, ϕ increases, the microrotation and temperature increase, whereas the velocity reduces at the centre of the wall, and rises near the end of the walls.

- Higher values of Darcy number (Da) indicate less restricted flow, leading to decreased axial velocity near the walls and increased transverse velocity at the upper wall due to higher vertical permeability. This also reduces microrotation effects. Understanding this relationship is essential for accurately modelling fluid behavior in micropolar systems, particularly in industrial and biomedical applications involving porous media. Additionally, the temperature tends to rise near the centre of the channel.

- Increasing coupling number N leads to a reduction in velocity and microrotation in conjunction with an increase in temperature, mostly due to the substantial micropolar effects.

- As the Brinkmann number Br increases, the viscous dissipation effects cause microrotation at the upper channel wall and temperature to decrease.

- Increase in Reynolds number Re, causes the microrotation to decrease after the middle of channel and the temperature distribution becomes less pronounced, indicating stronger convective effects.

- Higher Prandtl number Pr leads to reduced microrotation and increased temperature, indicating improved heat transfer efficiency attributed to increased thermal conductivity.

The convergence analysis demonstrated that the SQLM is effective. The residual errors for velocity and temperature profiles showed rapid convergence, with accuracy significantly improving after the fifth iteration. Accuracy reached its peak at 35-40 collocation points, but then gradually declined. The numerical method proved robust and efficient, with residual error norms ranging from 10^{-6} to 10^{-7} and 10^{-9} to 10^{-10} for various parameters.

The present work addresses a research gap by investigating the impact of micropolar fluid dynamics on fluid flow and heat transfer. The paper offers valuable recommendations for enhancing the transfer of heat and flow control in engineering applications that involve micropolar fluids. The numerical method is found to be robust and efficient.

ORCID

 R. Vijaya Sree, https://orcid.org/0009-0002-0047-302X; **V. K. Narla**, https://orcid.org/0000-0003-0994-3497

REFERENCES

[1] A.C. Eringen, "Theory of micropolar fluids," J. Math. Mech. **16**, 1–18 (1966). https://doi.org/10.1512/iumj.1967.16.16001

[2] R.S.R. Gorla, and A.S. Kumari, "Buoyancy effects on the boundary layer flow of a micropolar fluid along a vertical cylinder," Int. J. Eng. Sci. **26**(8), 883–892 (1988). https://doi.org/10.1016/0020-7225(88)90039-0

[3] R.S.R. Gorla, R. Pender, and J. Eppich, "Heat transfer in micropolar boundary layer flow over a flat plate," Int. J. Eng. Sci. **21**(7), 791–798 (1983). https://doi.org/10.1016/0020-7225(83)90062-9

[4] R.S.R. Gorla, "Mixed convection in a micropolar fluid from a vertical surface with uniform heat flux," Int. J. Eng. Sci. **30**(3), 349–358 (1992). https://doi.org/10.1016/0020-7225(92)90080-Z

[5] A. Arafa, and R.S.R. Gorla, "Mixed convection boundary layer flow of a micropolar fluid along vertical cylinders and needles," Int. J. Eng. Sci. **30**(12), 1745–1751 (1992). https://doi.org/10.1615/InterJFluidMechRes.v33.i3.10

[6] D.D. Ganji, and A. Mirzaaghaian, "Application of differential transformation method in micropolar fluid flow and heat transfer through permeable walls," Alex. Eng. J. **55**, 2183–2191 (2016). https://doi.org/10.1016/j.aej.2016.06.011

[7] J.K. Zhou, *Differential Transformation and its Applications for Electrical Circuits*, (Huazhong University Press, Wuhan, 1986).

[8] D.D. Ganji, and A.S. Dogonchi, "Analytical investigation of convective heat transfer of a longitudinal fin with temperature-dependent thermal conductivity, heat transfer coefficient and heat generation," Int. J. Phys. Sci. **9**(21), 466–474 (2014). https://academicjournals.org/journal/IJPS/article-full-text-pdf/417CC2548549

[9] A.S. Dogonchi, M. Hatami, and D.D. Ganji, "Motion analysis of a spherical solid particle in plane Couette Newtonian fluid flow," Powder Technol. **274**, (2015). https://doi.org/10.1016/j.powtec.2015.01.018

[10] A.S. Dogonchi, M. Hatami, Kh. Hosseinzadeh, and G. Domairry, "Non-spherical particles sedimentation in an incompressible Newtonian medium by Pade approximation," Powder Technol. **278**, 248–256 (2015). https://doi.org/10.1016/j.powtec.2015.03.036

[11] A.S. Dogonchi and D.D. Ganji, "Convection–radiation heat transfer study of moving fin with temperature-dependent thermal conductivity, heat transfer coefficient and heat generation," Appl. Therm. Eng. **103**, 705–712 (2016). https://doi.org/10.1016/j.applthermaleng.2016.04.121

[12] F. Mabood, S.M. Ibrahim, M.M. Rashidi, M.S. Shadloo, and G. Lorenzini, "Non-uniform heat source/sink and Soret effects on MHD non-Darcian convective flow past a stretching sheet in a micropolar fluid with radiation," Int. J. Heat Mass Transf. **93**, 674–682 (2016). https://doi.org/10.1016/j.ijheatmasstransfer.2015.10.014

[13] M. Fakour, A. Vahabzadeh, D.D. Ganji, and M. Hatami, "Analytical study of micropolar fluid flow and heat transfer in a channel with permeable walls," J. Mol. Liq. **204**, 198–204 (2015). https://doi.org/10.1016/j.molliq.2015.01.040

[14] N. Sandeep and C. Sulochana, "Dual solutions for unsteady mixed convection flow of MHD micropolar fluid over a stretching/shrinking sheet with non-uniform heat source/sink," Eng. Sci. Technol. Int. J. **18**(4), 738–745 (2015). https://doi.org/10.1016/j.jestch.2015.05.006

[15] M. Turkyilmazoglu, "Mixed convection flow of magnetohydrodynamic micropolar fluid due to a porous heated/cooled deformable plate: Exact solutions," Int. J. Heat Mass Transf. **106**, 127–134 (2017). https://doi.org/10.1016/j.ijheatmasstransfer.2016.10.056

[16] M. Turkyilmazoglu, "Flow of a micropolar fluid due to a porous stretching sheet and heat transfer," Int. J. Non-Linear Mech. **83**, 59–64 (2016). https://doi.org/10.1016/j.ijnonlinmec.2016.04.004

[17] P.P. Humane, V.S. Patil, A.B. Patil, and M.D. Shamshuddin, "Buongiorno modelled nanoliquid consequence of thermal and solutal convection on the magneto-micropolar fluid inside an inclined porous stretching device," J. Nanofluids, **12**(1), 211–222 (2023). https://doi.org/10.1166/jon.2023.1949

[18] V. Agarwal, B. Singh, A. Kumari, W. Jamshed, K.S. Nisar, A.H. Almaliki, and H.Y. Zahran, "Steady Magnetohydrodynamic Micropolar Fluid Flow and Heat and Mass Transfer in Permeable Channel with Thermal Radiation," Coatings, **12**(1), 11 (2021). https://doi.org/10.3390/coatings12010011

[19] B. Jalili, A.A. Azar, P. Jalili, and D.D. Ganji, "Analytical approach for micropolar fluid flow in a channel with porous walls," Alexandria Eng. J. **79**, 196–226 (2023). https://doi.org/10.1016/j.aej.2023.08.015

[20] M. D. Shamshuddin, F. Mabood, W.A. Khan, and G.R. Rajput, "Exploration of thermal Peclet number, vortex viscosity, and Reynolds number on two-dimensional flow of micropolar fluid through a channel due to mixed convection," Heat Transf. **52**(1), 854–873 (2023). https://doi.org/10.1002/htj.22719

[21] M. Abdalbagi, "Micropolar flow and heat transfer within a permeable channel using the successive linearization method," Open Physics, **21**(1), (2023). https://doi.org/10.1515/phys-2023-0177

[22] Z. Shah, A. Khan, W. Khan, M.K. Alam, S. Islam, P. Kumam, and P. Thounthong, "Micropolar gold blood nanofluid flow and radiative heat transfer between permeable channels," Comput. Methods Programs Biomed. **186**, 105197 (2020). https://doi.org/10.1016/j.cmpb.2019.105197

[23] S. Ahmad, M. Ashraf, K. Ali, and K.S. Nisar, "Computational analysis of heat and mass transfer in a micropolar fluid flow through a porous medium between permeable channel walls," Int. J. Nonlinear Sci. Numer. Simul. **23**(5), 761–775 (2022). https://doi.org/10.1515/ijnsns-2020-0017

[24] M. Akbarzadeh, S. Rashidi, M. Bovand, and R. Ellahi,"A sensitivity analysis on thermal and pumping power for the flow of nanofluid inside a wavy channel," J. Mol. Liq. **220**, 1–13 (2016). https://doi.org/10.1016/j.molliq.2016.04.058

[25] M.M. Bhatti, M.M. Rashidi, "Effects of thermo-diffusion and thermal radiation on Williamson nanofluid over a porous shrinking/stretching sheet," J. Mol. Liq. **221**, 567–573 (2016). https://doi.org/10.1016/j.molliq.2016.05.049

[26] M.M. Rashidi, N. Vishnu Ganesh, A.K. Abdul Hakeem, B. Ganga, , "Buoyancy effect on MHD flow of nanofluid over a stretching sheet in the presence of thermal radiation," J. Mol. Liq. **198**, 234–238 (2014). https://doi.org/10.1016/j.molliq.2014.06.037

[27] H.S. Takhar, R. Bhargava, R.S. Agrawal, and A.V.S. Balaji, "Finite element solution of micropolar fluid flow and heat transfer between two porous discs," Int. J. Eng. Sci. **38**(17), 1907–1922 (2000). https://doi.org/10.1016/S0020-7225(00)00019-7

[28] M. Pathak, P. Joshi, and K.S. Nisar, "Numerical investigation of fluid flow and heat transfer in micropolar fluids over a stretching domain," J. Therm. Anal. Calorim. **147**, 10637–10646 (2022). https://doi.org/10.1007/s10973-022-11268-w

[29] C. Boodoo,"Micropolar fluid flows past a porous shell: A model for drug delivery using porous microspheres," Eur. J. Eng. Technol. Res. **9**(3), 1–7 (2024). https://doi.org/10.24018/ejeng.2024.9.3.3162

[30] D. Srinivasacharya and K. Hima Bindu, "Entropy generation in a porous annulus due to micropolar fluid flow with slip and convective boundary conditions," Energy, **111**, 165–177 (2016). https://doi.org/10.1016/j.energy.2016.05.101

[31] R.A. Alharbey, H. Mondal, and R. Behl, "Spectral quasi-linearization method for non-Darcy porous medium with convective boundary condition," Entropy, **21**(9), 838 (2019). https://doi.org/10.3390/e21090838

[32] T. Karmakar, M. Reza, and G.P.R. Sekhar, "Forced convection in a fluid saturated anisotropic porous channel with isoflux boundaries," Physics of Fluids, **31**, 117109 (2019). https://doi.org/10.1063/1.5126892

[33] I.P. Grant, R.E. Bellman, and R.E. Kalaba, "Quasilinearization and Non-Linear Boundary Value Problems," Math. Gaz. **52**(380), 212 (1968). https://doi.org/10.2307/3612757

[34] C. Canuto, M.Y. Hussaini, A. Quarteroni, and T.A. Zang, *Spectral Methods*, Vol. 285, (Springer, 2006).

[35] D. Srinivasacharya, and K.H, Bindu, "Entropy generation in a micropolar fluid flow through an inclined channel with slip and convective boundary conditions," Energy, **91**(C), 72–83 (2015). https://doi.org/10.1016/j.energy.2016.05.101

ВПЛИВ АНІЗОТРОПНОЇ ПРОНИКНОСТІ НА МІКРОПОЛЯРНУ ДИНАМІКУ РІДИНИ ТА ТЕПЛОПЕРЕНОС У ПОРИСТИХ КАНАЛАХ

Р. Віджая срі[a,b], **В. К. Нарла**[b]

[a]*Інженерний коледж АСЕ, Гхаткесар Мандал, округ Медчал, Телангана, 501301, Індія*
[b]*GITAM, факультет математики, Хайдарабад, 502329, Індія*

У поточному дослідженні вивчається динаміка рідин та характеристики теплопередачі мікрополярних рідин у каналі, заповненому анізотропним пористим середовищем. Керівні рівняння для профілів потоку рідини, мікрообертання та температури розв'язуються чисельно за допомогою методу спектральної квазілінеаризації (SQLM). Дослідження вивчає вплив різних ключових параметрів, таких як коефіцієнт анізотропної проникності, анізотропний кут, число Дарсі, число Рейнольдса, число Брінкмана, число Прандтля та число зв'язку. Ключові висновки вказують на те, що коефіцієнт анізотропної проникності та анізотропний кут значно впливають на потік рідини та розподіл тепла, при цьому підвищена анізотропія призводить до посиленого мікрообертання та температури, хоча й зі зниженою швидкістю в центрі каналу. Вищі числа Дарсі призводять до менш обмеженого потоку, збільшення швидкості та зменшення ефектів мікрообертання, тоді як збільшення числа сполучення сприяє більш рівномірному температурному профілю. Ці результати дають суттєве уявлення про оптимізацію теплопередачі та керування потоком у інженерних додатках, які включають мікрополярні рідини в пористих середовищах. Ключові слова: мікрополярні рідини, анізотропні пористі середовища, анізотропна проникність, мікроротація, теплопередача, метод спектрально-квазілінеаризації.

Ключові слова: *мікрополярна рідина; анізотропні пористі середовища; анізотропна проникність; мікроротація; теплообмін; спектральний квазілінеаризаційний метод*

ENTROPY GENERATION OPTIMIZATION IN A REE-EYRING TERNARY HYBRID NANOFLUID FLOW OVER AN ELASTIC SURFACE WITH NON-FOURIER HEAT FLUX

Gadamsetty Revathi[a], D. Purnachandra Rao[b], S. Ramalingeswara Rao[c], K.S. Srinivasa Babu[c]*, T.R.K.D. Vara Prasad[c], M. Jayachandra Babu[d]

[a]Department of Mathematics, Gokaraju Rangaraju Institute of Engineering and Technology, Bachupally, Hyderabad – 500090, India
[b]Department of Mathematics, Matrusri Engineering College, Saidabad, Hyderabad – 500059, Telangana, India
[c]Department of EM&H, S.R.K.R. Engineering College, Bhimavaram, Andhra Pradesh – 534204, India
[d]Department of Mathematics, Government Degree College, Rajampeta, Annamayya district, Andhra Pradesh – 516115, India
*Corresponding Author e-mail: kssb@srkrec.ac.in
Received September 14, 2024; revised November 12, 2024; accepted November 20, 2024

The significance of Ree-Eyring ternary hybrid nanofluid flow lies in its potential applications in various fields. By incorporating three different types of nanoparticles into a base fluid using the Ree-Eyring model, this innovative fluid offers enhanced thermal conductivity, heat transfer efficiency, and rheological properties. These characteristics are particularly valuable in industries such as electronics cooling, solar energy systems, and heat exchangers, where efficient heat management is crucial. Additionally, the unique rheological behavior of Ree-Eyring nanofluids can provide advantages in processes like drilling, lubrication, and drug delivery. Under Thompson-Troian boundary conditions, this study aims to theoretically analyse 2D radiative flow of the Ree-Eyring ternary hybrid nanofluid over an angled sheet with Cattaneo-Christov heat flux and higher order chemical reaction parameters. In order to express them as ordinary differential equations (ODEs), flow-driven equations undergo suitable similarity transformations. The ensuing system is resolved by employing a bvp4c approach. The main takeaway from this study is that the thermal relaxation parameter reduces the width of the temperature profile and the fluid velocity is minimized by adjusting the slip parameter. The concentration profile is minimized by the chemical reaction parameter and the Ree-Eyring fluid parameter increases with the same (fluid velocity). In addition, we found that the skin friction coefficient is strongly correlated negatively with the Ree-Eyring fluid parameter, positively with the (thermal) relaxation parameter, and significantly correlated positively with the chemical reaction through the Nusselt number. When Brinkman number increases, Bejan number drops. Furthermore, a rise in thermal radiation parameter leads to the escalation in both entropy generation and Bejan number. We observed a worthy agreement when we checked the outcomes of this investigation with prior effects.
Keywords: *Viscous dissipation; Thermal Radiation; MHD; Non-Fourier Heat Flux; Nanofluid*
PACS: 47.15.-x, 47.50.-d

Nomenclature

u, v – Components of velocity in x, y directions respectively
ρ – Fluid density
μ – Dynamic viscosity
g – Acceleration due to gravity
α – Angle of inclination
v_w – Permeability of porous surface
σ – Electric conductivity
T – Fluid temperature (dimensional)
ξ^* - Critical shear rate
β, c – fluid constants
β_T – Thermal expansion coefficient
β_C – Concentration expansion coefficient
C_p – Specific heat capacity
k_0 – Chemical reaction parameter
B_0 – Initial magnetic strength
M – Magnetic field parameter

γ^*- Navier's slip length
v – Kinematic viscosity
C – Fluid concentration (dimensional)
k^* - Mean absorption coefficient
σ^* - Stefan-Boltzmann constant
D_m – Molecular diffusivity
Λ – Thermal relaxation parameter
Sc – Schmidt number
We – Ree-Eyring fluid parameter
λ_1 – Mixed convection parameter
λ_1^* – Buoyancy ratio parameter
R_a – Radiation parameter
E_c – Eckert number
Bn – Bejan number
Br – Brinkman number
θ – Fluid temperature (non-dimensional)
ϕ – Fluid concentration (non-dimensional)

1. INTRODUCTION

Nanofluids are the colloidal mixtures of ordinary liquid particles having a dimension of less than one nanometre. These particles will enhance the thermal properties of typical liquids with low thermal conductivity. The latest generations have used a number of innovative techniques to increase the heat transfer rates, which has allowed them to achieve different degrees of thermal adeptness. Enhancing heat conduction is necessary to do this. Thus, many attempts were made to increase heat conductivity in the liquids by dispersing higher, solid thermally conductive components throughout them. The goal of developing nanofluids to meet industrial demands has been attempted multiple times. While efforts to develop a superior fluid are still on, researchers and experts in energy use might discover that nanofluids meet their

requirements. For instance, Sheikholeslami and Rokni [1] has been studied the behaviour of heat transfer of a nanofluid along with magnetic effect. Ganvir et al. [2] discussed the characteristics of transmission of heat in a nanofluid. Revathi et al. [3] conducted research on the flow of Darcy–Forchheimer power-law (Ostwald-de Waele type) nanofluid past an inclined plate subject to the influences of thermal radiation, activation energy. Recently, Rasool et al. [4] reported the results for the MHD radiative Darcy-Forchheimer nanofluid flow. Along a porous rotating disk, a stagnant Maxwell nanofluid flow and heat transfer is another study of Li et al. [5]. Radiative motion of a Water-Al$_2$O$_3$ based nanoliquid past a Riga surface with thermal radiation is reported by Madhukesh et al. [6]. Modelling of nanofluids with a mixture of two or more special types of nanoparticles treating as hybrid as well as ternary hybrid nanofluids based on their greater heat transfer production is another interesting aspect in the present literature. Huge amount of research can be observed from the recent literature on it. For instance, Yasir et al. [7] conducted research on a mixed convective radiative Hybrid nanofluid with heat generation/absorption impacts. Kho et al. [8] discussed the impacts of viscous dissipation and thermal radiation in a MHD flow of hybrid nanofluid. Abbas et al. [9] presented the numerical findings on a convective motion of a hybrid nanofluid along an infinite disk. Focusing on the very recent articles Khan et al. [10], Mishra and Pathak [11], Najafpour et al. [12], Farooq et al. [13], Mahboobtosi et al. [14] and Mohanty et al. [15], one can notice the similar attempts which are noteworthy.

The Cattaneo-Christov heat flux model is a mathematical approach, which can be utilized to describe transfer of heat in fluids and materials. It represents an improvement over the classical Fourier's law on conduction of heat. In contrast to the instantaneous heat transmission assumed by Fourier's law, the Cattaneo-Christov model includes a thermal relaxation time. This time constant reflects the finite time it takes for a material's temperature to adjust to a change in heat flux. This is particularly important for studying heat transfer at the microscopic level or in situations with rapid temperature variations. The model is used to analyze heat transfer in boundary layer flows, where thin layers of fluid develop near surfaces with different temperatures. This is applicable in various engineering contexts like heat ex-changers and fluid flow over objects. Most relevant applications of said model particularly occurs in engineering and biomedical processes. Metal spinning, nuclear reactor cooling, magnetic drug targeting, hot rolling, drawing copper wires, heat conduction in tissues and in energy production etc. Hayat et al. [16] included Cattaneo-Christov (C-C) mass flux model to scrutinize the features of heat transmission in the investigation of non-Newtonian fluid flow. Ahmad et al. [17] considered a wedge and numerically examined micropolar fluid flow by using bvp4c technique in MATLAB with thermal relaxation time and observed that it alleviates fluid temperature. Ibrahim and Gadisa [18] considered CCHF and examined the Oldroyd-B fluid flow by an irregular elongating sheet. They emphasized that this fluid model is good at examining the dilute polymetric solutions for visco-elastic behaviour. Reddy et al. [19] and Gireesha et al. [20] discussed various dusty fluid flows by a stretching sheet with CCHF model. They identified the fact that radiation parameter is predominant in cooling procedure and observed that the melting parameter lessens fluid temperature. Ali et al. [21] applied variational FEM (finite element method) to unriddle the mathematical model in the rotational Casson fluid flow examination through an extendable surface with double diffusive Cattaneo-Christov and detected diminution in secondary velocity with larger magnetic field parameter. Tassaddiq [22] considered elastic body and elucidated a micropolar-hybrid fluid flow with CCHF and Ohmic heating. Jakeer et al. [23] identified that the larger Darcy number ameliorates the fluid velocity in the scrutiny of HNF within a porous cavity with CCHF model. Examination of HNF (water with graphene and silver) flow among rotating disks with CCHF is done by Mahesh et al. [24] and amelioration in tangential velocity with larger Reynolds number is one of their results. Ali et al. [25] utilized Galerkin technique to theoretically examine the rotational nanofluid flow by an elastic surface and discovered that the Lewis number escalates the value of Sherwood number. Recently, several authors [26-33] considered various geometries and scrutinised diverse fluid flows with CCHF model.

Surface stretching mechanism in flow dynamical problems has become widely accepted in many industrial and technological processes. In particular, the quantity and quality of industrial processes heavily rely on the stretching of sheets. Rubber sheeting, hot rolling, glass blowing, drawing of wires, manufacturing of glass, processes like polymerization of sheets are some of the usages of stretching mechanisms. By using numerical simulations, Khan et al. [34] were able to observe that the Soret effect improves the concentration profile when MHD nanofluid flows through an extending sheet. Activation energy included Nanofluid flow was studied by Rasool et al. [35], who found that it reduces the mass flux rate. Abbas et al. [36] applied HAM method to elucidate MHD flow of Carreau fluid with varying thermal conductivity. Yasmin et al. [37] examined the features of heat transfer in the flow of MHD micropolar fluid by a tilted stretchable surface and detected that fluid velocity is minified with larger curvature parameter. Sankar Giri et al. [38] considered stretching cylinder and scrutinized MHD nanofluid (CNT nanoparticles) flow with chemical reaction. Gayatri et al. [39] considered nonuniform elongating sheet and discussed MHD dissipative Carreau fluid flow with Ohmic heating. Kumar et al. [40] used FEM to unriddle the mathematical model in their study on MHD fluid flows with various spherical nanoparticles by a vertical plate and noticed an inverse relationship among magnetic field parameter and Nusselt number. Newly, several researchers [41-52] discussed various MHD fluid flows through a variety of stretchable geometries.

Upon reviewing the aforementioned literature, it became apparent that the Ree-Eyring ternary hybrid nanofluid flow across an angled stretchable sheet subjected to Thompson-Troian boundary conditions has not been previously investigated. The originality of this study is in its examination of the dissipative magnetohydrodynamic Ree-Eyring ternary hybrid nanofluid flow via an angled plate with boundary conditions imposed by Thompson Troian theory. Entropy

optimization and Bejan number calculation were also included in this study. Two events, suction and injection, are depicted graphically to show the consequences. Findings of this study are well agreed with already published results which was shown in validation section.

2. FORMULATION

A radiative and chemically reactive motion of a Ree-Eyring ternary hybrid nanofluid across an elastic surface (angled) in addition to Thompson-Troian boundary conditions is investigated theoretically in the present analysis. The following hypotheses form the basis of the current inquiry:

(i)   The utilisation of non-Fourier heat flux is aptly applied in the examination of thermal conduction processes.

(ii)   kindly see Table 1 for exact numerical calculations of the thermo-physical properties of water (H_2O), *Graphene,* SiO_2, and CuO.

(iii)   Sheet is inclined by an angle α (observe Fig. 1).

(iv)   An external magnetic field applied vertically with an intensity B_0 influences the flow.

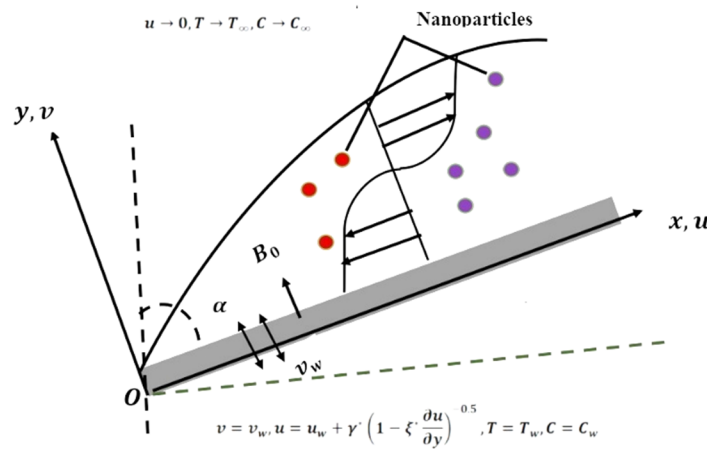(v)   In this work, the influence of induced magnetic fields is ignored.

Figure 1 Schematic representation of the present situation

Table 1. Key parameters' values of H_2O, *Graphene,* SiO_2, and CuO

S. No.	Properties	H_2O (f)	*Graphene* (Φ_G)	SiO_2 (Φ_S)	CuO (Φ_C)
1	$\sigma(S/m)$	0.005	10^7	10^{-25}	2.7×10^{-8}
2	$k(W/mK)$	0.613	2500	1.38	76.5
3	$\rho(Kg/m^3)$	997.1	2250	2200	6320
4	$C_p(J/KgK)$	4179	2100	703	531.8

Here are the conditions (prerequisites) and basic equations required for the study, based on these presumptions:

$$\frac{\partial u}{\partial x} + \frac{\partial v}{\partial y} = 0 , \tag{1}$$

$$v\frac{\partial u}{\partial y} + u\frac{\partial u}{\partial x} = \rho_{thnf}^{-1}\left(\mu_{thnf} + \frac{1}{\beta c}\right)\left(2\frac{\partial^2 u}{\partial x^2} + \frac{\partial^2 v}{\partial x\partial y} + \frac{\partial^2 u}{\partial y^2}\right) + \beta_c\left(C - C_\infty\right)g\cos\alpha$$
$$+ \beta_T\left(T - T_\infty\right)g\cos\alpha - \rho_{thnf}^{-1}\sigma_{thnf}uB_0^2 \tag{2}$$

$$u\frac{\partial T}{\partial x} + v\frac{\partial T}{\partial y} = k_{thnf}\left(\rho C_p\right)_{thnf}^{-1}\frac{\partial}{\partial y}\left(\frac{\partial T}{\partial y}\right) + \left(\rho C_p\right)_{thnf}^{-1}\frac{4}{3}\frac{4T_\infty^3\sigma^*}{k^*}\frac{\partial}{\partial y}\left(\frac{\partial T}{\partial y}\right)$$
$$-\gamma\left[\begin{array}{l}\left(u\frac{\partial v}{\partial x} + v\frac{\partial v}{\partial y}\right)\frac{\partial T}{\partial y} + v^2\frac{\partial^2 T}{\partial y^2} + 2uv\frac{\partial^2 T}{\partial x\partial y} + u^2\frac{\partial^2 T}{\partial x^2} \\ + \left(u\frac{\partial u}{\partial x} + v\frac{\partial u}{\partial y}\right)\frac{\partial T}{\partial x}\end{array}\right] + \left(\rho C_p\right)_{thnf}^{-1}\left(\mu_{thnf} + \frac{1}{\beta c}\right)\left(\frac{\partial u}{\partial y}\right)^2 \tag{3}$$

$$u\frac{\partial C}{\partial x}+v\frac{\partial C}{\partial y}=\frac{\partial^2 C}{\partial y^2}D_m-\left(C-C_\infty\right)^m k_0, \tag{4}$$

$$\left.\begin{array}{l} \text{at } y=0: v=v_w, u=u_w+u_f=bx+\gamma*\left(1-\xi*u_y\right)^{-0.5}\left.\frac{\partial u}{\partial y}\right|_{y=0}, T=T_w, C=C_w,\\[3mm] \text{as } y\to\infty: u\to 0, T\to T_\infty, \text{C}\to C_\infty. \end{array}\right\} \text{ (Ahmad and Nadeem [53])} \tag{5}$$

The following similarity transmutations for transforming controlling equations were offered by Rafique et al. [54]:

$$\left.\begin{array}{l} \theta=\frac{T-T_\infty}{T_w-T_\infty}, u=bx\frac{df}{d\eta}=bxf'(\eta), v=-f\left(b\upsilon\right)^{0.5},\\[3mm] C=C_\infty+\phi(\eta)\left(C_w-C_\infty\right), \eta=\sqrt{\frac{b}{\upsilon}}y. \end{array}\right\} \tag{6}$$

Through the use of (6), the continuity equation (1) is satisfied in a straightforward manner. Then (6) was skilfully used to alter (2, 3, 4 and 5) in the following procedure:

$$\frac{1}{S_1}\left(\frac{1}{S_2}+We\right)f'''+ff''-f'^2-\frac{S_3}{S_1}Mf'+\lambda_1\left(\theta+\phi\lambda_1*\right)\cos\alpha=0 \tag{7}$$

$$\frac{\left(S_4+R_a\right)}{S_5\Pr}\theta''+\left[f\theta'-\left(ff'\theta'+f^2\theta''\right)\Lambda+\frac{1}{S_2 S_5}E_c\left(We+1\right)f''^2\right]\Pr=0 \tag{8}$$

$$\frac{1}{Sc}\phi''-\Gamma\phi^m+f\phi'=0 \tag{9}$$

$$\left.\begin{array}{l} \text{at } \eta=0: f(\eta)=S, f'(\eta)=1+\delta\left(1-f''(\eta)\xi\right)^{-0.5}f''(\eta), \theta(\eta)=\phi(\eta)=1,\\[2mm] \text{as } \eta\to\infty: f'(\eta)\to 0, \theta(\eta)\to 0, \phi(\eta)\to 0. \end{array}\right\} \tag{10}$$

Here

$$\left.\begin{array}{l} \lambda_1=\frac{Gr}{\mathrm{Re}_x^2}, S=-\frac{v_w}{\sqrt{b\upsilon}}, E_c=\frac{u_w^2}{C_p\left(T_w-T_\infty\right)}, \lambda_1*=\frac{Gc}{Gr}, \delta=\gamma*\sqrt{\frac{b}{\upsilon}}, \xi=b\sqrt{\frac{b}{\upsilon}}\xi*x,\\[3mm] \Pr=\frac{\mu C_p}{k}, M=\frac{B_0^2\sigma}{b\rho}, \Lambda=\gamma b, We=\frac{1}{\mu\beta c}, R_a=\frac{16}{3}\frac{\sigma*T_\infty^3}{kk_\infty}, Gr=\frac{gx^3\beta_T\left(T_w-T_\infty\right)}{\upsilon^2},\\[3mm] Sc=\frac{\upsilon}{D_m}, Gc=\frac{gx^3\beta_C\left(C_w-C_\infty\right)}{\upsilon^2}, \Gamma=\frac{k_0\left(C_w-C_\infty\right)^{m-1}}{b}, \mathrm{Re}_x=\frac{xu_w}{\upsilon}. \end{array}\right\}$$

and

$$\left.\begin{array}{l} S_1=\left(1-\Phi_G\right)\left(\left(1-\Phi_S\right)\left[\left(1-\Phi_C\right)+\Phi_C\frac{\rho_C}{\rho_f}\right]+\Phi_S\frac{\rho_S}{\rho_f}\right)+\Phi_G\frac{\rho_G}{\rho_f}, S_{411}=\frac{k_C+2k_f-2\Phi_C\left(k_f-k_C\right)}{k_C+2k_f+\Phi_C\left(k_f-k_C\right)},\\[3mm] S_2=\left(1-\Phi_G\right)^{2.5}\left(1-\Phi_S\right)^{2.5}\left(1-\Phi_C\right)^{2.5}, \sigma_{311}=\frac{\sigma_C-2\left(\sigma_f-\sigma_C\right)\Phi_C+2\sigma_f}{\sigma_C+\left(\sigma_f-\sigma_C\right)\Phi_C+2\sigma_f},\\[3mm] S_{41}=\frac{k_S+2S_{411}k_f-2\Phi_S\left(S_{411}k_f-k_S\right)}{k_S+2S_{411}k_f+\Phi_S\left(S_{411}k_f-k_S\right)}, \sigma_{31}=\frac{\sigma_S+2S_{311}\sigma_f-2\Phi_S\left(S_{311}\sigma_f-\sigma_S\right)}{\sigma_S+2S_{311}\sigma_f+\Phi_S\left(S_{311}\sigma_f-\sigma_S\right)},\\[3mm] S_5=\left(1-\Phi_G\right)\left(\left(1-\Phi_S\right)\left[\left(1-\Phi_C\right)+\Phi_C\frac{\left(\rho C_p\right)_C}{\left(\rho C_p\right)_f}\right]+\Phi_S\frac{\left(\rho C_p\right)_S}{\left(\rho C_p\right)_f}\right)+\Phi_G\frac{\left(\rho C_p\right)_G}{\left(\rho C_p\right)_f},\\[3mm] S_4=\frac{k_G+2S_{41}k_f-2\Phi_G\left(S_{41}k_f-k_G\right)}{k_G+2S_{41}k_f+\Phi_G\left(S_{41}k_f-k_G\right)}, \sigma_3=\frac{\sigma_G+2S_{31}\sigma_f-2\Phi_G\left(S_{31}\sigma_f-\sigma_G\right)}{\sigma_G+2S_{31}\sigma_f+\Phi_G\left(S_{31}\sigma_f-\sigma_G\right)}. \end{array}\right\}.$$

Friction factor, Nusselt and Sherwood numbers are outlined as:

$$C_{f_x} = \frac{\left(\mu_{thnf} + \frac{1}{\beta c}\right)}{\frac{1}{2}\rho u_w^2}\left(\frac{\partial u}{\partial y} + \frac{\partial v}{\partial x}\right)\Bigg|_{y=0}, Nu_x = -x\frac{\left(k_{thnf} + \frac{16}{3}\frac{\sigma^* T_\infty^3}{k^*}\right)}{k_f\left(T_w - T_\infty\right)}\frac{\partial T}{\partial y}\Bigg|_{y=0}, Sh_x = -x\frac{D_m}{D_m\left(C_w - C_\infty\right)}\frac{\partial C}{\partial y}\Bigg|_{y=0}. \qquad (11)$$

Equation (6) allows us to rewrite (11) as

$$\left(\text{Re}_x\right)^{0.5} C_{fx} = 2\left(\frac{1}{S_2} + We\right)f''(\eta)\Bigg|_{\eta=0}, \left(\text{Re}_x\right)^{-0.5} Nu_x = -\left(S_4 + R_a\right)\theta'(\eta)\Big|_{\eta=0}, \left(\text{Re}_x\right)^{-0.5} Sh_x = -\phi'(\eta)\Big|_{\eta=0}.$$

2.1. Entropy generation and Bejan number
The formula below constitutes the dimensional representation used to calculate the entropy generation in the current work:

$$S_g = \left(\frac{k_{thnf}}{k_f} + \frac{16}{3}\frac{\sigma^* T_\infty^3}{k_f k^*}\right)\frac{k_f}{T_\infty^2}\left(\frac{\partial T}{\partial y}\right)^2 + \frac{1}{T_\infty}\left(\frac{\partial u}{\partial y}\right)^2\mu_{thnf} + \frac{1}{T_\infty}u^2\sigma_{thnf}B_0^2 +$$

$$\frac{\tilde{R}D_m}{C_\infty}\left(\frac{\partial C}{\partial y}\right)^2 + \frac{\tilde{R}D_m}{T_\infty}\frac{\partial C}{\partial y}\frac{\partial T}{\partial y}. \qquad (12)$$

By applying (6), equation (12) can be rewritten as follows:

$$EG = \left(S_4 + R_a\right)\alpha\theta'^2 + \frac{1}{S_2}Brf''^2 + S_3 MBrf'^2 + J\frac{\beta_1}{\alpha}\phi'^2 + J\phi'\theta', \qquad (13)$$

where:

$$EG = \frac{\upsilon T_\infty S_g}{b\left(T_w - T_\infty\right)k_\infty}, Br = \frac{\mu u_w^2}{\left(T_w - T_\infty\right)k_\infty}, J = \frac{\bar{R}\left(C_w - C_\infty\right)D_m}{k_f},$$

$$\beta_1 = \frac{C_w - C_\infty}{C_\infty}, \alpha = \frac{T_w - T_\infty}{T_\infty}.$$

The mathematical expression to find the Bejan number is:

$$Bn = \frac{\textit{Entropy formation due to the transfer of mass and heat}}{\textit{The overall generation of entropy}}.$$

Bn can be restated in the following way by using (13):

$$Bn = \frac{\left(S_4 + R_a\right)\alpha\theta'^2 + J\frac{\beta_1}{\alpha}\phi'^2 + J\phi'\theta'}{\left(S_4 + R_a\right)\alpha\theta'^2 + \frac{1}{S_2}Brf''^2 + S_3 MBrf'^2 + J\frac{\beta_1}{\alpha}\phi'^2 + J\phi'\theta'}.$$

3. VALIDATION
We verified our results with previous results under specific conditions (e.g., $We = 0$) and found a satisfactory agreement (see Table 2).

Table 2. Consistency with prior findings for $f''(0)$ and $-\theta'(0)$ to validate our findings

M	$f''(0)$		$-\theta'(0)$	
	Devi and Kumar [55]	Current result	Devi and Kumar [55]	Current result
0	-0.5608	-0.56081123	1.0873	1.08733452
0.1	-0.5659	-0.56590213	1.0863	1.08633192
0.2	-0.5810	-0.58101087	1.0833	1.08337829
0.5	-0.6830	-0.68300657	1.0630	1.06300176
1	-1.0000	-1.00000000	1	1
2	-1.8968	-1.89687214	0.8311	0.83118274
5	-4.9155	-4.91554536	0.4703	0.47030201

4. RESULTS AND DISCUSSION

Equations (7-9) along with (10) are puzzled out with the bvp4c solver. In this study, solutions are rendered for suction and injection cases.

4.1. Velocity profile

As displayed in Fig. 2, the fluid velocity declines as M upsurges. The Lorentz force grows in amplitude in proportion to the strength of the magnetic field. It leads to a greater reduction in the fluid's velocity. The increment in the Ree-Eyring fluid parameter corresponds to a decrement in the fluid's effective viscosity at higher shear rates. This reduction in viscosity lowers the resistance to flow, allowing the fluid to move more freely and resulting in an increase in fluid velocity [see Fig. 3]. The rise in the volume fraction of nanoparticles in a fluid causes to a rise in viscosity, enhanced inertia, increased drag, and potential microstructure formation. These factors collectively increase the resistance to flow, thereby reducing the overall velocity of the fluid [see Fig. 4].
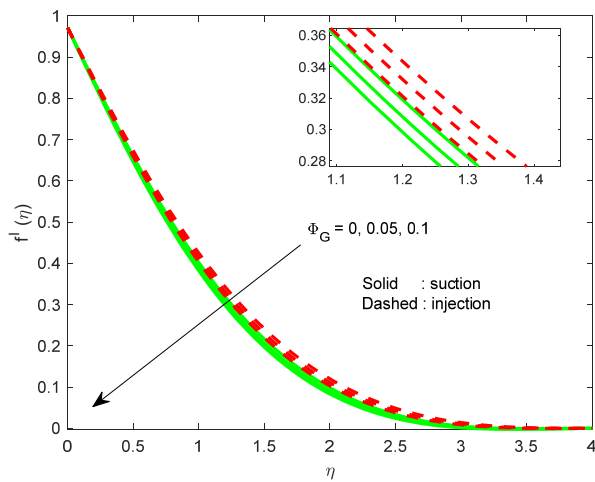
Figure 2. Situation in which $f'(\eta)$ is impacted by ϕ_G
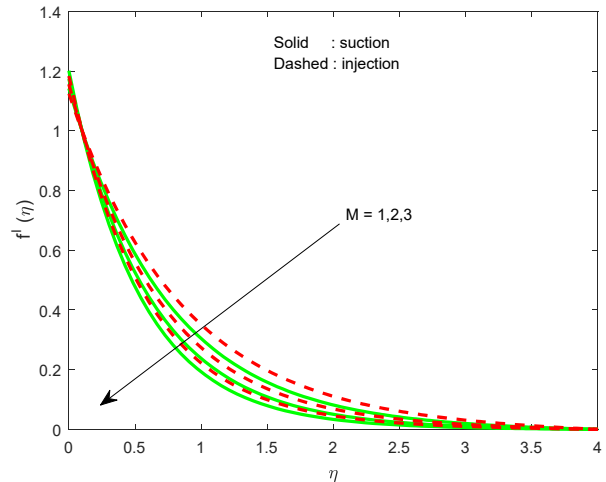
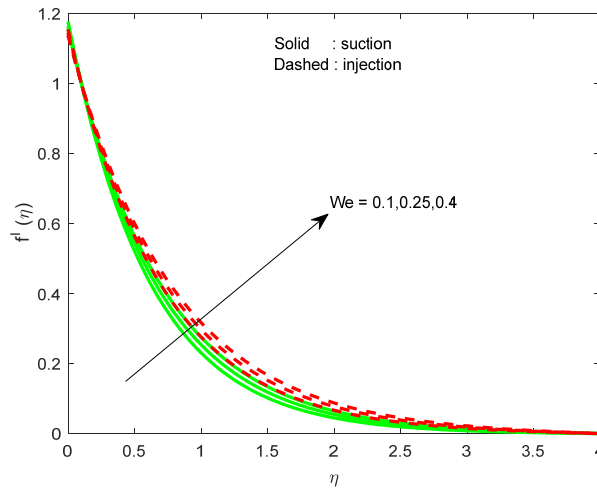**Figure 3.** Situation in which $f'(\eta)$ is impacted by M

Figure 4. Situation in which $f'(\eta)$ is impacted by We

4.2. Temperature profile

A rise in the Eckert number corresponds to a hike in the relative importance of kinetic energy compared to thermal energy. This results in more kinetic energy being converted into heat through viscous dissipation, causes to a rise in the fluid's temperature [see Fig. 5]. A rise in the thermal relaxation parameter causes the fluid to respond more slowly to thermal disturbances, reducing the rate of heat conduction and energy dispersal within the fluid. As a result, there is a reduction in temperature [see Fig. 6]. An increase in the thermal radiation parameter enhances the amount of radiant energy absorbed by the fluid. This absorbed energy raises the internal energy of the fluid, resulting in a higher temperature [see Fig. 7]. The effect is particularly significant in systems where thermal radiation plays a major role in the heat transfer process, such as in high-temperature applications or in fluids with strong radiative properties.
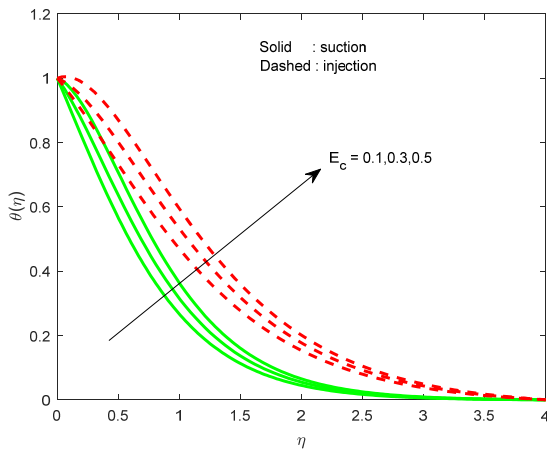
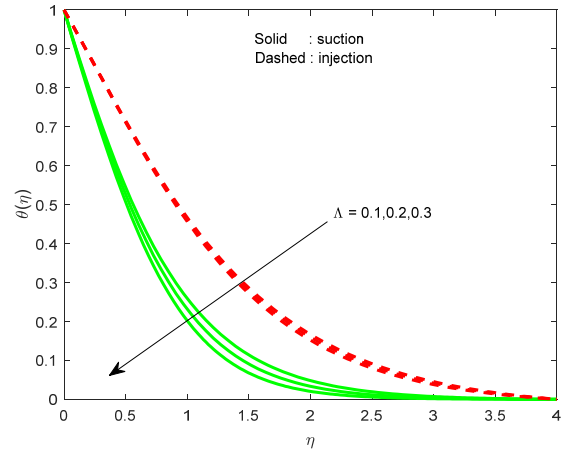**Figure 5.** Situation in which $\theta(\eta)$ is impacted by E_c

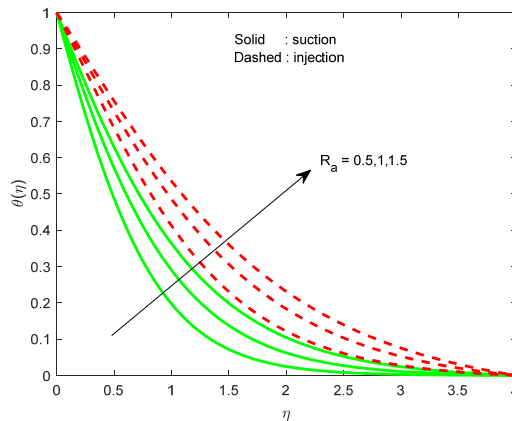**Figure 6.** Situation in which $\theta(\eta)$ is impacted by Λ

Figure 7. Situation in which $\theta(\eta)$ is impacted by R_a

4.3. Concentration profile

Raising the value of Sc causes the fluid's concentration to decline, as can be seen in Fig. 8. An increment in the parameter of chemical reaction accelerates the rate at which reactants are altered into products. This heightened reaction rate leads to a more rapid depletion of the reactants, thereby reducing their concentration in the fluid. The balance between mass transfer and chemical reaction shifts towards greater consumption, resulting in a lower overall concentration of the reactant species in the fluid (see Fig. 9).
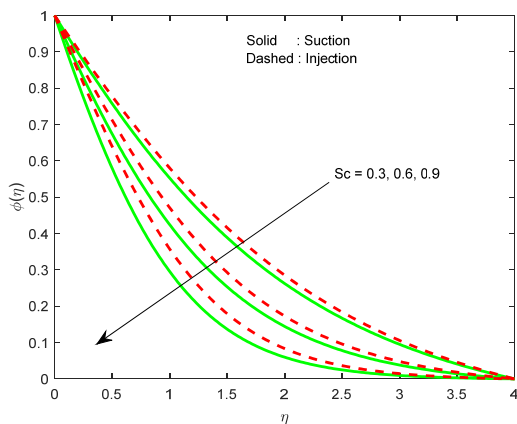

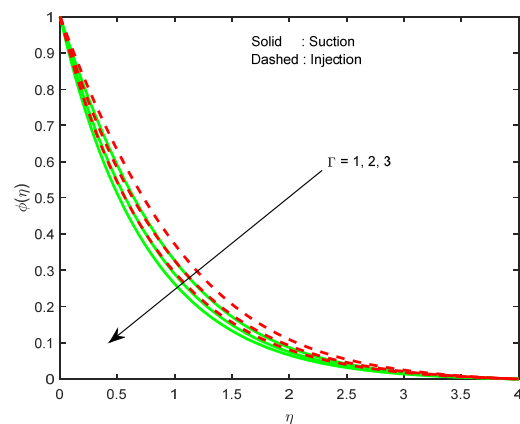**Figure 8.** Situation in which $\phi(\eta)$ is impacted by Sc

Figure 9. Situation in which $\phi(\eta)$ is impacted by Γ

4.4. Engineering quantities of interest

Figs. 10-15 explains the impression of pertinent parameters on heat transmission rate, surface friction drag and mass transmission rate.
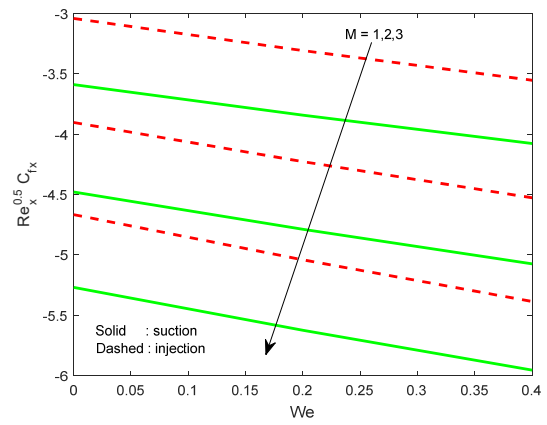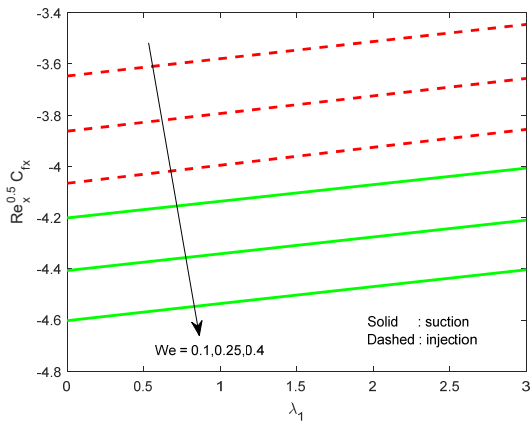
Figure 10. Situation in which friction factor is impacted by We

Figure 11. Situation in which friction factor is impacted by M

It is detected that both Ree-Eyring fluid parameter, magnetic field parameters minimize the surface friction drag (Fig. 10-11). As the Ree-Eyring fluid parameter increases, the fluid exhibits more pronounced shear-thinning behaviour, leading to a reduction in viscosity near the wall where shear rates are high. This reduction in viscosity lowers the wall shear stress, which directly reduces the skin friction coefficient. An increase in the Eckert number enhances viscous dissipation in the fluid, which generates additional heat and reduces the temperature gradient between the heated surface and the fluid. This reduction in the temperature gradient weakens the convective heat transfer, leading to a lower Nusselt number. In essence, the higher the Eckert number, the less efficient the heat transfer becomes, resulting in a reduced Nusselt number (Fig. 12). Rise in thermal relaxation parameter enhances the heat transmission rate as seen in Fig. 13. Furthermore, it is seen that chemical reaction and Schmidt numbers are cooperative to improve mass transmission rate of the fluid (Figs. 14-15).
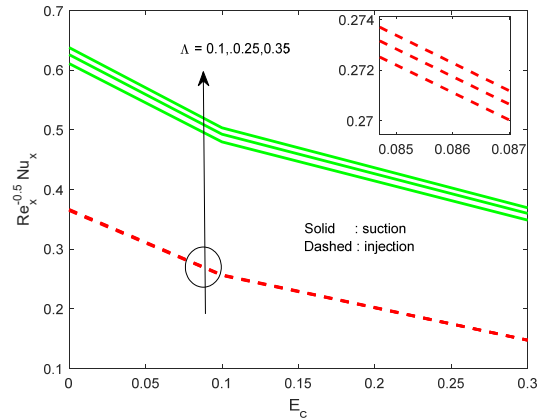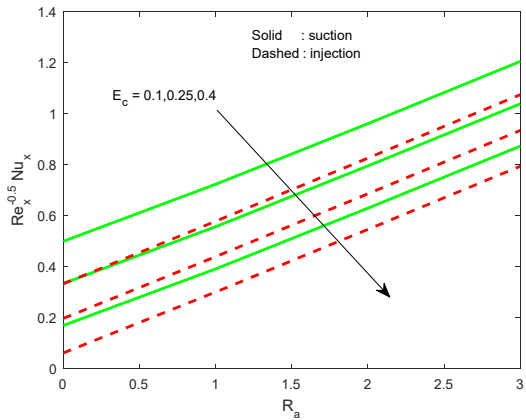

Figure 12. Situation in which Nusselt number is impacted by E_c

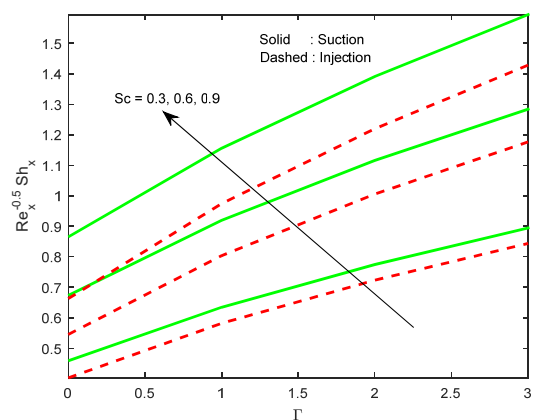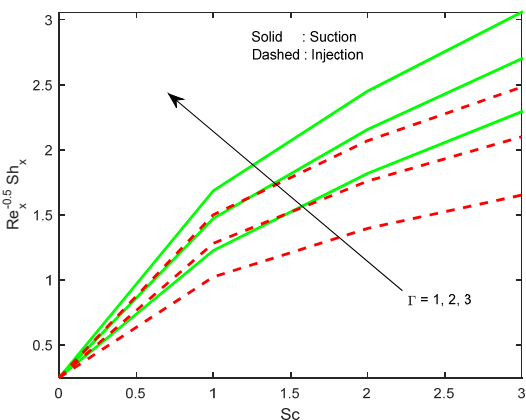**Figure 13.** Situation in which Nusselt number is impacted by Λ

Figure 14. Situation in which Sherwood number is impacted by Γ

Figure 15. Situation in which Sherwood number is impacted by Sc

4.5. Bejan number and other profiles

As the Brinkman number rises, indicating a higher ratio of viscous dissipation to thermal conduction, the internal heat generation in the fluid increases. This results in larger temperature gradients and greater irreversibility in the heat transfer processes, leading to increased entropy generation (see Fig. 16).
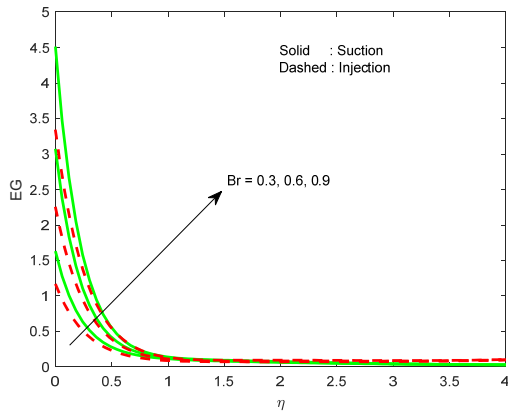

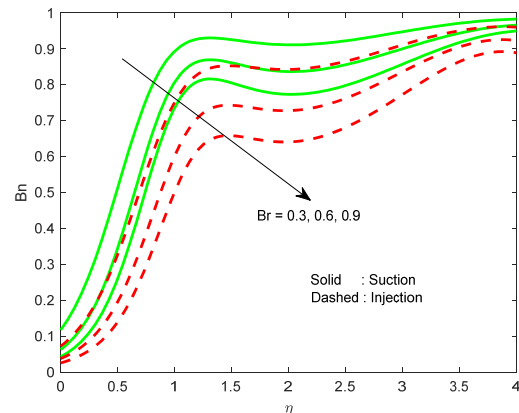**Figure 16.** Situation in which entropy generation is impacted by Br

Figure 17. Situation in which Bejan number is impacted by Br

An increase in the Brinkman number highlights the growing significance of viscous dissipation within the fluid, leading to greater irreversibility associated with fluid flow. This shift in the balance of irreversibility reduces the Bejan number, indicating that viscous dissipation becomes the dominant source of entropy generation in the system, overshadowing the irreversibility due to heat transfer (see Fig. 17). From Figs. 18-19, it is clear that the rise in thermal radiation parameter leads to the escalation in both entropy generation and Bejan number.
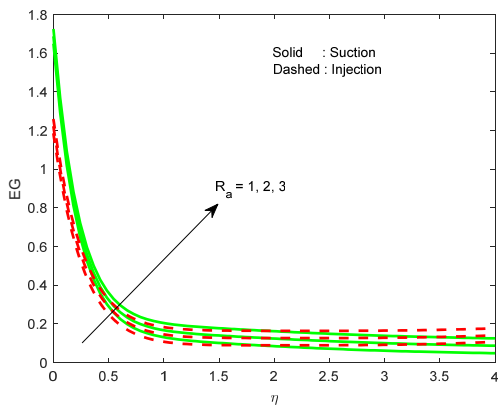

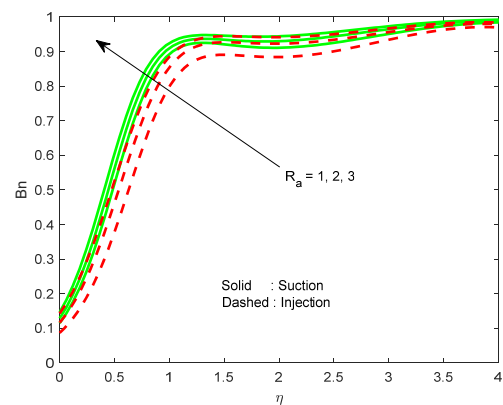**Figure 18.** Situation in which entropy generation is impacted by R_a

Figure 19. Situation in which Bejan number is impacted by R_a

5. CONCLUSIONS

Entropy generation optimization in Ree-Eyring ternary hybrid nanofluid flow across an angled stretched sheet subject to Thompson Troian boundary conditions has been investigated numerically. Careful observations from the numerical results, the following are the main takeaways from this study:

- Ree-Eyring parameter elevates fluid velocity.
- Raise in the slip parameter of velocity leads to the decrement in fluid velocity.
- Eckert number and thermal relaxation parameter exhibited different influences on temperature.
- Concentration profile contracts with bigger chemical reaction parameter.
- Friction factor is bearing a considerable negative connection with We.
- Sherwood number is bearing a significant progressive correlation with Sc, Γ.
- When Br enhances, Viscous dissipation's contribution to overall irreversibility becomes increasingly noticeable. So that Bejan number declines.
- Enhanced thermal radiation parameter causes to the escalation in both entropy generation and Bejan number.

ORCID
ⓘ**Gadamsetty Revathi,** https://orcid.org/0000-0001-9419-2637; ⓘ**D. Purnachandra Rao,** https://orcid.org/0000-0002-3128-8137
ⓘ**S. Ramalingeswara Rao,** https://orcid.org/0000-0002-4445-2637; ⓘ**K.S. Srinivasa Babu,** https://orcid.org/0000-0002-9292-8214
ⓘ**T.R.K.D. Vara Prasad,** https://orcid.org/0000-0001-5935-0230; ⓘ**M. Jayachandra Babu,** https://orcid.org/0000-0001-7645-6301

REFERENCES

[1]   M. Sheikholeslami, and H.B. Rokni, "Simulation of nanofluid heat transfer in presence of magnetic field: a review," International Journal of Heat and Mass Transfer, **115**, 1203-1233 (2017). https://doi.org/10.1016/j.ijheatmasstransfer.2017.08.108

[2]   R.B. Ganvir, P.V. Walke, and V.M. Kriplani, "Heat transfer characteristics in nanofluid—A review," Renewable and sustainable energy reviews, **75**, 451-460 (2017). https://doi.org/10.1016/j.rser.2016.11.010

[3]   G. Revathi, G. Veeram, M.J. Babu, K.S.S. Babu, and A. Suneel Kumar, "Darcy–Forchheimer flow of power-law (Ostwald-de Waele type) nanofluid over an inclined plate with thermal radiation and activation energy: an irreversibility analysis," International Journal of Ambient Energy, **44**(1), 1980–1989 (2023). https://doi.org/10.1080/01430750.2023.2200434

[4]   G. Rasool, A. Shafiq, X. Wang, A.J. Chamkha, and A. Wakif, "Numerical treatment of MHD Al2O3–Cu/engine oil-based nanofluid flow in a Darcy–Forchheimer medium: application of radiative heat and mass transfer laws," International Journal of Modern Physics B, **38**(09), 2450129 (2024). https://doi.org/10.1142/S0217979224501297

[5]   S. Li, M. Faizan, F. Ali, G. Ramasekhar, T. Muhammad, H.A.E.W. Khalifa, and Z. Ahmad, "Modelling and analysis of heat transfer in MHD stagnation point flow of Maxwell nanofluid over a porous rotating disk," Alexandria Engineering Journal, **91**, 237-248 (2024). https://doi.org/10.1016/j.aej.2024.02.002

[6]   J.K. Madhukesh, S.O. Paramesh, G.D. Prasanna, B.C. Prasannakumara, M.I. Khan, S. Abdullaev, and G. Rasool, "Impact of magnetized nanoparticle aggregation over a Riga plate with thermal radiation in water-Al2O3 based nanofluid flow," ZAMM-Journal of Applied Mathematics and Mechanics/Zeitschrift für Angewandte Mathematik und Mechanik, e202300270 (2024). https://doi.org/10.1002/zamm.202300270

[7]   M. Yasir, M. Khan, A.S. Alqahtani, and M.Y. Malik, "Heat generation/absorption effects in thermally radiative mixed convective flow of Zn−TiO2/H2O hybrid nanofluid," Case Studies in Thermal Engineering, **45**, 103000 (2023). https://doi.org/10.1016/j.csite.2023.103000

[8]   Y.B. Kho, R. Jusoh, M.Z. Salleh, M.H. Ariff, and N. Zainuddin, "Magnetohydrodynamics flow of Ag-TiO2 hybrid nanofluid over a permeable wedge with thermal radiation and viscous dissipation," Journal of Magnetism and Magnetic Materials, **565**, 170284 (2023). https://doi.org/10.1016/j.jmmm.2022.170284

[9]   M. Abbas, N. Khan, M.S. Hashmi, and J. Younis, "Numerically analysis of Marangoni convective flow of hybrid nanofluid over an infinite disk with thermophoresis particle deposition," Scientific Reports, **13**(1), 5036 (2023). https://doi.org/10.1038/s41598-023-32011-x

[10] S.A. Khan, M. Imran, H. Waqas, T. Muhammad, S. Yasmin, and A. Alhushaybari, "Numerical analysis of multiple slip effects on CuO/MgO/TiO2-water ternary hybrid nanofluid with thermal and exponential space-based heat source," Tribology International, **197**, 109778 (2024). https://doi.org/10.1016/j.triboint.2024.109778

[11] A. Mishra, and G. Pathak, "A comparative analysis of MoS2-SiO2/H2O hybrid nanofluid and MoS2-SiO2-GO/H2O ternary hybrid nanofluid over an inclined cylinder with heat generation/absorption," Numerical Heat Transfer, Part A: Applications, **85**(16), 2724-2753 (2024). https://doi.org/10.1080/10407782.2023.2228483

[12] Najafpour, K. Hosseinzadeh, J.R. Kermani, A.A. Ranjbar, and D.D. Ganji, "Numerical study on the impact of geometrical parameters and employing ternary hybrid nanofluid on the hydrothermal performance of mini-channel heat sink," Journal of Molecular Liquids, **393**, 123616 (2024). https://doi.org/10.1016/j.molliq.2023.123616

[13] U. Farooq, A. Bibi, J.N. Abbasi, A. Jan, and M. Hussain, "Nonsimilar mixed convection analysis of ternary hybrid nanofluid flow near stagnation point over vertical Riga plate," Multidiscipline Modeling in Materials and Structures, **20**(2), 261-278 (2024). https://doi.org/10.1108/MMMS-09-2023-0301

[14] M. Mahboobtosi, K. Hosseinzadeh, and D.D. Ganji, "Investigating the convective flow of ternary hybrid nanofluids and single nanofluids around a stretched cylinder: Parameter analysis and performance enhancement," International Journal of Thermofluids, **23**, 100752 (2024). https://doi.org/10.1016/j.ijft.2024.100752

[15] D. Mohanty, G. Mahanta, and S. Shaw, "Irreversibility and thermal performance of nonlinear radiative cross-ternary hybrid nanofluid flow about a stretching cylinder with industrial applications," Powder Technology, **433**, 119255 (2024). https://doi.org/10.1016/j.powtec.2023.119255

[16] T. Hayat, S.A. Khan, M.I. Khan, S. Momani, and A. Alsaedi, "Cattaneo-Christov (CC) heat flux model for nanomaterial stagnation point flow of Oldroyd-B fluid," Computer methods and programs in biomedicine, **187**, 105247 (2020). https://doi.org/10.1016/j.cmpb.2019.105247

[17] S. Ahmad, S. Nadeem, N. Muhammad, and M.N. Khan, "Cattaneo–Christov heat flux model for stagnation point flow of micropolar nanofluid toward a nonlinear stretching surface with slip effects," Journal of Thermal Analysis and Calorimetry, 1-13, (2020). https://doi.org/10.1007/s10973-020-09504-2

[18] W. Ibrahim, and G. Gadisa, "Finite element solution of nonlinear convective flow of Oldroyd-B fluid with Cattaneo-Christov heat flux model over nonlinear stretching sheet with heat generation or absorption," Propulsion and Power Research, **9**(3), 304-315 (2020). https://doi.org/10.1016/j.jppr.2020.07.001

[19] M.G. Reddy, M.S. Rani, K.G. Kumar, B.C. Prasannakumar, and H.J. Lokesh, "Hybrid dusty fluid flow through a Cattaneo–Christov heat flux model," Physica A: Statistical Mechanics and its Applications, **551**, 123975 (2020). https://doi.org/10.1016/j.physa.2019.123975

[20] B.J. Gireesha, B.M. Shankaralingappa, B.C. Prasannakumar, and B. Nagaraja, "MHD flow and melting heat transfer of dusty Casson fluid over a stretching sheet with Cattaneo–Christov heat flux model," International Journal of Ambient Energy, **43**(1), 2931-2939 (2020). https://doi.org/10.1080/01430750.2020.1785938

[21] A.R.A. Naqvi, A. Haider, D. Hussain, and S. Hussain, "Finite Element Study of MHD Impacts on the Rotating Flow of Casson Nanofluid with the Double Diffusion Cattaneo—Christov Heat Flux Model," Mathematics, **8**(9), 1555 (2020). https://doi.org/10.3390/math8091555

[22] Tassaddiq, "Impact of Cattaneo-Christov heat flux model on MHD hybrid nano-micropolar fluid flow and heat transfer with viscous and joule dissipation effects," Scientific Reports, **11**(1), 1-14 (2021). https://doi.org/10.1038/s41598-020-77419-x

[23] S. Jakeer, P.B. Reddy, A.M. Rashad, and H.A. Nabwey, "Impact of heated obstacle position on magneto-hybrid nanofluid flow in a lid-driven porous cavity with Cattaneo-Christov heat flux pattern," Alexandria Engineering Journal, **60**(1), 821-835 (2021). https://doi.org/10.1016/j.aej.2020.10.011

[24] Mahesh, S.V.K. Varma, C.S.K. Raju, M.J. Babu, I.L. Animasaun, and N.A. Shah, "Significance of Reynolds number, lower and upper rotating disks on the dynamics of water conveying graphene and silver nanoparticles between rotating disks," Physica Scripta, **96**(4), 045218 (2021). https://doi.org/10.1088/1402-4896/abe2d3

[25] Ali, S. Hussain, Y. Nie, A.K. Hussein, and D. Habib, "Finite element investigation of Dufour and Soret impacts on MHD rotating flow of Oldroyd-B nanofluid over a stretching sheet with double diffusion Cattaneo Christov heat flux model," Powder Technology, **377**, 439-452 (2021). https://doi.org/10.1016/j.powtec.2020.09.008

[26] H. Sharif, M.A. Khadimallah, M.N. Naeem, M. Hussain, S. Hussain, and A. Tounsi, "Flow of MHD Powell-Eyring nanofluid: Heat absorption and Cattaneo-Christov heat flux model," Advances in nano research, **10**(3), 221-234 (2021). https://doi.org/10.12989/anr.2021.10.3.221

[27] S. Ahmad, S. Nadeem, and M.N. Khan, "Mixed convection hybridized micropolar nanofluid with triple stratification and Cattaneo–Christov heat flux model," Physica Scripta, **96**, 075205 (2021). https://doi.org/10.1088/1402-4896/abf615

[28] A. Jafarimoghaddam, M. Turkyilmazoglu, and I. Pop, "Threshold for the generalized Non-Fourier heat flux model: Universal closed form analytic solution," International Communications in Heat and Mass Transfer, **123**, 105204 (2021). https://doi.org/10.1016/j.icheatmasstransfer.2021.105204

[29] Z. Hussain, A. Hussain, M.S. Anwar, and M. Farooq, "Analysis of Cattaneo–Christov heat flux in Jeffery fluid flow with heat source over a stretching cylinder," Journal of Thermal Analysis and Calorimetry, **147**, 3391-3402 (2021). https://doi.org/10.1007/s10973-021-10573-0

[30] A. Bhattacharyya, G.S. Seth, *et al.*, "Simulation of Cattaneo–Christov heat flux on the flow of single and multi-walled carbon nanotubes between two stretchable coaxial rotating disks," Journal of Thermal Analysis and Calorimetry, **139**, 1655–1670 (2020). https://doi.org/10.1007/s10973-019-08644-4

[31] S. Khattak, M. Ahmed, M.N. Abrar, S. Uddin, M. Sagheer, and M. Farooq Javeed, "Numerical simulation of Cattaneo–Christov heat flux model in a porous media past a stretching sheet," Waves in Random and Complex Media, 1-20 (2022). https://doi.org/10.1080/17455030.2022.2030503

[32] R.P. Gowda, R.N. Kumar, R. Kumar, and B.C. Prasannakumara "Three-dimensional coupled flow and heat transfer in non-Newtonian magnetic nanofluid: An application of Cattaneo-Christov heat flux model," Journal of Magnetism and Magnetic Materials, **567**, 170329 (2023). https://doi.org/10.1016/j.jmmm.2022.170329

[33] M.I.U. Rehman, H. Chen, A. Hamid, and K. Guedri, "Analysis of Cattaneo–Christov heat flux and thermal radiation on Darcy–Forchheimer flow of Reiner–Philippoff fluid," International Journal of Modern Physics B, **38**(03), 2450046 (2024). https://doi.org/10.1142/S0217979224500462

[34] S.A. Khan, Y. Nie, and B. Ali, "Multiple slip effects on MHD unsteady viscoelastic nano-fluid flow over a permeable stretching sheet with radiation using the finite element method," SN Applied Sciences, **2**(66), (2020). https://doi.org/10.1007/s42452-019-1831-3

[35] G. Rasool, T. Zhang, A.J. Chamkha, A. Shafiq, I. Tlili, and G. Shahzadi, "Entropy generation and consequences of binary chemical reaction on MHD Darcy–Forchheimer Williamson nanofluid flow over non-linearly stretching surface," Entropy, **22**(1), 18 (2020). https://doi.org/10.3390/e22010018

[36] T. Abbas, S. Rehman, R.A. Shah, M. Idrees, and M. Qayyum, "Analysis of MHD Carreau fluid flow over a stretching permeable sheet with variable viscosity and thermal conductivity," Physica A: Statistical Mechanics and its Applications, **551**, 124225 (2020). https://doi.org/10.1016/j.physa.2020.124225

[37] A.Yasmin, K. Ali, and M. Ashraf, "Study of heat and mass transfer in MHD flow of micropolar fluid over a curved stretching sheet," Scientific reports, **10**(1), 1-11 (2020). https://doi.org/10.1038/s41598-020-61439-8

[38] S.S. Giri, K. Das, and P.K. Kundu, "Homogeneous–heterogeneous reaction mechanism on MHD carbon nanotube flow over a stretching cylinder with prescribed heat flux using differential transform method," Journal of Computational Design and Engineeing, **7**(3), 337-351 (2020). https://doi.org/10.1093/jcde/qwaa028

[39] M. Gayatri, K.J. Reddy, and M.J. Babu, "Slip flow of Carreau fluid over a slendering stretching sheet with viscous dissipation and Joule heating," SN Applied Sciences, **2**(3), 1-11 (2020). https://doi.org/10.1007/s42452-020-2262-x

[40] M.A. Kumar, Y.D. Reddy, V.S. Rao, and B.S. Goud, 'Thermal radiation impact on MHD heat transfer natural convective nano fluid flow over an impulsively started vertical plate," Case Studies in Thermal Engineering, **24**, 100826 (2021). https://doi.org/10.1016/j.csite.2020.100826

[41] N.S. Elgazery, "CPSM Simulation of the Variable Properties' Role in MHD Non-Newtonian Micropolar Nanofluid Flow Over a Stretching Porous Sheet (Flow Filtration)," Arab Journal for Science and Engineering, **46**, 7661–7680 (2021). https://doi.org/10.1007/s13369-021-05489-8

[42] P. Pavar, L. Harikrishna, and M.S. Reddy, "Heat transfer over a stretching porous surface on a steady MHD fluid flow," International Journal of Ambient Energy, **43**(1), 4398-4405 (2022). https://doi.org/10.1080/01430750.2020.1848915

[43] S.M. Abo-Dahab, M.A. Abdelhafez, F. Mebarek-Oudina *et al.*, "MHD Casson nanofluid flow over nonlinearly heated porous medium in presence of extending surface effect with suction/injection," Indian Journal Physics, **95**, 2703–2717 (2021). https://doi.org/10.1007/s12648-020-01923-z

[44] A.M. Megahed, M.G. Reddy, and W. Abbas, "Modeling of MHD fluid flow over an unsteady stretching sheet with thermal radiation, variable fluid properties and heat flux," Mathematics and Computers in Simulation, **185**, 583-593 (2021). https://doi.org/10.1016/j.matcom.2021.01.011

[45] Nagaraja, and B.J. Gireesha, "Exponential space-dependent heat generation impact on MHD convective flow of Casson fluid over a curved stretching sheet with chemical reaction," Journal of Thermal Analysis and Calorimetry, **143**, 4071–4079 (2021). https://doi.org/10.1007/s10973-020-09360-0

[46] A.Hussain, and M.Y. Malik, "MHD nanofluid flow over stretching cylinder with convective boundary conditions and Nield conditions in the presence of gyrotactic swimming microorganism: A biomathematical model," International Communications in Heat and Mass Transfer, **126**, 105425 (2021). https://doi.org/10.1016/j.icheatmasstransfer.2021.105425

[47] K.S.S. Babu, A. Parandhama, and R.B. Vijaya, "Non-linear MHD convective flow of Carreau nanofluid over an exponentially stretching surface with activation energy and viscous dissipation," SN Applied Sciences, **3**(3), 382 (2021). https://doi.org/10.1007/s42452-021-04339-4

[48] H.U. Rasheed, S. Islam, Z.W. Khan, J. Khan, and T. Abbas, "Numerical modeling of unsteady MHD flow of Casson fluid in a vertical surface with chemical reaction and Hall current", Advances in Mechanical Engineering, **14**(3), (2022). https://doi.org/10.1177/16878132221085429

[49] K.S.S. Babu, A. Parandhama, and R.B. Vijaya, "Significance of heat source/sink on the radiative flow of Cross nanofluid across an exponentially stretching surface towards a stagnation point with chemical reaction," Heat Transfer, **51**(4), 2885-2904 (2022). https://doi.org/10.1002/htj.22428

[50] B. Jalili, A.M. Ganji, A. Shateri, P. Jalili, and D.D. Ganji, "Thermal analysis of Non-Newtonian visco-inelastic fluid MHD flow between rotating disks," Case Studies in Thermal Engineering, **49**, 103333 (2023). https://doi.org/10.1016/j.csite.2023.103333

[51] G. Revathi, V.S. Sajja, M.J. Babu, K.S.S. Babu, A.S. Kumar, C.S.K. Raju, and S.J. Yook, "Multiple linear regression analysis on the flow of ternary hybrid nanofluid by a quadratically radiated stretching surface with and second order slip," Waves in Random and Complex Media, 1-18 (2023). https://doi.org/10.1080/17455030.2023.2181645

[52] K. Ahmed, T. Akbar, I. Ahmed, T. Muhammad, and M. Amjad, "Mixed convective MHD flow of Williamson fluid over a nonlinear stretching curved surface with variable thermal conductivity and activation energy," Numerical Heat Transfer, Part A: Applications, **85**(6), 942-957 (2024). https://doi.org/10.1080/10407782.2023.2194689

[53] S. Ahmad, and S. Nadeem, "Flow analysis by Cattaneo–Christov heat flux in the presence of Thomson and Troian slip condition," Applied Nanoscience, **10**(12), 4673-4687 (2020). https://doi.org/10.1007/s13204-020-01267-4

[54] K. Rafique, M.I. Anwar, M. Misiran, I. Khan, and E.S.M. Sherif, "The implicit Keller Box scheme for combined heat and mass transfer of Brinkman-type micropolar nanofluid with Brownian motion and thermophoretic effect over an inclined surface," Applied Sciences, **10**(1), 280 (2019). https://doi.org/10.3390/app10010280

[55] S.P. Anjali Devi, and P. Suriyakumar, "Numerical investigation of mixed convective hydromagnetic nonlinear nanofluid flow past an inclined plate," AIP Conference Proceedings, **1557**(1), 281-285 (2013). https://doi.org/10.1063/1.4823920

ОПТИМІЗАЦІЯ ГЕНЕРАЦІЇ ЕНТРОПІЇ В ПОТРІЙНІЙ ГІБРИДНІЙ НАНОРІДИНІ РІ-ЕЙРІНГА ПО ПРУЖНІЙ ПОВЕРХНІ З НЕ ФУР'Є ТЕПЛОВИМ ПОТОКОМ

Гадамсетті Реваті[a], Д. Пурначандра Рао[b], С. Рамалінгесвара Рао[c], К.С. Шрініваса Бабу[c], Т.Р.К.Д. Вара Прасад[c], М. Джаячандра Бабу[d]

[a]Департамент математики, Інститут інженерії та технології Гокараджу Рангараджу, Бачупаллі, Хайдарабад, Індія
[b]Факультет математики, Інженерний коледж Матрусрі, Саїдабад, Хайдарабад, Телангана, Індія
[c]Департамент EM&H, S.R.K.R. Інженерний коледж, Бхімаварам, Андхра-Прадеш, Індія
[d]Факультет математики Державного коледжу, Раджампета, район Аннамайя, Андхра-Прадеш, Індія

Значення потрійного гібридного потоку нанорідин Ree-Eyring полягає в його потенційному застосуванні в різних областях. Завдяки введенню трьох різних типів наночастинок в базову рідину за допомогою моделі Рі-Айрінга ця інноваційна рідина забезпечує покращену теплопровідність, ефективність теплопередачі та реологічні властивості. Ці характеристики особливо цінні в таких галузях, як охолодження електроніки, сонячні енергетичні системи та теплообмінники, де ефективне керування теплом має вирішальне значення. Крім того, унікальна реологічна поведінка нанофлюїдів Рі-Айрінга може забезпечити переваги в таких процесах, як свердління, зміщення та доставка ліків. У граничних умовах Томпсона-Трояна це дослідження має на меті теоретично проаналізувати двовимірний радіаційний потік потрійної гібридної нанорідини Рі-Айрінга над кутовим листом з тепловим потоком Каттанео-Крістова та параметрами хімічної реакції вищого порядку. Щоб виразити їх як звичайні диференціальні рівняння (ОДУ), рівняння, керовані потоком, зазнають відповідних перетворень подібності. Наступна система вирішується за допомогою підходу bvp4c. Основний висновок цього дослідження полягає в тому, що параметр теплової релаксації зменшує ширину температурного профілю, а швидкість рідини мінімізується шляхом регулювання параметра ковзання. Профіль концентрації мінімізується параметром хімічної реакції, а параметр рідини Рі-Айрінга зростає з тим самим (швидкістю рідини). Крім того, ми виявили, що коефіцієнт шкірного тертя сильно негативно корелює з параметром рідини Рі-Айрінга, позитивно з параметром (термічної) релаксації та значно позитивно корелює з хімічною реакцією через число Нуссельта. Коли число Брінкмана збільшується, число Бежана падає. Крім того, підвищення параметра теплового випромінювання призводить до ескалації як генерації ентропії, так і числа Бежана. Ми помітили гідну згоду, коли перевіряли результати цього розслідування з попередніми наслідками.

Ключові слова: *в'язка дисипація; теплове випромінювання; МГД; не Фур'є тепловий потік; нанофлюїд*

RADIATION EFFECT ON MHD FREE CONVECTIVE FLOW PAST A SEMI-INFINITE POROUS VERTICAL PLATE THROUGH POROUS MEDIUM

Sweety Sharma[a], Kangkan Choudhury[a]*, Harun Al Rashid[b]
aDepartment of Mathematics, University of Science and Technology Meghalaya, India
bDepartment of Mathematics, Bilasipara College, Assam, India
Corresponding Author e-mail: kangkan22@gmail.com

The study of MHD heat and mass transfer dissipative free convective flow past a semi-infinite porous vertical plate through porous medium in presence of thermal radiation is considered. The novelty of the present work is to examine radiation effect (Rosseland Approximation) on the flow transport characteristics. The equations governing the flow of heat and mass transfer are solved by asymptotic series expansion method to evaluate the expressions for velocity, temperature, concentration fields, skin-friction, rate of heat and mass transfer. The influence of various physical parameters on the flow is discussed through graphs and in tabular form. It is found that an increase in radiation parameter to decrease the velocity and temperature. Further, it is seen that the skin -friction at the plate decreased with increasing values of radiation parameter.
Keywords: *Radiation; MHD; Porous medium; Free convection*
PACS: 44.25.+f

1. INTRODUCTION

The motion of fluid due to buoyancy forces is known as free or natural convection that occurs in the region of hot and cold through the method of heat transfer. Heat transfer is a exchange of energy through conduction, convection or radiation from high to low where conduction is through solid materials, convection is through liquids and gases and radiation is through electromagnetic waves. Mass transfer is the net movement of mass from one point to another. MHD refers to electrically conducting motion of fluids and nowadays it plays an important role in the application field of engineering and biomedical sciences.

Many authors contributed some works related to the MHD heat and mass transfer problems. Some of them are Jaluria [1], Javaherdeh et.al [2], Raju et al. [3], etc. The unsteady MHD free convection flow past a vertical plate with thermal diffusion and chemical reactions have been discussed by Hossain et.al [4]. Lavanya [5] analyzed the radiation and chemical reaction effects on a steady laminar forced convection flow of a viscous incompressible electrical conducting fluid over a plate embedded in a porous medium in the presence of heat generation. An exact solution of unsteady MHD free convective mass transfer flow past an infinite inclined plate embedded in a saturated porous medium has been presented by Agarwalla et.al [6]. Chamkha et.al [7] considered the problem of coupled heat and mass transfer by natural convection from a vertical, semi-infinite flat plate embedded in a porous medium. Sharma et.al [8] also considered the Soret and Dufour effects on unsteady MHD mixed convection flow past an infinite radiative vertical porous plate embedded in a porous medium in presence of chemical reaction. The investigation of Dufour effect and radiation effects on unsteady MHD free convection flow past an impulsively started infinite vertical plate with variable temperature and uniform mass diffusion in the presence of transverse applied magnetic field through porous medium is carried out by Prakash et.al [9]. Thermal radiative effects on moving infinite vertical plate in the presence of variable temperature and mass diffusion is considered by Muthucumaraswamy [10]. Ahmed e.al [11] also investigated the effect of thermal diffusion on unsteady free convective flow of an electrically conducting fluid over an infinite vertical oscillating plate immersed in porous medium. Seth et.al [12] investigated the unsteady hydromagnetic natural convection flow with heat and mass transfer of a viscous, incompressible, electrically conducting, chemically reactive and optically thin radiating fluid past an exponentially accelerated moving vertical plate with arbitrary ramped temperature is carried out with Laplace transform technique. The problem of a hydromagnetic convective flow of an electrically incompressible viscous conducting fluid past a uniformly moving vertical porous plate is investigated by Chamuah et.al [13]. An attempt has been made by Ahmed et.al [14] to perform a finite difference analysis to study the effects of the magnetic field, thermal radiation, Reynold's number, chemical reaction and of dissipating heat on the MHD transient dissipative flow past a suddenly started infinite vertical porous plate with ramped wall temperature. Ahmed et .al [15] also studied theoretically a three-dimensional mixed convective mass transfer flow past a semi-infinite vertical plate embedded in a porous medium. To analyze the effects of various parameters such as Soret and Dufour effects, chemical reaction, magnetic field, porosity on the fluid flow and heat and mass transfer of an unsteady Casson fluid flow past a flat plate is considered by Das et.al [16]. Kataria et.al [17] is considered with the study of flow, heat and mass transfer characteristics in the unsteady natural convective magnetohydrodynamics Casson fluid flow past over an oscillating vertical plate. Babu et.al [18] carried out to study the effects radiation and heat sink. Ragunath et.al [19] considered the heat and mass transfer on MHD flow

through porous medium between two vertical plates. The study of the heat and mass transfer on MHD boundary layer flow of a viscous incompressible and radiating fluid over an exponentially stretching sheet is carried out by Devi et.al [20]. Ravikumar et.al [21] investigated the heat and mass transfer effects on MHD flow of viscous incompressible and electrically conducting fluid through a non-homogeneous porous medium in presence of heat source, oscillatory suction velocity is considered. Very recently Mopuri et.al [22] investigated in the presence of a diffusion thermal and coupled magnetic field effect, this manuscript seeks continuous free convective motion by a viscous, incompressible fluid that conducts electrically past a sloping platform via a porous medium. By using perturbation technique, Choudhury et.al [23] investigated the heat and mass transfer in MHD convective flow past an infinite plate, through a porous media in presence of radiation, diffusion-thermo effect, and heat sink.

The main objective of the present work is to investigate the effects of diffusion-thermo and heat sink in MHD free convective flow through a porous media in presence of thermal radiation (Rosseland Approximation). The equations governing the flow, heat and mass transfer are transformed into non-dimensional forms by using some similarity parameters. The perturbation technique is used to solve the non-dimensional governing equations and the results obtained have been discussed through graphs and tables.

2. MATHEMATICAL FORMULATION

The equations which describe the motion of steady, incompressible, viscous, electrically conducting fluid in the existence of a uniform magnetic field in vector form are as:

Equation of continuity:

$$\vec{\nabla} \cdot \vec{q} = 0. \tag{1}$$

Gauss's law of magnetism:

$$\vec{\nabla} \cdot \vec{B} = 0. \tag{2}$$

Ohm's law:

$$\vec{J} = \sigma(\vec{E} + \vec{q} \times \vec{B}). \tag{3}$$

Momentum equation:

$$\rho(\vec{q} \cdot \vec{\nabla})\vec{q} = \rho\vec{g} - \vec{\nabla}p + \vec{J} \times \vec{B} + \mu\nabla^2\vec{q} - \frac{\mu\vec{q}}{K'}. \tag{4}$$

Energy equation

$$\rho C_p(\vec{q} \cdot \vec{\nabla})T = \kappa\nabla^2 T + \varphi + \frac{\vec{J}^2}{\sigma} + \frac{\rho D_M K_T}{C_S}\nabla^2 C + Q'^{(T'-T'_\infty)} - \vec{\nabla} \cdot \vec{q}_r. \tag{5}$$

Species continuity equation:

$$(\vec{q} \cdot \vec{\nabla})C\alpha = D_M\nabla^2 C + \bar{K}c(C_\infty - C). \tag{6}$$

Equation of state:

$$\rho_\infty = \rho[1 + \beta(T - T_\infty) + \bar{\beta}(C - C_\infty)]. \tag{7}$$

All the physical quantities are defined in the list of symbols.

We consider the two-dimensional natural convective flow of viscous, steady, incompressible, and radiating fluid through a porous vertical plate with uniform suction. The investigation is based on the following basic premises:

1. The entire fluid properties excluding the density are constant.
2. The plate is electrically insulated.
3. No external electric field is applied to the system.
4. Fluid motion is parallel to the plate.

We now introduce a Cartesian coordinate system (x', y', z') with x'-axis along the plate in the upward vertical direction, y'-axis normal to the plate directed into the fluid region, and z'-axis along the width of the plate and the induced magnetic field is negligible. A uniform magnetic field $\vec{B}_\circ = (0, B_\circ, 0)$ is applied transversely to the plate, along the y-axis. The fluid is subjected to a constant heat flux at the plate. With usual boundary layer conditions and above assumptions, we have the boundary layer equations as

Continuity Equation

$$\frac{\partial v'}{\partial y'} = 0. \tag{8}$$

MHD Equation

$$v'\frac{\partial u'}{\partial y'} = g\beta(T' - T'_\infty) + g\beta(C' - C'_\infty) + v\frac{\partial^2 u'}{\partial y'^2} - \frac{\sigma B_\circ^2 u'}{\rho} - \frac{vu'}{K'}. \tag{9}$$

Energy Equation

$$\rho C_P v' \frac{\partial T'}{\partial y'} = \kappa \frac{\partial^2 T'}{\partial y'^2} + \mu \left(\frac{\partial u'}{\partial y'}\right)^2 + \sigma B_\circ^2 u'^2 - \frac{\partial q'_r}{\partial y'} - Q'^{(T'-T'\infty)} + \frac{\rho D_M K_T}{C_S} \frac{\partial^2 C'}{\partial y'^2}. \tag{10}$$

Species continuity equation

$$v' \frac{\partial c'}{\partial y'} = D_M \frac{\partial^2 C'}{\partial y'^2} + \bar{K}_C (C'_\infty - C'). \tag{11}$$

The relevant boundary conditions are:

$$y'{=}0: \quad u'{=}U, \ \frac{\partial T'}{\partial y'} = -\frac{q^*}{\kappa}, \ C'{=}C'_w \tag{12}$$

$$y' \to \infty : \ u' \to 0, \ T' \to T'_\infty, \ C' \to C'_\infty \tag{13}$$

Equation (8) yields

$$\text{v'= a constant} = -V_0 (V_0 > 0) . \tag{14}$$

To make the mathematical model normalized, the following non-dimensional parameters are introduced

$$y = \frac{V_0 y'}{\vartheta}, u = \frac{u'}{U}, \theta = \frac{T'-T'_\infty}{\frac{q^* v}{\kappa v_0}}, \emptyset = \frac{C'-C'_\infty}{C'_w - C'_\infty}, Gr = \frac{v^2 g\beta q^*}{\kappa U V_0^3}, E = \frac{\rho U^2 V_0}{q^*}, Pr = \frac{\mu C_P}{\kappa}, K_C = \frac{\bar{K}cv}{V_0^2}, Gm = \frac{g\bar{\beta}(C'_w-C'_\infty)}{UV_0^2},$$

$$Sc = \frac{v}{D_M}, K = \frac{vK'}{UV_0^2}, M = \frac{\sigma B_0^2 v}{\rho V_0^2}, R = \frac{4vI^*}{\rho C_P q^* V_0^2}, Q = \frac{Q'v}{\rho C_P V_0^2}, Du = \frac{D_M K_T V_0 \kappa (C'_w-C'_\infty)}{C_S C_P v^2 q^*}$$

Radiative heat flux under Rosseland Approximation

$$\vec{q}_r = -\frac{4\sigma^*}{3K^*} \vec{\nabla} T^4$$

$$T^4 = (T - T_\infty + T_\infty)^4 = [T_\infty + (T - T_\infty)]^4 = T_\infty^4 + 4T_\infty^3(T - T_\infty) = T_\infty^4 + 4T_\infty^3 T - 4T_\infty^4 = 4T_\infty^3 T - 3T_\infty^4$$

Therefore,

$$\vec{\nabla} \cdot \vec{q}_r = -\frac{4\sigma^*}{3K^*} \nabla^2 T^4 = -\frac{4\sigma^*}{3K^*} 4T_\infty^3 \nabla^2 T$$

$$\frac{\partial q_r^*}{\partial y^*} = -\frac{16\sigma^* T_\infty^3}{3K^*} \nabla^2 T$$

Where σ^* and K^* are respectively the Seltan-Boltzmann constant and the mean absorption coefficient.

In dimensionless form, the governing equations are as follows:

$$\frac{d^2 u}{dy^2} + \frac{du}{dy} - \lambda_1 u = -Gr\theta - Gm\emptyset. \tag{15}$$

$$\frac{d^2 \theta}{dy^2} + \lambda_3 \frac{d\theta}{dy} - \lambda_4 \theta = -\frac{ME_C}{\lambda_2} u^2 - \frac{E_C}{\lambda_2} u'^2 - \frac{DuPr}{\lambda_2} \frac{d^2 \phi}{dy^2}. \tag{16}$$

$$\frac{d^2 \emptyset}{dy^2} + Sc \frac{d\emptyset}{dy} - K_C Sc\emptyset = 0. \tag{17}$$

Where

$$\lambda_1 = M + \frac{1}{K}, \lambda_2 = 1 + \frac{4}{3R}, \lambda_3 = \frac{Pr}{\lambda_2} \text{ and } \lambda_4 = \frac{QPr}{\lambda_2};$$

with boundary conditions

$$y = 0 : u = 1, \frac{d\theta}{dy} = -1, \emptyset = 1, \tag{18}$$

$$y \to \infty : u \to 0, \theta \to 0, \emptyset \to 0. \tag{19}$$

3.   METHOD OF SOLUTION

The solution of (17) under its boundary conditions (18) and (19) is

$$\emptyset(y) = e^{-a_1 y} , \text{ where } a_1 = \frac{Sc + \sqrt{Sc^2 + 4ScKc}}{2}. \tag{20}$$

But the system of equations (15) and (16) are non-linear. Assuming the asymptotic form of the solutions to equations (15) and (16) are as follows:

$$u = u_0(y) + E_C u_1(y) + O(E_C^2), \tag{21}$$

$$\theta = \theta_0(y) + E_C \theta_1(y) + O(E_C^2). \tag{22}$$

Here, E denotes the Eckert number (E<< 1). By substituting equations (21)-(22) into equations (15)-(16) and equating the coefficient values of similar terms while neglecting the terms of $O(E^2)$, the following equations are derived.

$$\frac{d^2u_0}{dy^2} + \frac{du_0}{dy} - \lambda_1 u_0 = -Gr\theta_0 - Gm\emptyset_0, \tag{23}$$

$$\frac{d^2\theta_0}{dy^2} + \lambda_3 \frac{d\theta_0}{dy} - \lambda_4\theta_0 = -A\frac{d^2\emptyset_0}{dy^2}, \tag{24}$$

$$\frac{d^2u_1}{dy^2} + \frac{du_1}{dy} - \lambda_1 u_1 = -Gr\theta_1, \tag{25}$$

$$\frac{d^2\theta_1}{dy^2} + \lambda_3 \frac{d\theta_1}{dy} - \lambda_4\theta_1 = -Bu_0^2 - Cu_0'^2. \tag{26}$$

Subject to the boundary conditions

$$y = 0: u_0 = 1; \theta_0' = -1; u_1 = 0; \theta_1' = 0; \tag{27}$$

$$y \rightarrow \infty: u_0 \rightarrow 0; \theta_0 \rightarrow 0; u_1 \rightarrow 0; \theta_1 \rightarrow 0. \tag{28}$$

The solutions to the equations (23)-(26) under the conditions (27) and (28) are

$$\theta_0 = K_1 e^{-a_2 y} - S_1 e^{-a_1 y} \tag{29}$$

$$u_0 = K_2 e^{-a_3 y} - S_2 e^{-a_2 y} + S_3 e^{-a_1 y} \tag{30}$$

$$\theta_1 = K_3 e^{-a_7 y} - S_4 e^{-2a_3 y} - S_5 e^{-2a_2 y} - S_6 e^{-2a_1 y} + S_7 e^{-a_4 y} + S_8 e^{-a_5 y} - S_9 e^{-a_6 y}, \tag{31}$$

$$u_1 = K_4 e^{-a_8 y} - S_{17} e^{-a_7 y} + S_{18} e^{-2a_3 y} + S_{19} e^{-2a_2 y} + S_{20} e^{-2a_1 y} - S_{21} e^{-a_4 y} - S_{22} e^{-a_5 y} + S_{23} e^{-a_6 y}, \tag{32}$$

where

$$a_2 = \frac{\lambda_3 + \sqrt{\lambda_3^2 + 4\lambda_4}}{2}, a_3 = \frac{1 + \sqrt{1 + 4\lambda_1}}{2}, a_4 = a_3 + a_4,$$

$$a_5 = a_2 + a_1, a_6 = a_1 + a_3,$$

$$K_1 = \frac{1}{-m_2}(1 + S_1 a_1), S_1 = \frac{Aa_1^2}{a_1^2 - \lambda_3 a_1 - \lambda_4}, K_2 = 1 + S_2 - S_3,$$

$$S_2 = \frac{D}{a_2^2 - a_2 - \lambda_1}, S_3 = \frac{E}{a_1^2 - a_1 - \lambda_1}, S_4 = \frac{F}{4a_3^2 - 2a_3\lambda_3 - \lambda_4},$$

$$S_5 = \frac{G}{4a_2^2 - 2a_2\lambda_3 - \lambda_4}, S_6 = \frac{H}{4a_1^2 - 2a_1\lambda_3 - \lambda_4}, S_7 = \frac{I}{a_4^2 - a_4\lambda_3 - \lambda_4},$$

$$S_8 = \frac{J}{a_5^2 - a_5\lambda_3 - \lambda_4}, S_9 = \frac{K}{a_6^2 - a_6\lambda_3 - \lambda_4}, S_{10} = GrK_3, S_{11} = GrS_4,$$

$$S_{12} = GrS_5, S_{13} = GrS_6, S_{14} = GrS_7, S_{15} = GrS_8, S_{16} = GrS_9,$$

$$S_{17} = \frac{S_{10}}{a_7^2 - a_7 - \lambda_1}, S_{18} = \frac{S_{11}}{4a_3^2 - 2a_3 - \lambda_1}, S_{19} = \frac{S_{12}}{4a_2^2 - 2a_2 - \lambda_1},$$

$$S_{20} = \frac{S_{13}}{4a_1^2 - 2a_1 - \lambda_1}, S_{21} = \frac{S_{14}}{a_4^2 - a_4 - \lambda_1}, S_{22} = \frac{S_{15}}{a_5^2 - a_5 - \lambda_1},$$

$$S_{23} = \frac{S_{16}}{a_6^2 - a_6 - \lambda_1}, K_3 = \frac{1}{m_2}(2a_3 S_4 + 2a_2 S_5 + 2a_1 S_6 - a_4 S_7 - a_5 S_8 + a_6 S_9),$$

$$K_4 = S_{17} - S_{18} - S_{19} - S_{20} + S_{21} + S_{22} - S_{23}, D = GrK_1, E = GrS_1 - Gm,$$

$$F = BK_2^2 + Ca_3^2 K_2^2, G = BS_2^2 + Ca_2^2 S_2^2, H = BS_3^2 + Ca_1^2 S_3^2,$$

$$I = 2BK_2 S_2 + 2CK_2 S_2 a_3 a_2, J = 2BS_2 S_3 + 2CS_2 S_3 a_2 a_1, K = 2BS_3 K_2 + 2CS_3 K_2 a_1 a_3.$$

3.1. Skin friction

The coefficient of skin friction is a dimensionless quantity obtained from the shear stress at the wall given by Newton's law of viscosity

$$\vec{\tau}_0 = -\mu\vec{\nabla}u',$$

where τ_0 is the shear stress.

The coefficient of skin friction is given by

$$\tau = -\frac{du}{dy}\big|_{y=0} = -[K_2a_3 + S_2a_2 - S_3a_1 + E_C(-K_4a_8 + S_{17}a_7 - 2S_{18}a_3 - 2S_{19}a_2 - 2S_{20}a_1 + S_{21}a_4 + S_{22}a_5 - S_{23}a_6)]. \quad (33)$$

3.2. Plate temperature

The dimensionless temperature field is given by,

$$\theta(y) = \theta_0(y) + E_C\theta_1(y).$$

The non-dimensional plate temperature is given by,

$$\theta_w = \theta_0(0) + E_C\theta_1(0). \quad (34)$$

3.3. Sherwood number

Sherwood number represents the ratio of the convective mass transfer to the rate of diffusive mass transport. It is a dimensionless quantity obtained from Fick's law of diffusion:

$$\vec{J} = -D_M\vec{\nabla}C',$$

where J is the diffusion flux.

The rate of mass transfer in terms of Sherwood number is given by

$$Sh = \frac{d\phi}{dy}\big|_{y=0} = -a_1. \quad (35)$$

3.4. Nusselt number

The rate of heat transfer in terms of the Nusselt number quantified by Fourier's law of conduction is as follows:

$$\vec{q} = -\kappa\vec{\nabla}T',$$

where $\vec{q}$ is the heat transfer rate.

Nusselt number is defined as

$$\frac{d\theta}{dy}\big|_{y=0} = [-K_1a_2 + S_1a_1 + E_C(-K_3a_7 + 2S_4a_3 + 2S_5a_2 + 2S_6a_1 - S_7a_4 - S_8a_5 + S_9a_6)]. \quad (36)$$

4. RESULTS AND DISCUSSIONS

The diffusion-thermo effect in MHD convective flow past a vertical plate through a porous media in presence of heat sink and thermal radiation have been presented in this work. Computational estimations of velocity, temperature and concentration for a variety of relevant non-dimensional flow parameters have been obtained to establish the physical relevance of the problem and graphically presented in Figures 1-10. In the Table 1, the numerical calculations that depict the effects of the flow parameters on skin friction and rate of heat transfer (at plate temperature) have been tabulated. In this section, the effects of the magnetic field, thermal Grashof number, mass Grashof number, permeability parameter, Schmidt number, Prandtl number, Dufour number, heat sink and radiation parameter are discussed. The default values for the flow parameters as Pr = 0.71, Sc =0.6, R =5, $K_C = 5$, Du =0.10, Gr =10, Gm =5, M =1.5, K =1, E =0.01, Q =5.

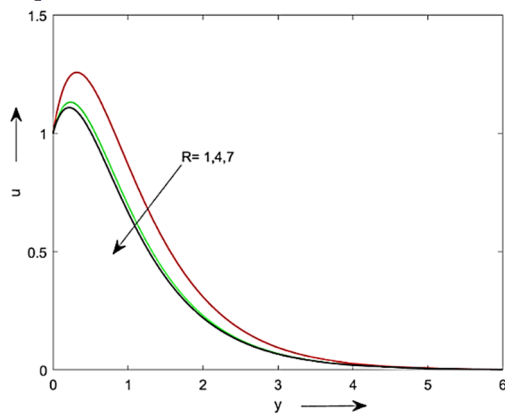**Figure 1.** Velocity profile for variations in R
when Pr = 0.71; Q = 5; Du = 0.1; Sc = 0.6; Kc=1; M = 1.5;
Gr = 10; Gm = 5; E = 0.01; k = 1

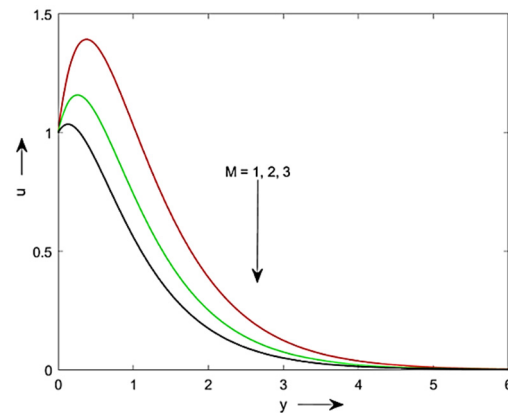**Figure 2.** Velocity profile for variations in M
When Pr = 0.71; R = 1; Q = 5; Du = 0.1; Sc = 0.6; Kc = 1;
Gr = 10; Gm = 5; E = 0.01; k = 1

The effects of radiation parameter R on the fluid velocity indicates by Figure 1. It may be noted to determine the relative importance of thermal energy on the fluid flow, the radiation parameter is used. Thermal energy results in a fall in thermal energy, which then depicts a loss in the fluid of kinetic energy, as a result of which the fluid velocity decreases.

The significance of the application of the magnetic field in a fluid flow display in Figure 2 and from the figure it is observed that as the value magnetic field parameter M increases the fluid velocity declines. This results that when a magnetic field is applied to an electrically conducting fluid, a resistive type of force is generated known as Lorentz force which has the tendency to retard the fluid motion.

Table 1. Skin friction τ at the plate for the values of M = 1.5; Pr = 0.71; Q = 5; Du = 0.1; Sc = 0.6; Kc = 1; Gr = 10; Gm = 5; E = 0.01; k = 1

M	*k*	*R*	*Du*	*τ*
2	1	1	0.1	1.4338
4	1	1	0.1	1.2055
6	1	1	0.1	0.0980
1.5	**1**	1	0.1	1.9428
1.5	**2**	1	0.1	2.5402
1.5	**3**	1	0.1	2.7655
1.5	1	**5**	0.1	1.2370
1.5	1	**10**	0.1	1.1033
1.5	1	**15**	0.1	1.0573
1.5	1	1	**0.1**	1.9428
1.5	1	1	**0.2**	1.0514
1.5	1	1	**0.3**	0.1601

Figure 3 depicts the effects of permeability. Fluid velocity is increased with the increasing values of the permeability parameter. Figure 4 and Figure 5 respectively shows the effects of the thermal Grashof number *Gr* and mass Grashof number *Gm*. The ratio of thermal buoyancy force and viscous hydrodynamic force in the boundary layer is the Thermal Grashof number. The thermal buoyancy force dominates over the viscosity of the fluid as *Gr* increases. Likewise. The mass Grashof number is the relative effect of mass buoyancy force and viscous hydrodynamic force and thus the fluid motion enhances with the increase of *Gm*.
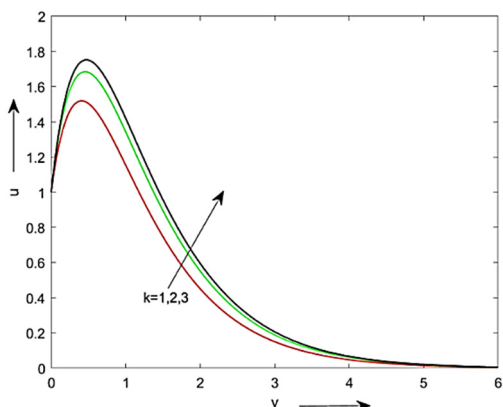

Figure 3. Velocity profile for variations in *k* when Pr = 0.71; R = 1; Q = 5; Du = 0.1; Sc = 0.6; Kc = 1; M = 1.5; Gr = 10; Gm = 5; E = 0.01

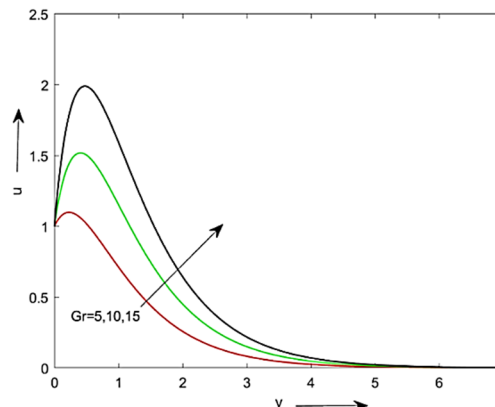**Figure 4.** Velocity profile for variations in *Gr* when Pr = 0.71; R = 1; Q = 5; Du = 0.1; Sc = 0.6; Kc = 1; M = 1.5; E = 0.01; k =1

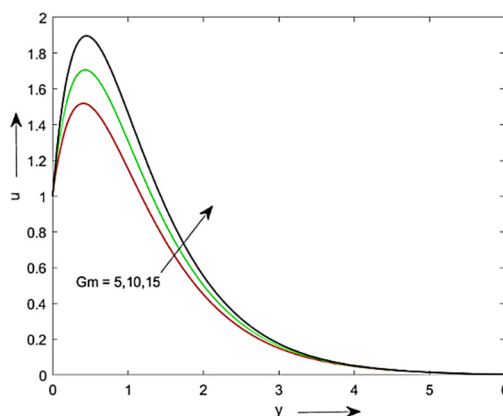**Figure 5.** Velocity profile for variations in *Gm* when Pr = 0.71; R =1; Q =5; Du = 0.1; Sc= 0.6; Kc =1; M = 1.5; Gr = 10; E = 0.01; k = 1

The Figures 6-8 displays the effects of various parameters on temperature. Figure 6 indicates that due to thermal radiation the temperature of the fluid diminishes. This result qualitatively meets the expectations as the effect of radiation is to decrease the rate of energy transport to the fluid, thereby decreasing the temperature of the fluid. A fall in temperature profile occurs with heat absorption which is demonstrated in Figure 7. Figure 8, depicts the Dufour's effect on the temperature profile. It is obvious that the temperature of the fluid falls with the diffusion-thermo effect. All these figures clearly indicates that at the plate, the fluid temperature is maximum.

In Figure 9 and Figure 10 respectively, the variations of concentration in the flow domain due to Schmidt number and permeability parameter are illustrated. Figure 10 displays with the increasing values of Schimdt number diminish the fluid concentration. Schimdt number is the ratio of the momentum diffusivity to the mass diffusivity. So, as Sc increases, the fluid concentration reduces. Figure 11 depicts that it lowers the concentration of the fluid as the porosity of the medium increases.
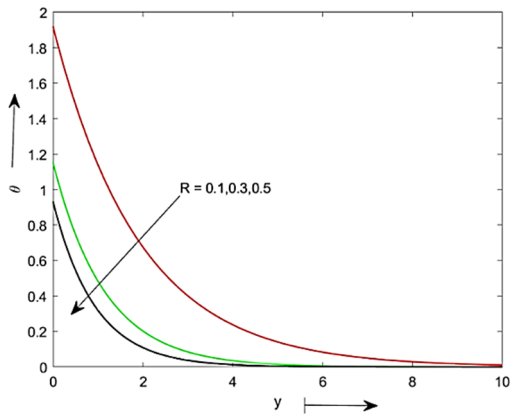

Figure 6. Temperature profile for variations in *R* when Pr = 0.71; Q = 5; Du = 0.1; Sc = 0.6; Kc = 1; M = 1.5; Gr = 10; Gm = 5; E = 0.01; K =1
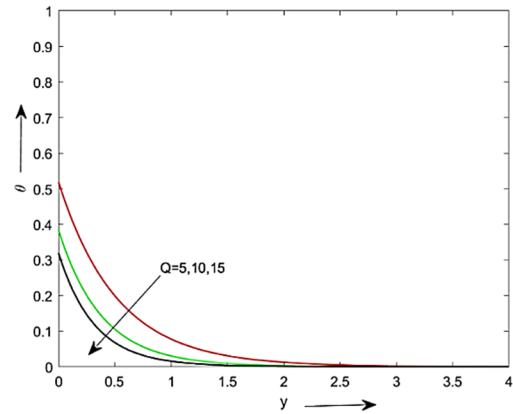
Figure 7. Temperature profile for variations in *Q* when Pr = 0.71; R = 5; Du = 0.1; Sc = 0.6; Kc = 1; M = 1.5; Gr = 10; Gm = 5; E = 0.01; k = 1

Figure 8. Temperature profile in variations *Du* when Pr = 0.71; Q = 5; R = 5; Sc = 0.6; Kc= 1; M = 1.5; Gr = 10; Gm = 5; E = 0.01; k =1

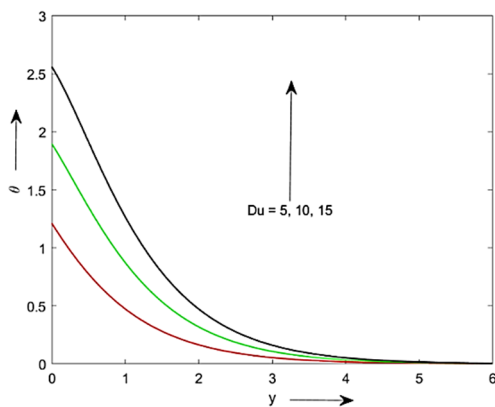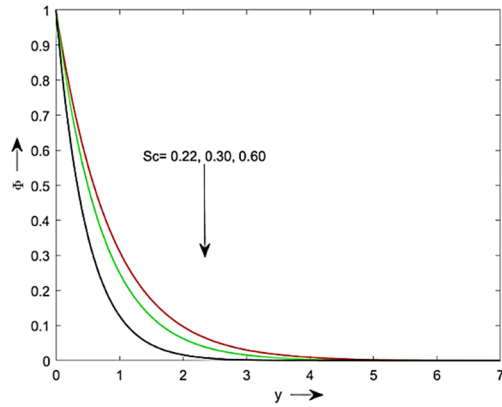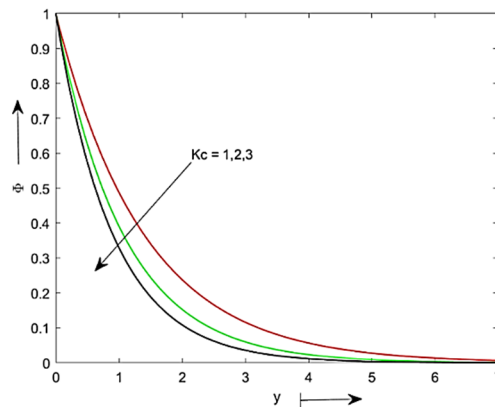**Figure 9.** Concentration profile for variations in Sc when Kc =5

Figure 10. Concentration profile for variations in Kc when Sc = 0.30

Table 1 shows that the change of skin friction coefficient for different values of the parameters. It is seen from the table that skin friction gets decreased in the increasing values of magnetic parameter, radiation and Dufour number. But viscous drag is increased due to the increasing values of permeability parameter.

5. CONCLUSION

The present investigation leads to the following conclusions:

❖ The fluid velocity increases as the Dufour number increases whereas it decreases with thermal radiation and heat sink.
❖ The fluid motion decelerates as the strength of the magnetic field increases whereas it enhances with thermal Grashof number and mass Grashof number.
❖ The temperature of the fluid falls under the influence of Prandtl number, Dufour number, thermal radiation and heat absorption.
❖ The concentration level of the fluid drops with the Schmidt number and permeability of the porous medium.
❖ Skin friction at the plate increases as the Dufour number and heat sink parameter values increases. Viscous drag at the plate was reduced for increasing values of the magnetic parameter.
❖ Plate temperature of the body's surface decreased due to the effect of the Dufour number and Prandtl number.

Nomenclature

$\vec{q}$	fluid velocity (m/s)	$\bar{\beta}$	solutal expansion coefficient ($kmol^{-1}$)
$\vec{J}$	current density (A/m^2)	T_∞	free stream concentration (k)
$\vec{g}$	acceleration vector due to gravity (m/s^2)	C_∞	free stream concentration (kmol)
$\vec{B}$	magnetic flux density vector (Wb/m^2)	B_0	applied magnetic field strength (T)
$\vec{J}^2/\sigma$	energy of ohmic dissipation per unit volume ($A^2\Omega/m^3$)	μ	viscosity coefficient (kg/m s)
p	fluid pressure (N/m^2)	K	porosity parameter
U	velocity of free stream (m/s)	q^*	heat flux (W/m^2)
C_w	plate species concentration (kmol/m^3)	T	fluid temperature (K)
C_∞	free stream concentration (kmol/m^3)	C	concentration (kmol/m^3)
D_M	mass diffusivity (m^2/s)	θ	nondimensional temperature
K_T	thermal diffusion ratio, m(kmol).	$\emptyset$	nondimensional concentration
ρ_∞	fluid density far away from the plate (kg/m^3)	g	acceleration due to gravity
φ	energy viscous dissipation per unit volume (J/m^2S)	E	Eckert number
C_S	concentration susceptibility ($kmol^2 s^2/m^2$)	Pr	Prandtl number
$\vec{q}_r$	radiation heat flux vector (W/m^2)	Q	heat sink parameter
$\overline{K}_C$	first order chemical reaction rate (s^{-1})	Sc	Schmidt number
ρ	fluid density (kg/m^3)	Gr	thermal Grashof number
v	kinematic viscosity (m^2/s)	M	magnetic parameter
κ	thermal conductivity (W/m K)	Gm	solutal Grashof number
κ^*	mean absorption coefficient (m^{-1})	R	radiation parameter
σ	electrical conductivity ($\Omega^{-1}m^{-1}$)	Du	Dufour number
$\vec{E}$	electrical field intensity vector (N/C)	K_C	chemical reaction parameter
β	thermal expression coefficient (k^{-1})		

ORCID

⊙**Sweety Sharma,** https://orcid.org/0009-0001-1119-9698; ⊙**Kangkan Choudhury,** https://orcid.org/0000-0003-2809-8428

REFERENCES

[1] Y. Jaluria, *Natural Convection Heat and Mass Transfer*, (Pergamon, 1980).
[2] K. Javaherdeh, M.M. Nejad, and M. Moslemi, "Natural Convection Heat and Mass Transfer in MHD fluid flow past a moving vertical plate with variable surface temperature and concentration in a process medium," Engineering Science and Technology, an International Journal, **18**(3), 423-431 (2015). https://doi.org/10.1016/j.jestch.2015.03.001
[3] M.C. Raju, and S.V.K. Varma, "Unsteady MHD free convection oscillatory Coutte flow through a porous medium with periodic wall temperature," J. Future Eng. Technol. 6(4), 7-12 (2011). https://doi.org/10.26634/jfet.6.4.1480
[4] M.S. Hossain, N. Samantha, and S.F. Ahmed, "Study of Unsteady MHD free convection flow past a vertical plate with thermal diffusion and chemical reaction," IJPMS, **5**(1), 206-215 (2015).
[5] B. Lavanya, "Radiation and Chemical Reaction Effects on MHD Convective Flow over a Porous Plate through a Porous medium with heat generation," Journal of Advanced Research in Fluid Mechanics and Thermal Sciences, **68**(1), (2020). https://doi.org/10.37934/arfmts.68.1.110
[6] S. Agarwalla, and N. Ahmed, "MHD mass transfer flow past an inclined plate with variable temperature and plate velocity embedded in a porous medium," Heat Transfer, **47**(1), 27-41 (2017). https://doi.org/10.1002/htj.21288
[7] J.A. Chamkha, and A.-R.A. Khaled, "Hydromagnetic combined heat and mass transfer by natural convection from a permeable surface embedded in a fluid satural porous medium," International Journal of Numerical Methods for Heat and amp Fluid Flow, **10**(5), 455-477 (2000). https://doi.org/10.1108/09615530010338097
[8] B.K. Sharma, K. Yadav, N.K. Mishra, and R.C. Chaudhury, "Soret and Dufour Effects on Unsteady MHD Mixed Convection Flow past a Radiative Vertical Porous Plate embedded in a porous medium with Chemical Reaction," Applied Mathematics, **3**(7), (2012). http://dx.doi.org/10.4236/am.2012.37105

[9] J. Prakash, A.G.V. Kumar, D. Bhanumathi, and S.V.K. Varma, "Dufour Effects on Unsteady Hydromagnetic Radiative fluid flow past a vertical plate through porous medium," Open Journal of Fluid Dynamics, **2**(4), 25721 (2012). http://dx.doi.org/10.4236/ojfd.2012.24017

[10] R. Muthucumaraswamy, and S. Kumar, "Heat and Mass Transfer effects on moving vertical plate in the presence of thermal radiation," Theoret. Appl. Mech. **31**(1), 35-46 (2004). https://doi.org/10.2298/TAM0401035M

[11] N. Ahmed, S. Sengupta, and D. Datta, "An exact analysis for MHD free convection mass transfer flow past an oscillatory plate embedded in a porous medium with Soret Effect," Chem. Eng. Commun. **200**, 494-513 (2013). https://doi.org/10.1080/00986445.2012.709474

[12] G.S. Seth, R. Sharma, and B. Kumbhakar, "Heat and Mass Transfer effects on Unsteady MHD Natural Convection Flow of a Chemically Reactive and Radiating Fluid through a porous medium past a moving vertical plate with Arbitrary Ramped Temperature," J. Appl Fluid Mech. **9**(1), 103-117 (2016). https://doi.org/10.18869/acadpub.jafm.68.224.23961

[13] K. Chamuah, and N. Ahmed, "MHD Free Convective dissipative flow past a porous plate in a porous medium in the presence of radiation and thermal diffusion effects," Heat Transfer, **51**, 1964-1981 (2021). https://doi.org/10.1002/htj.22383

[14] N. Ahmed, and M. Dutta, "Natural Convection in transient MHD dissipative flow past a suddenly started infinite vertical porous plate: a finite difference approach," Heat Transfer, **49**(6), 491-508 (2018). https://doi.org/10.1615/HeatTransRes.2018016823

[15] N. Ahmed, and K. Choudhury, "Heat and Mass transfer in three-dimensional flow through a porous medium with periodic permeability," Heat Transfer, **48**(2), 644-662 (2019). https://doi.org/10.1002/htj.21399

[16] M. Das, G. Mahanta, S. Shaw, and S.B. Parida, "Unsteady MHD chemically reactive double-diffusive Casson fluid past a flat plate in porous medium with heat and mass transfer," Heat Transfer, **48**(5), 1761-1777 (2019). https://doi.org/10.1002/htj.21456

[17] R.H. Kataria, and R.H. Patel, "Heat and Mass Transfer in Magnetohydrodynamics (MHD) Casson fluid flow past over an oscillating vertical plate embedded in porous medium with ramped wall temperature," Propulsion and Power Research, **7**(3), 257-267 (2018). https://doi.org/10.1016/j.jppr.2018.07.003

[18] R.P. Babu, A.J. Rao, and S. Sheri, "Radiation Effect on MHD Heat and Mass Transfer Flow over a Shrinking Sheet with Mass Suction," Journal of Applied Fluid Mechanics, **7**(4), 641-650 (2014). https://doi.org/10.36884/jafm.7.04.21389

[19] K. Raghunath, M. Obulesu, and R. Sivaprasad, "Heat and Mass Transfer on an unsteady MHD flow through porous medium between two porous vertical plates," in: *3rd International Conference on Condensed Matter and Applied Physics*, **2220**(1), (2020).

[20] L.V.R. Devi, T. Poornima, B.N. Reddy, and S. Venkataramana, "Radiation and Mass Transfer Effects on MHD Boundary Layer flow due to an Exponentially Stretching Sheet with Heat Source," International Journal of Engineering and Innovative Technology, **3**(8), 33-39 (2014). http://www.ijeit.com/Vol%203/Issue%208/IJEIT1412201402_07.pdf

[21] V. Ravikumar, C.M. Raju, and S.S.G. Raju, "Heat and Mass Transfer Effects on MHD Flow of Viscous Fluid through Non-homogeneous Porous medium in presence of Temperature Dependent Heat Source," Int. J. Contemp. Math. Sciences, **7**(32), 1597-1604 (2012).

[22] O. Mopuri, K. Raghunath, C. Ganteda, R. Srikakulapu, and G. Lorenzini, "MHD Heat and Mass Transfer Steady Flow of a Convective Fluid Through a Porous Plate in the presence of Diffusion Thermo and Aligned Magnetic field," Journal of Advanced Research in Fluid Mechanics and Thermal Sciences, **89**(1), (2022). https://doi.org/10.37934/arfmts.89.1.6276

[23] K. Choudhury, S. Agarwalla, and N. Ahmed, "Diffusion-thermo effect on MHD dissipative flow past a porous vertical platethrough porous media," Heat Transfer, **51**, 6836-6855 (2022). https://doi.org/10.1002/htj.22626

ВПЛИВ ВИПРОМІНЮВАННЯ НА МГД ВІЛЬНИЙ КОНВЕКТИВНИЙ ПОТІК ПОВЗ НАПІВНЕСКІНЧЕННУ ПОРИСТУ ВЕРТИКАЛЬНУ ПЛАСТИНУ ЧЕРЕЗ ПОРИСТЕ СЕРЕДОВИЩЕ

Світі Шарма[a], Кангкан Чоудхурі[a], Харун Аль Рашид[b]
[a]Факультет математики, Університет науки і технологій Мегхалая, Індія
[b]Департамент математики, коледж Біласіпара, Ассам, Індія

Розглянуто дослідження МГД-тепломасообміну дисипативного вільного конвективного обтікання напівнескінченної пористої вертикальної пластини через пористе середовище за наявності теплового випромінювання. Новизна даної роботи полягає в дослідженні впливу випромінювання (наближення Росселанда) на транспортні характеристики потоку. Рівняння, що керують потоком тепло- та масообміну, розв'язуються за допомогою методу розкладання в асимптотичний ряд для оцінки виразів для швидкості, температури, полів концентрації, поверхневого тертя, швидкості тепло- та масообміну. Вплив різних фізичних параметрів на потік обговорюється за допомогою графіків і в табличній формі. Встановлено, що збільшення параметра випромінювання зменшує швидкість і температуру. Далі видно, що шкірне тертя на пластині зменшувалося зі збільшенням значень параметра випромінювання.

Ключові слова: *радіація; МГД; пористе середовище; вільна конвекція*

RADIATIVE EFFECT ON AN UNSTEADY DARCY FORCHHEIMER MHD FLOW OVER A VERTICALLY INCLINED STRETCHING SHEET IN PRESENCE OF POROUS MEDIUM

Ankur Kumar Sarma[a,e]*, Sunmoni Mudoi[a], Palash Nath[b], Pankaj Kalita[c], Gaurab Bardhan[d]

[a]Department of Mathematics, Cotton University, Pan Bazaar, Guwahati-781001, India
[b]Department of Mathematics, Barbhag College, Kalag-781351, India
[c]Department of Mathematics, ADP College, Nagaon-782002, India
[d]Department of Mathematics, Tyagbir Hem Baruah College, Jamugurihat, Sonitpur, 784189, India
[e]Department of Mathematics, Baosi Banikanta Kakati College, Nagaon, Barpeta-781311, India
*Corresponding Author e-mail: ankurkumarsarma44@gmail.com
Received June 1, 2024; revised September 19, 2024; accepted September 29, 2024

This study looks at how radiation and heat move through a two-dimensional, unsteady Darcy-Forchheimer MHD flow that flows across a porous, stretched plate that is vertically inclined and has a transverse magnetic field applied to it. We use the MATLAB bvp4c approach to numerically translate the controlling boundary layer nonlinear PDEs, which are partial differential equations, into a set of nonlinear ODEs, which are ordinary differential equations, using the similarity transformation. We quantitatively assess the velocity and temperature profiles using graphs that represent the problem's various characteristics, including unsteadiness, Prandtl number, magnetic, Grashoff number, radiation parameter, and Eckert number. Tables illustrate the effects on skin friction (τ) and Nusselt number (Nu). The velocity profile decreases as the magnetic and inertial parameters increase, and the temperature profile decreases with the increases in the radiation parameters.

Keywords: *Magnetohydrodynamics (MHD); Radiation; Darcy-Forchheimer; Porous medium; Heat transfer; Unsteady*
PACS: 47.55.P-, 44.25.+f, 44.05.+e, 47.11.-j, 44.20.+b, 47.56.+r

INTRODUCTION

The study of magnetohydrodynamics (MHD) examines how magnetic fields affect the behavior of electrically conducting fluids, such as liquid metal and plasmas. This transdisciplinary area of study examines how fluid motion produces electric currents, which in turn produce magnetic fields that interact with the fluid by fusing concepts from electromagnetism and fluid dynamics. Applications for MHD may be found in geophysics, engineering, and astrophysics. In astrophysics, it explains phenomena like solar flares and star formation. In geophysics, it helps with the understanding of Earth's magnetic field and magnetospheric dynamics. MHD is crucial for researching phenomena ranging from space weather to industrial processes because of its intricate nonlinear equations regulating fluid motion, electric currents, and magnetic fields.

Any substance with holes or pores in it that let liquids through is called a porous media. These materials can be manufactured, like ceramics and foams made for certain uses, or they can be natural, like soils, rocks, and biological tissues. Numerous disciplines, including geology, hydrology, petroleum engineering, environmental science, and biomedical engineering, depend heavily on the study of fluid flow through porous media. The link between the fluid velocity and the pressure gradient inside the porous medium is described by Darcy's law, which controls the behavior of fluids in porous media. Fluid flow characteristics are influenced by variables including porosity (the percentage of empty space in the medium), permeability (a measure of how readily fluids may flow through the medium), and tortuosity (the increase in route length caused by obstructions). Porous media are useful in many different contexts. They have an impact on soil and aquifer contamination transfer as well as groundwater flow in hydrology. Understanding fluid movement through reservoir rocks is essential to petroleum engineering in order to maximize the extraction of oil and gas. Porous scaffolds are utilized in biomedical engineering to enhance cell development and enable waste and nutrition exchange in tissue engineering. Complicated mathematical and numerical simulations are frequently used to model fluid flow in porous media in order to forecast characteristics including fluid distribution, transport phenomena, and filtration procedures. Comprehending and refining these procedures is crucial in addressing pragmatic issues pertaining to resource allocation, environmental restoration, and technological progress.

Fluid motion in a porous material when viscous and inertial effects are important is described by Darcy-Forchheimer flow. In order to account for non-linear flow behavior at higher velocities or through extremely porous materials, it adds a term to Darcy's law. The resistance resulting from inertial forces is represented by the Forchheimer term in this model, and it becomes dominant as fluid velocities rise or the porosity of the porous medium increases. This phrase usually contains coefficients pertaining to the fluid density and viscosity, as well as the permeability and porosity of the medium. In order to represent fluid flow in porous tissues or scaffolds, Darcy-Forchheimer equations are used in a variety of domains, including groundwater hydrology, petroleum reservoir engineering, filtration processes, and biomedical engineering. Comprehending Darcy-Forchheimer flow is essential for precise fluid dynamics prediction and process optimization when fluid flow through porous media is important.

The flow field resulting from a continuous surface flowing at a constant speed was established by Saikiadis [1]. He [2] then examined the flow of fluid across a continuous, flat surface. Crane [3] examined the flow and heat transmission across a stretched sheet of an electrically conducting viscous fluid's boundary layer. Boundary-layer equations for flow driven exclusively by a stretched surface were introduced and studied by Banks [4]. Numerous scientists study radiation and transverse magnetic field effects, realizing the benefits of using MHD to solve a wide range of technical issues and natural phenomena. Wang [5] then looked at the flow that an expanded flat surface produced in three dimensions. A perfect similarity solution was discovered via the Navier-Stokes equations. The fluid motion arising from the expansion of a flat surface was represented in three dimensions by the solution. Viscoelastic fluid flow over a stretched sheet in the presence of a transverse magnetic field was investigated by Andersson [6]. Viscoelasticity is shown to affect flow in a manner akin to that of an external magnetic field by providing an accurate analytical solution to the governing non-linear boundary layer equation. Elbashbeshy [7] investigated how injection and suction affected heat transport across a stretched surface with a constant and fluctuating surface heat flux. Furthermore, in the presence of suction, Siri et al. [8] investigated heat transfer across a continuous stretched surface. Researchers Andersson et al. [9] looked at how a horizontal sheet affected the heat transmission in a liquid film. Researchers Raptis et al. [10], Ghaly [11], Ishak et al. [12], and a few others evaluated the effect of heat radiation on MHD flow problems using a stretched sheet. Ariel [13] investigated the effects of axisymmetric stretching on boundary layer flows using the Homotopy perturbation method. The behavior of an incompressible fluid passing through a stretched surface in an unstable boundary layer with a heat source present was studied by Elbashbeshy et al. [14]. The increasing velocity associated with the surface and the time dependency of the heat flux lead to the instability of the temperature and flow fields. The mobility of the boundary layer and heat transfer across an extended plate with variable thermal conductivity were examined by Ahmad et al. [15]. Heat transmission via a stretched plate in combination with unstable MHD laminar flow was also studied by Ishak et al. [16]. Expanding on Ishak's work, Jhankal et al. [17] studied the stretched plate in the presence of a porous material. Research on the issue of unstable viscous flow on a curved surface was done by Natalia Rosca et al. [18]. In order to account for a transverse magnetic field of constant intensity, Choudhary et al. [19] conducted a theoretical study to explain a 2-dimensional unsteady flow over a stretched permeable surface of a viscous, incompressible electrically conducting fluid. Alarifi et al. [20] looked at the source influence as well as the MHD flow across a vertically extending sheet. When thermal radiation, fluctuating heat flow, and porous media are present, the MHD fluid movement generated by a stretched sheet that is not constant is examined by Megahed et al. [21]. The effects of a porous media on the flow of MHD heat transfer fluid across a stretched cylinder were examined by Reddy et al. [22]. The effect of thermal radiation on convective heat transport in Carreau fluid was examined by Shah et al. [23].

Rasool et al. [24] used the Darcy-Forchheimer relationship to investigate the Casson-type MHD nanofluid flow that occurred on a nonlinear stretching surface. Patil et al. [25] did a study on unstable mixed convection over an exponentially stretched surface. They looked at the effects of cross diffusion and the Darcy-Forchheimer porous medium. Al-Kouz et al. [26] explored MHD Darcy-Forchheimer nanofluid flow and entropy optimization in an atypically shaped container filled with MWCNT-Fe3O4/water. They did this by using Galerkin finite element analysis. Mandal et al. [27] studied the steady two-dimensional laminar mixed convective flow, heat transfer, and mass transfer for a Newtonian fluid that conducts electricity but not very well on an isothermal stretched semi-infinite inclined plate in a Darcy porous medium. Recent years have seen a number of researchers [28-30] focusing their attention on the investigation of Darcy-Forchheimer MHD flow with a variety of flow effects.

The work by Ishak at al. [16] is generalised in this paper. We have examined the problem of 2D, laminar flow that is unstable when radiation and a transverse magnetic field occur across a vertically inclined porous stretching plate in a Darcy Forchheimer MHD flow.

MATHEMATICAL FORMULATION

We investigate the flow of a porous vertically stretched plate inclined at an angle α with the vertical across an unstable, laminar, 2D MHD boundary layer flow in the presence of heat radiation. It's a viscous incompressible fluid that conducts electricity. The Hall effect and the polarization of charges are neglected. Externally applied transverse magnetic field B_0 is perpendicular to the x-axis in the positive direction of the y-axis. While the x-axis is parallel to the stretching plate, the y-axis is normal to it. The origin is held fixed as the surface is extended along the x-axis with a velocity of $U_w = \frac{ax}{1-ct}$. The problem is formulated in presence of radiation and Joule's heating [24] effect which has been incorporated in the energy equation (3). The graphical representation of the problem is depicted in Figure 1.

Under these conditions and Boussinesq's approximation, the governing continuity, momentum and energy equations [16][29] are:

$$\frac{\partial u}{\partial x} + \frac{\partial v}{\partial y} = 0, \tag{1}$$

$$\frac{\partial u}{\partial t} + u\frac{\partial u}{\partial x} + v\frac{\partial u}{\partial y} = \nu\frac{\partial^2 u}{\partial y^2} - \frac{\sigma_e B_0^2 u}{\rho} + g\beta(T - T_\infty)\cos\alpha - \frac{\nu u}{k} - \frac{k'}{\sqrt{k}}u^2, \tag{2}$$

$$\frac{\partial T}{\partial t} + u\frac{\partial T}{\partial x} + v\frac{\partial T}{\partial y} = \frac{\kappa}{\rho C_p}\frac{\partial^2 T}{\partial y^2} + \frac{\sigma_e B_0^2 u^2}{\rho C_p} - \frac{1}{\rho C_p}\frac{\partial q_r}{\partial y}. \tag{3}$$

by virtue of boundary conditions [16] given by:

$$y = 0: \quad u = U_w, \quad v = 0, \quad T = T_w, \quad \text{and}$$

$$y \to \infty: \quad u \to 0, \quad T \to T_\infty, \tag{4}$$

q_r [12][30] is expressed as follows

$$q_r = -\frac{4\sigma_1}{3k_1}\frac{\partial T^4}{\partial y}, \tag{5}$$

where α indicates Stefan-Boltzmann constant, k_1 represents Rosseland mean absorption coefficient.
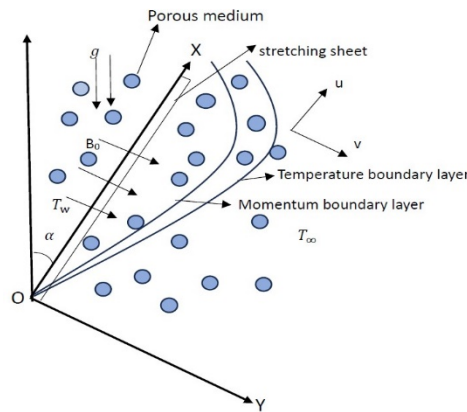

Figure 1. Graphical representation of the problem

Assuming that the difference in internal flow temperature is appropriately small, T^4 may be represented by the Taylor series around T_∞, omitting the components of higher order.

$$T^4 = 4T_\infty^3 T - 3T_\infty^4. \tag{6}$$

We consider the extending velocity $U_w(x,t)$ and surface temperature $T_w(x,t)$ are as follows:

$$U_w = \frac{ax}{1-ct}, \quad T_w = T_\infty + \frac{bx}{1-ct}. \tag{7}$$

Continuity equation (1) is fulfilled, by using a stream function ψ such that $u = \frac{\partial \psi}{\partial y}$ and $v = -\frac{\partial \psi}{\partial x}$.

The given nonlinear PDEs (2)- (3) are transformed to a set of nonlinear ODEs using following similarity variables and nondimensional quantities given as follows:

$$\eta = \left(\frac{a}{v(1-ct)}\right)^{\frac{1}{2}} y, \quad \psi = \left(\frac{avx^2}{(1-ct)}\right)^{\frac{1}{2}} f(\eta), \quad \theta(\eta) = \frac{T-T_\infty}{T_w-T_\infty}, \quad A = \frac{c}{a}.$$

$$M = \frac{\sigma_e B_0^2(1-ct)}{\rho a}, \quad S_p = \frac{v(1-ct)}{ka}, \quad Ec = \frac{U_w^2}{C_p(T_w-T_\infty)}, \quad F = \frac{k'}{\sqrt{k}},$$

$$N = \frac{\kappa k_1}{4\sigma_1 T_\infty^3}, \quad \lambda = \frac{4+3N}{3N}, \quad Pr = \frac{\mu C_p}{\kappa}, \quad Gr = \frac{g\beta(1-ct)^2(T_w-T_\infty)}{a^2 x}.$$

The transformed nonlinear ODEs are:

$$f''' + ff'' - (F+1)f'^2 - (M+S_p)f' - A\left(f' + \frac{1}{2}\eta f''\right) + Gr\theta\cos\alpha = 0, \tag{8}$$

$$\frac{\lambda}{Pr}\theta'' + MEcf'^2 + f\theta' - \theta f' - A(\theta + \frac{1}{2}\eta\theta') = 0. \tag{9}$$

Also, the transformed initial and boundary conditions are:

$$f(0) = 0, \quad f'(0) = 1, \quad \theta(0) = 1 \text{ and}$$

$$f'(\infty) \to 0, \quad \theta(\infty) \to 0. \tag{10}$$

METHOD OF SOLUTION

Equations (1) to (3) with boundary conditions (4) are converted into non-dimensional equations (8) and (9) with boundary conditions (10) by applying the dimensionless quantities. MATLAB's bvp4c technique is then used to solve those equations. To apply finite difference-based solver bvp4c the equations (8), (9) and (10) are transformed respectively as follows:

$$f = y_1, f' = y_1' = y_2, f'' = y_2' = y_3, \theta = y_4, \theta' = y_4' = y_5, \tag{11}$$

$$y_3' = -y_1 y_3 + (F + 1)y_2^2 + M y_2 + S_p y_2 + A\left(y_2 + \frac{1}{2}\eta y_3\right) - Gr y_4 \cos\alpha, \tag{12}$$

$$y_5' = \frac{Pr}{\lambda}[-MEc y_2^2 - y_1 y_5 + y_4 y_2 + A(y_4 + \frac{1}{2}\eta y_5)]. \tag{13}$$

Also, the initial and boundary conditions (10) are transformed as follows:

$$y_1(0) = 0, \quad y_2(0) = 1, \quad y_4(0) = 1, \tag{14}$$

$$y_2(\infty) = 0, \quad y_4(\infty) = 0. \tag{15}$$

The above transformed results are used by the MATLAB solver bvp4c to perform the numerical computation.

RESULTS AND DISCUSSION

The aforementioned factors are taken into account when solving the problem numerically, and the results are displayed in graphs in Figures 2 to 13 for various parameters, such as the unsteadiness parameter (A), radiation parameter (N), Grashoff number (Gr) owing to heat transfer, angle of inclination (α), Eckert number (Ec), Hartmann number (M), Prandtl number (Pr), inertial parameter (F) and Porosity parameter (S_p). Table 1 depicts the effects of the various parameters on Skin friction and Nusselt number.

Figures 2, 3, 4, 5, 6 and 7 show the variation in the velocity profile for different values of A, M, S_P, F, Gr and α, respectively, while the other parameters remain unchanged. As can be seen, the velocity profile constantly rises as Gr increases and decreases as A, M, S_P, F and α increases.
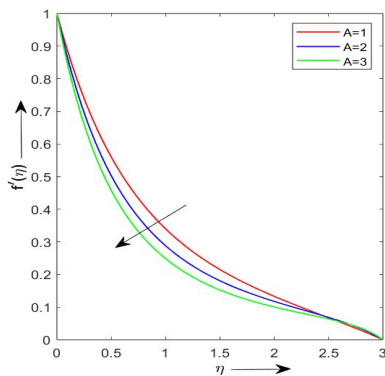

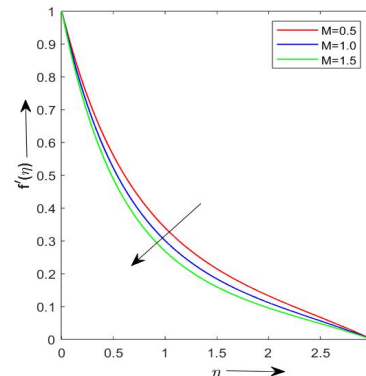
Figure 2. Velocity profile vs A
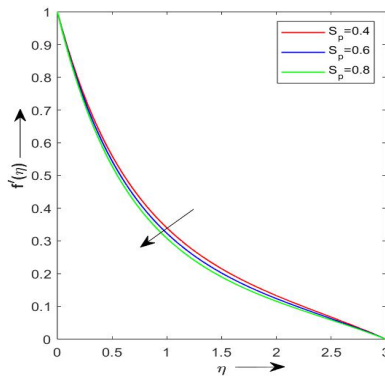

Figure 3. Velocity profile vs M

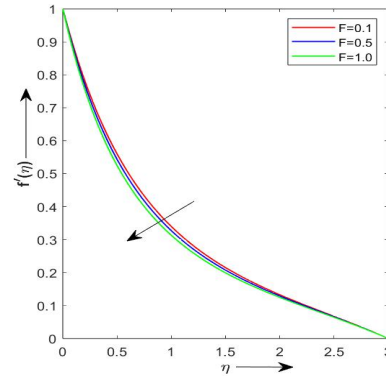**Figure 4.** Velocity profile vs S_P

Figure 5. Velocity profile vs F

From Fig. 2 it can be noticed that the velocity profile decreases with the rise in unsteadiness parameter because the parameter reflects the temporal changes in the flow. High unsteadiness implies rapid fluctuations in the flow's velocity over time, which tends to reduce the average velocity. These fluctuations cause increased energy dissipation and mixing, leading to a reduction in the momentum of the flow. This results in a flattened velocity profile, with lower peak velocities

and a more uniform distribution across the flow's cross-section. Fig. 3 depicts that when the magnetic parameter increases, the velocity profile in a conductive fluid decreases due to the Lorentz force. This force opposes the fluid motion and generates a magnetic drag, which resists the fluid's flow. As the magnetic parameter rises, the Lorentz force becomes stronger, enhancing the drag effect. This suppresses the fluid's momentum and slows down the flow, leading to a reduction in the overall velocity profile. Additionally, the interaction between the magnetic field and the electric currents within the fluid can increase the viscous dissipation, further decreasing the velocity. Fig. 4 shows that the velocity profile decreases with a rise in the porosity parameter because increased porosity enhances the resistance to fluid flow through a porous medium. Higher porosity reduces the effective area available for fluid to pass, increasing frictional resistance and drag forces within the medium. This results in greater energy dissipation and slower fluid movement. Consequently, as the porosity parameter rises, the ability of the fluid to maintain its momentum diminishes, leading to a reduction in the overall velocity profile through the porous structure. The increased resistance also disrupts the fluid's streamline, causing a more pronounced decline in velocity. Fig. 5 depicts that the velocity profile decreases with a rise in the inertial parameter because this parameter represents the ratio of inertial forces to viscous forces in fluid flow. As the inertial parameter increases, the influence of inertial forces becomes more significant relative to viscous forces. This leads to greater momentum diffusion and turbulence, which disrupts the orderly flow and reduces the fluid's velocity. Higher inertial forces also cause more resistance against the fluid's motion, contributing to a flattening and lowering of the velocity profile. The flow's instability and increased energy dissipation further contribute to the decreased velocity as the inertial parameter rises. Fig. 6 shows that the velocity profile increases with a rise in the Grashof number due to heat transfer because the Grashof number quantifies the buoyancy forces relative to viscous forces in a fluid. Higher Grashof numbers signify stronger buoyancy forces resulting from thermal gradients. This increase in buoyancy force enhances natural convection, driving the fluid more vigorously. The intensified buoyancy-driven flow contributes to higher velocities as warmer, less dense fluid rises, and cooler, denser fluid sinks. This promotes increased movement and momentum in the fluid, steepening the velocity profile and resulting in faster overall flow, especially in regions where buoyancy forces dominate over viscous resistance. Fig. 7 depicts that with the rise in α the fluid's velocity decreases. The velocity profile decreases with a rise in the angle of inclination because the gravitational component along the inclined surface increases, which opposes the fluid flow. As the angle of inclination increases, gravity acts more strongly against the direction of the flow, creating additional resistance and reducing the fluid's momentum. This leads to a decrease in velocity, as the fluid must work harder against the gravitational pull. Moreover, the increased gravitational component enhances the vertical stratification of the fluid, leading to more pronounced variations in the velocity profile and further flattening or lowering the average velocity across the inclined plane.
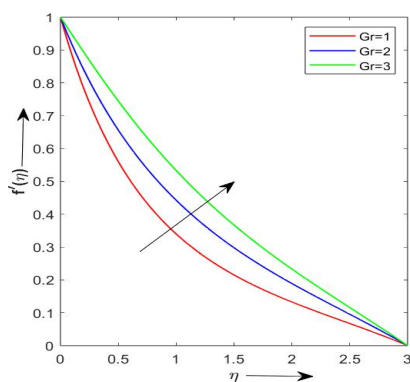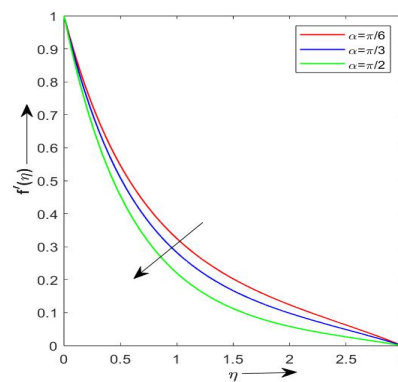

Figure 6. Velocity profile vs Gr   **Figure 7.** Velocity profile vs α

Figures 8, 9, 10, 11, 12 and 13 shows the variation in the temperature profile for different values of A, M, Pr, Ec, N and Gr, respectively, while the other parameters remain unchanged. As it can be seen that the temperature profile rises as M and Ec increases and decreases as A, Pr, N and Gr increases. Fig. 8 depicts that the temperature profile decreases with the unsteadiness parameter because this parameter reflects temporal variations in the heat transfer within the fluid. As unsteadiness increases, the temperature field fluctuates more rapidly, leading to enhanced mixing and diffusion of thermal energy. These fluctuations disrupt the temperature gradients, causing the heat to spread more uniformly throughout the fluid. This results in a more uniform and lower average temperature profile, as the thermal energy is distributed more evenly over time. Additionally, rapid changes in the flow's velocity and temperature can increase convective heat transfer, further contributing to the overall decrease in the temperature profile. Fig. 9 shows that the temperature profile increases with the magnetic parameter because the Lorentz force induced by the magnetic field slows down the fluid's motion, reducing convective heat transfer. This deceleration diminishes the ability of the fluid to carry heat away from the heated region efficiently. As a result, heat accumulates near the heat source, leading to higher temperatures in that area. Additionally, the magnetic field can induce Joule heating, where electrical currents generated by the magnetic field increase the internal energy of the fluid. This combined effect of reduced convective cooling and additional heating results in a rise in the temperature profile as the magnetic parameter increases. The temperature curve and Pr's influence are displayed in Fig. 10. As Pr increases, temperature is seen to drop, indicating a relationship between velocity and thermal

boundary layer thickness. It is believed that large values of Pr suggest a thermal diffusivity preponderance and, consequently, a smaller thermal boundary layer than a velocity boundary layer. As the surface distance grows, the temperature in the zone of unrestricted stream flow actually drops and asymptotically approaches zero. Fig. 11 shows the effect of Ec on temperature. When the fluid's temperature rises, the fluid's enthalpy decreases and its kinetic energy increases, as indicated by the rising Eckert number.
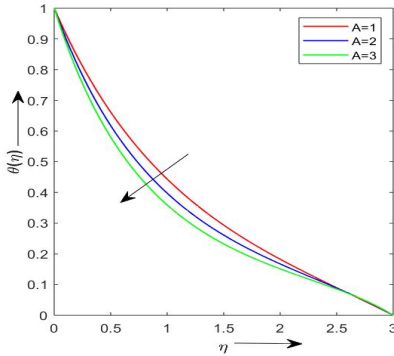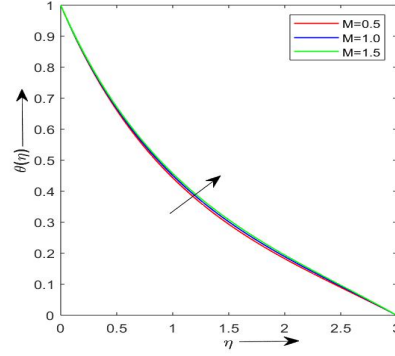

Figure 8. Temperature profile vs A
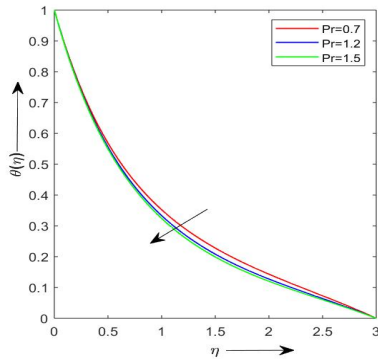

Figure 9. Temperature profile vs M

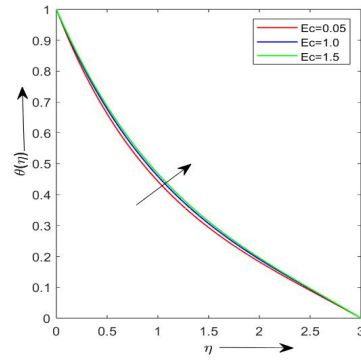**Figure 10.** Temperature profile vs Pr

Figure 11. Temperature profile vs Ec

Fig. 12 shows how radiation affects temperature profiles. It may be observed that as N grows, the fluid's temperature drops. This is due to the fact that rising N denotes rising radiation in the thermal boundary surface where temperature description declines. Fig. 13 shows the alteration of the temperature profile with respect to the change in Gr. It is clear that the fluid's temperature decreases as Gr values rise. As the Grashof number (Gr) increases in natural convection, buoyancy forces become stronger relative to viscous forces. This results in more vigorous fluid motion and enhanced convective heat transfer. The increased fluid movement facilitates more efficient mixing of temperature within the fluid. Consequently, the temperature gradient decreases because heat is distributed more evenly throughout the fluid volume. Near the heated surface, temperatures may still be higher due to direct heat input, but as Gr increases, the overall temperature profile becomes smoother with less steep variations. This phenomenon reflects the improved thermal homogenization and heat transfer efficiency characteristic of higher Grashof numbers in natural convection systems.
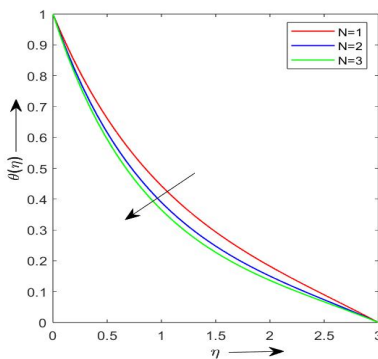
Figure 12. Temperature profile vs N

Figure 13. Temperature profile vs Gr
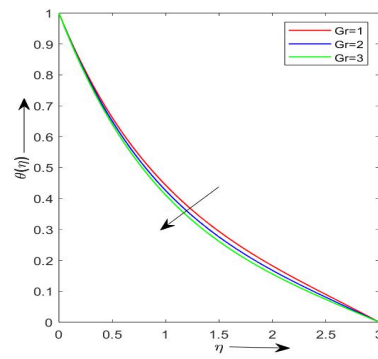
The effects of various parameters on the Skin friction and Nusselt number are shown in Table 1. The magnitude of the Skin friction escalates with the rise in A, M, S_p, F, α, Pr and N, while it decreases with the rise in Gr and Ec. The magnitude of rate of heat transfer escalates with the rise in A, Gr, Pr and N, while it decreases with the rise in M, S_p F, α and Ec.

Table 1. Variation of Skin Friction and Nusselt number for A, M, S_p, F, Gr, α, Pr, Ec, N.

A	M	S_p	F	Gr	$α$	Pr	Ec	N	$f''(0)$	$θ'(0)$
1	0.5	0.4	0.1	1	0	1.0	0.05	1	-1.2580	-0.8519
2									-1.5311	-1.0189
3									-1.7672	-1.1680
1	0.5								-1.2580	-0.8519
	1.0								-1.4194	-0.8473
	1.5								-1.5683	-0.8255
	0.5	0.4							-1.2580	-0.8519
		0.6							-1.3244	-0.8473
		0.8							-1.3884	-0.8430
		0.4	0.1						-1.2580	-0.8519
			0.5						-1.3507	-0.8475
			1.0						-1.4595	-0.8425
			0.1	1					-1.2580	-0.8519
				2					-0.8886	-0.8786
				3					-0.5343	-0.9079
				1	π/6				-1.3089	-0.8480
					π/3				-1.4498	-0.8369
					π/2				-1.6474	-0.8204
					0	0.7			-1.2401	-0.7199
						1.2			-1.2685	-0.9327
						1.5			-1.2823	-1.0452
						1.0	0.05		-1.2580	-0.8519
							1.0		-1.2514	-0.7862
							1.5		-1.2479	-0.7513
							0.05	1	-1.2580	-0.8519
								2	-1.2779	-1.0087
								3	-1.2872	-1.0862

CONCLUSIONS

The findings are translated into the following conclusions, which are given below:

- The velocity profile decreases with the rise in A. M. S_P, F and α.
- The velocity profile increases as Gr increases.
- The temperature profile falls with rise in A, Pr , N and Gr.
- The temperature profile escalates with the rise in M and Ec..
- The magnitude of the Skin friction escalates with the rise in A, M, S_p ,F, $α$, Pr and N, while it decreases with the rise in Gr and Ec.
- The magnitude of rate of heat transfer escalates with the rise in A, Gr, Pr and N, while it decreases with the rise in M, S_p F, α and Ec.

Nomenclature

a,b,c	Constant	v	Fluid's velocity along y-direction, (m/s)
A	Unsteady parameter (c/a),	(x,y)	Cartesian coordinates
B_0	Constant Magnetic field, (N m/A)	Gr	Grashoff number due to heat transfer
C_P	Specific heat at constant pressure, $(\frac{J}{kgK})$		**Greek Symbols**
f	Dimensionless stream function,	ρ	density of fluid, $(\frac{kg}{m^3})$
Ec	Eckert number,	μ	dynamic viscosity, (Pa s)
k	Permeability of porous medium, (m²)	$σ_e$	Electrical conductivity, $(\frac{1}{Ωm})$
k'	Forchheimer resistance factor,	η	Dimensionless similarity variable,
q_r	radiative heat flux, (W/m^2)	ν	Kinematic viscosity, (m^2/s)
M	Magnetic parameter (Hartmann number),	κ	Thermal conductivity, $(\frac{W}{mK})$
Pr	Prandtl number,	ψ	Stream function,
S_P	Porosity parameter,	τ	Skin friction,
N	Radiation parameter,	θ	Dimensionless temperature
Nu	Nusselt number,		**Superscript**
F	Inertial parameter,	'	With regard to η, differentiation
t	Dimensionless time, (K)		**Subscript**
T	Fluid's temperature, (K)	w	values at the plate
u	Fluid's velocity along x-direction, (m/s)	∞	conditions at the free stream

ORCID

Ⓘ**Ankur Kumar Sarma,** https://orcid.org/0009-0003-6209-8859; Ⓘ**Sunmoni Mudoi,** https://orcid.org/0009-0008-9200-5103

REFERENCES

[1] B.C. Sakiadis, "Boundary-layer behavior on continuous solid surfaces: I. boundary-layer equations for two-dimensional and axisymmetric flow," AIChE Journal, **7**(1), 26–28 (1961). https://doi.org/10.1002/aic.690070108

[2] B.C. Sakiadis, "Boundary-layer behavior on continuous solid surfaces: II. the boundary layer on a continuous flat surface," AIChE Journal, **7**(2), 221–225 (1961). https://doi.org/10.1002/aic.690070211

[3] L.J. Crane, "Flow past a stretching plate," Zeitschrift für Angewandte Mathematik und Physik (ZAMP), **21**, 645–647 (1970). https://doi.org/10.1007/BF01587695

[4] W. Banks, "Similarity solutions of the boundary-layer equations for a stretching wall," Journal de Mécanique théorique et appliquée, **2**(3), 375–392 (1983).

[5] C. Wang, "The three-dimensional flow due to a stretching flat surface," The physics of fluids, **27**(8), 1915–1917 (1984). http://dx.doi.org/10.1063/1.864868

[6] H. Andersson, "MHD flow of a viscoelastic fluid past a stretching surface," Acta Mechanica, **95**(1-4), 227–230 (1992). https://doi.org/10.1007/BF01170814

[7] E.M. Elbashbeshy, "Heat transfer over a stretching surface with variable surface heat flux," Journal of Physics D: Applied Physics **31**(16), 1951 (1998). https://doi.org/10.1088/0022-3727/31/16/002

[8] Z. Siri, N.A.C. Ghani, and R.M. Kasmani, "Heat transfer over a steady stretching surface in the presence of suction," Boundary Value Problems, **2018**, 126 (2018). https://doi.org/10.1186/s13661-018-1019-6

[9] H.I. Andersson, J.B. Aarseth, and B.S. Dandapat, "Heat transfer in a liquid film on an unsteady stretching surface," International Journal of Heat and Mass Transfer, **43**(1), 69–74 (2000). https://doi.org/10.1016/S0017-9310(99)00123-4

[10] A. Raptis, C. Perdikis, and H. Takhar, "Effect of thermal radiation on MHD flow," Applied Mathematics and Computation, **153**(3), 645–649 (2004). https://doi.org/10.1016/S0096-3003(03)00657-X

[11] A.Y. Ghaly, "Radiation effects on a certain MHD free-convection flow," Chaos, Solitons & Fractals, **13**(9), 1843–1850 (2002). https://doi.org/10.1016/S0960-0779(01)00193-X

[12] A. Ishak, et al. "MHD boundary layer flow due to an exponentially stretching sheet with radiation effect," Sains Malaysiana, **40**(4), 391–395 (2011). https://journalarticle.ukm.my/2406/1/17_Anuar_Ishak.pdf

[13] P.D. Ariel, T. Hayat, and S. Asghar, "Homotopy perturbation method and axisymmetric flow over a stretching sheet," International Journal of Nonlinear Sciences and Numerical Simulation, **7**(4), 399–406 (2006). https://doi.org/10.1515/IJNSNS.2006.7.4.399

[14] E.M. Elbashbeshy, and D.A. Aldawody, "Heat transfer over an unsteady stretching surface with variable heat flux in the presence of a heat source or sink," Computers & Mathematics with Applications, **60**(10), 2806–2811 (2010). https://doi.org/10.1016/j.camwa.2010.09.035

[15] N. Ahmad, Z. Siddiqui, and M. Mishra, "Boundary layer flow and heat transfer past a stretching plate with variable thermal conductivity," International Journal of Non-linear Mechanics, **45**(04), 306–309 (2010). https://doi.org/10.1016/j.ijnonlinmec.2009.12.006

[16] A. Ishak, "Unsteady MHD flow and heat transfer over a stretching plate," Journal of Applied Sciences, **10**(18), 2127-2131 (2010). https://doi.org/10.3923/jas.2010.2127.2131

[17] A.K. Jhankal, R.N. Jat, and D. Kumar, "Unsteady MHD flow and heat transfer over a porous stretching plate," International Journal of Computational and Applied Mathematics, **2**, 325-333 (2017). https://www.ripublication.com/ijcam17/ijcamv12n2_15.pdf

[18] N.C. Rosca, and I. Pop, "Unsteady boundary layer flow over a permeable curved stretching/shrinking surface," European Journal of Mechanics - B/Fluids, **51**, 61–67 (2015). https://doi.org/10.1016/j.euromechflu.2015.01.001

[19] M.K. Choudhary, S. Chaudhary, and R. Sharma, "Unsteady MHD flow and heat transfer over a stretching permeable surface with suction or injection," Procedia Engineering, **127**, 703–710 (2015). https://doi.org/10.1016/j.proeng.2015.11.371

[20] I. Alarifi, A. Abo-Khalil, A. Osman, L. Lund Baloch, B.A. Mossaad, H. Belmabrouk, and I. Tlili, "MHD flow and heat transfer over vertical stretching sheet with heat sink or source effect," Symmetry, **11**(3), 297 (2019). https://doi.org/10.3390/sym11030297

[21] A.M. Megahed, N.I. Ghoneim, M.G. Reddy, and M. El-Khatib, "Magnetohydrodynamic fluid flow due to an unsteady stretching sheet with thermal radiation, porous medium, and variable heat flux," Advances in Astronomy, **2021**, 686-883 (2021). https://doi.org/10.1155/2021/6686883

[22] Y.D. Reddy, B.S. Goud, K.S. Nisar, B. Alshahrani, M. Mahmoud, and C. Park, "Heat absorption/generation effect on MHD heat transfer fluid flow along a stretching cylinder with a porous medium," Alexandria Engineering Journal, **64**, 659–666 (2023). https://doi.org/10.1016/j.aej.2022.08.049

[23] S.A.G.A. Shah, A. Hassan, H. Karamti, A. Alhushaybari, S.M. Eldin, and A.M. Galal, "Effect of thermal radiation on convective heat transfer in MHD boundary layer carreau fluid with chemical reaction," Scientific Reports, **13**(1), 4117 (2023). https://doi.org/10.1038/s41598-023-31151-4

[24] B.K. Swain, B.C. Parida, S. Kar, and N. Senapati, "Viscous dissipation and joule heating effect on MHD flow and heat transfer past a stretching sheet embedded in a porous medium," Heliyon, **6**(10), e05338 (2020). https://doi.org/10.1016/j.heliyon.2020.e05338

[25] G. Rasool, A.J. Chamkha, T. Muhammad, A. Shafiq, and I. Khan, "Darcy-Forchheimer relation in Casson type MHD nanofluid flow over non-linear stretching surface," Propulsion and Power Research, **9**(2), 159–168 (2020). https://doi.org/10.1016/j.jppr.2020.04.003

[26] P.M. Patil, N. Kumbarwadi, and A.J. Chamkha, "Unsteady mixed convection over an exponentially stretching surface: Influence of Darcy-forchheimer porous medium and cross diffusion," Journal of Porous Media, **24**(2), 29-47 (2021). https://doi.org/10.1615/jpormedia.2020026016

[27] W. Al-Kouz, A. Aissa, A. Koulali, W. Jamshed, H. Moria, K.S. Nisar, A. Mourad, *et al.*, "MHD Darcy-Forchheimer nanofluid flow and entropy optimization in an odd-shaped enclosure filled with a (mwcnt-Fe$_3$ O$_4$/water) using galerkin finite element analysis," Scientific Reports. **11**, 22635 (2021). https://doi.org/10.1038/s41598-021-02047-y

[28] B. Mandal, K. Bhattacharyya, A. Banerjee, A.K. Verma, and A.K. Gautam, "MHD mixed convection on an inclined stretching plate in darcy porous medium with soret effect and variable surface conditions," Nonlinear Engineering, **9**, 457–469 (2022). https://doi.org/10.1515/nleng-2020-0029

[29] A.K. Sarma, "Unsteady radiative MHD flow over a porous stretching plate," in: *Modeling and Simulation of Fluid Flow and Heat Transfer*, (CRC Press, 2024), pp. 96–109. https://doi.org/10.1201/9781032712079-7

[30] A.K. Sarma, and D. Sarma, "MHD flow in free convection over an exponentially stretched sheet submerged in a double-stratified medium," International Journal of Ambient Energy, **45**(1), 2356060 (2024). https://doi.org/10.1080/01430750.2024.2356060

РАДІАЦІЙНИЙ ЕФЕКТ НА НЕСТАЦІОНАРНИЙ МГД-ПОТІК ДАРСІ ФОРХГЕЙМЕРА ПО ВЕРТИКАЛЬНОМУ ПОХИЛОМУ ЛИСТУ, ЩО РОЗТЯГУЄТЬСЯ У ПРИСУТНОСТІ ПОРИСТОГО СЕРЕДОВИЩА

Анкур Кумар Сарма[a,e], Сунмоні Мудої[a], Палаш Нат[b], Панкадж Каліта[c], Гаураб Бардхан[d]

[a]Факультет математики, університет Коттона, Пан Базар, Гувахаті, Індія
[b]Кафедра математики, коледж Барбаг, Калаг-781351, Індія
[c]Кафедра математики, коледж ADP, Нагаон-782002, Індія
[d]Факультет математики, коледж Тягбір Хем Баруа, Джамугуріхат, Сонітпур, 784189, Індія
[e]Факультет математики, Коледж Баосі Баніканта Какаті, Нагаон, Барпета-781311, Індія

У цьому дослідженні розглядається, як випромінювання та тепло переміщуються через двовимірний, нестаціонарний МГД-потік Дарсі-Форхгеймера, який протікає через пористу розтягнуту вертикально нахилену пластину, до якої прикладено поперечне магнітне поле. Ми використовуємо підхід MATLAB bvp4c для чисельного перетворення нелінійних PDE керуючого граничного шару, які є рівняннями в часткових похідних, у набір нелінійних ODE, які є звичайними диференціальними рівняннями, використовуючи перетворення подібності. Ми кількісно оцінюємо профілі швидкості та температури за допомогою графіків, які представляють різні характеристики проблеми, включаючи нестаціонарність, число Прандтля, магнітне поле, число Грашоффа, параметр випромінювання та число Екерта. Таблиці ілюструють вплив на тертя шкіри (τ) і число Нуссельта (Nu). Профіль швидкості зменшується зі збільшенням магнітних та інерційних параметрів, а профіль температури зменшується зі збільшенням параметрів випромінювання.

Ключові слова: *магнітогідродинаміка (МГД); випромінювання; Дарсі-Форххаймер; пористе середовище; теплообмін; нестабільність*

CHEMICAL REACTION, ELECTRIFICATION, BROWNIAN MOTION AND THERMOPHORESIS EFFECTS OF COPPER NANOPARTICLES ON NANOFLUID FLOW WITH SKIN FRICTION, HEAT AND MASS TRANSFER

Aditya Kumar Pati[a]*, Madan Mohan Rout[a], Runu Sahu[b], I. Siva Ramakoti[a],
Koustava Kumar Panda[a], Krushna Chandra Sethi[a]

aCenturion University of Technology and Management, Paralakhemundi, Odisha, India
bNIST University, Berhampur, Ganjam, Odisha, India
Corresponding Author e-mail: apati@cutm.ac.in

This study investigates the effects of first-order chemical reaction, thermophoresis, electrification, and Brownian motion on Cu nanoparticles within a free convective nanofluid flow past a vertical plane surface, focusing on skin friction, heat and mass transfer. The unique combination of chemical reaction and electrification effects sets this study apart from previous research on nanofluid flow. By utilizing similarity functions, the governing PDEs of the flow are converted into a system of locally similar equations. These equations are then solved using MATLAB's bvp4c function, incorporating dimensionless boundary conditions. The findings are verified through a comparison with previous studies. Graphical illustrations show the numerical explorations for concentration, velocity, and temperature profiles in relation to the electrification parameter, thermophoresis parameter, chemical reaction parameter, and Brownian motion parameter. The computational results for heat transfer, mass transfer and dimensionless skin friction coefficients are presented in tabular form. The primary finding indicates that the electrification parameter accelerates heat transfer, while the electrification parameter, Brownian motion parameter, and chemical reaction parameter enhance the rate of mass transfer from the plane surface to the nanofluid. This indicates encouraging potential for cooling plane surfaces in manufacturing industries.
Keywords: *Chemical Reaction; Thermophoresis; Electrification; Brownian Motion; Nanofluid*
PACS: 47.70.Fw, 44.20.+b, 44.25.+f, 47.10.ad, 47.15.Cb

Nomenclature

c	specific heat capacity	Ra_x	local Rayleigh number
C	local concentration	s	dimensionless concentration
C_f	Local skin friction coefficient	Sc	Schmidt number
D_B	Brownian diffusion coefficient	Sh_x	local Sherwood number
D_T	Thermophoresis diffusion coefficient	T	local temperature
(E_x, E_y)	electric intensity components	(u, v)	velocity components
f	dimensionless stream function	α	thermal diffusivity
F	time constant for momentum transfer between the fluid and nanoparticles	β_f	volumetric thermal expansion coefficient
g	gravitational acceleration	ε_0	permittivity
k	thermal conductivity	η	similarity variable
k_1	rate of chemical reaction	γ	chemical reaction parameter
m	nanoparticle mass	μ	dynamic viscosity
M	electrification parameter	θ	temperature in dimensionless form
Nb	Brownian motion parameter	ρ	density
Nc	concentration ratio	υ	kinematic viscosity
N_F	momentum transfer number	ψ	stream function
Nr	buoyancy ratio	*Subscripts*	
N_{Re}	electric Reynolds number	s	nanoparticle phase
Nt	thermophoresis parameter	nf	nanofluid phase
Nu_x	local Nusselt number	f	base fluid phase
Pr	Prandtl number	w	condition at the plane surface
q	charge of the nanoparticle	∞	free stream condition

1. INTRODUCTION

Recent progress in nanoscience arises from exploring the physical properties of matter on the nanoscale. One notable area of industrial application is nanofluids, which have become prominent in the field of heat transfer. These nanofluids have garnered significant attention because of their exceptional thermal transport properties and their fascinating uses across several industries. The motivation for researching nanofluids stems from the improved heat transfer in applications such as nuclear engineering, computer processor microchips, air conditioning and refrigeration systems, space cooling, micromanufacturing, and fuel cells. The classical theory of single-phase fluids can be adapted for nanofluids by treating

their thermophysical properties as dependent on both the base fluids and their individual components. It is crucial to recognize that factors such as thermal conductivity, volume fraction, particle size, and temperature all play a role in enhancing the thermal conductivity of nanofluids. Buongiorno [1] formulated a dual-phase framework aimed at investigating thermal energy transfer utilizing nanofluids. Subsequently, Tiwari and Das [2] introduced a more streamlined approach where the thermophysical characteristics varied with the nanoparticle volume fraction. These models have proven highly effective in addressing diverse flow challenges related to nanofluids. For example, Kuznetsov and Nield [3] were the first to use the Buongiorno model to study the effects of thermophoresis and Brownian motion on free convective nanofluid flow near a vertical plate. Since then, numerous researchers (Khan and Aziz [4], Ibrahim and Makinde [5], Khan et al. [6], Ganga et al. [7], Mohamed et al. [8], Goyal and Bhargava [9], Rana et al. [10], and Dey et al. [11]) have examined the impacts of Brownian motion and thermophoresis on nanofluid flow past a plate surface. Some researchers (Dey et al. [11], Padmaja and Kumar [12], Padmaja and Kumar [13], Dey et al. [14]) have recently reported on the influences of chemical reaction on nanofluids.

The effect of electrification on nanofluid flow has recently garnered significant interest. The pioneering examination of the improvement in heat and mass transfer due to nanoparticle electrification was conducted by Pati et al. [15] in a study of nanofluid flow over a stretching cylinder. Further investigations into the impact of nanoparticle electrification on nanofluid flow have been carried out by researchers such as Panda et al. [16], Pati et al. [17, 18] and Pattanaik et al. [19]. In a more recent study, Pati et al. [20] explored the effects of electrified nanoparticles and the electric Reynolds number on nanofluid flow past a vertical flat surface, concluding that the electrification mechanism significantly enhances both heat and mass transfer.

Previous studies have rarely explored the impact of nanoparticle electrification on nanofluid flow. Additionally, there are no existing studies that consider both electrification and chemical reaction effects on nanofluid flow. This study aims to investigate the combined effects of electrification and chemical reaction on the free convective flow of Cu -water nanofluid past a vertical plane surface. It incorporates Brownian motion and thermophoresis, using Buongiorno's model.

2. MATHEMATICAL FORMULATION

A laminar incompressible steady free convective flow is analyzed, with the vertical plane surface aligned along the x-axis. The plane surface consistently maintains fixed values for both concentration (C_w) and temperature (T_w). A schematic representation is shown in Fig. 1.
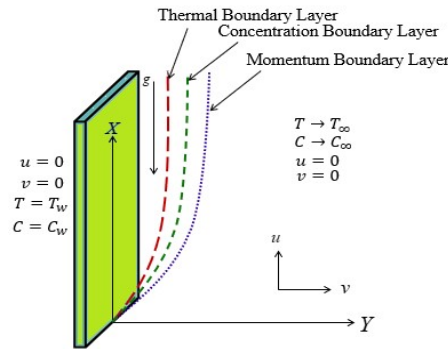

Figure 1. Schematic representation

The governing equations (Pati et al. [21]) incorporating first-order chemical reaction, thermophoresis, electrification, and Brownian motion, and utilizing the Oberbeck-Boussinesq approach, can be formulated as follows:

$$\frac{\partial u}{\partial x} + \frac{\partial v}{\partial y} = 0, \tag{1}$$

$$u\frac{\partial u}{\partial x} + v\frac{\partial u}{\partial y} = \frac{\mu_{nf}}{\rho_{nf}}\left(\frac{\partial^2 u}{\partial y^2}\right) + \frac{\rho_s}{\rho_{nf}}\frac{q}{m}E_x(C - C_\infty) + \frac{\rho_{f\infty}}{\rho_{nf}}(1 - C_\infty)\beta_{f\infty}g(T - T_\infty) - \frac{1}{\rho_{nf}}(C - C_\infty)(\rho_s - \rho_{f\infty})g, \tag{2}$$

$$u\frac{\partial T}{\partial x} + v\frac{\partial T}{\partial y} = \frac{(\rho c)_s}{(\rho c)_{nf}}D_B\frac{\partial C}{\partial y}\frac{\partial T}{\partial y} + \frac{(\rho c)_s}{(\rho c)_{nf}}\frac{q}{m}\frac{C}{F}\left(E_x\frac{\partial T}{\partial x} + E_y\frac{\partial T}{\partial y}\right) + \frac{k_{nf}}{(\rho c)_{nf}}\left(\frac{\partial^2 T}{\partial y^2}\right) + \frac{(\rho c)_s}{(\rho c)_{nf}}\frac{D_T}{T_\infty}\left(\frac{\partial T}{\partial y}\right)^2, \tag{3}$$

$$u\frac{\partial C}{\partial x} + v\frac{\partial C}{\partial y} = \frac{D_T}{T_\infty}\frac{\partial^2 T}{\partial y^2} + D_B\frac{\partial^2 C}{\partial y^2} + \left(\frac{q}{m}\right)\frac{1}{F}\left[\frac{\partial(CE_x)}{\partial x} + \frac{\partial(CE_y)}{\partial y}\right] - k_1(C - C_\infty), \tag{4}$$

along with the boundary conditions:

$$\begin{aligned} y = 0, \ \ v = 0, u = 0, \ T = T_w, \ \ C = C_w \\ y \to \infty, v = 0, u = 0, \ T \to T_\infty, C \to C_\infty \end{aligned}\Bigg\}. \tag{5}$$

The electric field equation is expressed as follows:

$$\frac{\partial E_y}{\partial y} = \frac{\rho_s}{\varepsilon_0}\frac{q}{m}. \tag{6}$$

The equations are converted into a non-dimensional format by defining the following dimensionless functions:

$$\psi = (Ra_x)^{\frac{1}{4}}\alpha_f f(\eta), \eta = \frac{y}{x}(Ra_x)^{\frac{1}{4}}, \theta(\eta) = \frac{T-T_\infty}{T_w-T_\infty}, s(\eta) = \frac{C-C_\infty}{C_w-C_\infty}, \tag{7}$$

where $Ra_x = \frac{(1-C_\infty)x^3(T_w-T_\infty)\beta_f g}{\nu_f \alpha_f}$.

The stream function, denoted by ψ, can be defined as follows:

$$v = -\frac{\partial\psi}{\partial x} \text{ and } \frac{\partial\psi}{\partial y} = u. \tag{8}$$

By substituting equations (6), (7), and (8) into equations (1) to (4), the non-dimensional equations are obtained as follows:

$$f''' = -\frac{\varphi_1}{4Pr}[3ff'' - 2(f')^2] - \frac{\varphi_1\varphi_2 M\,Nb\,Sc}{PrN_F}s - \frac{1}{\varphi_5}(\theta - Nr\,s), \tag{9}$$

$$\theta'' = -\frac{1}{\varphi_4}Pr\,Nt(\theta')^2 - \frac{1}{\varphi_4}Sc\,Nb\left[\frac{N_F}{N_{Re}} - \frac{1}{4}M\right](s+Nc)\eta\theta' - \frac{1}{\varphi_4}Pr\,Nbs'\theta' - \frac{3}{4}\frac{1}{\varphi_3\varphi_4}f\theta', \tag{10}$$

$$s'' = -\frac{Nt}{Nb}\theta'' + \frac{1}{4}\frac{M\,Sc}{Pr}\eta s' - \frac{N_F Sc}{PrN_{Re}}(\eta s' + s + Nc) + \frac{Sc}{Pr}\gamma s - \frac{3}{4}\frac{Sc}{Pr}fs', \tag{11}$$

where prime ($'$) denotes differentiation with respect to η.
The equations (5) are transformed to

$$\left.\begin{array}{l} At\ \eta = 0, f = 0, f' = 0, \theta = 1, s = 1 \\ As\ \eta \to \infty, f' \to 0, \theta \to 0, s \to 0 \end{array}\right\}. \tag{12}$$

The nondimensional parameters are represented as

$$\gamma = \frac{k_1 x}{\frac{\alpha_f(Ra_x)^{\frac{1}{2}}}{x}}, M = \left(\frac{q}{m}\right)\frac{1}{F\left(\frac{\alpha_f(Ra_x)^{\frac{1}{2}}}{x}\right)}E_x, Nb = \frac{(\rho c)_s D_B(C_w-C_\infty)}{(\rho c)_f \nu_f}, Nt = \frac{(\rho c)_s D_T(T_w-T_\infty)}{(\rho c)_f \nu_f T_\infty}, N_F = \frac{\left(\frac{\alpha_f(Ra_x)^{\frac{1}{2}}}{x}\right)}{Fx},$$

$$Nr = \frac{(\rho_s-\rho_f)(C_w-C_\infty)}{(1-C_\infty)\rho_f\beta_f(T_w-T_\infty)}, Sc = \frac{\nu_f}{D_B}, Nc = \frac{C_\infty}{(C_w-C_\infty)}, Pr = \frac{\nu_f}{\alpha_f}, \frac{1}{N_{Re}} = \left(\frac{q}{m}\right)^2\frac{\rho_s}{\epsilon_0}\frac{x^2}{\left(\frac{\alpha_f(Ra_x)^{\frac{1}{2}}}{x}\right)^2}.$$

The thermophysical constants ϕ_1, ϕ_2, ϕ_3, ϕ_4 and ϕ_5 are expressed according to Pati et al. [20]. This study employs a nanofluid with a 1% concentration of Cu nanoparticles. The thermophysical properties of both pure water and the nanoparticles are assessed following the data provided by Oztop and Abu-Nada [22].
C_f, Nu_x and Sh_x are presented for use in skin friction, heat and mass transfer applications as follows:

$$C_f = \frac{x^2\tau_w}{\mu_f\alpha_f(Ra_x)^{\frac{3}{4}}}, \text{ where } \tau_w = \mu_f\left(\frac{\partial u}{\partial y}\right)_{y=0},$$

$$Nu_x = \frac{xq_w}{(T_w-T_\infty)k_f}, \text{ where } q_w = -k_f\left(\frac{\partial T}{\partial y}\right)_{y=0},$$

$$Sh_x = \frac{xq_m}{(C_w-C_\infty)D_B}, \text{ where } q_m = -D_B\left(\frac{\partial C}{\partial y}\right)_{y=0}.$$

The reduced skin friction coefficient $(f''(0))$, heat transfer coefficient $(-\theta'(0))$ and mass transfer coefficient $(-s'(0))$ in non-dimensional form are expressed as follows:

$$C_f = f''(0), -\theta'(0) = Nu_x/Ra_x^{1/4}, -s'(0) = Sh_x/Ra_x^{1/4}.$$

3. NUMERICAL SOLUTION AND COMPARISON OF RESULTS

The MATLAB bvp4c function is used to derive numerical solutions of the equations (9) to (11) along with boundary condition (12), which are recognized as local similarity equations since the parameters γ, M, N_{Re} and N_F depend on x. Numerical results are considered valid as long as they produce a locally similar solution, as highlighted by Farooq et al. [23]. In this context, γ, M, N_{Re} and N_F are treated as constants, as per [23].
The computed numerical values of the non-dimensional heat transfer coefficient for a regular fluid without considering chemical reaction, thermophoresis, electrification, or Brownian motion have been compared and validated against the results obtained by Bejan [24]. Table 1 demonstrates a significant agreement between both results.

Table 1. Comparison of $-\theta'(0)$.

Pr	$-\theta'(0)$ [Bejan]	$-\theta'(0)$ [present]
1.0	0.40100	0.40099
10.0	0.46500	0.46267

4. ANALYSIS OF RESULTS

The influence of key governing parameters, including γ, Nb, M and Nt on the dimensionless profiles of velocity ($f'(\eta)$), temperature ($\theta(\eta)$), and nanoparticle concentration ($s(\eta)$) with respect to η were examined numerically. The findings are illustrated through graphs. Additionally, the impact of these parameters on $f''(0)$, $-\theta'(0)$ and $-s'(0)$ is displayed in a table.

4.1 Velocity Profiles

$f'(\eta)$ profiles are shown in Figures 2 to 5. These figures explore the effect of γ, Nb, M and Nt on $f'(\eta)$ against η. Figure 2 shows that dimensionless velocity decreases as γ increases. Figure 3 illustrates that dimensionless velocity increases with Nb due to the rise in the number of fluid particles colliding with nanoparticles. In Figure 4, $f'(\eta)$ increases with an increase in M. Finally, Figure 5 shows that $f'(\eta)$ increases with an increase in Nt. This is because the increased thermophoresis force causes nanoparticles to move faster, thereby raising the dimensionless velocity profiles.
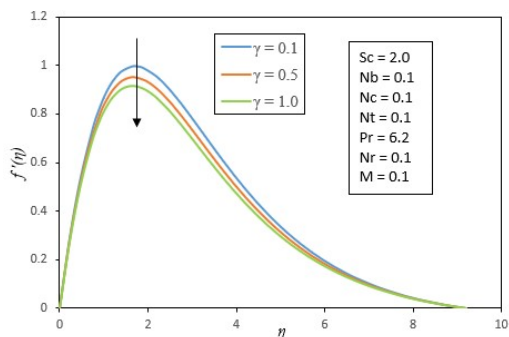

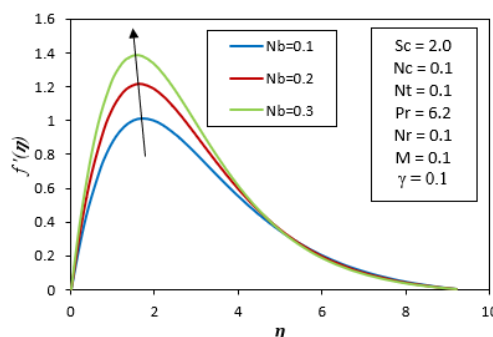**Figure 2.** Effects of γ on $f'(\eta)$ when $N_{Re} = 2.0, N_F = 0.1$

Figure 3. Effects of Nb on $f'(\eta)$ when $N_{Re} = 2.0, N_F = 0.1$

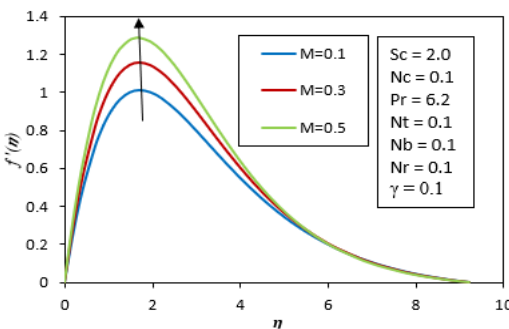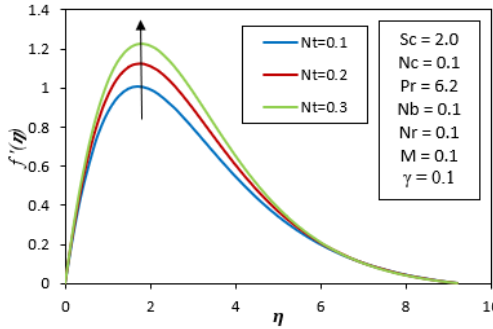**Figure 4.** Effects of M on $f'(\eta)$ when $N_{Re} = 2.0, N_F = 0.1$

Figure 5. Effects of Nt on $f'(\eta)$ when $N_{Re} = 2.0, N_F = 0.1$

4.2 Temperature Profiles

Figures 6 to 9 illustrate $\theta(\eta)$ profiles corresponding to $f'(\eta)$ profiles depicted in Figures 2 to 5. In every illustration, the surface's peak temperature is standardized to one, gradually diminishing to the free stream temperature ($\theta = 0$) at the thermal boundary layer's outer edge.
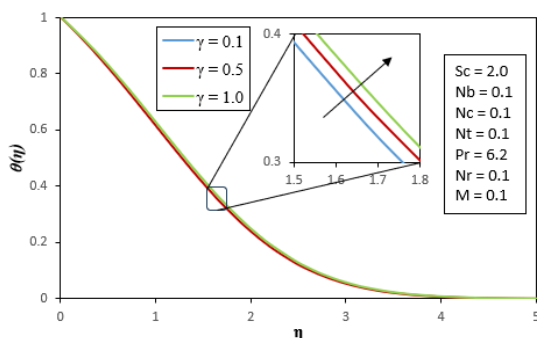

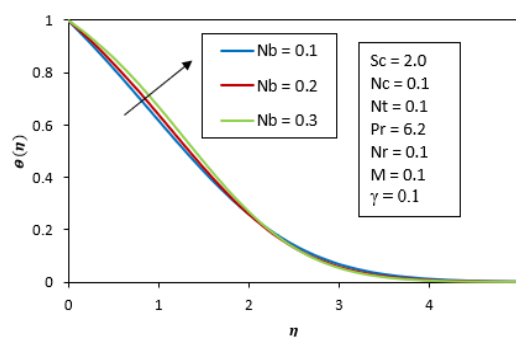**Figure 6.** Effects of γ on $\theta(\eta)$ when $N_{Re} = 2.0, N_F = 0.1$

Figure 7. Effects of Nb on $\theta(\eta)$ when $N_{Re} = 2.0, N_F = 0.1$

Figure 6 shows the temperature profiles for γ, while Figure 7 demonstrates the impact of Nb. Increasing γ slightly enhances the dimensionless temperature, as depicted in Fig. 6. Figure 7 illustrates that increasing Nb enhances temperature, attributed to increased diffusion of nanoparticles due to higher Brownian motion. The presence of nanoparticles induces Brownian motion in the nanofluid, which intensifies with higher Nb values. This motion enhances thermal conduction through two mechanisms: direct heat transfer via nanoparticles and indirect micro-convection around them. Brownian motion exerts significant influence on small particles under high Nb conditions, whereas it has the opposite effect on large particles under low Nb conditions. Figure 8 reveals that increasing M decreases $\theta(\eta)$. The parameter Nt, highlighted in Figure 9, enhances thermophoresis force, prompting nanoparticles to migrate from warmer to cooler regions and amplifying temperature profiles.
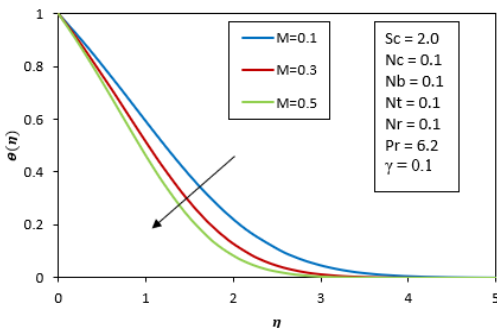

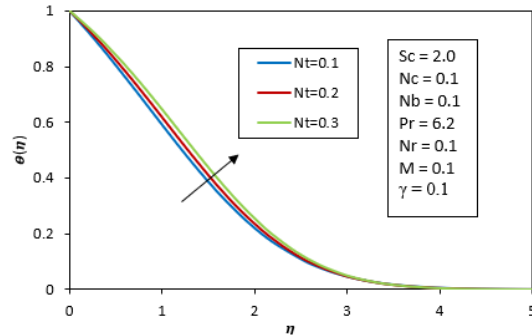**Figure 8.** Effects of M on $\theta(\eta)$ when $N_{Re} = 2.0, N_F = 0.1$

Figure 9. Effects of Nt on $\theta(\eta)$ when $N_{Re} = 2.0, N_F = 0.1$

4.3 Concentration Profiles

Figures 10 to 13 illustrate the impact of γ, Nb, M and Nt on $s(\eta)$. Figure 10 shows that $s(\eta)$ decreases with increasing γ. Figure 11 demonstrates that as Nb increases, the concentration of nanoparticles decreases, primarily due to enhanced Brownian motion warming the boundary layer and leading to increased nanoparticle deposition away from the fluid region (onto the plane surface), thus reducing $s(\eta)$. Figure 12 indicates that nanoparticle concentration decreases with increasing M, attributed to heightened electrification causing nanoparticles to migrate from the fluid region towards the plane surface, thereby lowering their concentration. Figure 13 reveals that increasing Nt results in higher nanoparticle concentration, as greater Nt intensifies forces on nanoparticles away from the heated plane surface, enhances nanoparticle diffusion into the nanofluid region, and ultimately increases concentration magnitude.
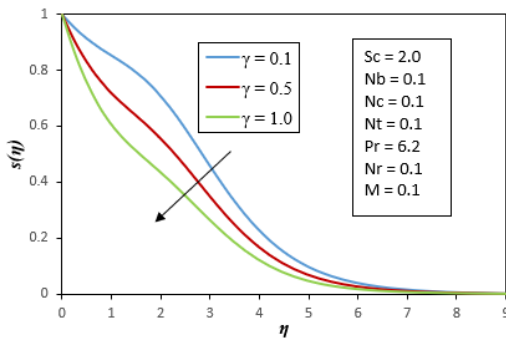

Figure 10. Effects of γ on $s(\eta)$ when $N_{Re} = 2.0, N_F = 0.1$
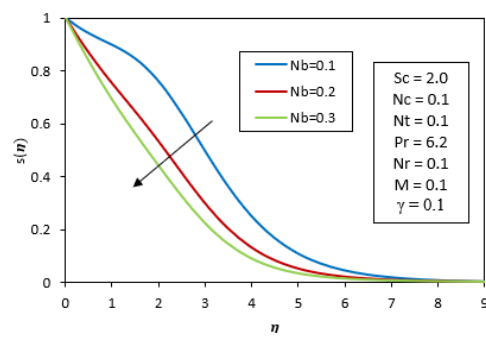

Figure 11. Effects of Nb on $s(\eta)$ when $N_{Re} = 2.0, N_F = 0.1$
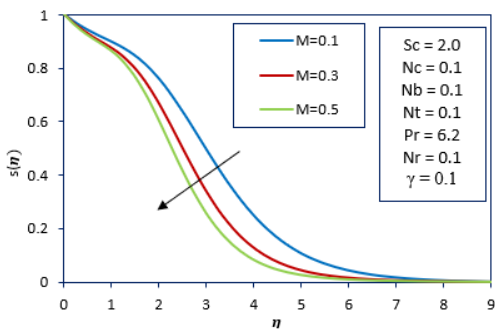
Figure 12. Effects of M on $s(\eta)$ when $N_{Re} = 2.0, N_F = 0.1$
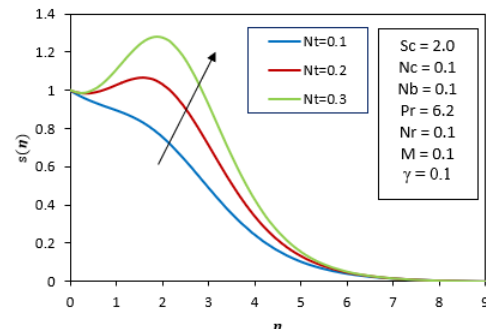
Figure 13. Effects of Nt on $s(\eta)$ when $N_{Re} = 2.0, N_F = 0.1$

4.4 Non-dimensional Skin Friction, Heat and Mass Transfer Coefficients

Table 2 illustrates how changes in γ, M, Nb and Nt affect $f''(0)$, $-\theta'(0)$ and $-s'(0)$ while keeping other parameters fixed ($Sc = N_{Re} = 2.0$, $N_F = Nr = Nc = 0.1$ and $Pr = 6.2$). $f''(0)$ increases with higher values of M, Nb

and Nt, but decreases as γ rises. This trend is attributed to the velocity distribution near the plane surface, which intensifies with M, Nb and Nt, but diminishes with γ. Similarly, $-\theta'(0)$ increases as M rises and decreases with higher values of γ, Nb and Nt. This trend occurs because increasing M reduces the temperature distribution near the surface, whereas higher values of γ, Nb and Nt enhance temperature. Values of $-s'(0)$ increases with γ, M, and Nb, but decreases with increasing Nt. This pattern arises because the nanoparticle concentration near the surface decreases with higher values of γ, Nb, and M, thereby enhancing $-s'(0)$. Conversely, increasing Nt leads to higher nanoparticle concentrations near the surface, resulting in a decrease in $-s'(0)$.

Table 2. The effects of γ, M, Nb and Nt on $f''(0)$, $-\theta'(0)$ and $-s'(0)$

γ	M	Nb	Nt	$f''(0)$	$-\theta'(0)$	$-s'(0)$
0.0				1.41442	0.36235	0.14057
0.1				1.40370	0.35248	0.20466
0.5	0.1	0.1	0.1	1.37049	0.32358	0.41039
1.0				1.34253	0.30120	0.59803
	0.0			0.97884	0.30109	0.17498
	0.1			1.40370	0.35248	0.20466
0.1	0.2	0.1	0.1	1.79457	0.38830	0.22064
	0.3			2.16287	0.41670	0.23155
		0.1		1.40370	0.35248	0.20466
0.1	0.1	0.2	0.1	1.58380	0.32715	0.28574
		0.3		1.75312	0.29981	0.33132
			0.1	1.40370	0.35248	0.20466
0.1	0.1	0.1	0.2	1.45044	0.32904	0.17859
			0.3	1.49351	0.30635	0.17309

5. CONCLUSIONS

The influences of some key governing parameters, such as γ, Nb, M and Nt on velocity, concentration and temperature profiles are graphically demonstrated in free convective nanofluid flow past a plane surface. Numerical results for $f''(0)$, $-\theta'(0)$ and $-s'(0)$ are highlighted in tabular form. The study yields the following conclusions:

- An increase in Nb, Nt and M enhances velocity within the boundary layer, while velocity reduces with increasing γ.
- Higher values of Nb, Nt and γ intensify temperature, whereas increasing M reduces temperature.
- Increasing Nt enhances concentration, whereas Nb, γ and M lead to decreased concentration.
- Nb, Nt and M all enhance the dimensionless reduced skin friction coefficient, while γ reduces it.
- The dimensionless heat transfer coefficient diminishes with increasing Nb, Nt and γ, but significantly rises with an increase in M.
- The rate of heat transfer from the plane surface to nanofluid rises with increasing M and conducts heat into the cooler fluid, cooling the plane surface.
- The dimensionless mass transfer coefficient improves with γ, Nb and M but diminishes with Nt.

ORCID

Aditya Kumar Pati, https://orcid.org/0000-0003-0966-5773

REFERENCES

[1] J. Buongiorno, "Convective transport in nanofluids," ASME J. Heat Transf. **128**, 240-250 (2006). https://doi.org/10.1115/1.2150834

[2] R.K. Tiwari, and M.K. Das, "Heat transfer augmentation in a two-sided lid-driven differentially heated square cavity utilizing nanofluids," Int. J. Heat Mass Transf. **50**, 2002-2018 (2007). https://doi.org/10.1016/j.ijheatmasstransfer.2006.09.034

[3] A.V. Kuznetsov, and D.A. Nield, "Natural convective boundary-layer flow of a nanofluid past a vertical plate," Int. J. Thermal Sci. **49**, 243-247 (2010). https://doi.org/10.1016/j.ijthermalsci.2009.07.015

[4] W.A. Khan, and A. Aziz, "Natural convection flow of a nanofluid over a vertical plate with uniform surface heat flux," Int. J. Therm. Sci. **50**, 1207-1214 (2011). https://doi.org/10.1016/j.ijthermalsci.2011.02.015

[5] W. Ibrahim, and O.D. Makinde, "The effect of double stratification on boundary-layer flow and heat transfer of nanofluid over a vertical plate," Computers & Fluids, **86**, 433-441 (2013). https://doi.org/10.1016/j.compfluid.2013.07.029

[6] W.A. Khan, O.D. Makinde, and Z.H. Khan, "MHD boundary layer flow of a nanofluid containing gyrotactic microorganisms past a vertical plate with Navier slip," International Journal of Heat and Mass Transfer, **74**, 285-291 (2014). https://doi.org/10.1016/j.ijheatmasstransfer.2014.03.026

[7] S. Ganga, M.Y. Ansari, N.V. Ganesh, and A.K.A. Hakeem, "MHD radiative boundary layer flow of nanofluid past a vertical plate with internal heat generation/absorption, viscous and ohmic dissipation effects," Journal of the Nigerian Mathematical Society, **34**, 181-194 (2015). https://doi.org/10.1016/j.jnnms.2015.04.001

[8] M.K.A. Mohamed, N.A.Z. Noar, M.Z. Salleh, and A. Ishak, "Mathematical model of boundary layer flow over a moving plate in a nanofluid with viscous dissipation," Journal of Applied Fluid Mechanics, **9**(5), 2369-2377 (2016). https://doi.org/10.18869/acadpub.jafm.68.236.25247

[9]   M. Goyal, and R. Bhargava, "Simulation of natural convective boundary layer flow of a nanofluid past a convectively heated inclined plate in the presence of magnetic field," Int. J. Appl. Comput. Math, **4**, 63 (2018). https://doi.org/10.1007/s40819-018-0483-0

[10] P. Rana, B. Mahanthesh, J. Mackolil, and W. Al-Kouz, "Nanofluid flow past a vertical plate with nanoparticle aggregation kinematics, thermal slip and significant buoyancy force effects using modified Buongiorno model," Waves in Random and Complex Media, **34**, 3425-3449 (2021). https://doi.org/10.1080/17455030.2021.1977416

[11] S. Dey, S. Mukhopadhyay, and K. Vajravelu, "Nonlinear natural convective nanofluid flow past a vertical plate," Numerical Heat Transfer, Part A: Applications, 1-23 (2024). https://doi.org/10.1080/10407782.2024.2302966

[12] K. Padmaja, and R.B. Kumar, "Viscous dissipation and chemical reaction effects on MHD nanofluid flow over a vertical plate in a rotating system. ZAMM-J Appl Math Mech. **103**(3), e202200471 (2023). https://doi.org/10.1002/zamm.202200471

[13] K. Padmaja, and R.B. Kumar, "Higher order chemical reaction effects on Cu-H$_2$O nanofluid flow over a vertical plate," Sci. Rep. **12**, 17000 (2022). https://doi.org/10.1038/s41598-022-20155-1

[14] S. Dey, S. Ghosh, and S. Mukhopadhyay, "MHD mixed convection chemically reactive nanofluid flow over a vertical plate in presence of slips and zero nanoparticle flux," Waves in Random and Complex Media, 1-20 (2023). https://doi.org/10.1080/17455030.2022.2148014

[15] A.K. Pati, A. Misra, and S.K. Mishra, "Effect of electrification of nanoparticles on heat and mass transfer in boundary layer flow of a copper water nanofluid over a stretching cylinder with viscous dissipation," JP journal of heat and mass transfer, **17**(1), 97-117 (2019). http://dx.doi.org/10.17654/HM017010097

[16] S. Panda, A. Misra, S.K. Mishra, and A.K. Pati, "Flow and Heat Transfer Analysis of H$_2$O-Al$_2$O$_3$ Nanofluid Over a Stretching Surface with Electrified Nanoparticles and Viscous Dissipation," Advances in Dynamical Systems and Applications, **16**(2), 1533-1545 (2021).

[17] A.K. Pati, A. Misra, and S.K. Mishra, "Heat and mass transfer analysis on natural convective boundary layer flow of a Cu-Water nanofluid past a vertical flat plate with electrification of nanoparticles," Advances and Applications in Fluid Mechanics, **23**(1), 1-15 (2019). http://dx.doi.org/10.17654/FM023010001

[18] A.K. Pati, A. Misra, and S.K. Mishra, "Effect of electrification of nanoparticles on natural convective boundary layer flow and heat transfer of a Cu-Water nanofluid past a vertical flat plate," International Journal of Engineering, Science and Mathematics, **6**(8), 1254-1264 (2017). https://www.ijmra.us/project%20doc/2017/IJESM_DECEMBER2017_Special_Issue/4553_pdf.pdf

[19] R. Pattnaik, A. Misra, S.K. Mishra, K.K. Pradhan, S. Panda, and A.K. Pati, "Thermal performance analysis of nanofluid past an exponentially stretching surface due to the electrification effect of nanoparticles," International Journal of Difference Equations (IJDE), **16**, 189-203 (2021). https://www.ripublication.com/ijde21/v16n2p02.pdf

[20] A.K. Pati, S. Mishra, A. Misra, and S.K. Mishra, "Heat and mass transport aspects of nanofluid flow towards a vertical flat surface influenced by electrified nanoparticles and electric Reynolds number," East Eur. J. Phys. (2), 234-241 (2024). https://doi.org/10.26565/2312-4334-2024-2-22

[21] A.K. Pati, A. Misra, S.K. Mishra, S. Mishra, R. Sahu, and S. Panda, "Computational modelling of heat and mass transfer optimization in copper water nanofluid flow with nanoparticle ionization," JP Journal of Heat and Mass Transfer, **31**, 1-18 (2023). https://doi.org/10.17654/0973576323001

[22] H.F. Oztop, and E. Abunada, "Numerical study of natural convection in partially heated rectangular enclosures filled with nanofluids," International Journal of Heat Fluid Flow, **29**, 1326-1336 (2008). https://doi.org/10.1016/j.ijheatfluidflow.2008.04.009

[23] U. Farooq, H. Waqas, A. Bariq, S.K. Elagan, N. Fatima, M. Imran, S.A. Khan, *et al*., "Local similar solution of magnetized hybrid nanofluid flow due to exponentially stretching/shrinking sheet," BioNanoSci. **14**, 368-379 (2024). https://doi.org/10.1007/s12668-023-01276-x

[24] A. Bejan, *Convection Heat Transfer*, (Wiley, New York, 1984).

ХІМІЧНА РЕАКЦІЯ, ЕЛЕКТРИЗАЦІЯ, БРОУНІВСЬКИЙ РУХ ТА ТЕРМОФОРЕЗНИЙ ЕФЕКТ НАНОЧАСТИНОК МІДІ НА ПОТОК НАНОРІДИНИ З ПОВЕРХНЕВИМ ТЕРТЯМ, ТЕПЛО-ТА МАСОПЕРЕНОСОМ

Адітья Кумар Паті[a], Мадан Мохан Роут[a], Руну Саху[b], І. Сіва Рамакоті[a], Коустава Кумар Панда[a], Крушна Чандра Сеті[a]
[a]Університет технології та менеджменту Центуріон, Паралахемунді, Одіша, Індія
[b]Університет NIST, Берхампур, Ганджам, Одіша, Індія

У цьому дослідженні досліджується вплив хімічної реакції першого порядку, термофорезу, електризації та броунівського руху на наночастинки Cu у вільному конвективному потоці нанофлюїду повз вертикальну плоску поверхню, з тертям поверхні, тепло- та масообміном. Унікальне поєднання хімічної реакції та ефектів електризації відрізняє це дослідження від попередніх досліджень потоку нанорідини. Використовуючи функції подібності, керуючі PDE потоку перетворюються на систему локально подібних рівнянь. Потім ці рівняння розв'язуються за допомогою функції bvp4c MATLAB, що включає безрозмірні граничні умови. Висновки підтверджуються шляхом порівняння з попередніми дослідженнями. Графічні ілюстрації показують чисельні дослідження профілів концентрації, швидкості та температури у зв'язку з параметром електризації, параметром термофорезу, параметром хімічної реакції та параметром броунівського руху. Результати розрахунків коефіцієнтів теплообміну, масообміну та безрозмірного шкірного тертя подано у вигляді таблиці. Основне відкриття вказує на те, що параметр електризації прискорює передачу тепла, тоді як параметр електризації, параметр броунівського руху та параметр хімічної реакції збільшують швидкість передачі маси від плоскої поверхні до нанорідини. Це вказує на обнадійливий потенціал для охолодження плоских поверхонь у промисловості.
Ключові слова: *хімічна реакція; термофорез; електрифікація; броунівський рух; нанофлюїд*

A BIOMAGNETIC COUPLE STRESS FLUID FLOW IN AN ANISOTROPIC POROUS CHANNEL WITH STRETCHING WALLS

 R. Vijaya Sree[a,b], V. K. Narla[b*], K. Suresh Babu[c]

aACE Engineering College, Department of Mathematics, Hyderabad, Telangana, 501301, India.
bGITAM Deemed to be University, Department of Mathematics, Hyderabad, 502329, India.
cGokaraju Rangaraju Institute of Engineering & Technology, Department of Mathematics, Hyderabad, 500090, India.
*Corresponding Author e-mail: vnarla@gitam.edu

 The present study investigates the dynamics of a biomagnetic couple stress fluid within an anisotropic porous channel where the channel walls are stretchable. This study examines the flow behavior under the influence of an external magnetic field generated by a magnetic dipole. Appropriate dimensionless parameters are introduced to simplify the equations of the problem. A suitable numerical approach based on the Spectral Quasi-Linearization Method is utilized to obtain a solution to the problem. In this work, influence of several important parameters like the anisotropic permeability ratio, couple stress parameter, anisotropic angle, Darcy number, ferromagnetic interaction parameter, Reynolds number, and Prandtl number are examined. The results indicate that ferromagnetic interaction parameter and couple stress parameter significantly impact heat transfer and fluid flow. Permeability ratio and angle also affect the flow dynamics. Furthermore, the coefficient of skin friction and rate of heat transfer were examined, varying the couple stress and ferromagnetic interaction parameters. The findings demonstrate that an existence of magnetic dipole and anisotropic permeability significantly influences the flow and thermal properties of ferrofluids, providing valuable insights for optimizing heat transfer and controlling fluid flow in diverse engineering and medical applications.

Keywords: *Couple stress fluid; Magnetic dipole; Anisotropic porous media; Anisotropic permeability; Heat transfer; Spectral Quasi-Linearization method*

PACS: 47.50.-d; 47.65.Cb; 47.35.Tv; 47.56.+r; 44.30.+v; 44.15.+a; 02.70.Hm

1. INTRODUCTION

The research on biomagnetic ferrofluids has gained remarkable significance in recent times owing to their distinctive characteristics and possible uses in diverse domains including biomedical engineering, pharmaceutical administration, and thermal transport systems [1]. A key area of interest in biomagnetic ferrofluid research is understanding the behaviour of these fluids when subjected to a magnetic dipole, especially in confined geometries such as channels with stretching walls. The stretching walls introduce a shear force, which can significantly influence the flow dynamics within the channel. Understanding these interactions is crucial for optimizing the design and operation of devices that utilize biomagnetic fluids, particularly in processes where efficient heat transfer and fluid control are essential like applications related to engineering, biomedicine, and materials science [2, 3]. Ferrofluids demonstrate controllable flow behaviour and enhanced thermal conductivity under magnetic influence, and have a range of fascinating applications across various fields which include magnetic resonance imaging (MRI) enhancement, drug delivery systems, cooling systems, magnetic separation and filtering, optical devices, magnetic sensors and actuators [4]–[7]. A mathematical model of magnetic field-induced blood flow was developed by E.E. Tzirtzilakis [8]. The magnetic dipole-induced dynamics of visco-elastic fluid were examined by Misra and Shit [9, 10]. They examined the variation in the velocity of blood with respect to a magnetic field, viscoelastic parameter and thermal diffusivity using the method of finite difference. They concluded that by enhancing the intensity of magnetic force field, regulation of wall temperature can be achieved by eliminating occurrence of flow reversal. An observation was made that larger magnetic strength corresponds to higher temperature. The applicability of these analyses was demonstrated by studying blood flow in arteries within walls, which are stretchable. A second-grade electrically conducting fluid, which is both steady and incompressible, was investigated by Misra et al. [11] in channel while a transverse uniform magnetic field was present. All the studies carried out by Misra et al. are driven by various potential uses in the biomedical engineering domain. Couple stress fluids, which are a particular category of non-Newtonian fluids, have a nonsymmetric stress tensor and microstructure in their fluid structure, which makes them defy the Newtonian fluid theory. Stokes[12] developed the theory of couple stress fluids in 1966, expanding classical fluid mechanics to account for couple stresses. Because of their potential applications in a wide range of fluid flow systems, couple stress fluids have garnered significant interest from many researchers [13]–[15]. Ramesh [16] examined the propagation of a couple stress fluid having peristaltic behaviour, in an inclined asymmetrical porous channel. It was noted in the study that the pressure gradient declines as the Reynolds number and the channel's angle of inclination are raised. Studies have shown that the heat transfer and temperature exhibit positive correlations with the Darcy number and also

---

angle of inclination. A study conducted by Ramanamurthy and Pavan Kumar [17] examined couple stress fluid flow in a channel of rectangular shape formed due to a magnetic field applied transversely. Some more studies on couple stress fluids and power-law fluids which are subjected to magnetic field can be found in [18]–[22]. In their study, Nadeem et al. [23] analysed impact of nanoparticles on magnetohydrodynamic (MHD) flow of a Casson fluid over an exponentially permeable shrinking sheet. Coupled stress fluids in curved porous channels were investigated by Pramod et al.[24]. The flow governing equations, which are highly non-linear, were solved by HAM(Homotopy Analysis Method). They concluded that when compared with the Newtonian fluids, for couple stress fluids the magnitude of velocity and temperature profiles are smaller. Ishaq et al. [25] investigated the behaviour of couple stress fluid traversing a porous slit which is linear in a Darcy porous media. The flow was considered creeping and the solution was obtained using an Inverse method technique. Their research explored kidney disease's impact on renal tubule fluid flow, highlighting potential clogging by fibers, lipids, and waste particles, aiding in disease management and improving renal medicine development. Using a Boussinesq couple stress fluid, Patra et al. [26] analysed the characteristics of flow across a stretched sheet in porous media. The flow was exposed to varying magnetic fields and thermal radiation. An order-4 RK method was applied to obtain the solution numerically. They discovered that the distributions of velocity and temperature were impacted by parameters like Darcy number, magnetic field strength, and couple stress parameter. Recent advanced research has primarily focused on developing effective numerical methods to solve the intricate, nonlinear differential equations that govern fluid flow dynamics. To linearise and solve nonlinear terms with high accuracy, one such method is Spectral Quasi-Linearization Method (SQLM), which combines the Quasilinearization technique with spectral methods. Numerous fluid flow applications, such as the investigation of flows across boundary layer over stretching/shrinking sheets in non-Darcy porous media, have benefited from the successful application of this technique [27]–[29]. With a focus on nanofluid flow, Rai and Mondal [30] examined modern spectral approaches for solving nonlinear fluid flow problems. It consists of various spectral-based techniques such as Spectral Quasi-Linearization (SQLM), spectral relaxation (SRM), and spectral local linearisation (SLLM) which are most effective and precise than finite difference methods, in solving both ordinary and partial differential equations.

Most studies on ferrofluid flow dynamics and heat transfer do not take into account the impact of coupled stress fluid dynamics, magnetic dipoles, and anisotropic porous medium. Using a mathematical model and solving the governing equations, this work aims to elucidate the impact of the interaction among magnetic dipole, stretching walls, anisotropic permeability and ferrofluid characteristics on the system's overall performance. The flow governing equations, which take into account couple stresses and magnetic forces, are numerically solved by applying Spectral Quasi-Linearization Method (SQLM), after making similarity transformations. Our study examines how the key parameters, including couple stress, ferromagnetic interaction, Prandtl number, Reynolds number, Darcy number, anisotropic permeability, and angle affect velocity and temperature profiles in boundary layers. The findings give a thorough understanding of the intricate interactions between these variables and show how they impact the flow and thermal properties of ferrofluids. The results demonstrate the method's resilience and efficacy in handling challenging fluid dynamics applications by providing insightful guidance for optimising heat transfer and flow control in various engineering applications involving magnetic fluids.

2. MATHEMATICAL FORMULATION

A two-dimensional flow of a couple stress fluid within a channel bounded by parallel plates located at $y = \pm h$ is considered. The channel is saturated with anisotropic porous media and the temperature of channel walls maintained at (T_w), a constant. A magnetic dipole is positioned at a distance **a** above the channel wall, exerting an influence on the flow. The walls of the channel, which are assumed to be stretching, induce the flow, with the surface velocity being directly proportional to the horizontal axis X. The porous medium is assumed to be anisotropic, and consequently, the anisotropic permeability matrix $\mathbb{K}$ is defined as [31]–[39]

$$\mathbb{K} = \begin{bmatrix} k_{22}\cos^2(\phi) + k_{11}\sin^2(\phi) & (k_{22} - k_{11})\sin(\phi)\cos(\phi) \\ (k_{22} - k_{11})\sin(\phi)\cos(\phi) & k_{22}\sin^2(\phi) + k_{11}\cos^2(\phi) \end{bmatrix}. \tag{1}$$

k_{11} and k_{22}, the permeabilities along the two main axes are taken to be constant. The angle formed by positive X axis and horizontal permeability k_{22} is the anisotropic angle ϕ. Figure (1) depicts the above consideration. The governing equations for couple stress fluid with consideration of anisotropic porous permeability are stated below, taking into account the aforementioned factors:

$$\frac{\partial u}{\partial x} + \frac{\partial v}{\partial y} = 0, \tag{2}$$

$$\rho\left[u\frac{\partial u}{\partial x} + v\frac{\partial u}{\partial y}\right] = -\frac{\partial p}{\partial x} + \mu\left[\frac{\partial^2 u}{\partial x^2} + \frac{\partial^2 u}{\partial y^2}\right] - \gamma\left[\frac{\partial^4 u}{\partial x^4} + \frac{\partial^4 u}{\partial y^4} + 2\frac{\partial^4 u}{\partial x^2 \partial y^2}\right] + \mu_0 M\frac{\partial H}{\partial x}$$

$$-\frac{\mu}{k_{11}k_{22}}\left[(k_{11}\cos^2(\phi) + k_{22}\sin^2(\phi))u + (\frac{k_{11} - k_{22}}{2}\sin(2\phi))v\right], \tag{3}$$
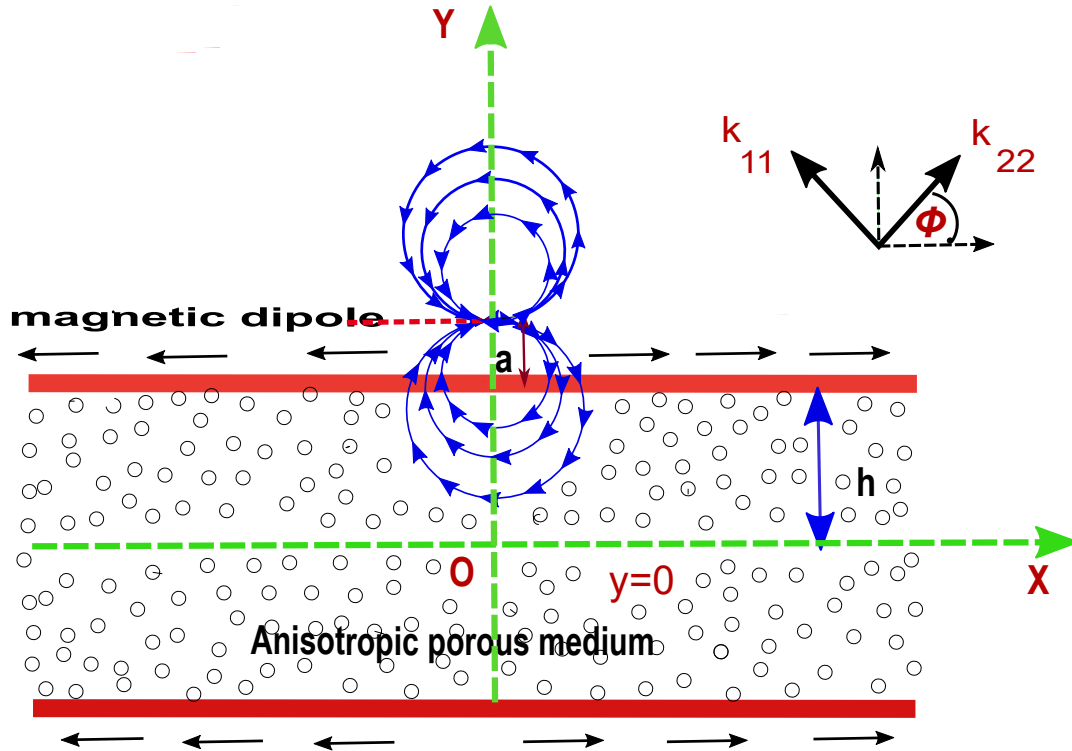
Figure 1. Illustration of physical problem.

$$\rho\Big[u\frac{\partial v}{\partial x} + v\frac{\partial v}{\partial y}\Big] = -\frac{\partial p}{\partial y} + \mu\Big[\frac{\partial^2 v}{\partial x^2} + \frac{\partial^2 v}{\partial y^2}\Big] - \gamma\Big[\frac{\partial^4 v}{\partial x^4} + \frac{\partial^4 v}{\partial y^4} + 2\frac{\partial^4 v}{\partial x^2 \partial y^2}\Big] + \mu_0 M\frac{\partial H}{\partial y}$$
$$-\frac{\mu}{k_{11}k_{22}}\Big[\frac{k_{11} - k_{22}}{2}\sin(2\phi)u + (k_{11}\sin^2(\phi) + k_{22}\cos^2(\phi))v\Big], \tag{4}$$

$$\rho c_p\Big[u\frac{\partial T}{\partial x} + v\frac{\partial T}{\partial y}\Big] = k\Big[\frac{\partial^2 T}{\partial x^2} + \frac{\partial^2 T}{\partial y^2}\Big] - \mu_0 T\frac{\partial M}{\partial T}\Big[u\frac{\partial H}{\partial x} + v\frac{\partial H}{\partial y}\Big] + \mu\Big[2\Big(\frac{\partial u}{\partial x}\Big)^2 +$$
$$2\Big(\frac{\partial v}{\partial y}\Big)^2 + \Big(\frac{\partial u}{\partial y} + \frac{\partial v}{\partial x}\Big)^2\Big] + \gamma\Big[\Big(\frac{\partial^2 u}{\partial x^2} + \frac{\partial^2 u}{\partial y^2}\Big)^2 + \Big(\frac{\partial^2 v}{\partial x^2} + \frac{\partial^2 v}{\partial y^2}\Big)^2\Big] +$$
$$\frac{\mu}{k_{11}k_{22}}\Big[(k_{11}\cos^2(\phi) + k_{22}\sin^2(\phi))u^2 + (k_{11} - k_{22})\sin(2\phi)uv$$
$$+(k_{22}\cos^2(\phi) + k_{11}\sin^2(\phi))v^2\Big]. \tag{5}$$

In the context of the flow problem, the boundary conditions can be mathematically expressed as:

$$\frac{\partial u}{\partial y} = 0, \; v = 0, \; \frac{\partial T}{\partial y} = 0, \; \text{at } y = 0, \tag{6}$$

$$\frac{\partial^2 u}{\partial y^2} = 0, \; u = cx, \; v = 0, \; T = T_w, \; p + \frac{1}{2}\rho(u^2 + v^2) = 0 \; \text{at } y = h. \tag{7}$$

In equations aforementioned variables u, v represent fluid velocity's dimensional components in the direction of X, Y axes. Additionally $p, \mu_0, \mu, \rho, \gamma, k, H, M, T$ and c_p denotes the pressure, magnetic permeability, dynamic viscosity, biomagnetic fluid density, couple stress coefficient, thermal conductivity, magnetic field strength, magnetisation, temperature and fluid's specific heat respectively. In equations (3) and (4), the terms $\mu_0 M\frac{\partial H}{\partial x}$, $\mu_0 M\frac{\partial H}{\partial y}$ on the right side represent the magnetic field's influence in fluid flow, the terms $\gamma\Big[\frac{\partial^4 u}{\partial x^4} + \frac{\partial^4 u}{\partial y^4} + 2\frac{\partial^4 u}{\partial x^2 \partial y^2}\Big]$, $\gamma\Big[\frac{\partial^4 v}{\partial x^4} + \frac{\partial^4 v}{\partial y^4} + 2\frac{\partial^4 v}{\partial x^2 \partial y^2}\Big]$ reflect the internal frictional forces within the fluid and additional couple stresses of the fluid which lead to higher order stress effects that are crucial for accurately describing behavior of non-Newtonian fluids, and the last terms in the equations reflect the Darcy resistance to flow due to the porous medium, modulated by its anisotropic permeability characteristics. In equation (5), the term $\mu_0 T\frac{\partial M}{\partial T}\Big[u\frac{\partial H}{\partial x} + v\frac{\partial H}{\partial y}\Big]$, represents the magneto-caloric effect, where the magnetic field influences the distribution of temperature and heat transfer in fluid.

The biomagnetic fluid flow is influenced by magnetic dipole which produces a magnetic field. The scalar potential that represents the magnetic force field is given by:

$$\Phi(x,y) = \frac{\alpha}{2\pi}\left[\frac{x}{x^2 + (y-b)^2}\right] \tag{8}$$

where $b = a + h$ and α represents the strength of magnetic force field at the point $(0, b)$. The elements corresponding to the magnetic field intensity H are :

$$H_x = -\frac{\partial\Phi}{\partial x} = \frac{\alpha}{2\pi}\cdot\frac{x^2 - (y-b)^2}{[x^2 + (y-b)^2]^2} \tag{9}$$

$$H_y = -\frac{\partial\Phi}{\partial y} = \frac{\alpha}{2\pi}\cdot\frac{2x(y-b)}{[x^2 + (y-b)^2]^2} \tag{10}$$

The resultant magnitude of intensity of magnetic field is

$$H = \sqrt{H_x^2 + H_y^2} = \frac{\alpha}{2\pi.[x^2 + (y-b)^2]} \tag{11}$$

$$\frac{\partial H}{\partial x} = -\frac{\alpha}{2\pi}\cdot\frac{2x}{(y-b)^4} \tag{12}$$

considering only x and neglecting higher powers

$$\frac{\partial H}{\partial y} = \frac{\alpha}{2\pi}\cdot\left[-\frac{2}{(y-b)^3} + \frac{4x^2}{(y-b)^5}\right] \tag{13}$$

Magnetisation M, is shown to be a function of temperature T and exhibits linear variation according to the principle of FHD[40]. Thus we consider $M = k_f T$, where k_f is the pyromagnetic constant.

2.1. Transformation of equations

We present the following dimensionless variables:

$$\Psi(\xi,\eta) = ch^2\xi f(\eta) \tag{14}$$

$$P(\xi,\eta) = \frac{p}{\rho c^2 h^2} = -P_1(\eta) - \xi^2 P_2(\eta), \tag{15}$$

$$\theta(\xi,\eta) = \frac{T}{T_w} = \theta_1(\eta) + \xi^2\theta_2(\eta), \tag{16}$$

$$\xi(x) = \frac{x}{h} \tag{17}$$

$$\eta(y) = \frac{y}{h} \tag{18}$$

where $\Psi(\xi,\eta), P(\xi,\eta), \theta(\xi,\eta)$ are the stream function, the pressure function and the temperature function respectively. Non-dimensionalization of u, v can be made as :

$$u = \frac{\partial\Psi}{\partial y} = ch\xi f'(\eta) \tag{19}$$

$$v = -\frac{\partial\Psi}{\partial x} = -chf(\eta) \tag{20}$$

The continuity equation is clearly satisfied by the variables u and v. After equations (14)- (20) are substituted in equations (3)-(5), and thereafter equating the coefficients of ξ^0, ξ, and ξ^2, we derive the subsequent equations:

$$-\frac{1}{\Gamma^2}f^V + f''' + Re[ff'' - (f')^2] + 2ReP_2 - \frac{2\beta\theta_1}{Re(\eta-d)^4} - \frac{1}{Da}\Big[K\cos^2(\phi) + \sin^2(\phi))\Big]f'(\eta) = 0, \tag{21}$$

$$\frac{1}{\Gamma^2}f^{IV} - f'' - Reff' + ReP_1' - \frac{2\beta\theta_1}{Re(\eta-d)^3} + \frac{1}{Da}\Big[K\sin^2(\phi) + \cos^2(\phi))\Big]f(\eta) = 0, \tag{22}$$

$$ReP_2' + \frac{4\beta\theta_1}{Re(\eta-d)^5} - \frac{2\beta\theta_2}{Re(\eta-d)^3} = 0 \tag{23}$$

$$\theta_1'' + 2\theta_2 + RePrf\theta_1' - \frac{2\lambda\beta(\theta_1)f}{(\eta-d)^3} + \frac{\lambda}{\Gamma^2}(f'')^2 + 4Re\lambda(f')^2 + \frac{1}{Da}\lambda Re[\cos^2(\phi) + K\sin^2(\phi)]f^2 = 0 \quad (24)$$

$$\theta_2'' - RePr[2f'\theta_2 - f\theta_2'] + \lambda\beta\theta_1\left[\frac{2f'}{(\eta-d)^4} + \frac{4f}{(\eta-d)^5}\right] - \frac{2\lambda\beta f\theta_2}{(\eta-d)^3} + \lambda\frac{1}{\Gamma^2}(f''')^2 + \lambda Re(f'')^2$$
$$+ \frac{1}{Da}\lambda Re[K\cos^2(\phi) + \sin^2(\phi)]f^2 = 0. \quad (25)$$

The boundary conditions in equations (6) and (7) get transformed as:

$$f(0) = 0, \; f''(0) = 0, \; \theta_1'(0) = 0, \; \theta_2'(0) = 0$$
$$f(1) = 0, f'(1) = 1, f'''(1) = 0, \; \theta_1(1) = 1, \; \theta_2(1) = 0, \; P_1(1) = 0, \; P_2(1) = \frac{1}{2}. \quad (26)$$

In the transformed equations written above, the other non-dimensional parameters present are outlined as follows:

$$\Gamma = \sqrt{\frac{\mu}{\gamma}}h, \; \beta = \frac{\alpha\mu_0 T_w \rho k_f}{2\pi\mu^2}, \; Pr = \frac{\mu c_p}{k}, \; \lambda = \frac{\mu^2 c}{\rho k_f T_w},$$
$$Da = \frac{k_{11}}{h^2}, \; Re = \frac{\rho c h^2}{\mu}, \; d = \frac{b}{h} \; and \; K = \frac{k_{11}}{k_{22}}.$$

where the couple stress parameter is denoted as Γ, ferromagnetic interaction parameter as β, Prandtl number as Pr, viscous dissipation parameter as λ, Darcy number as Da, Reynolds number as Re, dimensionless distance as d, and anisotropic permeability ratio as K.

3. METHOD OF SOLUTION

A fifth-order coupled nonlinear system is established by the sets of equations (21)–(25) together with the boundary conditions (26). This system characterises the dynamics of the problem under consideration. A numerical solution to the problem considered is obtained by applying the Spectral Quasi-Linearization Method. For the set of equations (21) to (25), the approximate current solution and the improved solution are considered as $f_r, (\theta_1)_r, (\theta_2)_r, (P_1)_r, (P_2)_r$ and $f_{r+1}, (\theta_1)_{r+1}, (\theta_2)_{r+1}, (P_1)_{r+1}, (P_2)_{r+1}$ respectively. The procedure yields the linear differential equations shown below:

$$a_{1,r}f_{r+1}^V + f_{r+1}''' + a_{2,r}f_{r+1}'' + a_{3,r}f_{r+1}' + a_{4,r}f_{r+1} + a_{5,r}(\theta_1)_{r+1} + a_{6,r}(P_2)_{r+1} = S_1, \quad (27)$$

$$a_{7,r}f_{r+1}^{IV} - f_{r+1}'' + a_{8,r}f_{r+1}' + a_{9,r}f_{r+1} + a_{10,r}(\theta_1)_{r+1} + a_{11,r}(P_1)_{r+1}' = S_2, \quad (28)$$

$$a_{12,r}(\theta_1)_{r+1} + a_{13,r}(\theta_2)_{r+1} + a_{14,r}(P_2)_{r+1}' = S_3, \quad (29)$$

$$a_{15,r}f_{r+1}'' + a_{16,r}f_{r+1}' + a_{17,r}f_{r+1} + (\theta_1)_{r+1}'' + a_{18,r}(\theta_1)_{r+1}' + a_{19,r}(\theta_1)_{r+1} + a_{20,r}(\theta_2)_{r+1} = S_4, \quad (30)$$

$$a_{21,r}f_{r+1}''' + a_{22,r}f_{r+1}'' + a_{23,r}f_{r+1}' + a_{24,r}f_{r+1} + a_{25,r}(\theta_1)_{r+1} + (\theta_2)_{r+1}'' + a_{26,r}(\theta_2)_{r+1}' + a_{27,r}(\theta_2)_{r+1} = S_5, \quad (31)$$

The transformed boundary conditions are found as below:

$$f_{r+1} = 0, \; f_{r+1}'' = 0, \; (\theta_1)_{r+1}' = 0, \; (\theta_2)_{r+1}' = 0 \; at \; \eta = 0,$$
$$f_{r+1} = 0, \; f_{r+1}' = 1, \; f_{r+1}''' = 0, \; (\theta_1)_{r+1} = 1, \; (\theta_2)_{r+1} = 0, \; (P_1)_{r+1} = 0, \; (P_2)_{r+1} = \frac{1}{2} \; at \; \eta = 1. \quad (32)$$

The coefficients obtained are:

$$a_{1,r} = -\frac{1}{\Gamma^2}, \quad a_{2,r} = Ref_r, \quad a_{3,r} = -2Ref_r' - \frac{1}{Da}(K\cos^2(\phi) + \sin^2(\phi)), \quad a_{4,r} = Ref_r'',$$

$$a_{5,r} = \frac{-2\beta}{Re(\eta-d)^4}, \quad a_{6,r} = 2Re, \quad a_{7,r} = \frac{1}{\Gamma^2}, \quad a_{8,r} = -Ref,$$

$$a_{9,r} = -Ref_r' + \frac{1}{Da}(\cos^2(\phi) + K\sin^2(\phi)), \quad a_{10,r} = \frac{-2\beta}{(\eta-d)^3}, \quad a_{11,r} = Re,$$

$$a_{12,r} = \frac{4\beta}{(\eta-d)^5}, \quad a_{13,r} = \frac{-2\beta}{(\eta-d)^3}, \quad a_{14,r} = Re, \quad a_{15,r} = \frac{2\lambda f_r''}{\Gamma^2}, \quad a_{16,r} = 8Re\lambda f_r',$$

$$a_{17,r} = RePr\theta_1' - \frac{2\lambda\beta\theta_1}{(\eta-d)^3} + \frac{2}{Da}\lambda f_r Re[\cos^2(\phi) + K\sin^2(\phi)], \quad a_{18,r} = RePrf_r,$$

$$a_{19,r} = \frac{-2\beta\lambda f_r}{(\eta-d)^3}, \quad a_{20,r} = 2, \quad a_{21,r} = 2\lambda\frac{1}{\Gamma^2}f_r''', \quad a_{22,r} = 2\lambda Ref_r'',$$

$$a_{23,r} = \frac{2}{Da}\lambda Re f'_r[(K\cos^2(\phi) + \sin^2(\phi))] + \frac{2\lambda\beta\theta_1}{(\eta-d)^4} - 2RePr\theta_2,$$

$$a_{24,r} = RePr(\theta'_2)_r - \frac{2\lambda\beta(\theta_2)_r}{(\eta-d)^3} + \frac{4\lambda\beta(\theta_1)_r}{(\eta-d)^5}, \quad a_{25,r} = \frac{2\lambda\beta f'_r}{(\eta-d)^4} + \frac{4\lambda\beta f_r}{(\eta-d)^5},$$

$$a_{26,r} = RePr f_r, \quad a_{27,r} = -2RePr f'_r - \frac{2\lambda\beta f_r}{(\eta-d)^3},$$

$$S_1 = Re(f_r f''_r - f'^2_r), \quad S_2 = -Re f_r f'_r, \quad S_3 = 0,$$

$$S_4 = RePr f_r \theta'_1 - \frac{2\lambda\beta f_r \theta_1}{(\eta-d)^3} + 4Re\lambda f'^2_r + \frac{\lambda f''^2_r}{\Gamma^2} + \frac{\lambda Re}{Da}[\cos^2(\phi) + K\sin^2(\phi)]f^2_r,$$

$$S_5 = -2RePr f'_r(\theta_2)_r + RePr f_r(\theta'_2)_r - \frac{2\lambda\beta f_r(\theta_2)_r}{(\eta-d)^3} + \frac{2\lambda\beta f'_r(\theta_1)_r}{(\eta-d)^4} + \frac{4\lambda\beta(\theta_1)_r f_r}{(\eta-d)^5}$$

$$+ \lambda\frac{1}{\Gamma^2}(f'''_r)^2 + Re\lambda(f''_r)^2 + \frac{\lambda Re}{Da}[\cos^2(\phi) + K\sin^2(\phi)]f'^2_r.$$

To solve the linearised equations (21) to (25), a Chebyshev spectral collocation approach is used. Chebyshev interpolating polynomials are used to estimate the functions unknown. The Gauss-Lobatto points are defined as $\zeta_j = \cos(\pi j/N)$, where $j = 1, 2, \cdots N$ of collocation points at which these polynomials are collocated. Derivatives of $f(\eta)$, $\theta_1(\eta)$, $\theta_2(\eta)$, $P_1(\eta)$, and $P_2(\eta)$ are determined by using the differential matrix $\mathbf{D}$ to calculate Chebyshev polynomials at the collocation points. Near collocation nodes the derivatives of f_{r+1}, $(\theta_1)_{r+1}$, $(\theta_2)_{r+1}$, $(P_1)_{r+1}$, and $(P_2)_{r+1}$ are represented as:

$$\frac{\partial^p f_{r+1}}{\partial\eta^p} = \left(\frac{2}{L}\right)^p \sum_{i=0}^{N} D^p_{N,i} f_{r+1}(\eta_i) = \mathbf{D}^p F,$$

$$\frac{\partial^p (\theta_1)_{r+1}}{\partial\eta^p} = \left(\frac{2}{L}\right)^p \sum_{i=0}^{N} D^p_{N,i} (\theta_1)_{r+1}(\eta_i) = \mathbf{D}^p \Theta_1,$$

$$\frac{\partial^p (\theta_2)_{r+1}}{\partial\eta^p} = \left(\frac{2}{L}\right)^p \sum_{i=0}^{N} D^p_{N,i} (\theta_2)_{r+1}(\eta_i) = \mathbf{D}^p \Theta_2, \tag{33}$$

$$\frac{\partial^p (P_1)_{r+1}}{\partial\eta^p} = \left(\frac{2}{L}\right)^p \sum_{i=0}^{N} D^p_{N,i} (P_1)_{r+1}(\eta_i) = \mathbf{D}^p \mathbf{P}_1,$$

$$\frac{\partial^p (P_2)_{r+1}}{\partial\eta^p} = \left(\frac{2}{L}\right)^p \sum_{i=0}^{N} D^p_{N,i} (P_2)_{r+1}(\eta_i) = \mathbf{D}^p \mathbf{P}_2.$$

where the Chebyshev differentiation matrix $\mathbf{D}$ scaled by $L/2$, is of order $(M+1) \times (M+1)$ with p derivative order. On substituting equation(33) into equations (27)- (31), we obtain

$$[a_{1,r}\mathbf{D}^5 + \mathbf{D}^3 + a_{2,r}\mathbf{D}^2 + a_{3,r}\mathbf{D} + a_{4,r}I]f_{r+1} + a_{5,r}(\theta_1)_{r+1} + a_{6,r}(P_2)_{r+1} = S_1, \tag{34}$$

$$[a_{7,r}\mathbf{D}^4 - \mathbf{D}^2 + a_{8,r}\mathbf{D} + a_{9,r}I]f_{r+1} + [a_{10,r}I](\theta_1)_{r+1} + a_{11,r}\mathbf{D}(P_1)_{r+1} = S_2, \tag{35}$$

$$a_{12,r}(\theta_1)_{r+1} + a_{13,r}(\theta_2)_{r+1} + a_{14,r}\mathbf{D}(P_2)_{r+1} = S_3 \tag{36}$$

$$[a_{15,r}\mathbf{D}^2 + a_{16,r}\mathbf{D} + a_{17,r}I]f_{r+1} + [\mathbf{D}^2 + a_{18,r}\mathbf{D} + a_{19,r}I](\theta_1)_{r+1} + [a_{20,r}I](\theta_2)_{r+1} = S_4, \tag{37}$$

$$[a_{21,r}\mathbf{D}^3 + a_{22,r}\mathbf{D}^2 + a_{23,r}\mathbf{D} + a_{24,r}I]f_{r+1} + a_{25,r}(\theta_1)_{r+1} + [\mathbf{D}^2 + a_{26,r}\mathbf{D} + a_{27,r}I](\theta_2)_{r+1} = S_5. \tag{38}$$

Applying spectral method on the boundary conditions gives:

$$f_{r+1}(\zeta_0) = 0, \quad \sum_{k=0}^{N} \mathbf{D}_{N,k} f_{r+1}(\zeta_0) = 1,$$

$$f_{r+1}(\zeta_N) = 0, \quad \sum_{k=0}^{N} \mathbf{D}^2_{N,k} f_{r+1}(\zeta_N) = 1, \quad \sum_{k=0}^{N} \mathbf{D}^3_{N,k} f_{r+1}(\zeta_0) = 0,$$

$$\sum_{k=0}^{N} \mathbf{D}_{N,k}(\theta_1)_{r+1}(\zeta_N) = 0, \quad \sum_{k=0}^{N} \mathbf{D}_{N,k}(\theta_2)_{r+1}(\zeta_N) = 0, \quad (\theta_1)_{r+1}(\zeta_0) = 1, \quad (\theta_2)_{r+1}(\zeta_0) = 0, \tag{39}$$

$$(P_1)_{r+1}(\zeta_0) = 0, \quad (P_2)_{r+1}(\zeta_0) = \frac{1}{2}.$$

The matrix form of the aforementioned equation system is written as

$$
\begin{bmatrix}
\mathbf{B}_{11} & \mathbf{B}_{12} & \mathbf{B}_{13} & \mathbf{B}_{14} & \mathbf{B}_{15} \\
\mathbf{B}_{21} & \mathbf{B}_{22} & \mathbf{B}_{23} & \mathbf{B}_{24} & \mathbf{B}_{25} \\
\mathbf{B}_{31} & \mathbf{B}_{32} & \mathbf{B}_{33} & \mathbf{B}_{34} & \mathbf{B}_{35} \\
\mathbf{B}_{41} & \mathbf{B}_{42} & \mathbf{B}_{43} & \mathbf{B}_{44} & \mathbf{B}_{45} \\
\mathbf{B}_{51} & \mathbf{B}_{52} & \mathbf{B}_{53} & \mathbf{B}_{54} & \mathbf{B}_{55}
\end{bmatrix}
\times
\begin{bmatrix}
F_{r+1} \\
\Theta_{1r+1} \\
\Theta_{2r+1} \\
P_{1r+1} \\
P_{2r+1}
\end{bmatrix}
=
\begin{bmatrix}
S_1 \\
S_2 \\
S_3 \\
S_4 \\
S_5
\end{bmatrix},
\tag{40}
$$

The boundary conditions are placed on the separate matrices as follows:

$$
\mathbf{B}_{11} =
\begin{bmatrix}
1 & 0 & \cdots & 0 & 0 \\
\mathbf{D_{1,0}} & \mathbf{D_{1,1}} & \cdots & \mathbf{D_{1,N-1}} & \mathbf{D_{1,N}} \\
\mathbf{D^3_{2,0}} & \mathbf{D^3_{2,1}} & \cdots & \mathbf{D^3_{2,N-1}} & \mathbf{D^3_{2,N}} \\
\hline
& & B_{11} & & \\
\hline
\mathbf{D^2_{N-1,0}} & \mathbf{D^2_{N-1,1}} & \cdots & \mathbf{D^2_{N-1,N-1}} & \mathbf{D^2_{N-1,N}} \\
0 & 0 & \cdots & 0 & 1
\end{bmatrix},
\quad
\mathbf{B}_{12} =
\begin{bmatrix}
0 & 0 & \cdots & 0 & 0 \\
0 & 0 & \cdots & 0 & 0 \\
0 & 0 & \cdots & 0 & 0 \\
\hline
& & B_{12} & & \\
\hline
0 & 0 & \cdots & 0 & 0 \\
0 & 0 & \cdots & 0 & 0
\end{bmatrix},
$$

$$
\mathbf{B}_{13} =
\begin{bmatrix}
0 & 0 & \cdots & 0 & 0 \\
0 & 0 & \cdots & 0 & 0 \\
0 & 0 & \cdots & 0 & 0 \\
\hline
& & B_{13} & & \\
\hline
0 & 0 & \cdots & 0 & 0 \\
0 & 0 & \cdots & 0 & 0
\end{bmatrix},
\quad
\mathbf{B}_{14} =
\begin{bmatrix}
0 & 0 & \cdots & 0 & 0 \\
0 & 0 & \cdots & 0 & 0 \\
0 & 0 & \cdots & 0 & 0 \\
\hline
& & B_{14} & & \\
\hline
0 & 0 & \cdots & 0 & 0 \\
0 & 0 & \cdots & 0 & 0
\end{bmatrix},
\quad
\mathbf{B}_{15} =
\begin{bmatrix}
0 & 0 & \cdots & 0 & 0 \\
0 & 0 & \cdots & 0 & 0 \\
0 & 0 & \cdots & 0 & 0 \\
\hline
& & B_{15} & & \\
\hline
0 & 0 & \cdots & 0 & 0 \\
0 & 0 & \cdots & 0 & 0
\end{bmatrix},
$$

$$
\mathbf{B}_{21} =
\begin{bmatrix}
0 & 0 & \cdots & 0 & 0 \\
\hline
& & B_{21} & & \\
\hline
0 & 0 & \cdots & 0 & 0
\end{bmatrix},
\quad
\mathbf{B}_{22} =
\begin{bmatrix}
1 & 0 & \cdots & 0 & 0 \\
\hline
& & B_{22} & & \\
\hline
\mathbf{D_{N,0}} & \mathbf{D_{N,1}} & \cdots & \mathbf{D_{N,N-1}} & \mathbf{D_{N,N}}
\end{bmatrix},
$$

$$
\mathbf{B}_{23} =
\begin{bmatrix}
0 & 0 & \cdots & 0 & 0 \\
\hline
& & B_{23} & & \\
\hline
0 & 0 & \cdots & 0 & 0
\end{bmatrix},
\quad
\mathbf{B}_{24} =
\begin{bmatrix}
0 & 0 & \cdots & 0 & 0 \\
\hline
& & B_{24} & & \\
\hline
0 & 0 & \cdots & 0 & 0
\end{bmatrix},
\quad
\mathbf{B}_{25} =
\begin{bmatrix}
0 & 0 & \cdots & 0 & 0 \\
\hline
& & B_{25} & & \\
\hline
0 & 0 & \cdots & 0 & 0
\end{bmatrix},
$$

$$
\mathbf{B}_{31} =
\begin{bmatrix}
0 & 0 & \cdots & 0 & 0 \\
\hline
& B_{31} & \\
\hline
0 & 0 & \cdots & 0 & 0
\end{bmatrix},
\quad
\mathbf{B}_{32} =
\begin{bmatrix}
0 & 0 & \cdots & 0 & 0 \\
\hline
& B_{32} & \\
\hline
0 & 0 & \cdots & 0 & 0
\end{bmatrix},
\quad
\mathbf{B}_{33} =
\begin{bmatrix}
1 & 0 & \cdots & 0 & 0 \\
\hline
& & B_{33} & & \\
\hline
\mathbf{D_{N,0}} & \mathbf{D_{N,1}} & \cdots & \mathbf{D_{N,N-1}} & \mathbf{D_{N,N}}
\end{bmatrix},
$$

$$
\mathbf{B}_{34} =
\begin{bmatrix}
1 & 0 & \cdots & 0 & 0 \\
\hline
& & B_{34} & & \\
\hline
0 & 0 & \cdots & 0 & 1
\end{bmatrix},
\quad
\mathbf{B}_{35} =
\begin{bmatrix}
1 & 0 & \cdots & 0 & 0 \\
\hline
& & B_{35} & & \\
\hline
0 & 0 & \cdots & 0 & 1
\end{bmatrix},
\quad
\mathbf{B}_{41} =
\begin{bmatrix}
0 & 0 & \cdots & 0 & 0 \\
\hline
& & B_{41} & & \\
\hline
0 & 0 & \cdots & 0 & 0
\end{bmatrix},
$$

$$
\mathbf{B}_{42} =
\begin{bmatrix}
0 & 0 & \cdots & 0 & 0 \\
\hline
& & B_{42} & & \\
\hline
0 & 0 & \cdots & 0 & 0
\end{bmatrix},
\quad
\mathbf{B}_{43} =
\begin{bmatrix}
0 & 0 & \cdots & 0 & 0 \\
\hline
& & B_{43} & & \\
\hline
0 & 0 & \cdots & 0 & 0
\end{bmatrix},
\quad
\mathbf{B}_{44} =
\begin{bmatrix}
1 & 0 & \cdots & 0 & 0 \\
\hline
& & B_{44} & & \\
\hline
0 & 0 & \cdots & 0 & 0
\end{bmatrix},
$$

$$
\mathbf{B}_{45} =
\begin{bmatrix}
0 & 0 & \cdots & 0 & 0 \\
\hline
& & B_{45} & & \\
\hline
0 & 0 & \cdots & 0 & 0
\end{bmatrix},
\quad
\mathbf{B}_{51} =
\begin{bmatrix}
0 & 0 & \cdots & 0 & 0 \\
\hline
& & B_{51} & & \\
\hline
0 & 0 & \cdots & 0 & 0
\end{bmatrix},
\quad
\mathbf{B}_{52} =
\begin{bmatrix}
0 & 0 & \cdots & 0 & 0 \\
\hline
& & B_{52} & & \\
\hline
0 & 0 & \cdots & 0 & 0
\end{bmatrix},
$$

$$\mathbf{B}_{53} = \begin{bmatrix} 0 & 0 & \cdots & 0 & 0 \\ & & B_{53} & & \\ 0 & 0 & \cdots & 0 & 0 \end{bmatrix}, \mathbf{B}_{54} = \begin{bmatrix} 0 & 0 & \cdots & 0 & 0 \\ & & B_{54} & & \\ 0 & 0 & \cdots & 0 & 0 \end{bmatrix}, \quad \mathbf{B}_{55} = \begin{bmatrix} 1 & 0 & \cdots & 0 & 0 \\ & & B_{55} & & \\ 0 & 0 & \cdots & 0 & 0 \end{bmatrix},$$

$$\mathbf{F}_{r+1} = \begin{bmatrix} f_{r+1,0} \\ f_{r+1,1} \\ \vdots \\ f_{r+1,N-2} \\ f_{r+1,N-1} \\ f_{r+1,N} \end{bmatrix}, \mathbf{\Theta_1}_{r+1} = \begin{bmatrix} \theta_{1r+1,0} \\ \vdots \\ \vdots \\ \theta_{1r+1,N} \end{bmatrix}, \quad \mathbf{\Theta_2}_{r+1} = \begin{bmatrix} \theta_{2r+1,0} \\ \vdots \\ \vdots \\ \theta_{2r+1,N} \end{bmatrix}, \quad \mathbf{P_1}_{r+1} = \begin{bmatrix} P_{1r+1,0} \\ \vdots \\ \vdots \\ 0 \end{bmatrix},$$

$$P_{2r+1} = \begin{bmatrix} \mathbf{P}_{2r+1,0} \\ \vdots \\ \vdots \\ 0 \end{bmatrix}, S_1 = \begin{bmatrix} 0 \\ 1 \\ 0 \\ \mathbf{s_1} \\ 1 \\ 0 \end{bmatrix}, \quad S_2 = \begin{bmatrix} 0 \\ \mathbf{s_2} \\ 1 \end{bmatrix}, \quad S_3 = \begin{bmatrix} 0 \\ \mathbf{s_3} \\ 0 \end{bmatrix}, \quad S_4 = \begin{bmatrix} 0 \\ \mathbf{s_4} \\ 0 \end{bmatrix}, \quad S_5 = \begin{bmatrix} \frac{1}{2} \\ \mathbf{s_5} \\ 0 \end{bmatrix},$$

where

$$B_{11} = [\text{diag}(\mathbf{a}_{1,r}) \quad 1 \quad \text{diag}(\mathbf{a}_{2,r}) \quad \text{diag}(\mathbf{a}_{3,r}) \quad \text{diag}(\mathbf{a}_{4,r})][\mathbf{D}^5 \quad \mathbf{D}^3 \quad \mathbf{D}^2 \quad \mathbf{D} \quad I]^T,$$

$$B_{12} = \text{diag}(\mathbf{a}_{5,r}), \ B_{13} = 0, \quad B_{14} = 0, \quad B_{15} = \text{diag}(\mathbf{a}_{6,r}),$$

$$B_{21} = [\text{diag}(\mathbf{a}_{7,r}) - 1 \quad \text{diag}(\mathbf{a}_{8,r}) \quad \text{diag}(\mathbf{a}_{9,r})][\mathbf{D}^4 \quad \mathbf{D}^2 \quad \mathbf{D} \quad I]^T,$$

$$B_{22} = \text{diag}(\mathbf{a}_{10,r}), \quad B_{23} = 0, \quad B_{24} = [\text{diag}(\mathbf{a}_{11,r})]\mathbf{D}, \quad B_{25} = 0,$$

$$B_{31} = 0, \quad B_{32} = \text{diag}(\mathbf{a}_{12,r}), \quad B_{33} = [\text{diag}(\mathbf{a}_{13,r}), \quad B_{34} = 0, \quad B_{35} = [\text{diag}(\mathbf{a}_{14,r})][\mathbf{D}],$$

$$B_{41} = [\text{diag}(\mathbf{a}_{15,r}) \quad \text{diag}(\mathbf{a}_{16,r}) \quad \text{diag}(\mathbf{a}_{17,r})][\mathbf{D}^2 \quad \mathbf{D} \quad I]^T,$$

$$B_{42} = [1 \quad \text{diag}(\mathbf{a}_{18,r}) \quad \text{diag}(\mathbf{a}_{19,r})][\mathbf{D}^2 \quad \mathbf{D} \quad I]^T, \ B_{43} = \text{diag}(\mathbf{a}_{20,r}), \quad B_{44} = 0, \quad B_{45} = 0,$$

$$B_{51} = [\text{diag}(\mathbf{a}_{21,r}) \quad \text{diag}(\mathbf{a}_{22,r}) \quad \text{diag}(\mathbf{a}_{23,r}) \quad \text{diag}(\mathbf{a}_{24,r})][\mathbf{D}^3 \quad \mathbf{D}^2 \quad \mathbf{D} \quad I]^T, \ B_{52} = \text{diag}(\mathbf{a}_{25,r}),$$

$$B_{53} = [1 \quad \text{diag}(\mathbf{a}_{26,r}) \quad \text{diag}(\mathbf{a}_{27,r})][\mathbf{D}^2 \quad \mathbf{D} \quad I]^T, \ B_{54} = 0, \quad B_{55} = 0,$$

where $\mathbf{a}$, I, 0 are diagonal, unit, and null matrices, respectively, of order (N + 1)×(N + 1).

4. CONVERGENCE ANALYSIS AND RESULTS

Convergence analysis entails demonstrating that the iterative approach converges to an exact solution for the non-linear system of equations (21) and (25), by taking boundary conditions (26) into account. The calculation of residual errors is performed to guarantee the precision of the numerical results. Inaccuracies measure the extent of discrepancy between the numerical and the precise original solution. These errors quantify the degree of deviation experienced by the numerical solution from the original solution. For equations (27) and (29), the residual errors obtained are as follows:

$$Res(f) = -\frac{1}{\Gamma^2}f^V + f''' + Re[ff'' - (f')^2] + 2ReP_2 - \frac{2\beta\theta_1}{Re(\eta - d)^4}$$
$$- \frac{1}{Da}\Big[(K\cos^2(\phi) + \sin^2(\phi))\Big]f'(\eta), \tag{41}$$

$$Res(\theta_1) = \theta_1'' + 2\theta_2 + RePrf\theta_1' - \frac{2\lambda\beta(\theta_1)f}{(\eta - d)^3} + \frac{\lambda}{\Gamma^2}(f'')^2 + 4Re\lambda(f')^2$$
$$+ \frac{1}{Da}\lambda Re[\cos^2(\phi) + K\sin^2(\phi)]f^2. \tag{42}$$

$\|Res(f)\|_\infty$, $\|Res(\theta_1)\|_\infty$, are the infinity norms (or maximum norm) of equations (41) and (42), which quantify the largest absolute value of the error throughout the domain. The impact of increasing the count of collocation points (N) on the accuracy of the solution produced by the SQLM (Spectral Quasi-linearization Method) is examined in Fig (2). In figure 2(a), the residual error in f over 30 iterations for various numbers of collocation points (N = 25, 30, 35) is displayed. Collocation points between 25 and 35 yield the best accuracy, with residual errors of about 10^{-6}. Similarly, for the residual error in θ_1 that is shown in 2(b), the ideal residuals are obtained with values of about 10^{-9}. The accuracy

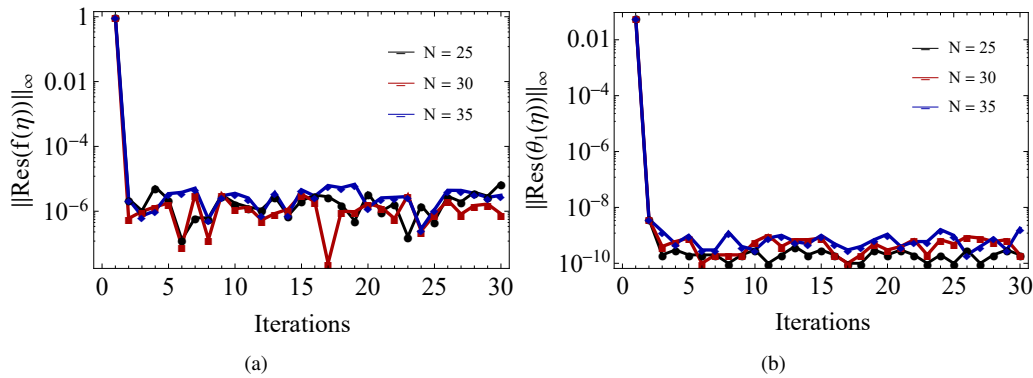(a)   (b)

Figure 2. Influence of iterations on (a) $\|Res(f(\eta))\|_\infty$ and (b) $\|Res(\theta_1)\|_\infty$ for collocation points when $\Gamma = 2$, $d = 2$, β = 5, $\lambda = 0.01$, $Da = 1$, $Pr = 1$, $K = 0.05$, $\phi = \pi/4$, $Re = 1$.

steadily decreases after this range of collocation points. According to these findings, the numerical approach achieves maximum accuracy with 30-35 collocation points and performs optimally after the fifth iteration. Beyond this range, the accuracy is observed to decrease, as the number of collocation points are increased, and the residual errors stabilise at values that suggest optimal convergence.

Theoretical estimates of the influence of couple stress parameter, ferromagnetic interaction parameter, anisotropic permeability ratio, anisotropic angle, Reynolds number, Darcy number, and Prandtl number on the distributions of velocity and temperature have been determined. Additionally, the influence of β and Pr on the distribution of pressure is also determined. Figures in (3) - (5) depict the variation of the dimensionless axial velocity $f'(\eta)$ for a given cross-section η of channel for different parameters. In figure 3(a), it is observed that higher values of Γ lead to an increase of axial velocity up to a certain height and a slow decrease towards the upper channel wall. An increase of couple stress parameter leads to increase in viscosity, thereby reducing the flow of fluid, and also indicates that the wider the channel, the smaller the magnitude of velocity. This is consistent with the concept that the couple stress fluids experience additional resistance or internal friction due to microstructural interactions. From figure 3(b), it can be noticed that higher values of ferromagnetic
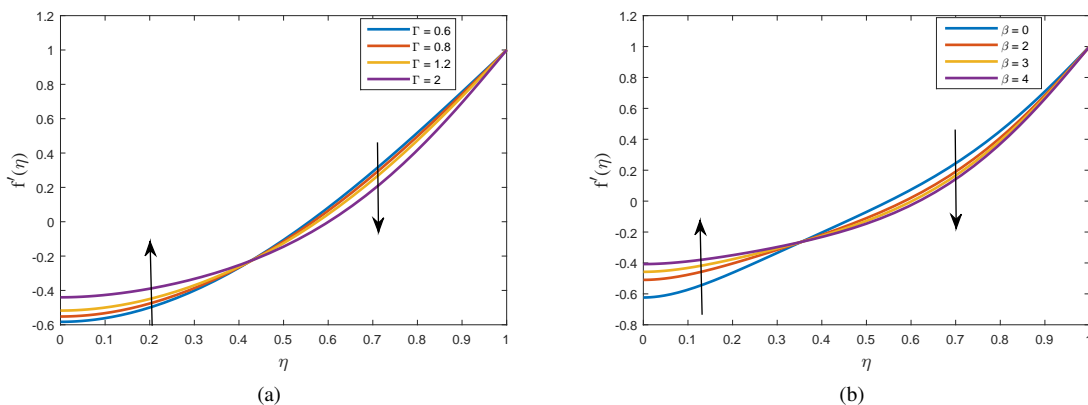

(a)   (b)

Figure 3. Axial velocity profile for different values of (a) Couple stress parameter Γ (b) Ferromagnetic interaction parameter β for $\Gamma = 3$, $d = 2$, β = 5, $\lambda = 0.2$, $Da = 0.01$, $Pr = 1$, $K = 0.005$, $\phi = \pi/4$, $Re = 1$.

interaction parameter β lead to an increase in velocity up to a certain height, after which it reduces. A magnetic force generated by an applied magnetic field opposes the fluid motion. Figures in (4) illustrate the impact of K and Da on $f'(\eta)$, the axial velocity. Figure 4(a) depicts a reduction in magnitude of velocity with a rise in values of anisotropic ratio $K = k_{11}/k_{22}$ and fixed $Da(< 1)$ towards the upper boundary. As anticipated, for a given Da, increasing the permeability ratio K lowers the permeability in the flow direction and consequently, declines the velocity's magnitude. Figure 4(b) illustrates that higher values of Da result in a decrease of velocity in vicinity of the center line and then gradually increase from the centre line towards the upper boundary. When Darcy number is high, viscous effects dominate inertial effects which result in decrease of fluid's total velocity. Figures in (5) depict the impacts of ϕ, Pr, and Re upon axial velocity. The profile of axial velocity for various anisotropic angles ϕ is illustrated in figure 5(a). Optimal velocity is attained
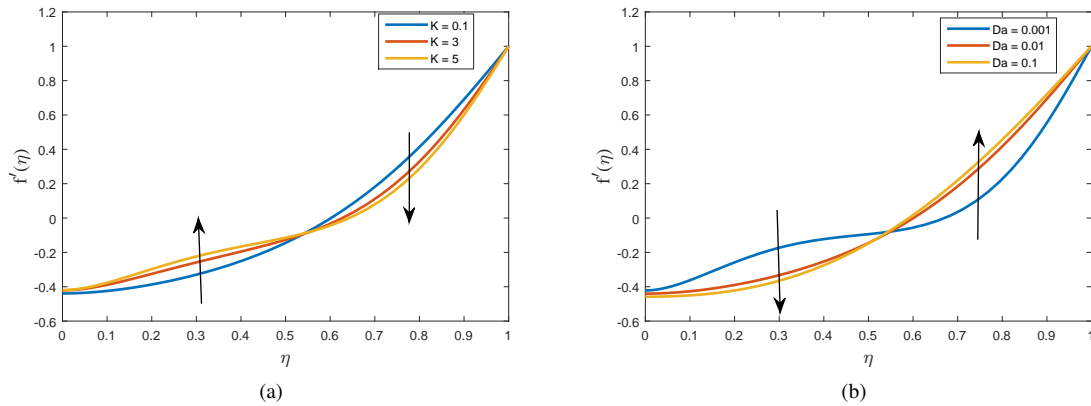
Figure 4. Axial velocity profile for different values of (a) Anisotropic permeability ratio K (b) Darcy number Da for Γ = 2, d = 2, β = 5, λ = 0.2, Da = 0.01, Pr = 1, K = 0.005, ϕ = $\pi/4$, Re = 1.
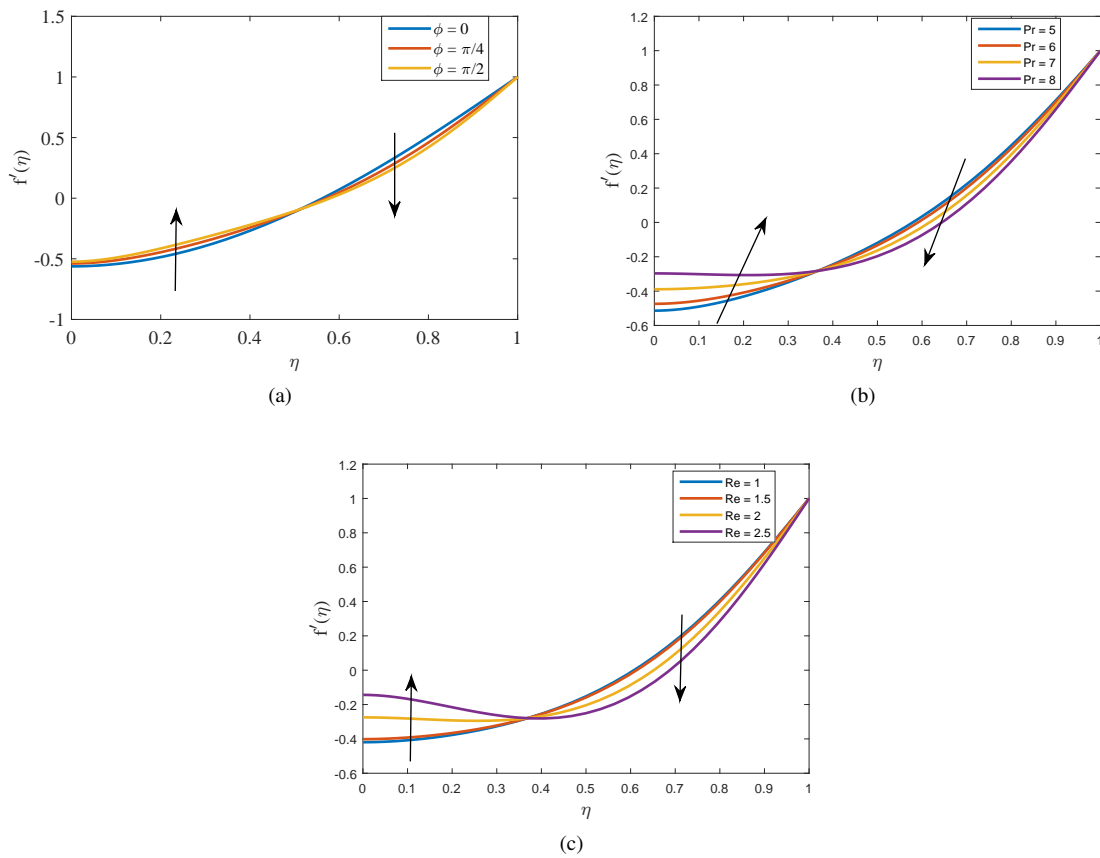

Figure 5. Axial velocity profile for different values of (a) Anisotropic angle ϕ (b) Prandtl number Pr for Γ = 2, d = 2, β = 1, λ = 0.2, Da = 0.01, Pr = 1, K = 0.005, ϕ = $\pi/4$, Re = 0.5 (c) Reynolds number Re for Γ = 2, d = 2, β = 5, λ = 0.2, Da = 0.01, Pr = 2, K = 0.005, ϕ = $\pi/4$.

A Biomagnetic Couple Stress Fluid Flow in an Anisotropic Horous Channel...

169
EEJP. 4 (2024)

when $\phi = 0$, while the lowest velocity is seen when $\phi = \frac{\pi}{2}$. This behaviour is consistent with the concept that when the value of K is less than or equal to 1 and keeps Da or k_{11} constant, a value of $\phi = 0$ indicates a higher horizontal permeability k_{22}. Conversely, if the value of K is greater than 1, the behaviour will be the opposite. The value of $\phi = 0$ is equivalent to k_{22} the horizontal permeability, resulting in the permeability to reduce in the flow direction. With an increase in values of anisotropic angle, velocity increases up to a certain height and then decreases towards the upper wall. In figure 5(b), up to a certain channel height, axial velocity is noticed to increase and decrease thereafter towards the boundary with an increase of Prandtl number Pr. Prandtl number Pr is a dimensionless number that charaterises the relative thickness of the boundary layers formed by both momentum and heat. Fluid accelerates more effectively within a thicker momentum boundary layer. Figure 5(c) illustrates the increase of velocity up to a certain height and a gradual decrease towards the upper wall, as Reynolds number Re increases. The magnetic force exerts a substantial influence on the flow near the vicinity of magnetic field within a channel, leading to reduction in velocity. Figures (6)-(7) illustrate the
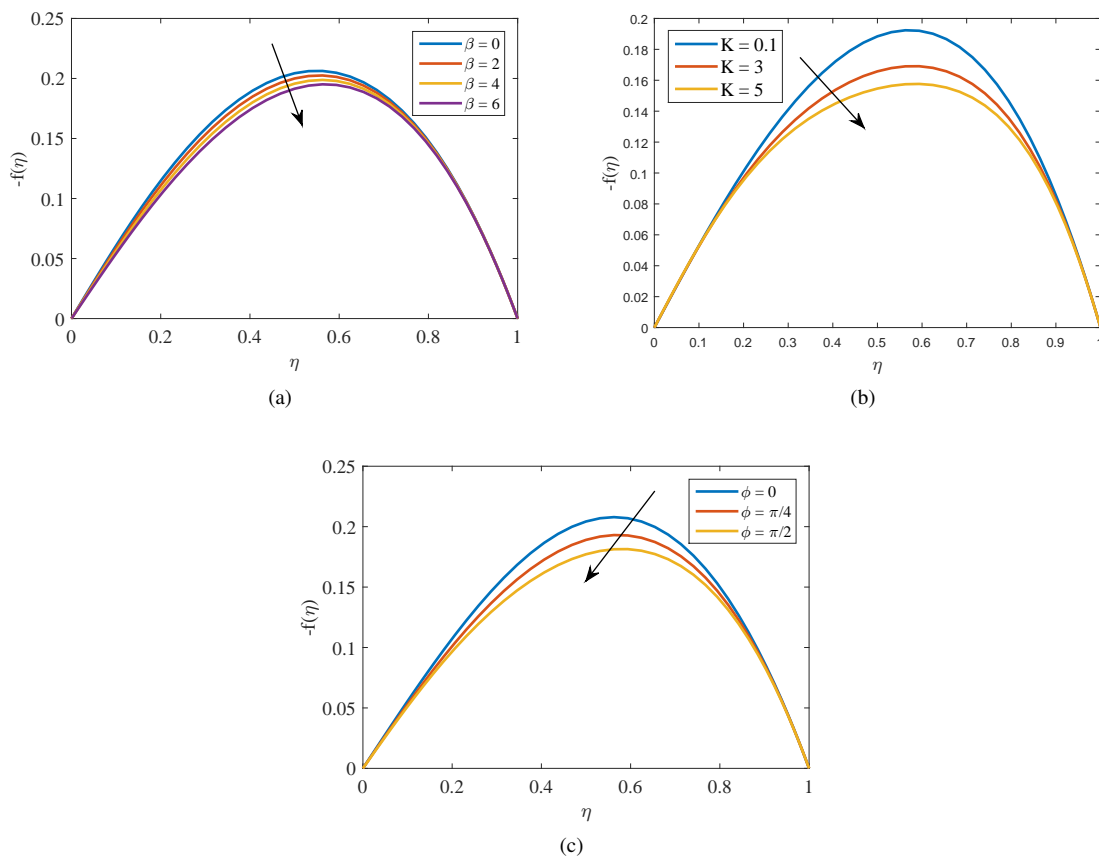

Figure 6. Transverse velocity profile for different values of (a) Ferromagnetic interaction parameter β (b) Anisotropic permeability ratio K (c) Anisotropic angle ϕ for $\Gamma = 2$, $d = 2$, $\beta = 5$, $\lambda = 0.2$, $Da = 0.01$, $Pr = 5$, $K = 0.005$, $\phi = \pi/4$, $Re = 2$.

distribution of dimensionless transverse velocity $-f(\eta)$ for different values of β, K, ϕ, Γ, and Re. Figure 6(a) depicts that transverse velocity decreases with increasing values of β. Transverse motion is reduced when β increases because it strengthens the relation between ferromagnetic particles and the magnetic field. In practical situations, this phenomenon controls the motion and stability of magnetic fluids. In figure 6(b) the velocity is seen reducing for higher values of anisotropic permeability ratio K. For a fixed Da (fixed k_{11}), an increase in K implies a reduction or decrease in k_{22} the horizontal permeability. As k_{22} decreases, the shear resistance increases in the horizontal direction, thereby increasing the dissipation of energy due to internal friction in the flow. This energy dissipation affects the overall reduction of the momentum of fluid and indirectly, the transverse velocity also. In figure 6(c) the velocity is seen reducing for higher values of anisotropic angle ϕ. Elevating anisotropic angle ϕ has dampening effect on velocity, which may be due to permeability ratio K and magnetic parameter that inhibits the flow. Figure 7(a) shows that higher values of Γ result in reduction of velocity. The decrease in transverse velocity within a fluid is due to the increased rotational resistance experienced by the fluid. Figure 7(b), demonstrates a reduction in transverse velocity as the Prandtl number Pr is increased. This phenomenon is because the higher momentum diffusivity compared to thermal diffusivity amplifies thermal gradients and buoyancy effects, resulting in stronger convective currents in the transverse direction. Moreover, the increased viscosity

aids in maintaining these lateral movements. Figure 7(c) illustrates that higher values of Reynolds number Re lead to a reduction in velocity. Generally this is due to the growing influence of inertia in the flow. This leads to a stabilisation in the primary flow direction and a decrease in contribution of viscous forces that facilitate transverse motion.
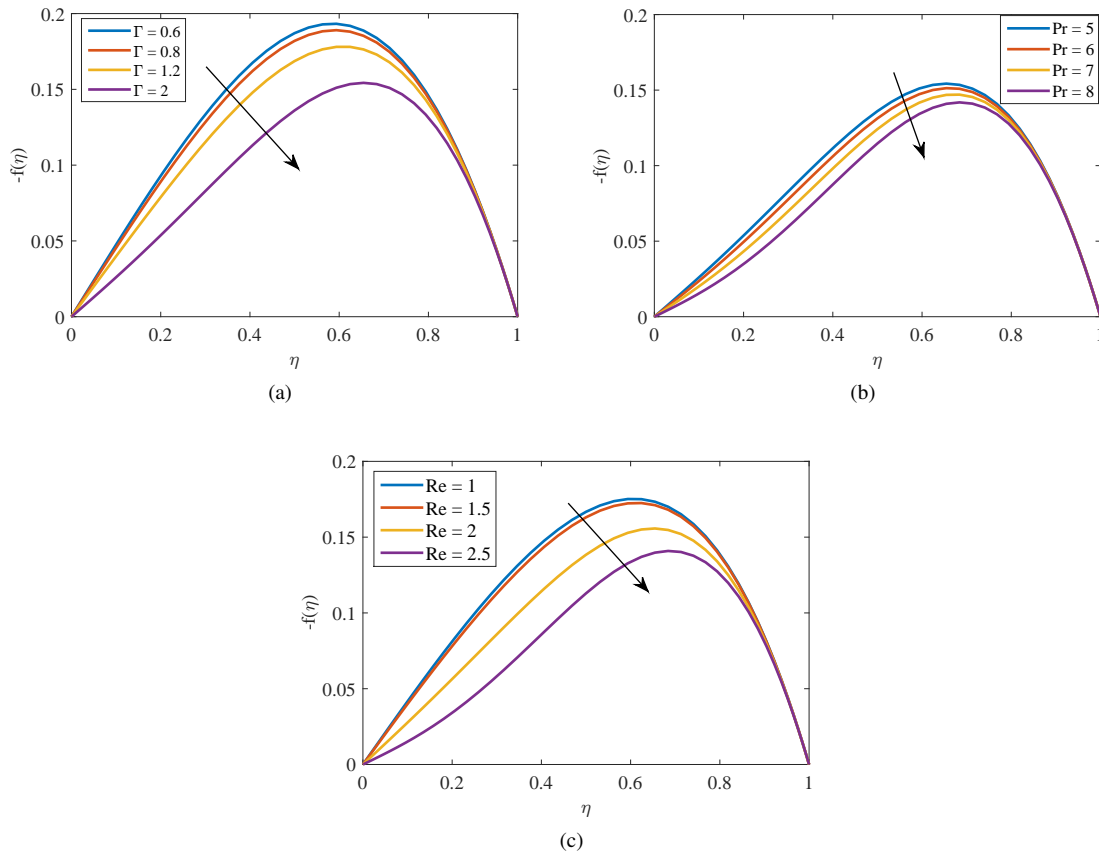

(a)

(b)

(c)

Figure 7. Transverse velocity profile for different values of (a) Couple stress parameter Γ (b) Prandtl number Pr (c) Reynolds number Re for $\Gamma = 2$, $d = 2$, $\beta = 5$, $\lambda = 0.2$, $Da = 0.01$, $Pr = 5$, $K = 0.005$, $\phi = \pi/4$, $Re = 0.5$.
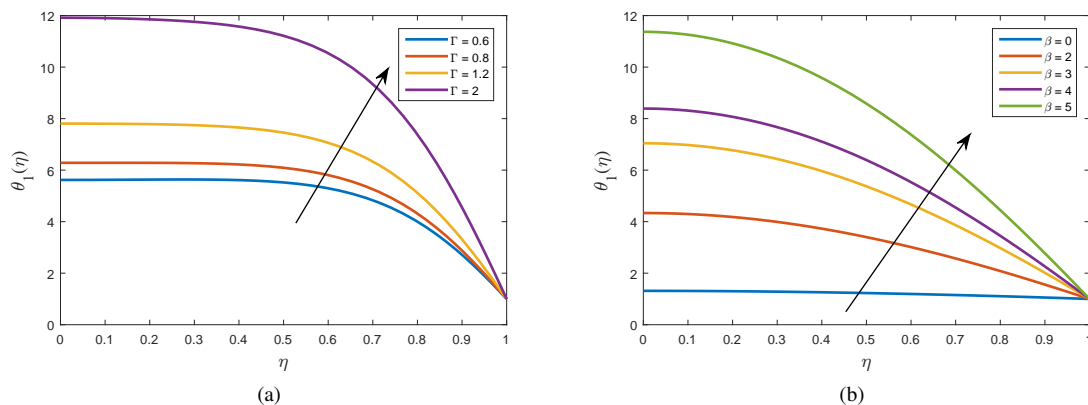
(a)

(b)

Figure 8. Temperature profile for different values of (a) Couple stress parameter Γ for $d = 2$, $\beta = 1$, $\lambda = 0.2$, $Da = 0.01$, $Pr = 1$, $K = 0.005$, $\phi = \pi/4$, $Re = 21$ (b) Ferromagnetic interaction parameter β for $\Gamma = 2$, $d = 2$, $\lambda = 0.2$, $Da = 0.01$, $Pr = 1$, $K = 0.005$, $\phi = \pi/4$, $Re = 0.01$.

The variation of temperature profile for different parameters is illustrated in figures (8)-(10). Figure 8(a) illustrates that higher values of couple stress parameter Γ result in an increase in temperature. A greater temperature gradient
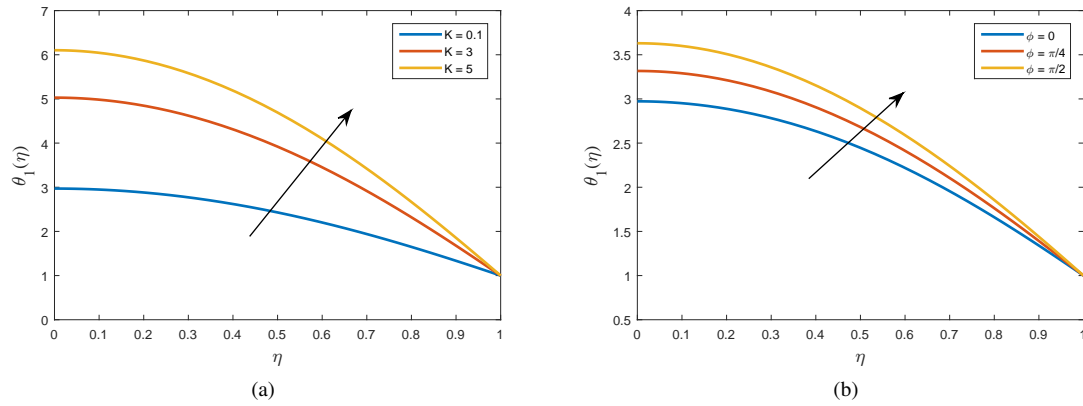
Figure 9. Temperature profile for different values of (a) Anisotropic permeability ratio K (b) Anisotropic angle ϕ for $\Gamma = 2$, $d = 2$, $\beta = 1$, $\lambda = 0.2$, $Da = 0.01$, $Pr = 1$, $K = 0.5$, $\phi = \pi/4$, $Re = 1$.
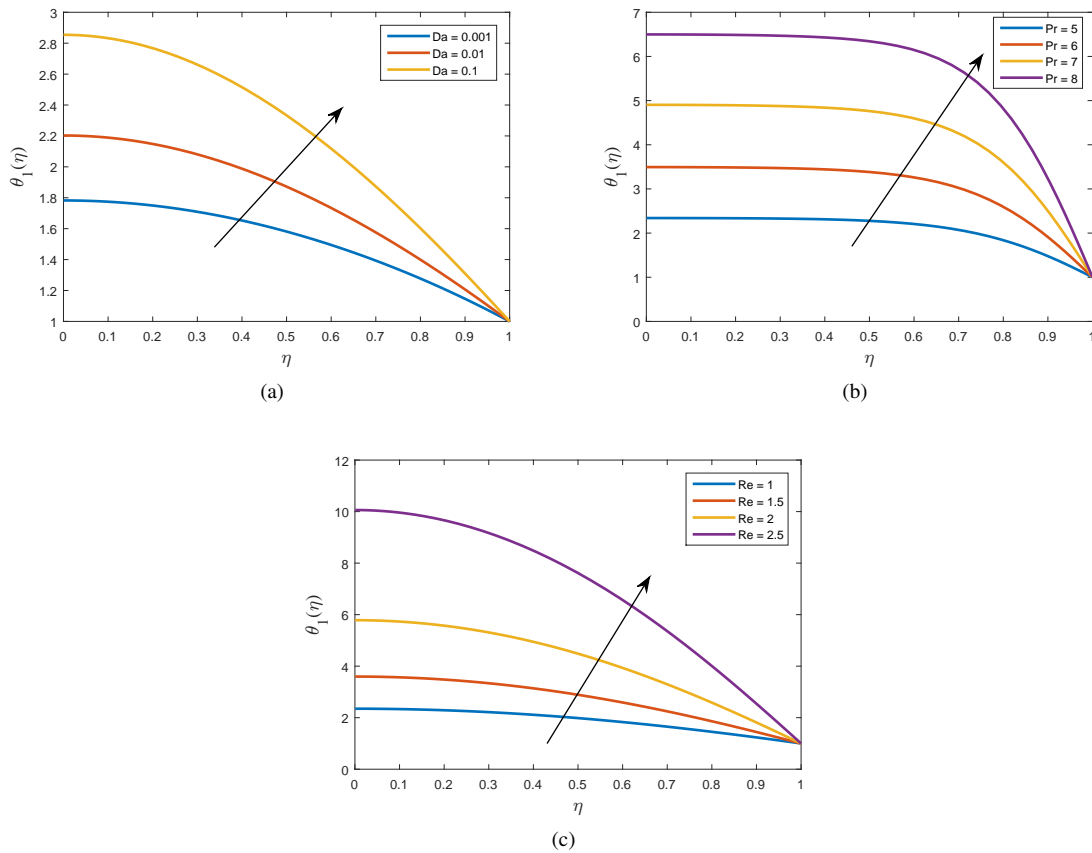

Figure 10. Temperature profile for different values of (a) Darcy number Da (b) Prandtl number Pr (c) Reynolds number Re for $\Gamma = 2$, $d = 2$, $\beta = 1$, $\lambda = 0.2$, $Da = 0.01$, $Pr = 1$, $K = 0.005$, $\phi = \pi/4$, $Re = 0.05$.

results from a thinner thermal boundary layer, which is indicated by a rise in Γ. This leads to enhanced heat transfer at the wall's surface and contributes to the deceleration of fluid. Figure 8(b) depicts an increase of temperature with an increase of ferromagnetic interaction parameter β. A more pronounced temperature difference resulting from an increase in β suggests a reduced thermal boundary layer in close proximity to wall. Enhancement of effective heat transfer from the fluid's surface to its interior occurs at higher values of β. The findings indicate that when the ferromagnetic interaction parameter β is increased, boundary layer temperature and velocity profiles have a significant impact. The findings depicted in figure 8(b) hold significant implications for the management of tumours and cancer therapy, as the aim of hyperthermia is to elevate the temperature of malignant tissues beyond the therapeutic range of 42°C. Plasma protein undergoes irreversible damage when blood temperatures rise above 42°C. Figure 9(a) shows a rise in temperature, with increase in values of K. Increased permeability results in enhanced convection, improved mixing, and consistent temperatures. On the other hand, when permeability is reduced, it limits the movement of fluids, resulting in more pronounced variations in temperature. Figure 9(b) illustrates the increase of temperature when the anisotropic angle ϕ is raised. Figure 10(a) shows that higher Da values typically correspond to more permeable media, allowing for more efficient heat transfer. Figures 10(b) and 10(c) show that higher values of Prandtl number Pr and Reynolds number Re lead to an increase in temperature. A high Pr value, exceeding 5, suggests that fluid momentum is a more advantageous means of heat transfer compared to thermal diffusion. Stated differently, a large Pr value suggests that fluid momentum, rather than fluid conduction, is more prone to induce heat transfer. An illustration of the pressure profile variation for
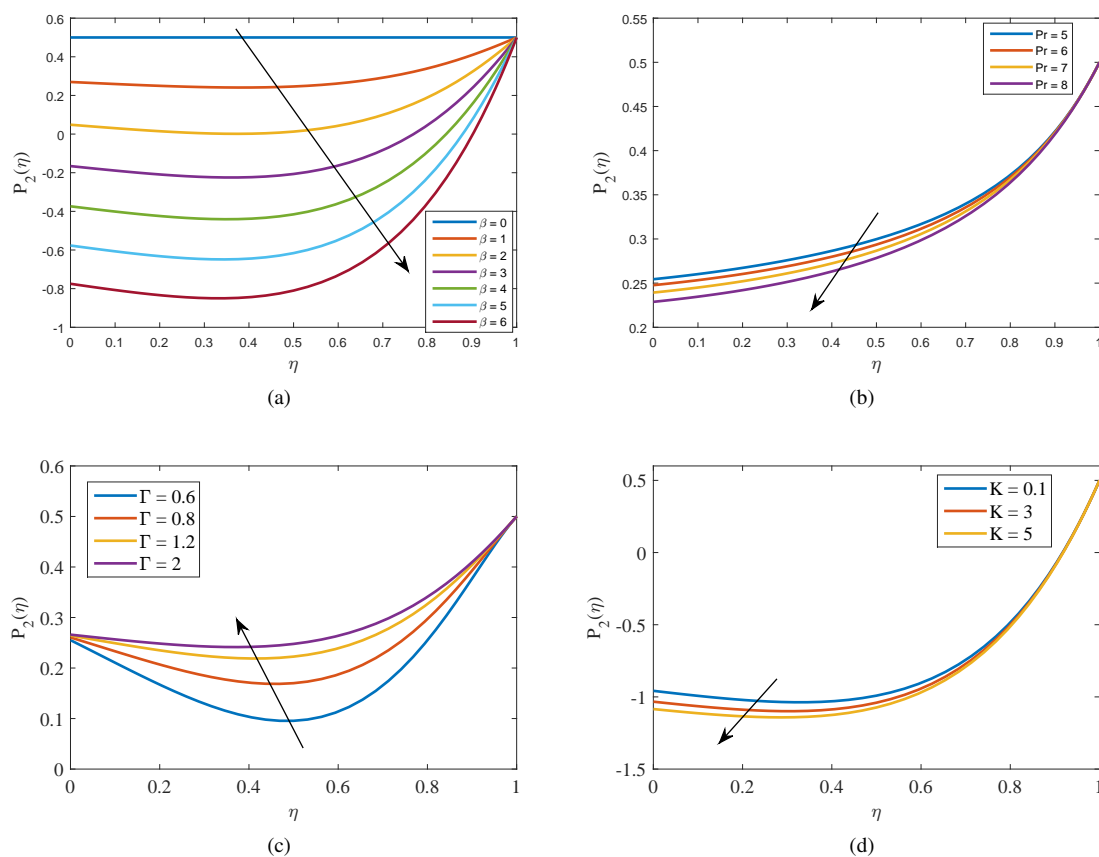

Figure 11. Pressure profile for different values of (a) Ferromagnetic interaction parameter β (b) Prandtl number Pr (c) Couple stress parameter Γ (d) Anisotropic permeability ratio K for $\Gamma = 2$, $d = 2$, $\beta = 7$, $\lambda = 0.2$, $Da = 0.1$, $Pr = 1$, $K = 0.5$, $\phi = \pi/2$, $Re = 2$.

different values of β, Pr, Γ, and K can be seen in figure (11). This figure demonstrates that higher values of β, Pr, and K result in pressure drops while a rise in pressure when Γ is increased. Hypothetical findings in figure 11(a) are highly relevant for clinical interventions, where the application of a suitably powerful magnetic force field can be utilized to control blood pressure. As the fluid resists both thermal and momentum diffusion more strongly, higher values of Pr (fig.11(b)) generally lead to greater pressure drops across the channel, so increasing the overall resistance to flow. In figure 11(c), we observe the rise in pressure with an increase of Γ. The pressure profile can be noticed to be flattened, indicating less and smoother variation. Figure 11(d) depicts a decline in pressure as the values of K are increased which suggests a more streamlined flow and maximum pressure can be noticed at the upper boundary wall. The parameters of

local skin friction and rate of heat transfer are essential for the analysis of flow and heat transfer. The following relations are used to define these quantities:

$$C_f = \frac{\tau_\omega}{\rho c^2 x^2}, \quad Nu_x = \frac{x}{T_w}\frac{\partial T}{\partial y}\big|_{y=1} \tag{43}$$

Using equations (16-20) in equation (43) we get:

$$C_f Re_x^{\frac{1}{2}} = [f''(1) - \frac{1}{\Gamma^2}f''''(1)], \qquad Nu_x Re_x^{\frac{-1}{2}} = (\theta_1'(1) + \xi^2\theta_2'(1)) \tag{44}$$

In the above equations $\tau_\omega = \left[\mu(\frac{\partial u}{\partial y}) - \gamma(\frac{\partial^3 u}{\partial y^3})\right]_{y=1}$ represents shear stress at wall, Nu_x is local Nusselt number, and $Re_x = \frac{\rho c x^2}{\mu}$ is local Reynolds number. Also $\theta'(1) = (\theta_1'(1) + \xi^2\theta_2'(1))$ is the dimensionless heat transfer parameter at wall. It is evident that the ferromagnetic interaction parameter β has an impact on the flow field. However, the flow problem is separated from the thermal energy problem in the hydrodynamic case ($\beta=0$), where P_2 becomes constant and zero (See Equations (23) and (26)). Therefore it is more intriguing and practical to replace the dimensionless wall heat transfer parameter $\theta'(1) = (\theta_1'(1) + \xi^2\theta_2'(1))$ by the ratio $\theta^*(1) = \frac{\theta_1'(1)}{\theta_1'(1)|_{\beta=0}}$ which is dimensionless and independent of ξ and represents coefficient of heat transfer rate at the wall.

Γ	$f''(1) - \frac{1}{\Gamma^2}f''''(1)$					
	$\beta=0$	$\beta=3$	$\beta=5$	$\beta=7$	$\beta=9$	$\beta=11$
0.2	123.3324773	127.257181	129.8463308	132.4148978	134.9635621	137.4935335
0.3	56.6660337	59.61461236	61.56274982	63.49615971	65.41650618	67.32454648
0.4	33.333494	35.93842135	37.65954421	39.36947234	41.06914359	42.75847324
0.5	22.53442963	24.97755792	26.59253685	28.19715192	29.79325785	31.38089637
1	8.140794606	10.34148191	11.79708708	13.24627189	14.69095588	16.13263003
10	3.433573507	5.00769968	6.06391105	7.133794256	8.219453759	9.322318935
100	3.292810745	4.83203191	5.871098686	6.930397385	8.012385729	9.118768452

Table 1. Distribution of dimensionless wall shear parameter $f''(1) - \frac{1}{\Gamma^2}f''''(1)$

Tables (1) and (2) display variations in Skin friction cofficient and heat transfer rate for different values of Γ and β. The other parameters are maintained at following values: $d = 2$, $\lambda = 0.2$, $Da = 0.1$, $Pr = 1$, $K = 0.05$, $\phi = \pi/4$, $Re = 1$.

Γ	$\theta^*(1) = \frac{\theta_1'(1)}{\theta_1'(1)|_{\beta=0}}$				
	$\beta=0$	$\beta=3$	$\beta=5$	$\beta=7$	$\beta=9$
0.2	-3.4970961551	-3.4986914879	-3.4997561776	-3.5008218082	-3.5018883853
0.3	-1.5708573035	-1.5724195493	-1.5734629036	-1.5745077275	-1.5755540441
0.4	-0.8966478411	-0.8981991396	-0.8992365341	-0.9002764930	-0.9013190138
0.5	-0.5845572012	-0.5861041374	-0.5871404232	-0.5881807258	-0.5892250551
1	-0.1681483019	–0.1696977885	-0.1718171673	-0.1718171673	-0.1729002803
10	-0.0278343318	-0.0299616020	-0.0313761276	-0.0328310790	-0.0343730535

Table 2. Distribution of coefficient of heat transfer rate $\theta^*(1)$

Table (1) presents variations of the local skin friction coefficient for various values of the parameters Γ and β. At the surface, the drag force is decreased by higher couple stress parameters, as Table (1) shows. Microstructural effects of couple stress fluids can reduce the total frictional resistance against fluid flow, producing a smoother fluid motion. Higher values of the ferromagnetic interaction parameter result in an increase in the magnetic force, which acts as a resistive force like drag force, within the fluid. Consequently, the velocity gradient near the wall becomes more pronounced, resulting in an elevation in the shear stresses. Hence the coefficient of skin friction rises with increase of magnetic parameter. The variations in heat transfer rate at channel wall's surface for different values of Γ and β are summarised in Table (2). It can be inferred from this that higher values of Γ lead to an increased heat transfer rate near the surface. For a given Γ, increasing β leads to a reduction in heat transfer rate. The microstructural effects in a couple stress fluids obstruct thermal conductivity and hence reduce heat transfer efficiency. This table supports the conclusion that microstructural effects from couple stress and ferromagnetic interaction parameters significantly influence heat transfer behaviour.

5. CONCLUSION

In this paper, the dynamics of biomagnetic couple stress fluid in a channel with stretchable walls, are analysed. The channel is saturated with an anisotropic porous medium. The governing equations, accounting for couple stresses and magnetic forces, are solved using the Spectral Quasi-Linearization Method (SQLM). To examine how key parameters,

including couple stress, ferromagnetic interaction, Prandtl number, Reynolds number, Darcy number, anisotropic permeability, and angle affect velocity, temperature, and pressure profiles in boundary layers, graphs were created using an in-house developed MATLAB program. The findings are outlined below:

- Couple stress parameter and ferromagnetic interaction parameter significantly impact the flow characteristics of fluid. Higher values of Γ and β lead to a reduction in both axial and transverse velocities and a rise in temperature.

- Higher values of K and ϕ result in a reduction in both axial and transverse velocities and a rise in temperature.

- Higher values of Da indicate less restricted flow, so the axial velocity increases near the upper boundary and the temperature increases.

- A higher Prandtl number Pr results in the decrease of both axial and transverse velocities near the upper boundary and the temperature increases.

- Higher β, Pr, and K values result in pressure drops whereas a rise in Γ leads to a rise in pressure. As the fluid resists both thermal and momentum diffusion more strongly, higher values of Pr generally lead to greater pressure drops across the channel, so increasing the overall resistance to flow.

- Higher values of Γ lead to a reduction in skin friction coefficient and an enhancement in rate of heat transfer.

- Higher values of β result in an enhancement in both skin friction and rate of heat transfer coefficient.

The convergence analysis demonstrated that the SQLM was effective. The velocity and temperature profiles' residual errors showed quick convergence, with accuracy greatly increasing after the fifth iteration. Accuracy was optimal with 25-35 collocation points but gradually declined after that. The numerical method is robust and efficient, as evidenced by residual error norms ranging from 10^{-6} to 10^{-9} for different parameters. Overall, this work fills a gap in the literature by providing in-depth insights into the combined impacts of couple stress fluid dynamics, magnetic dipoles, and anisotropic porous media on fluid flow and heat transfer. The current study offers valuable recommendations for enhancing heat transfer and flow control in engineering applications that involve couple stress ferrofluids.

ORCID

 R. Vijaya Sree, https://orcid.org/0009-0002-0047-302X; **V. K. Narla**, https://orcid.org/0000-0003-0994-3497;
K. Suresh Babu, https://orcid.org/0000-0003-1538-1072

REFERENCES

[1] L.J. Crane, "Flow past a stretching plate," Z. Angew. Math. Phys. **21**, 645-647 (1970). https://doi.org/10.1007/BF01587695

[2] R.E. Rosensweig, *Ferrohydrodynamics*, (Cambridge University Press. Cambridge, (1985).

[3] S. Odenbach, *Magnetoviscous Effects in Ferrofluids*, (Springer, Berlin, 2002).

[4] N.H. Abu-Hamdeh, R.A.R. Bantan, F. Aalizadeh, and A. Alimoradi, "Controlled drug delivery using the magnetic nanoparticles in non-Newtonian blood vessels," Alexandria Engineering Journal, **59**, 4819–4828 (2020). https://doi.org/10.1016/j.aej.2020.07.010

[5] M. Kole, and S. Khandekar, "Engineering applications of ferrofluids: A review," Journal of Magnetism and Magnetic Materials, **537**, 168222 (2021). https://doi.org/10.1016/j.jmmm.2021.168222

[6] M.S. Pattanaik, V.B. Varma, S.K. Cheekati, V. Chaudhary, and R.V. Ramanujan, "Optimal ferrofluids for magnetic cooling devices," Scientific Reports, **11**(1), (2021). https://doi.org/10.1038/s41598-021-03514-2

[7] N. Kastor, B. Dandu, V. Bassari, G. Reardon, and Y. Visell, "Ferrofluid electromagnetic actuators for high-fidelity haptic feedback," Sensors and Actuators a Physical, **355**, 114252 (2023). https://doi.org/10.1016/j.sna.2023.114252

[8] E.E. Tzirtzilakis, "A mathematical model for blood flow in magnetic field," Physics of Fluids, **17**(7), (2005). https://doi.org/10.1063/1.1978807

[9] J.C. Misra, G.C. Shit, and H.J. Rath, "Flow and heat transfer of a MHD viscoelastic fluid in a channel with stretching walls: Some applications to haemodynamics," Computers and Fluids, **37**(1), 1–11 (2008). https://doi.org/10.1016/j.compfluid.2006.09.005

[10] Misra, J.C., and Shit, G.C., "Flow of a biomagnetic visco-elastic fluid in a channel with stretching walls," J. Appl. Mech. **76**(6), 061006 (2009). https://doi.org/10.1115/1.3130448.

[11] J.C. Misra, B. Pal, and A.S. Gupta, "Hydromagnetic flow of a second-grade fluid in a channel—Some applications to physiological systems," Math. Models Meth. Appl. Sci. **8**, 1323-1342 (1998). https://doi.org/10.1142/S0218202598000627

[12] V.K. Stokes, "Couple stress in fluids," Phys. Fluids, **9**, 1709-1715 (1966). https://doi.org/10.1063/1.1761925

[13] K. Abbas, X. Wang, G. Rasool, T. Sun, G. Yin, and I. Razzaq, "Recent developments in the application of ferrofluids with an emphasis on thermal performance and energy harvesting," J. Magn. Magn. Mater. **587**, 171311 (2023). https://doi.org/10.1016/j.jmmm.2023.171311

[14] R.K. Shah and S. Khandekar, "Exploring ferrofluids for heat transfer augmentation," J. Magn. Magn. Mater. **475**, 389-400 (2019). https://doi.org/10.1016/j.jmmm.2018.11.034

[15] M. Nandeppanavar, K. Vajravelu, M. Abel, and M.N. Siddalingappa, "Second order slip flow and heat transfer over a stretching sheet with non-linear Navier boundary condition," Int. J. Therm. Sci. **58**, 143-150 (2012). https://doi.org/https://doi.org/10.1016/j.ijthermalsci.2012.02.019

[16] K. Ramesh, "Influence of heat and mass transfer on peristaltic flow of a couple stress fluid through porous medium in the presence of inclined magnetic field in an inclined asymmetric channel," J. Mol. Liq. **219**, 256-271 (2016). https://doi.org/10.1016/j.molliq.2016.03.010

[17] M. Reddy and R.M. Josyula, "Effect of magnetic field on couple stress fluid flow in a rectangular channel," AIP Conf. Proc. **2246**, 020057 (2020). https://doi.org/10.1063/5.0014635

[18] R. Mahesh, A.B. Vishalakshi, U. Mahabaleshwar, and F. Sofos, "Impact of an inclined magnetic field on couple stress fluid flow over a stretching surface with effect of Stefan blowing, radiation and chemical reaction," J. Magn. Magn. Mater. **580**, 170953 (2023). https://doi.org/10.1016/j.jmmm.2023.170953

[19] M. Naveed, M. Imran, and S. Gul, "Heat transfer analysis in hydromagnetic flow of couple stress fluid in presence of homogeneous and heterogeneous chemical reactions over a porous oscillatory stretchable sheet," Adv. Mech. Eng. **15**(2), 16878132231155823 (2023). https://doi.org/10.1177/16878132231155823

[20] H.I. Andersson, K.H. Bech, and B.S. Dandapat, "Magnetohydrodynamic flow of a power-law fluid over a stretching sheet," Int. J. Non-Linear Mech. **27**, 929-936 (1992). https://doi.org/10.1016/0020-7462(92)90045-9

[21] M.A.A. Mahmoud and M.A.E. Mahmoud, "Analytical solutions of hydromagnetic boundary layer flow of a non-Newtonian power-law fluid past a continuously moving surface," Acta Mech. **181**, 83-89 (2006). https://doi.org/10.1007/s00707-005-0268-5

[22] M.Yang, and Y. Lin, "Flow and heat transfer of non-Newtonian power-law fluids over a stretching surface with variable thermal conductivity," Multidiscip. Model. Mater. Struct. **15**(4), 678-695 (2019). https://doi.org/10.1108/MMMS-08-2018-0147

[23] S. Nadeem, R.U. Haq, and C. Lee, "MHD flow of a Casson fluid over an exponentially shrinking sheet," Scientia Iranica, **19**(6), 1550–1553 (2012). https://doi.org/10.1016/j.scient.2012.10.021

[24] P.K. Yadav and N. Yadav, "A study on the flow of couple stress fluid in a porous curved channel," Comput. Math. Appl. **15**2, 1-15 (2023). https://doi.org/10.1016/j.camwa.2023.10.004

[25] M. Ishaq, S.U. Rehman, M.B. Riaz, and M. Zahid, "Hydrodynamical study of couple stress fluid flow in a linearly permeable rectangular channel subject to Darcy porous medium and no-slip boundary conditions," Alexandria Engineering Journal, **91**, 50–69 (2024). https://doi.org/10.1016/j.aej.2024.01.066

[26] S. Das, R.R. Patra, and R.N. Jana, "The layout of Boussinesq couple-stress fluid flow over an exponentially stretching sheet with slip in porous space subject to a variable magnetic field," Multidiscipline Modeling in Materials and Structures, **16**(5), 1131–1154 (2020). https://doi.org/10.1108/MMMS-09-2019-0168

[27] R.A. Alharbey, H. Mondal, and R. Behl, "Spectral Quasi-Linearization Method for Non-Darcy Porous Medium with Convective Boundary Condition," Entropy, **21**(9), 838 (2019). https://doi.org/10.3390/e21090838

[28] H. Mondal and S. Bharti, "Spectral Quasi-linearization for MHD Nanofluid Stagnation Boundary Layer Flow due to a Stretching/Shrinking Surface," J. Appl. Comput. Mech. **6**(4), 1058-1068 (2020). https://doi.org/10.22055/jacm.2020.33097.2207

[29] D. Srinivasacharya, and K.H. Bindu, "Entropy generation in a micropolar fluid flow through an inclined channel with slip and convective boundary conditions," Energy, **91**, 72–83 (2015). https://doi.org/10.1016/j.energy.2015.08.014

[30] K. Raj, B. Moskowitz, and R. Casciari, "Advances in ferrofluid technology," Journal of Magnetism and Magnetic Materials, **149**(1–2), 174–180 (1995). https://doi.org/10.1016/0304-8853(95)00365-7

[31] T. Karmakar, M. Reza, and G.P.R. Sekhar, "Forced convection in a fluid saturated anisotropic porous channel with isoflux boundaries," Physics of Fluids, **31**(11), (2019). https://doi.org/10.1063/1.5126892

[32] T. Karmakar, M. Alam, M. Reza, and G.P.R. Sekhar, "Couette-Poiseuille flow in a fluid overlying an anisotropic porous layer," Comput. Math. Appl. **151**, 346-358 (2023). https://doi.org/10.1016/j.camwa.2023.10.006

[33] N. Ghosh, T. Karmakar, and G.P. Raja Sekhar, "Application of conformal mapping to two-dimensional flows in an anisotropic aquifer," Indian J. Pure Appl. Math. **53**, 617–626 (2022). https://doi.org/10.1007/s13226-021-00153-1

[34] T. Karmakar, and G.P. Raja Sekhar, "A note on flow reversal in a wavy channel filled with anisotropic porous material," Proc. R. Soc. A, **473**, 20170193 (2017). https://doi.org/10.1098/rspa.2017.0193

[35] T. Karmakar, and G. P. Raja Sekhar, "Squeeze-film flow between a flat impermeable bearing and an anisotropic porous bed," Phys. Fluids, **30**, 042001 (2018). https://doi.org/10.1063/1.5020135

[36] T. Karmakar, and G.P. Raja Sekhar, "Effect of anisotropic permeability on fluid flow through composite porous channel," J. Eng. Math. **100**, 33-51 (2016). https://doi.org/10.1007/s10665-015-9831-9

[37] S. Pramanik, and T. Karmakar, "Couette–Poiseuille flow of variable viscosity in a multilayered channel partially filled with a homogeneous anisotropic porous layer: Role of the glycocalyx in attenuating shear stress on endothelial cells," Physics of Fluids, **36**(3), (2024). https://doi.org/10.1063/5.0188683

[38] D.A.S. Rees, L. Storesletten, and A. Postelnicu, "The onset of convection in an inclined anisotropic porous layer with oblique principal axes," Transp. Porous Media, **62**, 139–156 (2006). https://doi.org/10.1007/s11242-005-0618-8

[39] M. Norouzi, and M.R. Shoghi, "A numerical study on miscible viscous fingering instability in anisotropic porous media," Phys. Fluids, **26**, 084102 (2014). https://doi.org/10.1063/1.4891228

[40] E.E. Tzirtzilakis, N.G. Kafoussias, and P.M. Hatzikonstantinou, "Biomagnetic fluid flow in a 3D rectangular duct," Int. J. Numer. Methods Fluids, **44**(12), 1279-1298 (2004). https://doi.org/10.1002/fld.618

ПОТІК РІДИНИ В УМОВАХ ПОДВІЙНОГО БІОМАГНІТНОГО СТРЕСУ В АНІЗОТРОПНОМУ ПОРИСТОМУ КАНАЛІ З РОЗТЯГНУТИМИ СТІНКАМИ

П. Віджая Срі[a,b], **В. К. Нарла**[b*], **К. Суреш Бабу**[c]

[a]Інженерний коледж ACE, математичний факультет, Хайдарабад, Телангана, 501301, Індія
[b]GITAM, факультет математики, Хайдарабад, 502329, Індія
[c]Інженерно технологічний інститут Гокараджу Рангараджу, кафедра математики, Гайдарабад, 500090, Індія

У цій роботі досліджується динаміка потоку рідини в умовах подвійного біомагнітного стресу в анізотропному пористому каналі, де стінки каналу розтягуються. Це дослідження вивчає поведінку потоку під впливом зовнішнього магнітного поля, створюваного магнітним диполем. Для спрощення рівнянь задачі вводяться відповідні безрозмірні параметри. Щоб отримати рішення проблеми, використовується відповідний чисельний підхід, заснований на методі спектральної квазілінеаризації. У цій роботі досліджується вплив кількох важливих параметрів, таких як коефіцієнт анізотропної проникності, параметр парних напруг, анізотропний кут, число Дарсі, параметр феромагнітної взаємодії, число Рейнольдса та число Прандтля. Результати вказують на те, що параметр феромагнітної взаємодії та параметр напруги з'єднання суттєво впливають на теплообмін і потік рідини. Коефіцієнт проникності та кут також впливають на динаміку потоку. Крім того, досліджували коефіцієнт поверхневого тертя та швидкість теплообміну, змінюючи параметри парних напруг та феромагнітної взаємодії. Отримані дані демонструють, що існування магнітного диполя та анізотропної проникності значно впливає на течію та теплові властивості феррорідини, надаючи цінну інформацію для оптимізації теплопередачі та контролю потоку рідини в різноманітних інженерних і медичних застосуваннях.

Ключові слова: *рідина під парним стресом; магнітний диполь; анізотропні пористі середовища; анізотропна проникність; теплообмін; метод спектральної квазілінеаризації*

MAGNETO HYDRODYNAMIC AND BIO-CONVECTION EFFECTS ON HYBRID NANOFLUID DYNAMICS OVER AN INVERTED ROTATING CONE WITH DIFFERENT BASE FLUIDS

Balaji Padhy[a]*, Archana Senapati[b], Goutam Kumar Mahato[a], P.K. Rath[a]

aCenturion University of Technology and Management, Odisha, India
bDepartment of Mathematics, School of Applied Sciences, KIIT Deemed to be University, Bhubaneswar, Odisha, India
*Corresponding Author e-mail: Balaji.padhy11@gmail.com

This study explores the combined effects of magnetohydrodynamics (MHD) and bio-convection on the flow dynamics of hybrid Nanofluids over an inverted rotating cone with different base fluids. The hybrid Nanofluids, composed of nanoparticles suspended in various base fluids, exhibit unique thermal and flow characteristics due to the interplay between magnetic fields and bio-convection phenomena. The governing equations, incorporating the principles of MHD and bio-convection, are derived and solved using numerical methods. The analysis considers the impact of key parameters such as magnetic field strength, the rotation rate of the cone, nanoparticle volume fraction, and types of base fluids on the flow behaviour, heat transfer, and system stability. Results indicate that the MHD significantly influences the velocity and temperature profiles of the hybrid Nanofluids, while bio-convection contributes to enhanced mixing and heat transfer rates. Additionally, the choice of base fluid plays a critical role in determining the overall performance of the hybrid Nano fluid system. This study provides valuable insights into optimizing the design and operation of systems utilizing hybrid Nanofluids in applications where MHD and bio-convection effects are prominent.

Keywords: *Magnetohydrodynamics (MHD); Bio-convection; Hybrid nanofluids; Inverted rotating cone; Base fluids; Nanoparticles; Flow dynamics*
PACS: 47.65.-d, 47.63.-b,47.35. Pq,83.50.-v

1. INTRODUCTION

The movement of heat studied in different fields through cones has acquired remarkable research attention owing to its realistic applications in modern life. Appropriate design and application information are crucial for achieving industrial and technological goals. This study explores the combined effects of magnetohydrodynamics (MHD) and bio-convection on the flow dynamics of hybrid nanofluids over an inverted rotating cone with different base fluids. The hybrid nanofluids, composed of nanoparticles suspended in various base fluids, exhibit unique thermal and flow characteristics due to the interplay between magnetic fields and bio-convection phenomena. The governing equations, incorporating the principles of MHD and bio-convection, are derived and solved using numerical methods. The analysis considers the impact of critical parameters such as magnetic field strength, the rotation rate of the cone, nanoparticle volume fraction, and types of base fluids on the flow behaviour, heat transfer, and system stability. Results indicate that the MHD significantly influences the velocity and temperature profiles of the hybrid nanofluids, while bio-convection contributes to enhanced mixing and heat transfer rates. Additionally, the choice of base fluid plays a critical role in determining the overall performance of the hybrid nanofluid system. This study provides valuable insights into optimizing the design and operation of systems utilizing hybrid nanofluids in applications where MHD and bio-convection effects are prominent.

Many researchers have studied the natural convective heat transfer phenomena over vertical cones, focusing on the effects of cone geometry. These investigations have provided valuable insights into optimizing heat transfer in various engineering and industrial applications [1-4]. Liu *et al.[5]* compared cerebral hemodynamic metrics from CFD models using Newtonian and non-Newtonian fluid assumptions to simulate blood flow in intracranial atherosclerotic stenosis (ICAS). Aloliga *et al.*[6] investigates the magnetohydrodynamic boundary layer flow of non-Newtonian Casson fluids over a magnetised, exponentially stretching sheet. Loganathan *et al.* [7] examine the thermally radiative flow of a Casson fluid over a cylinder with velocity slip, suction/injection, and Newtonian heating. Fatunmbi *et al.*[8] Investigates quadratic thermal convection in Magneto-Casson fluid flow influenced by stretchy material, tiny particles, and viscous dissipation effects. Shankar *et al.*[9] investigate Casson fluid flow over an inclined, stretching cylindrical surface, incorporating heat generation, viscous dissipation, thermal radiation, magnetic fields, and mixed convection. Raja *et al.* [10] investigate free convection heat transfer in hybrid nanofluids over an inclined porous plate, considering asymmetrical flow behaviour and sinusoidal heat transfer boundary conditions with an angled magnetic field. Elattar *et al.*[11] studied three-dimensional heat transfer induced by a non-Newtonian Eyring–Powell fluid containing sodium alginate-based $CoFe_2O_4$ nanoparticles over a deformable horizontal surface.

Bio-convection, a captivating phenomenon in nanofluids, arises from the motion of microorganisms propelled by swimming. These microorganisms generate a thicker boundary layer that breaks into bio-convection cells, inducing instability and higher density gradients at the surface. Gyrotactic and oxytactic microorganisms represent two distinct types influencing this behaviour. Applications of bio-convection span diverse fields, including pharmaceutical

manufacturing, gas-bearing processes, hydrodynamics research, and wine-making, highlighting its relevance across industrial and scientific domains. Mkhatshwa *et al.* [12] investigates the bio-convective flow of magneto-Williamson nanofluids with motile microbes through a porous medium in a horizontal circular cylinder. Alhussain et al. [13] examine the bioconvective flow of magneto-Williamson nanofluids with motile microbes through a porous medium in a horizontal circular cylinder. Zohra *et al.*[14] analyses about convective anisotropic slip boundary layer flow from a rotating vertical cone in ethylene glycol nanofluid, considering Stefan blowing. The study of Hiemenz and Homann flow over a plate was explored by Sarfraz *et al.* [15].

Upon review, it is evident that the impact of bioconvection on magnetohydrodynamic hybrid nanofluid flow through a rotating cone with distinct base fluids remains unexplored. This study aims to investigate the influence of bioconvection on MHD hybrid nanofluid flow modelled with the Casson fluid approach over a spinning cone.

Key novel aspects of this study include:
- Introduction of motile microorganisms into the flow over a rotating cone.
- Application of MHD effects to a hybrid nanofluid comprising H2O and NaC6H9O7 base fluids.
- In the hybrid nanofluid flow, which consists of Aluminum oxide – Titanium oxide, Titanium oxide – Copper, and Aluminum oxide – Copper hybrid nanoparticles, along with Newtonian (H2O) and non-Newtonian (NaC6H9O7) base fluids, the interactions between these nanoparticles and fluids influence the thermal and flow characteristics significantly. These combinations are crucial for studying enhanced heat transfer and fluid dynamics in various industrial and technological applications.

2. PROPOSED MATHEMATICAL MODEL

Let us consider the incompressible, steady-state boundary layer flow combined with bio-convection phenomena around a rotating downward-pointing vertical cone. The system employs two novel base fluids: Ethanol (C_3H_5OH) and Propylene Glycol ($C_3H_8O_2$), integrated with hybrid nanoparticles composed of Zinc Oxide (ZnO) – Silicon Dioxide (SiO$_2$), Copper (Cu) – Silver (Ag), and Zinc Oxide (ZnO) – Silver (Ag) combinations. The analysis incorporates surface temperature and concentration gradients and evaluates the system under a generalized magnetic field. Both thermal and concentration boundary conditions are considered, with Newtonian base fluids serving as a reference point. The spatial setup includes the modified Cartesian coordinates where the ξ-axis is along the cone surface, and the η-axis is perpendicular to it. The azimuthal angle α describes the plane rotation around the vertical symmetry axis. A magnetic field of strength $B = B_o\, f(\xi)/\sqrt{1 - \xi'^2}$ is applied along the η-axis, and the radius of the cone is given by $r = \xi\,cos\delta$ where δ is the cone's half-angle. We assume thermal equilibrium between the base fluids and nanoparticles, and no slip conditions apply. The study begins with an overview of the bio-convection and hybrid nanofluid systems within the boundary layer. The two novel base fluids, Ethanol and Propylene Glycol, are mixed with nanoparticles for improved heat transfer characteristics. This exploration is conducted under boundary-layer approximations, ensuring that the base fluids and nanoparticles remain in thermal equilibrium with no relative slip by Hassan et al.[16].

The boundary layer equations are derived based on the following assumptions and flow conditions:

$$\frac{\partial}{\partial \xi}(r\,u) + \frac{\partial}{\partial \eta}(rv) = 0. \tag{1}$$

where u and v are velocity components along ξ and η axis, respectively, and $r = \xi\,cos\delta$ represents the cone radius. Now the momentum equation (for the axial component) is given by

$$\rho hnf\left(u\frac{\partial u}{\partial \xi} + v\frac{\partial u}{\partial \eta} - \frac{w^2}{\xi}\right) = \left(1 + \frac{1}{\gamma}\right)\mu hnf\frac{\partial^2 u}{\partial \eta^2} + (\rho\beta_T)hnf\,g\,cos\delta(T - T_0) + (\rho\beta_C)hnf\,g\,cos\delta(C - C_0) - \sigma_{hnf}B^2 u. \tag{2}$$

The Azimuthal momentum equation is given by

$$\rho hnf\left(u\frac{\partial w}{\partial \xi} + v\frac{\partial w}{\partial \eta} - \frac{uw}{\xi}\right) = \left(1 + \frac{1}{\gamma}\right)\mu_{hnf}\frac{\partial^2 w}{\partial \eta^2} - \sigma_{hnf}B^2 w. \tag{3}$$

The Energy equation (temperature distribution) is given by

$$(\rho C_p)hnf\left(u\frac{\partial T}{\partial \xi} + v\frac{\partial T}{\partial \eta}\right) = k_{hnf}\frac{\partial^2 T}{\partial \eta^2}. \tag{4}$$

The Species concentration equation is given by

$$u\frac{\partial C}{\partial \xi} + v\frac{\partial C}{\partial \eta} = D_B\frac{\partial^2 C}{\partial \eta^2}. \tag{5}$$

The Microorganism concentration equation is given by

$$u\frac{\partial n}{\partial \xi} + v\frac{\partial n}{\partial \eta} - \frac{\partial}{\partial \eta}\left(n\frac{\partial C}{\partial \eta}\right)\frac{PW_c}{C_r - C_0}\frac{L}{\xi} = D_n\frac{\partial^2 n}{\partial \eta^2}. \tag{6}$$

The boundary condition for current flow system are as follows:
At the cone surface $\eta = 0$;

$$u = 0, v = 0, w = r\Omega, T = T_0 + (T_r - T_0)\frac{\xi}{L}, C = C_0 + (C_r - C_0)\frac{\xi}{L}, n = n_0 + (n_r + n_0)\frac{\xi}{L}. \quad (7)$$

At $\eta \to \infty$:

$$\text{u} \to 0, w \to 0, T \to T_0, C \to C_0 \text{ and } n \to n_0. \quad (8)$$

The hybrid nanofluid properties are redefined in terms of the volume fractions φ_{np1} (for the first nanoparticle) and φ_{np2} (for the second nanoparticle):

$$\mu_{hnf} = \frac{\mu_f}{(1-\phi_{np1})^{2.5}(1-\phi_{np2})^{2.5}}. \quad (9)$$

$$\rho_{hnf} = \{(1 - \phi_{np2})[(1 - \phi_{np1})\rho_f + \phi_{np1}\rho_{np1}]\} + \phi_2\rho_{np2} \quad (10)$$

$$\alpha_{hnf} = \frac{k_{hnf}}{(\rho C_p)_{hnf}}. \quad (11)$$

The heat capacity of a hybrid nanofluid is calculated by using a weighted average of the specific heat capacities of the base fluid and the nanoparticles.

$$(C_p)_{hnf} = \frac{(1-\phi_{np1}-\phi_{np2})(\rho C_p)_f + \phi_{np1}(\rho C_p)_{np1} + \phi_{np2}(\rho C_p)_{np2}}{(1-\phi_{np1}-\phi_{np2})\rho_f + \phi_{np1}\rho_{np1} + \phi_{np2}\rho_{np2}}. \quad (12)$$

The thermal expansion coefficient of the hybrid nanofluid can be approximated as a volume-weighted sum of the thermal expansion coefficients of the base fluid and the nanoparticles:

$$(\beta_T)_{hnf} = (1 - \phi_{np1} - \phi_{np2})(\beta_T)_f + \phi_{np1}(\beta_T)_{np1} + \phi_{np2}(\beta_T)_{np2}. \quad (13)$$

The thermal conductivity of a hybrid nanofluid is more complex to model due to the interaction between nanoparticles and the base fluid. A common model is based on Maxwell's effective medium theory, which can be extended to hybrid nanofluids as follows:

$$k_{hnf} = k_f \left[\frac{k_{np1}+2k_f-2\phi_{np1}(k_f-k_{np1})}{k_{np1}+2k_f+\phi_{np1}(k_f-k_{np1})}\right]\left[\frac{k_{np2}+2k_f-2\phi_{np2}(k_f-k_{np2})}{k_{np2}+2k_f+\phi_{np2}(k_f-k_{np2})}\right]. \quad (14)$$

The electrical conductivity of hybrid nanofluids is enhanced due to the addition of nanoparticles, and can also be modelled using Maxwell's effective medium theory, similar to the thermal conductivity. The electrical conductivity σ_{hnf} is given by:

$$\sigma_{hnf} = \sigma_f \left[\frac{\sigma_{np1}+2\sigma_f-2\phi_{np1}(\sigma_f-\sigma_{np1})}{\sigma_{np1}+2\sigma_f+\phi_{np1}(\sigma_f-\sigma_{np1})}\right]\left[\frac{\sigma_{np2}+2\sigma_f-2\phi_{np2}(\sigma_f-\sigma_{np2})}{\sigma_{np2}+2\sigma_f+\phi_{np2}(\sigma_f-\sigma_{np2})}\right]. \quad (15)$$

To further simplify the equations, the following dimensionless variables are introduced: (Alhussain et al.0, Aghamajidi et al. [17])

$$\xi = \frac{\xi^*}{L}, \eta = \frac{\eta^*}{L}, u = \frac{u^*}{L}, v = \frac{v^*}{L}, w = \frac{w^*}{\Omega L}, \Theta = \frac{T-T_0}{T_r-T_0}, \varphi = \frac{C-C_0}{C_r-C_0}, \chi = \frac{n-n_0}{n_r-n_0}. \quad (16)$$

Solve the equation from 1-6 and applying equation (16), we get

$$u\frac{\partial w}{\partial \xi} + v\frac{\partial w}{\partial \eta} + uw\frac{r'}{r} = \frac{1}{\left[(1-\phi_{np2})\left[1-\phi_{np1}+\phi_{np1}\frac{\rho_{np1}}{\rho_f}\right]+\phi_{np2}\frac{\rho_{np2}}{\rho_f}\right]}\left\{\frac{1}{(1-\phi_{np1})^{2.5}(1-\phi_{np2})^{2.5}}\left(1+\frac{1}{\beta}\right)\frac{\partial^2 w}{\partial \eta^2} - \frac{\sigma_{hnf}}{\sigma_f}M\Lambda^2 w\right\}. \quad (17)$$

$$u\frac{\partial \Theta}{\partial \xi} + v\frac{\partial \Theta}{\partial \eta} = \frac{1}{Br}\left\{\frac{1}{\left(1-\phi_{np2}\right)\left[1-\phi_{np1}+\phi_{np1}\frac{(\rho C_p)_{np1}}{(\rho C_p)_f}\right]+\phi_{np2}\left(\frac{(\rho C_p)_{np2}}{(\rho C_p)_f}\right)}\right\}\frac{k_{hnf}}{k_f}\frac{\partial^2 \Theta}{\partial \eta^2}. \quad (18)$$

$$u\frac{\partial \varphi}{\partial x} + v\frac{\partial \varphi}{\partial y} = \frac{1}{Sc}\frac{\partial^2 \varphi}{\partial y^2}. \quad (19)$$

$$u\frac{\partial \chi}{\partial x} + v\frac{\partial \chi}{\partial y} = \frac{1}{Lb}\frac{\partial^2 \chi}{\partial y^2} - \frac{1}{x}\frac{Pe}{Lb}\left[\frac{\partial \chi}{\partial y}\cdot\frac{\partial \varphi}{\partial y} + \chi\frac{\partial^2 \varphi}{\partial y^2}\right]. \quad (20)$$

After applying initial conditions, we get the following differential equations

$$\frac{1}{(1-\phi_{np1})^{2.5}(1-\phi_{np2})^{2.5}}\left(1+\frac{1}{\beta}\right)W'' + [2VW' - 2V'W]\left[(1-\phi_{np2})\left[1-\phi_{np1}+\phi_{np1}\frac{\rho_{np1}}{\rho_f}\right]+\phi_{np2}\frac{\rho_{np2}}{\rho_f}\right] - \frac{\sigma_{hnf}}{\sigma_f}M\Lambda^2 W = 0. \quad (21)$$

$$X'' + Pr\left[\left(1 - \phi_{np2}\right)\left[1 - \phi_{np1} + \phi_{np1}\frac{(\rho c_p)_{np1}}{(\rho c_p)_f}\right] + \phi_{np2}\left(\frac{(\rho c_p)_{np2}}{(\rho c_p)_f}\right)\right]\left[\frac{k_f}{k_{hnf}}\right][2VX' - V'X] = 0. \tag{22}$$

$$Y'' + Sc\,[2VY' - V'Y] = 0. \tag{23}$$

$$Z'' - Pe\,[Z'Y' + ZY''] + Lb[2VZ' - V'Z] = 0. \tag{24}$$

Again, apply the following boundary conditions we obtained

$$V = 0,\ V' = 0,\ W = 1,\ X = 1,\ Y = 1,\ Z = 1\ \ at\ \ y = 0,$$

$$V' \to 0,\ W \to 0,\ X \to 0,\quad Y \to 0,\quad Z \to 0\ \ as\ \ y \to \infty. \tag{25}$$

3.   Numerical Method: 4th-Order Runge-Kutta and Shooting Technique

The 4th-order Runge-Kutta method is used to solve this system of first-order ODEs. The steps of this method are as follows:

Step 1: Start with initial guesses for the unknown boundary values at $y = 0$(for example, $y_2, y_4, y_6, \dots$etc., for the velocity, temperature, etc.).

Step 2: Integrate the system of ODEs using the Runge-Kutta method from $y = 0$ to a large value of y (denoted as $y = \infty$) where the boundary conditions at infinity are applied.

Step 3: Compare the computed values at $y = \infty$ with the boundary conditions at infinity (e.g. $y_2(\infty),\ y_4(\infty),\ y_6(\infty), \dots$, etc.).

Step 4: Adjust the initial guesses iteratively using the shooting technique until the boundary conditions at infinity are satisfied to a desired level of accuracy.

4.   Transformation of Governing Equations to First-Order ODEs

To apply numerical methods such as the 4th-order Runge-Kutta method, the system of second- and third-order ODEs needs to be transformed into a system of first-order ODEs.

The ODEs derived from the governing equations are expressed in terms of the functions V(y), W(y), X(y), Y(y), and Z(y), which describe the radial velocity, axial velocity, temperature, concentration, and microorganism distribution, respectively. These functions are transformed into first-order ODEs using the following designations:

$$V = y_1, V' = y_2, V'' = y_3, W = y_4, W' = y_5, X = y_6, X' = y_7, Y = y_8,\ Y' = y_9, Z = y_{10},\ Z' = y_{11}\,.$$

Using these designations, the system of equations (21)-(25) is transformed into the following set of first-order ODEs:

1.   For the radical velocity V:
$$y_1' = y_2\ , y_2' = y_3$$

$$y_3' = \left(1 + \frac{1}{\beta}\right)^{-1}\left(\left(1 - \phi_{np1}\right)^{2.5}\left(1 - \phi_{np2}\right)^{2.5}\right)$$

$$\left\{
\begin{aligned}
&-[2y_1 y_3 - y_2{}^2 + \varepsilon y_4{}^2]\left[\left(1 - \phi_{np2}\right)\left[1 - \phi_{np1} + \phi_{np1}\frac{\rho_{np1}}{\rho_f}\right] + \phi_{np2}\frac{\rho_{np2}}{\rho_f}\right] + \frac{\sigma_{hnf}}{\sigma_f}M\Lambda^2 y_2\\
&-\left[\left(1 - \phi_{np2}\right)\left[1 - \phi_{np1} + \phi_{np1}\frac{(\rho\beta_T)_{np1}}{(\rho\beta_T)_f}\right] + \phi_{np2}\frac{(\rho\beta_T)_{np2}}{(\rho\beta_T)_f}\right][y_6 + Nc\,y_8 + Nn\,y_{10}]
\end{aligned}
\right\} \tag{26}$$

2.   For the axial velocity W:
$$y_4' = y_5$$
$$y_5' = \left(1 + \frac{1}{\beta}\right)^{-1}\left(\left(1 - \phi_{np1}\right)^{2.5}\left(1 - \phi_{np2}\right)^{2.5}\right)\left[\frac{\sigma_{hnf}}{\sigma_f}M\Lambda^2 y_4 - \left[\left(1 - \phi_{np2}\right)\left[1 - \phi_{np1} + \right.\right.\right.$$

$$\left.\left.\left.\phi_{np1}\frac{\rho_{np1}}{\rho_f}\right] + \phi_{np2}\frac{\rho_{np2}}{\rho_f}\right][2y_1 y_5 - 2y_2 y_4]\right]. \tag{27}$$

3.   For the temperature X:
$$y_6' = y_7$$
$$y_7' = -\Pr\left[\frac{k_f}{k_{hnf}}\right][2y_1 y_7 - y_2 y_6]\left[\left(1 - \phi_{np2}\right)\left[1 - \phi_{np1} + \phi_{np1}\frac{(\rho c_p)_{np1}}{(\rho c_p)_f}\right] + \phi_{np2}\left(\frac{(\rho c_p)_{np2}}{(\rho c_p)_f}\right)\right]. \tag{28}$$

4.   For the concentration Y:
$$y_8' = y_9,\ y_9' = -Sc[2y_1 y_9 - y_2 y_8]. \tag{29}$$

5.   For the microorganism distribution Z:
$$y_{10}' = y_{11}$$
$$y_{11}' = Pe[y_{11} y_9 + y_{10}(-Sc[2y_1 y_9 - y_2 y_8])] - Lb[2y_1 y_{11} - y_2 y_{10}]. \tag{30}$$

The boundary conditions are translated into the following form for the system of first-order ODEs:

At $y = 0$,

$$y_1(0) = 0, \ y_2(0) = 0, y_4(0) = 1, \ y_6(0) = 1, \ y_8(0) = 1, \ y_{10}(0) = 1,$$

At $y = \infty$,

$$y_2(\infty) = 0, \ y_4(\infty) = 0, \ y_6(\infty) = 0, \quad y_8(\infty) = 0, \ y_{10}(\infty) = 0.$$

5. NUMERICAL EXAMPLE

In this section, we will analyse the sensitivity of the system to various flow parameters by examining their effects on Sherwood number, Nusselt number, and skin friction. The parameters considered include:

1. Magnetic Parameter (M)
2. Volume Fraction of Nanoparticles (ϵ)
3. Bioconvection Parameters (Nc,Nn)
4. Schmidt Number (Sc)

Example: Consider the following parameter values based on the typical setup for nanofluid flow:

$$M = 1, Nc = 0.1 = Nn, Sc = 0.6, Pr = 6.5, \varphi_{np1} = 0.005, \varphi_{np2} = 0.015, \epsilon = 1, \Lambda = 1, \beta = 1$$

These values represent a non-Newtonian fluid with bio-convection and magnetohydrodynamic.

Sol: The 4th-order Runge-Kutta method is used to integrate the system from $y = 0$ to a sufficiently large value of $y_\infty = 10$. To apply iteration procedure, we get numerical solution for $y_1(y), y_2(y), y_3(y), \ldots, y_{10}(y), y_{11}(y)$. These correspond to the velocity, temperature, concentration, and microorganism profiles.

Table 1. The effect of varying flow parameters on the Sherwood number for both Newtonian and non-Newtonian base fluids. This analysis focuses on how changes in parameters such as M, ϵ, Nc, Nn, and Sc influence the Sherwood number in the presence of different nanoparticle combinations.

M	Nc	Nn	Sc	$Al_2O_3 - TiO_2$	$TiO_2 - Cu$	$Al_2O_3 - Cu$	ϵ	$F''(0)$ Ajhamajidi	$F''(0)$ Modified
1	0.1	0.1	0.1	0.20434	0.20490	0.20489	0.0	0.65	0.65
	0.5			0.19424	0.19457	0.19456			
	0.9			0.18905	0.18928	0.18928			
1	0.1	0.1	0.1	0.20434	0.20490	0.20489	0.2	0.73	0.70
		0.3		0.21337	0.21382	0.21382			
		0.6		0.22576	0.22604	0.22604			
1			0.1	0.20434	0.20490	0.20489	0.4	0.82	0.77
			0.4	0.30051	0.30244	0.30242			
			0.7	0.37883	0.38183	0.38179			
1	0.1	0.1	0.1	0.20395	0.20451	0.20451	0.6	0.89	0.85
1	0.1	0.1	0.1	0.20375	0.20430	0.20429	0.8	0.96	0.93
1	0.1	0.1	0.1	0.20734	0.20774	0.20774	1.0	1.02	1.00

6. SENSITIVITY ANALYSIS

This section has explored the impact of different factors on bio-convection and steady two-dimensional magnetohydrodynamic (MHD) free convection in Casson nanofluid flow over a spinning cone.
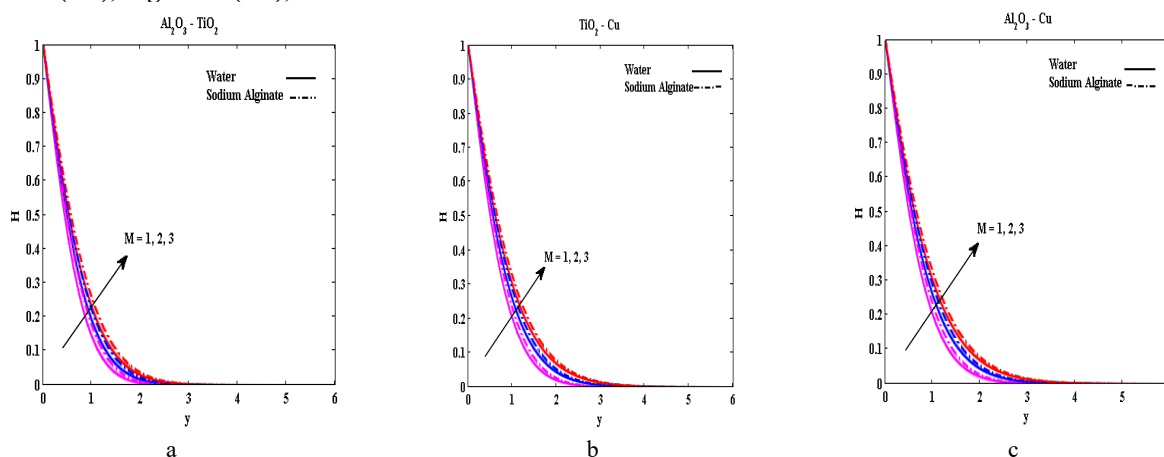
Figure 1. (a-c), Figure 2. (a-c), and Table 1.

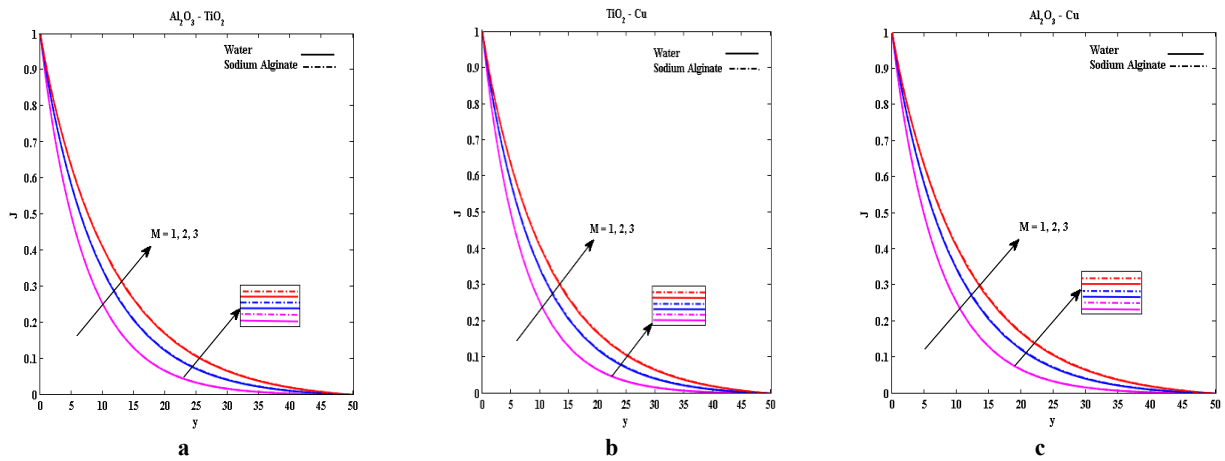**Figure 1.** (a-c) Graph of M on the temperature profile

Figure 2. (a-c) Graph of M on the microorganism profile

- Figs. 1(a-c) and 2(a-c) were analyzed to observe heat and motile microorganism profiles across a wide range of magnetic parameters (M = 1, 2, 3) in hybrid nanofluids.
- As the magnetic parameter (M) increases, both temperature and motile microorganism profiles show an increase in hybrid nanofluids.
- it is demonstrated that the thermal and motile microorganism boundary layer thicknesses increase due to the release of additional heat in the hybrid nanofluids as the magnetic parameter (M) is increased.
- Furthermore, it is demonstrated that non-Newtonian-based hybrid nanofluids outperform Newtonian-based ones. This superiority is attributed to sodium alginate, which exhibits a significantly higher Prandtl number and thermal diffusivity compared to water-based hybrid nanofluids.

Figure 3. (a-c), Figure 4. (a-c) and Table 1.
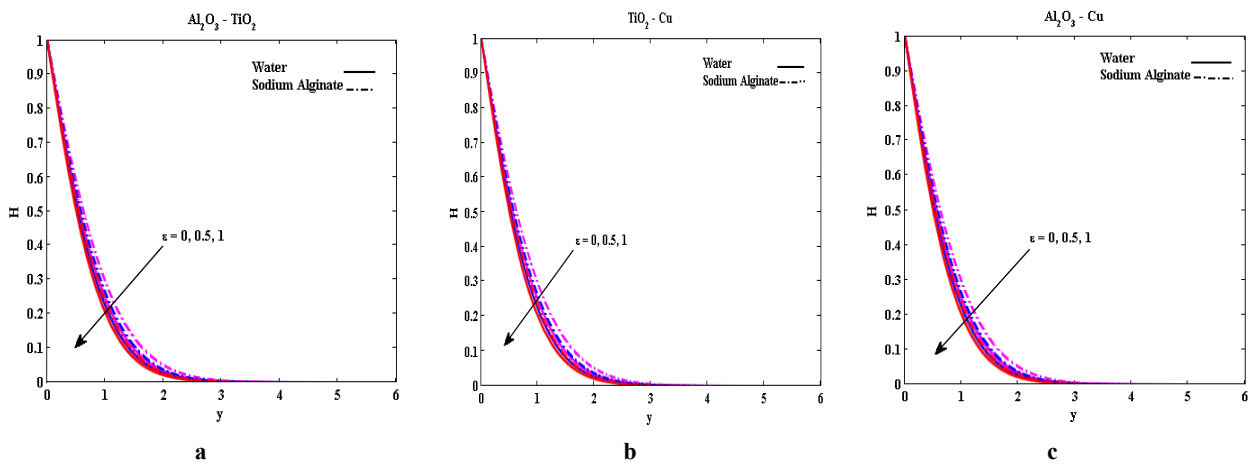
Figure 3. (a-c) Graph of ε on the temperature profile
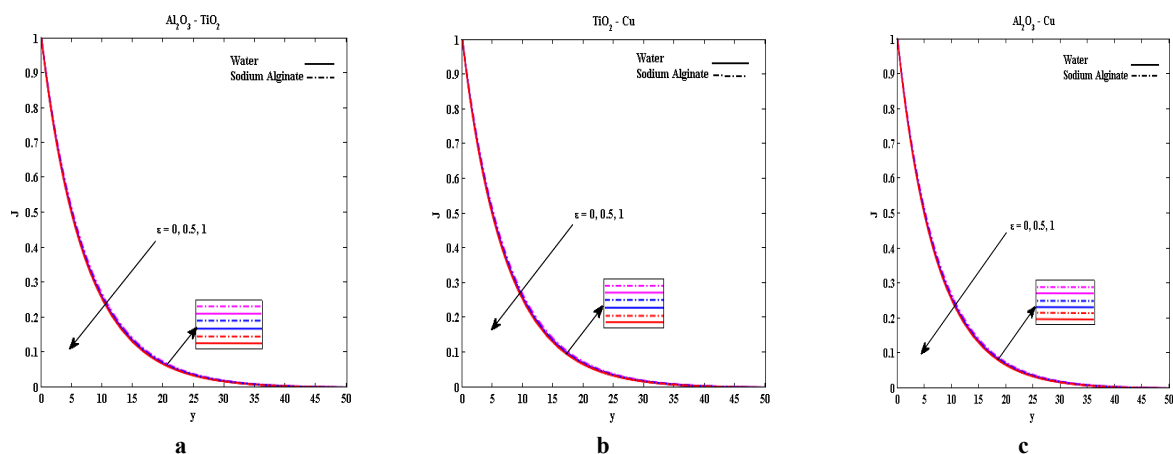
Figure 4. (a-c) Graph of ε on the microorganism profile

- It illustrates the impact of spin parameter (ε = 0, 0.5, 1) on temperature and microorganism species density profiles in hybrid nanofluids.

- The heat profiles (Fig. 3 (a-c)) and microorganism profiles (Fig. 4 (a-c)) show a decreasing trend across all three hybrid nanofluids as the spin parameter ε increases.

- This decline is attributed to the thinning of the boundary layer as ε increases. The Newtonian base fluid exhibits a similar decline in thermal expansion within the hybrid nanofluids.

- Graph depict variations in microorganism species density for different values of Nc (Nc = 0.1, 0.5, 0.9) (from Fig. 5.).

- The microorganism profiles show symmetrical motion of hybrid nanoparticles with various base fluids and a tendency to aggregate. Non-Newtonian base fluids exhibit faster acceleration compared to Newtonian base fluids, resulting in a reduction in flow patterns within hybrid nanofluids.

- **Figure 5. (a-c) and Table 1.**
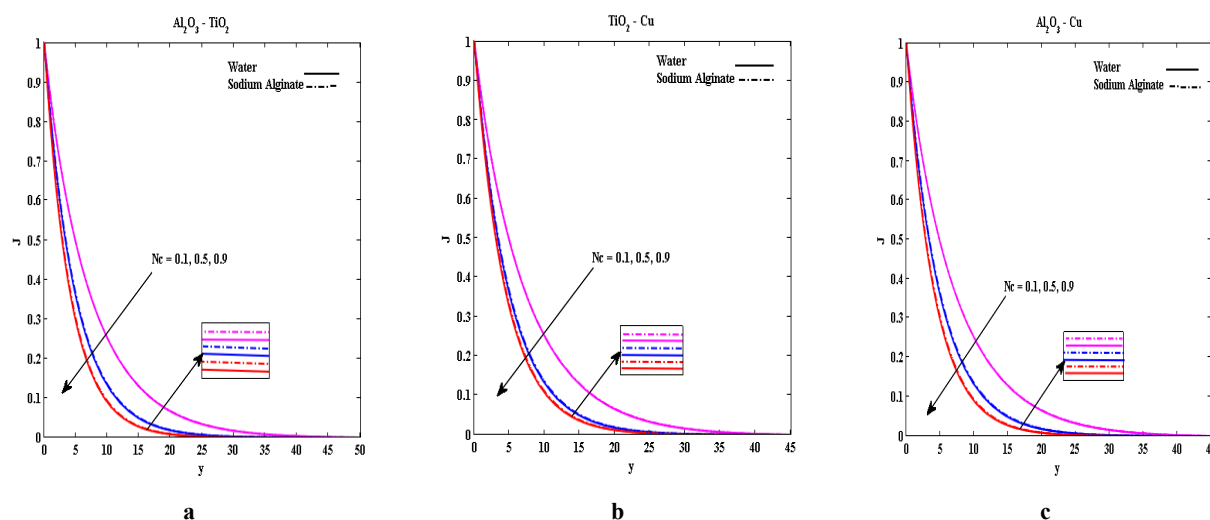
Figure 5. (a-c) Graph of Nc on the microorganism profile

Figure 6. (a-c) and Table 1.
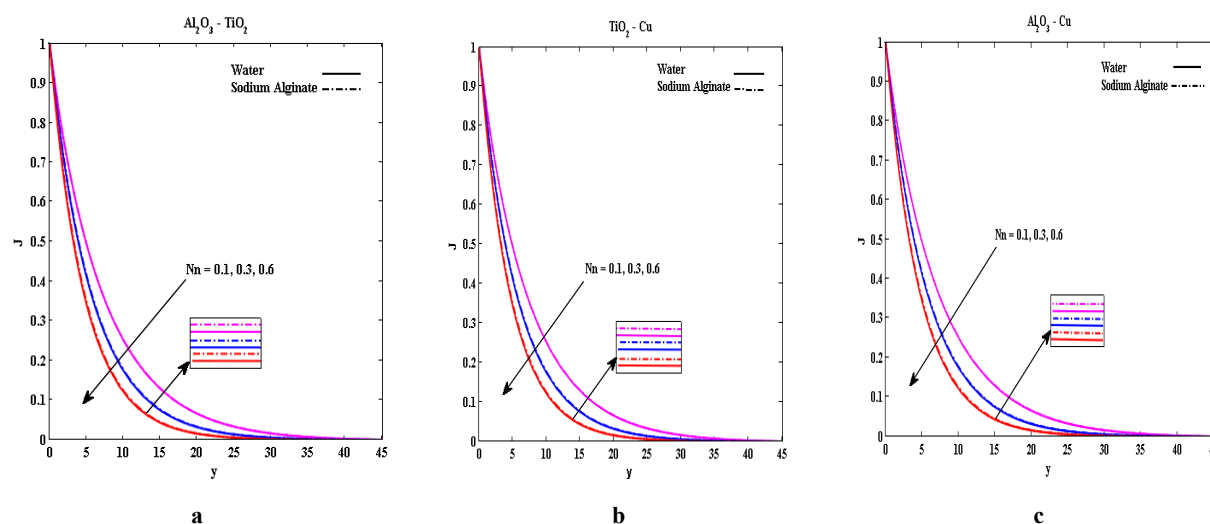
Figure 6. (a-c) Graph of Nn on the microorganism profile

- Graph (Fig-6) illustrate the impact of hybrid nanoparticles with Nn values (Nn = 0.1, 0.3, 0.6) on the microorganism species density profile using two base fluids.

- The buoyancy effects associated with increasing Nn result in a significant decrease in microorganism species density across all three hybrid nanofluids. Non-Newtonian base fluids exhibit more excellent acceleration, leading to stiffening of the boundary layer as Nn increases in the three hybrid nanoparticles.
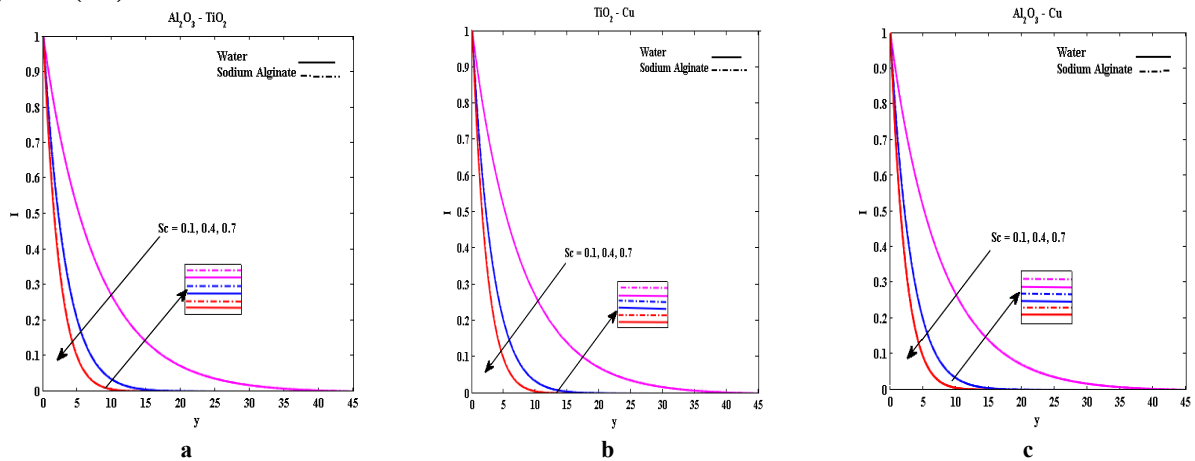
Figure 7. (a-c) and Table 1.

Figure 7. (a-c) Graph of Sc on the concentration profile

- Graph illustrates the influence of Schmidt number Sc (Sc = 0.1, 0.4, 0.7) on the concentration flow fields in hybrid nanofluids. The concentration profiles (Fig. 7(a-c)) show a decrease as Sc increases, reflecting a reduction in mass diffusion due to the ratio of momentum diffusivity to mass diffusivity.
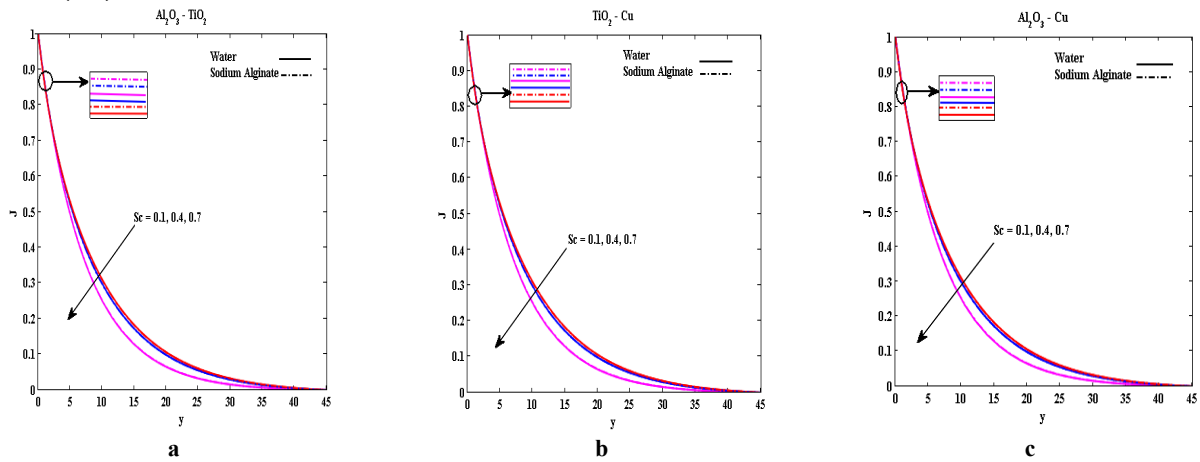
Figure 8 (a-c) and Table 1.

Figure 8. (a-c) Graph of Sc on the microorganism profile

- Graph depict the impact of Schmidt number Sc on the microorganism species density flow fields in hybrid nanofluids. The microorganism species density profiles (Fig. 8(a-c)) decrease with increasing Sc, indicating that advection transport dominates over diffusive transport rates.
- Non-Newtonian base fluids exhibit enhanced kinematic viscosity in concentration and microorganism species density profiles.
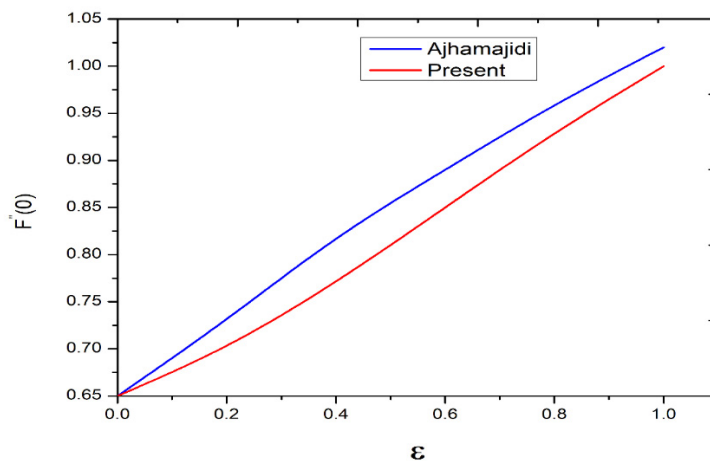
Figure 9. Comparative study of ϵ and $F''(0)$.

Figure 9 and Table 1.

- Demonstrates comparing the current study's results and those published previously [17], showing excellent agreement under limited considerations.
- It Provides numerical values of local Sherwood numbers across three hybrid nanoparticles with two base fluids, categorised by variables such as M, ε, Nc, Nn, and Sc. The local Sherwood number increases with larger values of ε, Nc, Nn, and Sc and decreases with increasing M. Additionally, it is noted that Newtonian base fluids exhibit higher mass transfer rates in Aluminum oxide – Titanium oxide, Titanium oxide – Copper and Aluminum oxide – Copper hybrid nanoparticles.

7. CONCLUSION

This study analysed the magnetic bio-convective flow of Casson hybrid nanofluids through a spinning cone, presenting thermal, mass, and microorganism profiles graphically and tabulating physical quantities. Key findings indicate that an increase in the magnetic parameter (M) enhances heat and motile microorganism profiles, while a more significant spin parameter reduces the temperature profile. The microorganism flow field decreases with increasing Sc values for all hybrid nanofluids. Mass transfer rates in a non-Newtonian base fluid improve with higher β values. For Newtonian base fluids, mass transfer rates increase with ascending ε, Nc, Nn, and Sc. Notably, TiO_2-Cu hybrid nanoparticles exhibit superior Sherwood numbers. The potential applications of hybrid nanofluids in rotating cones span food technology, aeronautical engineering, the pharmaceutical industry, and endoscopy scanning, suggesting future exploration of the benefits and limitations of these nanofluids in such fields.

ORCID

Ⓓ**Balaji Padhy,** https://orcid.org/0000-0002-3447-2917; Ⓓ**Archana Senapati,** https://orcid.org/0009-0001-7180-5194
Ⓓ**Goutam Kumar Mahato,** https://orcid.org/0000-0003-4549-0042; Ⓓ**P.K. Rath,** https://orcid.org/0000-0002-3869-9705

REFERENCES

[1] C.K. Ajay, M.A. Kumar, and A.H. Srinivasa, "The effects of thermal radiation, internal heat generation (absorption) on unsteady MHD free convection flow about a truncated cone in presence of pressure work," Materials Today: Proceedings, (2023). https://doi.org/10.1016/j.matpr.2023.05.632

[2] A. Hossain, M.J. Anee, S. Thohura, and M.M. Molla, "Finite difference simulation of free convection of non-Newtonian nanofluids with radiation effects over a truncated wavy cone," Pramana, **97**(4), 168 (2023). https://doi.org/10.1007/s12043-023-02642-w

[3] M.K.A. Mohamed, A.M. Ishak, I. Pop, N.F. Mohammad, and S.K. Soid, "Free convection boundary layer flow from a vertical truncated cone in a hybrid nanofluid," Malaysian Journal of Fundamental and Applied Sciences, **18**(2), 257-270 (2022). https://doi.org/10.11113/mjfas.v18n2.2410

[4] R. Ellahi, A. Zeeshan, A. Waheed, N. Shehzad, and S.M. Sait, "Natural convection nanofluid flow with heat transfer analysis of carbon nanotubes–water nanofluid inside a vertical truncated wavy cone," Mathematical Methods in the Applied Sciences, **46**(10), 11303-11321 (2023). https://doi.org/10.1002/mma.7281

[5] H. Liu, L. Lan, J. Abrigo, H.L. Ip, Y. Soo, D. Zheng, K.S. Wong, *et al.*, "Comparison of Newtonian and non-Newtonian fluid models in blood flow simulation in patients with intracranial arterial stenosis," Frontiers in physiology, **12**, 718540 (2021). https://doi.org/10.3389/fphys.2021.718540

[6] G. Aloliga, Y. Ibrahim Seini, and R. Musah, "Heat transfer in a magnetohydrodynamic boundary layer flow of a non-newtonian casson fluid over an exponentially stretching magnetized surface," Journal of Nanofluids, **10**(2), 172-185 (2021). https://doi.org/10.1166/jon.2021.1777

[7] K. Loganathan, M. Sivakumar, M. Mohanraj, and P. Sakthivel, "Thermally radiative Casson fluid flow over a cylinder with Newtonian heating and heat generation/absorption," Journal of Physics: conference series, **1964**(2), 022001 (2021). https://doi.org/10.1088/1742-6596/1964/2/022001

[8] E.O. Fatunmbi, and O.A. Agbolade, "Quadratic Thermal Convection in Magneto-Casson Fluid Flow Induced by Stretchy Material with Tiny Particles and Viscous Dissipation Effects," Physical Science International Journal, **27**(4), 1-11 (2023). https://doi.org/10.9734/psij/2023/v27i4795

[9] U. Shankar, and N.B. Naduvinamani, "Magnetized impacts of Cattaneo-Christov double-diffusion models on the time-dependent squeezing flow of Casson fluid: A generalized perspective of Fourier and Fick's laws," The European Physical Journal Plus, **134**(7), 344 (2019). https://doi.org/10.1140/epjp/i2019-12715-x

[10] A. Raza, M.Y. Almusawa, Q. Ali, A.U. Haq, K. Al-Khaled, and I.E. Sarris, "Solution of water and sodium alginate-based casson type hybrid nanofluid with slip and sinusoidal heat conditions: A prabhakar fractional derivative approach," Symmetry, **14**(12), 2658 (2022). https://doi.org/10.3390/sym14122658

[11] S. Elattar, U. Khan, A. Zaib, A. Ishak, N. Alwadai, and A.M. Abed, "Heat transfer characteristics of cobalt ferrite nanoparticles scattered in sodium alginate-based non-Newtonian nanofluid over a stretching/shrinking horizontal plane surface," Open Physics, **22**(1), 20230182 (2024). https://doi.org/10.1515/phys-2023-0182

[12] M.P. Mkhatshwa, "Overlapping Grid-Based Spectral Collocation Technique for Bioconvective Flow of MHD Williamson Nanofluid over a Radiative Circular Cylindrical Body with Activation Energy," Computation, **12**(4), 75 (2024). https://doi.org/10.3390/computation12040075

[13] Z.A. Alhussain, A. Renuka, and M. Muthtamilselvan, "A magneto-bioconvective and thermal conductivity enhancement in nanofluid flow containing gyrotactic microorganism," Case Studies in Thermal Engineering, **23**, 100809 (2021). https://doi.org/10.1016/j.csite.2020.100809

[14] F.T. Zohra, M.J. Uddin, A.I.M. Ismail, O.A. Bég, and A. Kadir, "Anisotropic slip magneto-bioconvection flow from a rotating cone to a nanofluid with Stefan blowing effects," Chinese journal of physics, **56(**1), 432-448 (2018). https://doi.org/10.1016/j.cjph.2017.08.031

[15] M. Sarfraz, and M. Khan, "Cattaneo-Christov double diffusion-based heat transport analysis for nanofluid flows induced by a moving plate," Numerical Heat Transfer, Part A: Applications, **85**(3), 351-363 (2024). https://doi.org/10.1080/10407782.2023.2186551

[16] A. Hussanan, M. Qasim, and Z.M. Chen, "Heat transfer enhancement in sodium alginate based magnetic and non-magnetic nanoparticles mixture hybrid nanofluid," Physica A: Statistical Mechanics and its Applications, **550**, 123957 (2020). https://doi.org/10.1016/j.physa.2019.123957

[17] M. Aghamajidi, M. Yazdi, S. Dinarvand, and I. Pop, "Tiwari-Das nanofluid model for magnetohydrodynamics (MHD) natural-convective flow of a nanofluid adjacent to a spinning down-pointing vertical cone," Propulsion and Power Research, **7**(1), 78-90 (2018). https://doi.org/10.1016/j.jppr.2018.02.002

[18] Z.A. Alhussain, A. Renuka, and M. Muthtamilselvan, "A magneto-bioconvective and thermal conductivity enhancement in nanofluid flow containing gyrotactic microorganism," Case Studies in Thermal Engineering, **23**, 100809 (2021). https://doi.org/10.1016/j.csite.2020.100809

МАГНІТОГІДРОДИНАМІЧНИЙ ТА БІОКОНВЕКЦІЙНИЙ ВПЛИВ НА ГІБРИДНУ ДИНАМІКУ НАНОРІДИН НАД ПЕРЕВЕРНУТИМ ОБЕРТОВИМ КОНУСОМ З РІЗНИМИ ОСНОВНИМИ РІДИНАМИ

Баладжі Падхі[a], Арчана Сенапаті[b], Гутам Кумар Махато[a], П.К. Рат[a]

[a]Університет технології та управління Центуріон, Одіша, Індія

[b]Факультет математики школи прикладних наук КІІТ Deemed to be University, Бхубанешвар, Одіша, Індія.

У цій роботі досліджується комбінований вплив магнітогідродинаміки (МГД) і біоконвекції на динаміку потоку гібридних нанофлюїдів над перевернутим обертовим конусом з різними базовими рідинами. Гібридні нанофлюїди, що складаються з наночастинок, суспендованих у різних базових рідинах, демонструють унікальні теплові та текучі характеристики завдяки взаємодії між магнітними полями та явищами біоконвекції. Основні рівняння, що включають принципи МГД та біоконвекції, отримані та розв'язані чисельними методами. Аналіз розглядає вплив ключових параметрів, таких як напруженість магнітного поля, швидкість обертання конуса, об'ємна частка наночастинок і типи базових рідин на поведінку потоку, теплопередачу та стабільність системи. Результати показують, що МГД суттєво впливає на профілі швидкості та температури гібридних нанофлюїдів, тоді як біоконвекція сприяє підвищенню швидкості змішування та теплопередачі. Крім того, вибір базової рідини відіграє вирішальну роль у визначенні загальної продуктивності гібридної системи Nano fluid. Це дослідження дає цінну інформацію щодо оптимізації дизайну та роботи систем, що використовують гібридні нанофлюїди в програмах, де МГД та біоконвекційні ефекти є помітними.

Ключові слова: *магнітогідродинаміка (МГД); біоконвекція; гібридні нанофлюїди; перевернутий обертовий конус; базові рідини; наночастинки; динаміка течії*

HEAT GENERATION EFFECT ON 3D MHD FLOW OF CASSON FLUID VIA POROUS STRETCHING/SHRINKING SURFACE WITH VELOCITY SLIP CONDITION

⬤B. Jagadeesh Kumar*, ⬤Nainaru Tarakaramu

Department of Mathematics, School of Liberal Arts and Sciences, Mohan Babu University, Sree Sainath Nagar, Tirupati-517102, Andrapradesh, India
*Corresponding Author Email: induharicharan@gmail.com, nainaru143@gmail.com

There are extensive range of applications related to nuclear industry, industrial manufacturing, science and engineering processing, in which the boundary layer hydromagnetic motion of Casson liquids perform vital role. Casson liquid is a useful liquid in the nuclear industry for optimizing the design and operation of nuclear reactors. Researchers have investigated transfer of heat in liquid motions with linear stratification, which is a phenomenon where the temperature varies linearly with height, affecting various fields such as medical equipment, glass fiber production, electronic devices, polymer sheets, paper production, filaments, and medicine. However, the most discussion of heat transfer problems is to get numerical solutions of a comprehensive Casson liquid model with heat generation described by the BVP4 via shooting method. In this study, a new velocity slip boundary condition is applied at the stretching or shrinking surface. These conditions are grounded in the previously established Buongiorno model, providing a more practical and realistic approach compared to previous study. The time independent Gov. Eqs. changed into a set of couple non-linear ODEs with help of suitable similarity conversions. The equations are evaluating via R-K-F by help of MATLAB software programming.
Keywords: *Magnetohydrodynamic; Shrinking/stretching surface; Velocity slip; Heat Generation/absorption; Casson fluid; 3D*
PACS: 04.25.D, 47.50.-d, *43.28.JS, 62.60. +v.

INTRODUCTION

Till date, lots of plentiful fields (such as astrophysics, oceanography) in analytical, experimental and exact solutions are studied to describe the NNF because in view of their real time applications existing in biological lubricants and biomedical flows, industrial processes ("Metal extrusion, drawing of plastics and rubber sheets, coal-oil slurries, blowing, manufacturing, extrusion of polymeric fluids"), polymer and metal extrusion mechanisms and technological applications like coating of wires, oil recovery. Therefore, the upcoming research scholars and scientists are doing towards rheological features of NNF. In 1959, Casson [1] introduce Casson liquid as a NN model. The laminar motion of pseudo-plastic NN NFs ("Al_2O_3 + CMC") within the porous circular concentric region was examined by Barnoon and Toghraie [2]. Peri P.K. Kameswaran et al. [3] developed the SP motion of NN Casson liquid via SS with Soret and Dufour effects. The transfer of heat of Casson viscous gad motion on linear SS was created by Mahabaleswar et al. [4]. Duguma et al. [5] described the 2D BL motion of incompressible viscous Casson NFs via permeable SS. Himanshu et al. [6] exhibited the SP motion of Au-blood liquid via SS. The non-linear mixed convective HMT features of a NN Casson liquid motion via SS was explored by Vishnu Ganesh et al. [7]. Shankar Goud et al. [8] studied the streamline BL Casson liquid motion via wedge inspired by magnetic effect. Recently some of scientists respectively, NNF model [9], Eyring-Powell fluid model [10], Casson nanofluid with mixed convection model [11], Maxwell fluid with Cattaneo-Christov model [12], Williamson nanofluid model [13], Walter's nanofluid model [14], and Casson NFs with convective condition [15].

Recently, Adel et al. [16] exhibited the behavior of a slippery NFs flowing via permeable SS. The rate of HMT in an MHD viscoelastic NFs via SS with HG was described by Raja Sekhar et al. [17]. Ali et al. [18] described the motion of a Ree-Eyring HNFs by a stretch motion. Akolade et al. [19] created the heat source and generalized Fourier's law on Carreau liquid motion via NLSS. Saleem et al. [20] examine and comparison of the effects of momentum fields. The Artificial neural networks are applied in Casson liquid motion past via SS was examination by Srinivasacharya and Shravan Kumar [21]. Ouyang et al. [22] developed the thermal conductivity and stability by delving into VD via SS with velocity slip. Biswal et al. [23] created an exciting and rapidly developing field takes thermal radiation in blood motion. Eid et al. [24] presented the MF and ohmic dissipation on NN Casson liquid motion via VSS. Some of the numerical solutions in SS medals [25-31].

The heat generation effect on fluid motion has been expansive motivation research work in heat transfer problems and it is attractive applications in practical, numerical fields and industrial ("such as the storage of nuclear wastes, heaters and coolers of electrical and mechanical devices, thermal insulation, chemical factories etc."). In general, the term "Heat Generation" is occurring high temperature variation between the surface and ambient liquid. Some of the problem of HG on Casson liquid motion is considered to be a constant, space dependent or temperature dependent. The 3D motion and transfer of heat caused by a bidirectional SS with HG was created by Khan et al. [32]. Javed and Siddiqui [33] presented the numerical computation for mixed convection transfer of heat motion of micropolar NFs. Some of authors [34-42] described the numerical computation for HG effect on NNNFs motions via linear or non-linear SS.

MATHEMATICAL ANALYSIS

The 3D NFs motion via shrinking or SS with VS with MHD is considered. The physical model of the coordinate system is explored in **Fig. 1**.
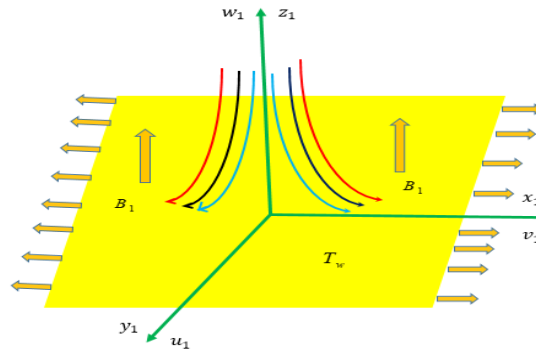

Figure 1. Flow Chart of the Problem

1. The problem created by the SS in x_1 y_1 – surface area with VS.

2. The z_1 directional area is orthogonally to SS $b_1 > 0$ or SHS $b_1 < 0$.

3. The NFs motion occupies area at $z_1 > 0$ and VC of the surface trough x_1 and y_1 directional areas are $u_w(x) = a_1 x_1$ and $v_w(y_1) = b_1 y_1$, respectively.

4. The liquid is EC under influence of UMF B_1 as well as VMF is $w_1 = w_0$, where $w_0 < 0$ then it is called suction and $w_0 > 0$ then it is known as injection.
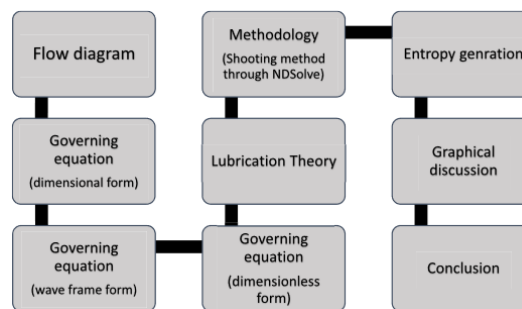
Figure 4. Problem Layout

Under the above considerations, the basic Gov. Eqs are:

$$\frac{\partial u_1}{\partial x_1} + \frac{\partial v_1}{\partial y_1} + \frac{\partial w_1}{\partial z_1} = 0, \tag{1}$$

$$u_1 \frac{\partial u_1}{\partial x_1} + v_1 \frac{\partial u_1}{\partial y_1} + w_1 \frac{\partial u_1}{\partial z_1} = v_1 \left(1 + \frac{1}{\beta_1}\right) \frac{\partial^2 u_1}{\partial z_1^2} - \frac{\sigma_1 B_1^2}{\rho_f 0} u_1 - \frac{\mu_e}{\rho K} \mu_1, \tag{2}$$

$$u_1 \frac{\partial v_1}{\partial x_1} + v_1 \frac{\partial v_1}{\partial y_1} + w_1 \frac{\partial v_1}{\partial z_1} = v_1 \left(1 + \frac{1}{\beta_1}\right) \frac{\partial^2 v_1}{\partial z_1^2} - \frac{\sigma_1 B_1^2}{\rho_f} v_1 - \frac{\mu_e}{\rho K} \mu_1,, \tag{3}$$

$$u_1 \frac{\partial T_1}{\partial x_1} + v_1 \frac{\partial T_1}{\partial y_1} + w_1 \frac{\partial T_1}{\partial z_1} = \alpha_1 \left(\frac{\partial^2 T_1}{\partial z_1^2}\right) + \frac{Q_0 (T_1 - T_\infty)}{(\rho_1 c_p)_f}. \tag{4}$$

Corresponding B.Cs. are

$$\left. \begin{array}{l} u_1 = u_w(x_1) = U_w(x_1) + N_1 \mu_1 \frac{\partial u_1}{\partial z_1}, \ v_1 = v_w(x_1) = V_w(x_1) + N_2 \mu_1 \frac{\partial v_1}{\partial z_1}, \ w_1 = 0, \\[3mm] T_1 = T_w, \ -k_1 \frac{\partial T_1}{\partial z_1} = h_f (T_f - T_1) = 0, \quad at \quad z_1 = o \\[3mm] u_1 \to 0, \ v_1 \to 0, \ T_1 \to T_\infty, \ C_1 \to C_\infty, \quad as \quad z_1 \to \infty \end{array} \right\}. \tag{5}$$

The below dimensionless functions and translated variables are:

$$\eta_1 = z_1 \sqrt{\frac{a_1}{\upsilon_1}}, \ u_1 = a_1 x_1 f'(\eta_1), \ v_1 = a_1 y_1 g'(\eta_1),$$

$$\left. w_1 = -\sqrt{a_1 \upsilon_1} \left(f(\eta_1) + g(\eta_1)\right), \ \theta(\eta_1) = \frac{T_1 - T_\infty}{T_f - T_\infty}, \ \phi(\eta_1) = \frac{C_1 - C_\infty}{C_w - C_\infty}. \right\} \tag{6}$$

Utilizing the above dimensions, **Eq. (6)** is identically satisfied and translate **Eqs. (2)- (4)** becomes:

$$f''' = -f''(f+g) + \left(f'\right)^2 + \left(M+P\right)f' - 1, \tag{7}$$

$$g''' = -g''(f+g) + \left(g'\right)^2 + \left(M+P\right)g' - 1, \tag{8}$$

$$\theta'' = -\Pr\left((f+g)\theta' - H\theta\right). \tag{9}$$

With subject to the B.Cs. are:

$$\left. \begin{array}{l} f(0) = 0, \ g(0) = 0, \ f'(0) = 1 + A f''(0), \ g'(0) = \lambda + B g''(0), \\ \theta(0) = 1, \ \theta'(0) = -Bi(1 - \theta(0)), \\ f'(\eta_1) \to 0, \ g'(\eta_1) \to 0, \ \theta(\eta_1) \to 0, \ \phi(\eta_1) \to 0 \quad \text{as} \quad \eta_1 \to \infty \end{array} \right\} \tag{10}$$

The physical quantities of practical interest are C_{fx_1} and C_{fy_1}, and Nu_{x_1}, it is defined as

$$C_{fx_1} = \frac{\tau_{wx_1}}{\rho_1 U_{w_1}^2}, \quad C_{fy} = \frac{\tau_{w_1 y_1}}{\rho_1 V_{w_1}^2}, \quad Nu_{x_1} = \frac{x_1 q_{x_1}}{k(T_w - T_\infty)}, \text{ and } Sh_{x_1} = \frac{x_1 q_m}{D_B(C_w - C_\infty)}. \tag{11}$$

Defines the SF via x_1, y_1 directional area, HF q_{w_1} and MF q_m from SS are

$$\tau_{wx_1} = \mu_1 \left(\frac{\partial u_1}{\partial z_1}\right)_{z_1=0}, \quad \tau_{w_1 y_1} = \mu_1 \left(\frac{\partial v_1}{\partial z_1}\right)_{z_1=0}, \quad q_{w_1} = -k\left(\frac{\partial T_1}{\partial z_1}\right)_{z_1=0}, \quad q_{w_1} = -D_B\left(\frac{\partial C_1}{\partial z_1}\right)_{z_1=0}. \tag{12}$$

Substituting the u_1, v_1, T_1 from the **Eq. (11)** onto **Eq. (12)** and using **Eq. (6)**, we getting

$$\operatorname{Re}_{x_1}^{1/2} C_{fx_1} = f''(0), \quad \operatorname{Re}_{x_1}^{1/2} C_{fy_1} = g''(0), \quad Nu_{x_1} \operatorname{Re}_{x_1}^{-1/2} = -\theta'(0), \quad Sh_{x_1} \operatorname{Re}_{x_1}^{1/2} = -\phi'(0), \tag{13}$$

where $\operatorname{Re}_{x_1} = U_{w_1}\left(x_1 / v_1\right)$ and $\operatorname{Re}_{y_1} = U_{w_1}\left(y_1 / v_1\right)$ are LRN.

RESULTS AND DISCUSSION

To discuss the outstanding variations of velocity of NN motion and $\operatorname{Re}_x^{-1/2} Nu_x$ ("Heat Transfer Rate") due to relevant physical parameters involved in this study with statistical solutions are explained through their plotted graphs: **2-10**. The present work is considering different cases, like pure fluid, NN liquid, stretching $(\lambda \geq 0)$ and shrinking cases $(\lambda < 0)$.

The physical parameter Pr ("Prandtl number") on $\theta(\eta_1)$ ("Temperature Profile") and $\operatorname{Re}_x^{1/2} Nu_x$ ("Heat transfer rate") as predict **Figs. 2(a)-2(b)** with higher statistical values of Pr for the cases of Pure liquid $(\beta = 0)$, NN liquid ("Casson liquid") $(\beta = 0.5)$ and presence of slip parameter on axial direction $(A = B = 0.1)$, absence of $(A = B = 0)$ slip parameter on transverse direction. It is perceived, the $\theta(\eta_1)$ decline the layer in region $0.02 \leq \eta_1 \leq 1.5$ as well as $\operatorname{Re}_x^{1/2} Nu_x$ with distinct statistical values of Pr. We noticed that the temperature is more in pure fluid when compared with NN liquid, because of thermal conductivity is more in Casson liquid.

Figs. 3(a)-3(b) presented $\theta(\eta_1)$ ("Temperature Profile"), $\operatorname{Re}_x^{1/2} Nu_x$ ("Heat Transfer Rate") with higher numerical values of H for the cases of Pure liquid $(\beta = 0)$ and non-Newtonian liquid ("Casson Liquid") $(\beta = 0.5)$ respectively. It is perceived, the $\theta(\eta_1)$ decline the layer in region $0.0015 \leq \eta_1 \leq 1$ as well as $\operatorname{Re}_x^{1/2} Nu_x$. We noticed that the temperature, heat transfer is more in pure fluid when compared with NN liquid, because of thermal conductivity is more in Casson liquid.
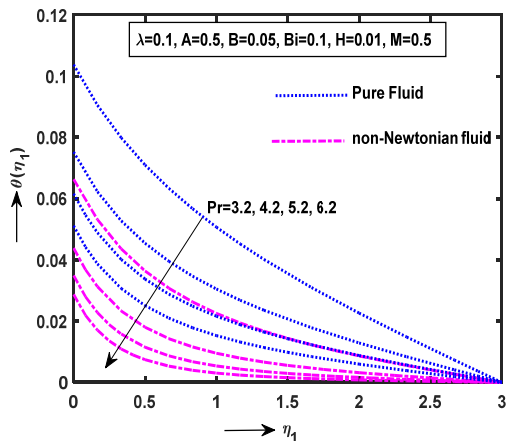
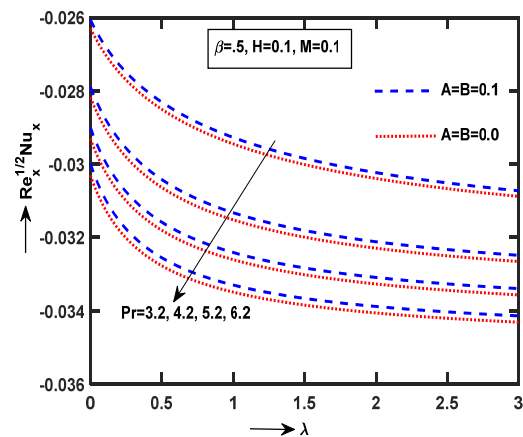**Figure 2(a).** Outline of Pr on $\theta(\eta_1)$

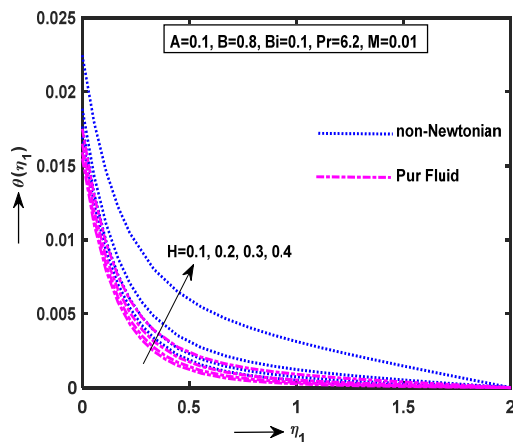**Figure 2(b).** Outline of Pr on $Re_x^{1/2} \, Nu_x$

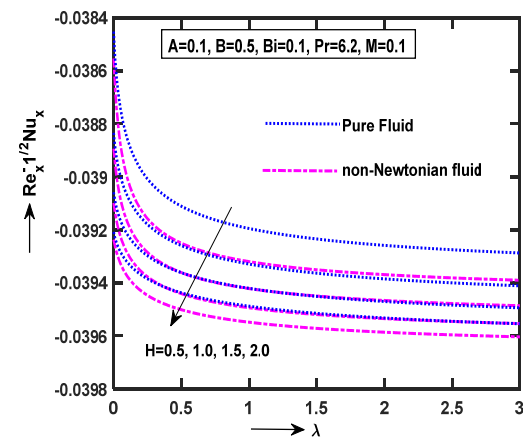**Figure 3(a).** Outline of H on $\theta(\eta_1)$

Figure 3(b). Outline of H on $Re_x^{1/2} \, Nu_x$

The main characteristics of this model is β ("Casson Parameter") on $f(\eta_1)$ ("Axial Direction"), g(η_1) ("Transverse Direction") as predict **Fig. 4**. It is perceived, the decline of both axial and transverse direction with distinct numerical values of β. We observe that, the Casson liquid motion is very high motion in axial direction on stretching surface while compare to transverse direction. Because, the plastic dynamic viscosity of Casson liquid motion is very high. Due to this, the Casson liquid is slow motion on surface in axial direction.

The physical parameter M ("Magnetic Field Parameter") on $f(\eta_1)$ ("Axial Direction"), g(η_1) ("Transverse Direction") as predict **Fig. 5**. It is perceived, the decline of both axial and transverse direction with high distinct numerical values of M. We observe that, the magnetic field parameter is very high motion in transverse direction on SS while compare to axial direction. Because, the magnetic force applied to Casson liquid which has generate drag force named as "Lorentz force". This force acts Casson liquid in opposite direction to the motion.
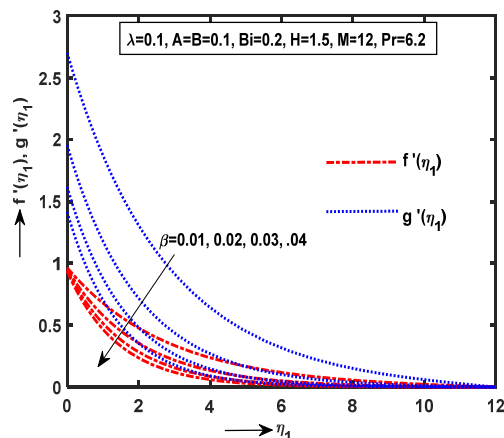

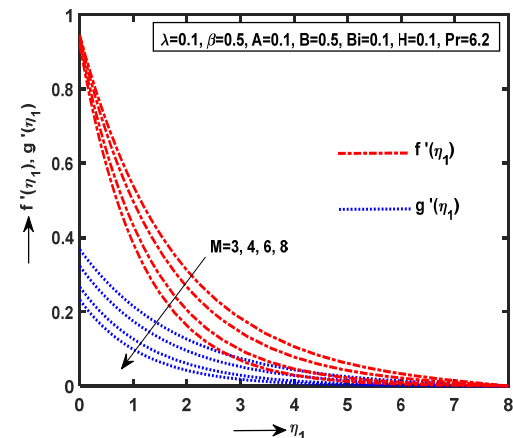**Figure 4.** Outline of β on $f'(\eta_1)$, g'(η_1)

Figure 5. Outline of M on $f'(\eta_1)$, g'(η_1)

The characteristics of Bi ("Stretching/Shrinking Parameter") on $\theta(\eta_1)$ ("Temperature Profile") and B ("Slip Parameter on Transverse Direction") for Stretching $(Bi \geq 0)$ and shrinking $(Bi < 0)$ cases as depicted **Fig. 6(a)-6(b)**. It is perceived, the Bi improves temperature while opposite direction of B with distinct enlarge statistical values. We observe that, the Casson liquid flow is very high temperature motion in case of $(Bi \geq 0)$ ("Stretching") while compare to $(Bi < 0)$ ("Shrinking"). Because, the viscosity of Casson liquid motion in stretching sheet is very high.
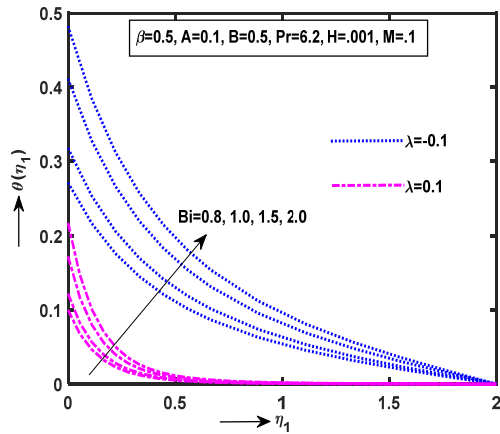
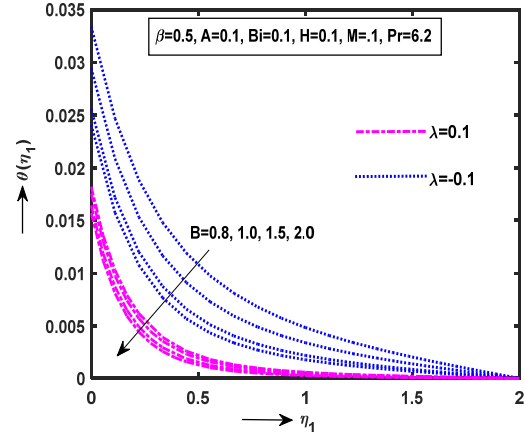**Figure 6(a).** Outline of Bi on $\theta(\eta_1)$

Figure 6(b). Outline of B on $\theta(\eta_1)$

Figs. 7(a)-7(b) illustrate the characteristics of A ("Slip Parameter on Axial Direction") on $\mathrm{Re}_x^{1/2} C_{fx}$ ("Skinfriction" coefficient along axial direction"), $\mathrm{Re}_x^{1/2} C_{fy}$ ("Skinfriction" Coefficient along Transverse Direction") respectively. It is clear that, the A ("Slip Parameter on Axial Direction") declined both axial and transverse directions of Skinfriction coefficient foe higher enlarge statistical values of "A". We noticed that, the Skinfriction is less movement in Casson liquid flow via stretching surface.
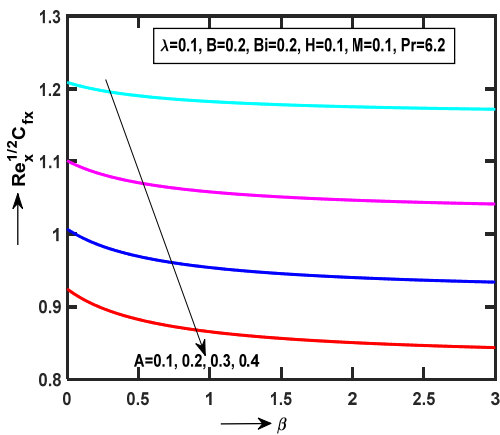

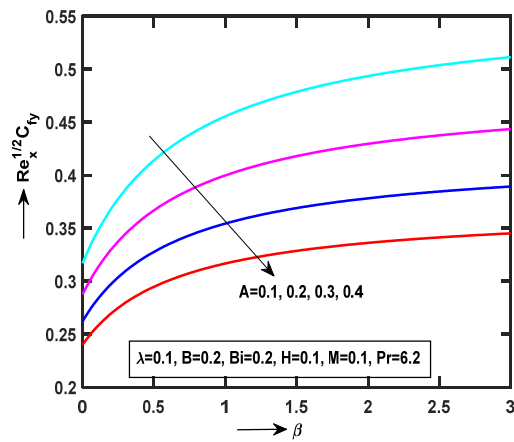**Figure 7(a).** Outline of A on $\mathrm{Re}_x^{1/2} C_{fx}$

Figure 7(b). Outline of A on $\mathrm{Re}_x^{1/2} C_{fy}$

The Table 1 and 2 presented that, the comparison study of present and previous study for Skinfriction coefficient with various numerical cases of magnetic parameter M.

Table. 1 Evaluation of SFC $-f''(0)$ for $A = B = Bi = 0$

M	Present study	Sarah et al. [36]	Nadeem et al. [37]	Gupta and Sharma [38]	Ahmad and Nazar [39]
0.0	1.000000	1.00000	1.0004	1.0003181	1.0042
10	3.316624	3.31662	3.3165	3.3165824	3.3165
100	10.04987	10.04987	10.049	10.049864	10.049

Table. 2 Comparison of SFC $-f''(\infty)$ for $A = B = Bi = 0$

M	Present study	Nadeem et al. [37]
0.0	1.173719	--
10	3.367222224	3.3667
100	10.06646642	10.066

CONCLUSIONS

A statistical analysis has been done for HG effect on 3D MHD motion of Casson liquid via SS with VS Condition. The main contribution of the present investigations is mentioned below:

❖ The $\text{Re}_x^{1/2} Nu_x$ is very less motion in Casson liquid when presence of slip parameter while comparing with absence of slip parameter for higher values of Pr.

❖ The temperature is less transfer in NN liquid motion when compares with pure liquid motion with higher statistical values of Pr.

❖ The HG is high in pure fluid while opposite motion in HTR when compared with Casson liquid for escalate values of H.

Nomenclature			
(x_1, y_1)	Cartesian coordinate's	T_w	Constant fluid Temperature of the wall
u_1, v_1, w_1	velocity components along x_1, y_1, z_1 -axis	U_w	Stretching velocity
A	Velocity slip along x-axes $\sqrt{a\gamma_0}N_1$	U_∞	Free stream velocity
B	Velocity slip along y-axes $\sqrt{a\gamma_0}N_2$	*Greek symbols*	
f	Dimensionless stream function	ρ_1	Density
$f^{'}$	Dimensionless velocity	σ_1	Boltzmann constant
H	Heat Generation Parameter $\left(\dfrac{Q_0}{a_1(\rho_1 c)_f}\right)$	λ	Constant stretching/shrinking parameter b_1/a_1
M	Magnetic field parameter $= \dfrac{\sigma_1 B_0^2}{a_1 \rho_f}$	v_1	Kinematic viscosity of the fluid
P	Porous Parameter $= \left(\dfrac{\mu_e}{\rho v}\right)$	θ	Dimensionless temperature
Pr	Prandtl number $= \left(\dfrac{v_1}{\alpha_1}\right)$	α_1	Thermal diffusivity $= k/(\rho c_p)_f$
Re_x	Reynolds number	*Subscripts*	
T_1	Temperature of the fluid	∞	condition at free stream
T_∞	fluid temperature far away from the surface		
Abbreviations			
NFs	Nanofluids	HTR	Heat Transfer Rate
HT	Heat TRansfer	SS	Stretching Sheet
HMT	Heat and Mass Transfer	VD	Viscous Dissipation
HG	Heat generation	SHS	Shrinking Sheet
MHD	Magnetohydrodynamic	3D	Three Dimensional
MF	Magnetic Field	NN	non-Newtonian
BL	Boundary Layer	B.Cs.	Boundary Conditions
SP	Stagnation Point	HNFs	Hybrid Nanofluids
BVP	Boundary Value Problem	RKF	Range Kutta Fehlberg
SFC	Skinfriction Coefficient	NNF	non-Newtonian Nanofluid

ORCID

B. Jagadeesh Kumar, https://orcid.org/0009-0008-0534-7712
Nainaru Tarakaramu, https://orcid.org/0000-0001-6049-424X

REFERENCES

[1] N. Casson, in: *Rheology of disperse systems in Flow Equation for Pigment Oil Suspensions of the Printing Ink Type. Rheology of Disperse Systems*, edited by C.C. Mill, (Pergamon Press, London, UK, 1959). pp. 84-102.

[2] P. Barnoon, and D. Toghraie, "Numerical investigation of laminar flow and heat transfer of non-Newtonian nanofluid within a porous medium," Powder Technology, **325**, 78-91 (2018). https://doi.org/10.1016/j.powtec.2017.10.040

[3] P.K. Kameswaran, S. Shaw, and P. Sibanda, "Dual solutions of Casson fluid flow over a stretching or shrinking sheet," Sadhana, **39**, 1573-1583 (2014). https://doi.org/10.1007/s12046-014-0289-7

[4] U.S. Mahabaleshwar, G.P. Vanitha, and B.A. Souayeh, "Study of Casson Viscous Gas Flows and Heat Transfer Across a Linear Stretching/Shrinking Sheet by Considering Induced Slip, Mass Transpiration, Inclined Magnetic Force, and Radiation Effect," BioNanoSci. **13**, 1052–1063 (2023). https://doi.org/10.1007/s12668-023-01128-8

[5] K.A. Duguma, O.D. Makinde, and L.G. Enyadene, "Stability Analysis of Dual Solutions of Convective Flow of Casson Nanofluid past a Shrinking/Stretching Slippery Sheet with Thermophoresis and Brownian Motion in Porous Media," Journal of Mathematics, **2023**, 1-25 (2023). https://doi.org/10.1155/2023/5954860

[6]   H. Himanshu, S.R. Mishra, A.K. Pandey, and Priya Bartwal, "Shape factor analysis in stagnation point flow of Casson nanofluid over a stretching/shrinking sheet using Cattaneo-Christov model," Numerical Heat Transfer, Part B: Fundamentals, 1–17 (2023). https://doi.org/10.1080/10407790.2023.2265555

[7]   N. Vishnu Ganesh, Q.M. Al-Mdallal, R. Kalaivanan, and K. Reena, "Arrhenius kinetics driven nonlinear mixed convection flow of Casson liquid over a stretching surface in a Darcian porous medium," Heliyon, **9**(6), E16135 (2023). https://doi.org/10.1016/j.heliyon.2023.e16135

[8]   B.S. Goud, Y.D. Reddy, and Adnan, "Numerical Investigation of the Dynamics of Magnetized Casson Fluid Flow over a Permeable Wedge Subject to Dissipation and Thermal Radiations," Surface Review and Latter, **31**, 2450054 (2024). https://doi.org/10.1142/S0218625X24500549

[9]   K.U. Rehman, A.A. Khan, M.Y. Malik, and O.D. Makinde, "Thermophysical aspects of stagnation point magnetonanofluid flow yields by an inclined stretching cylindrical surface: a non-Newtonian fluid model," J Braz. Soc. Mech. Sci. Eng. **39**, 3669-3682 (2017). https://doi.org/10.1007/s40430-017-0860-3

[10] S.A. Gaffar, V. Ramachandra Prasad, and B. Vijaya, Computational study of non-Newtonian Eyring–Powell fluid from a vertical porous plate with biot number effects, J Braz. Soc. Mech. Sci. Eng. (2017) 1-35. https://doi.org/10.1007/s40430-017-0761-5

[11] M. Imtiaz, T. Hayat, and A. Alsaedi, "Mixed convection flow of Casson nanofluid over a stretching cylinder with convective boundary conditions," Advanced Powder Tech. **27**, 2245-2256 (2016). https://doi.org/10.1016/j.apt.2016.08.011

[12] M. Ramzan, M. Bilal, and J.D. Chung, "Influence of homogeneous-heterogeneous reactions on MHD 3D Maxwell fluid flow with Cattaneo-Christov heat flux and convective boundary condition," J. Mole. Liq. **230**, 415-422 (2017). https://doi.org/10.1016/j.molliq.2017.01.061

[13] M.M. Bhatti, and M.M. Rashidi, "Effects of thermo-diffusion and thermal radiation on Williamson nanofluid over a porous shrinking/stretching sheet," J. Mole. Liq. **221**, 567-573 (2016). https://doi.org/10.1016/j.molliq.2016.05.049

[14] G.M. Moatimid, and M.A. Hassan, "Convection instability of non-Newtonian Walter's nanofluid along a vertical layer," J. Egyptian Math. Soc. **25**, 220-229 (2017). https://doi.org/10.1016/j.joems.2016.09.001

[15] A. Rauf, M.K. Siddiq, F.M. Abbasi, M.A. Meraj, M. Ashraf, and S.A. Shehzad, "Influence of convective conditions on three dimensional mixed convective hydromagnetic boundary layer flow of Casson nanofluid," J. Magn. Magnet. Mater. **416**, 200-207 (2016). https://doi.org/10.1016/j.jmmm.2016.04.092

[16] M. Adel, M.M. Khader, and Hijaz Ahmad, "MHD nanofluid flow and heat transfer caused by a stretching sheet that is heated convectively: An approximate solution using ADM," Case Studies in Thermal Engineering, **60**, 104683 (2024). https://doi.org/10.1016/j.csite.2024.104683

[17] P.R. Sekhar, S. Sreedhar, S.M. Ibrahim, P.V. Kumar, and B. Omprakash, "Numerical investigation of heat radiation on MHD viscoelastic nanofluid flow over a stretching sheet with heat source and slip conditions," Int. J. Interact Des. Manuf. **18**, 2991–3000 (2024). https://doi.org/10.1007/s12008-023-01407-4

[18] F. Ali, A. Zaib, M. Faizan, S.S. Zafar, S. Alkarni, N. Ali Shah, and J.D. Chung, "Heat and mass exchanger analysis for Ree-Eyring hybrid nanofluid through a stretching sheet utilizing the Homotopy perturbation method," Case Studies in Thermal Engineering, **54**, 104014 (2024). https://doi.org/10.1016/j.csite.2024.104014

[19] M.T. Akolade, S.A. Agunbiade, and T.L. Oyekunle, "Onset modules of heat source and generalized Fourier's law on Carreau fluid flow over an inclined nonlinear stretching sheet," International Journal of Modelling and Simulation, **44**(1), (2024). https://doi.org/10.1080/02286203.2022.2151964

[20] M. Saleem, M. Hussain, and I. Mustafa, "Significance of Darcy-Forchheimer law and magnetic field on the comparison of Williamson-Casson fluid subject to an exponential stretching sheet," **37**(27), 2350315 (2023). https://doi.org/10.1142/S0217979223503150

[21] D. Srinivasacharya, and R.S. Kumar, "An Artificial Neural Network Solution for the Casson Fluid Flow Past a Radially Stretching Sheet with Magnetic and Radiation Effect," Mathematical Models and Computer Simulations, **15**, 944-955 (2023). https://doi.org/10.1134/S2070048223050101

[22] Y. Ouyang, Md.F.Md. Basir, K. Naganthran, and I. Pop, "Dual solutions in Maxwell ternary nanofluid flow with viscous dissipation and velocity slip past a stretching/shrinking sheet," Alexandria Engineering Journal, **105**, 437-448 (2024). https://doi.org/10.1016/j.aej.2024.07.093

[23] M.M. Biswal, K. Swain, G.C. Dash, and S. Mishra, "Study of chemically reactive and thermally radiative Casson nanofluid flow past a stretching sheet with a heat source," **52**(1), 333-353 (2023). https://doi.org/10.1002/htj.22697

[24] A. Eid, M.M. Khader, and A.M. Megahed, "Vieta-Lucas Collocation Technique for Examination of the Flow of Casson Fluid over a Slippery Stretching Sheet Which Is Impacted by Thermal Slip, Ohmic Dissipation, and Variable Thermal Conductivity," Journal of Mathematics, **2023**, 8723343, (2023). https://doi.org/10.1155/2023/8723343

[25] O.D. Makinde, Z.H. Khan, R. Ahmad, and W.A. Khan, "Numerical study of unsteady hydromagnetic radiating fluid flow past a slippery stretching sheet embedded in a porous medium," Phys. Fluids, **30**, 083601 (2018). https://doi.org/10.1063/1.5046331

[26] M.E. Rao, "The effects of thermal radiation and chemical reaction on MHD flow of a Casson fluid over and exponentially inclined stretching surface," IOP Conf. Series: Journal of Physics: Conf. Series, **1000**, 012158 (2018). https://doi.org/10.1088/1742-6596/1000/1/012158

[27] B. Mahanthesh, B.J. Gireesha, R.S.R. Gorla, and O.D. Makinde, "Magnetohydrodynamic three-dimensional flow of nanofluids with slip and thermal radiation over a nonlinear stretching sheet: a numerical study," Neural Comput Appl. **30**, 1557–1567 (2018). https://doi.org/10.1007/s00521-016-2742-5

[28] N. Tarakaramu, N. Sivakumar, P.V.S. Narayana, and R. Sivajothi, "Viscous Dissipation and Joule Heating Effects on 3D Magnetohydrodynamics Flow of Williamson Nanofluid in a Porous Medium Over a Stretching Surface With Melting Condition," ASME Open J. Engineering, **2022**(1), 0110331 (2022). https://doi.org/10.1115/1.4055183

[29] K.B. Lakshmi, V. Sugunamma, N. Tarakaramu, N. Sivakumar, and R. Sivajothi, "Cross-dispersion effect on magnetohydrodynamic dissipative Casson fluid flow via curved sheet," Heat Transfer, **51**(8), 7822-7842 (2022).. https://doi.org/10.1002/htj.22668

[30] N. Tarakaramu, P.V.S. Narayana, R. Sivajothi, K.B. Lakshmi, D.H. Babu, and B. Venkateswarlu, "Three-dimensional non-Newtonian couple stress fluid flow over a permeable stretching surface with nonlinear thermal radiation and heat source effects," Heat Transfer, **51**(6), 5348-5367 (2022). https://doi.org/10.1002/htj.22550

[31] M. Khan, H. Sardar, and Hashim, "Heat generation/absorption and thermal radiation impacts on three-dimensional flow of Carreau fluid with convective heat transfer," Mole. Liq. **272**, 474-480 (2018). https://doi.org/10.1016/j.molliq.2018.08.088

[32] T. Javed, and M.A. Siddiqui, "Mixed convection in micropolar nanofluid flow through entrapped triangular enclosures and linear stability analysis considering magnetic effects and heat generation/absorption," Can. J. Phys. **97**(3), 252-266 (2018). https://doi.org/10.1139/cjp-2017-0974

[33] A.G. Madaki, R. Roslan, M.S. Rusiman, and C.S.K. Raju, "Analytical and numerical solutions of squeezing unsteady Cu and TiO$_2$-nanofluid flow in the presence of thermal radiation and heat generation/absorption," Alexandria Eng. J. **57**(2), 1033-1040 (2017). https://doi.org/10.1016/j.aej.2017.02.011

[34] S. Qayyum, T. Hayat, and A. Alsaedi, "Chemical reaction and heat generation/absorption aspects in MHD nonlinear convective flow of third grade nanofluid over a nonlinear stretching sheet with variable thickness," Results Phys. **7**, 2752–2761 (2017). https://doi.org/10.1016/j.rinp.2017.07.043

[35] P.S. Reddy, A.J. Chamkha, and A.A. Mudhaf, "MHD heat and mass transfer flow of a nanofluid over an inclined vertical porous plate with radiation and heat generation/absorption," Advanced Powder Tech. **28**, 1008-1017 (2017). https://doi.org/10.1016/j.apt.2017.01.005

[36] Ch. Ram Reddy, O. Surender, Ch. Venkata Rao, and T. Pradeepa, "A domain decomposition method for Hall and ion-slip effect son mixed convection flow of a chemically reacting Newtonian fluid between parallel plates with heat generation/absorption," Propulsion Power Res. **6**(4), 296–306 (2017). https://doi.org/10.1016/j.jppr.2017.11.001

[37] K.U. Rehman, A.S. Alshomrani, and M.Y. Malik, "Carreau fluid flow in a thermally stratified medium with heat generation/absorption effects," Case Studies Thermal Eng. **12**, 16–25 (2018). https://doi.org/10.1016/j.csite.2018.03.001

[38] G. Sarojamma, K. Vajravelu, and K. Sreelakshmi, "A study on entropy generation on thin film flow over an unsteady stretching sheet under the influence of magnetic field, thermocapillarity, thermal radiation and internal heat generation/absorption," Communications Numerical Analysis, **2017**(2), 141-156 (2017). http://dx.doi.org/10.5899/2017/cna-00319

[39] I.S. Oyelakin, S. Mondal, and P. Sibanda, "Unsteady Casson nanofluid flow over a stretching sheet with thermal radiation, convective and slip boundary conditions," Alexandria Eng. J. **55**, 1025-1035 (2015). https://doi.org/10.1016/j.aej.2016.03.003

[40] S. Nadeem, R.U. Haq, and N.S. Akbar, "MHD three-dimensional boundary layer flow of Casson nanofluid past a linearly stretching sheet with convective boundary condition," IEEE Trans. Nanotech. **13**(1), 109-115 (2014). https://doi.org/10.1109/TNANO.2013.2293735

[41] S. Gupta, and K. Sharma, "Numerical simulation for magnetohydrodynamic three-dimensional flow of Casson nanofluid with convective boundary conditions and thermal radiation," Eng. Comp. **34**(8), 2698-2722 (2017).

[42] K. Ahmad, and R. Nazar, "Magnetohydrodynamic three-dimensional flow and heat transfer over a stretching surface in a viscoelastic fluid," J. Sci. Technol. **3**(1), 1-14 (2011).

ВПЛИВ ГЕНЕРАЦІЇ ТЕПЛА НА 3D МГД ПОТІК КАССОНОВОЇ РІДИНИ ЧЕРЕЗ ПОРИСТУ ПОВЕРХНЮ ЩО РОЗТЯГУЄТЬСЯ/СКОРОЧУЄТЬСЯ З УМОВОЮ ШВИДКІСНОГО КОВЗАННЯ

Б. Джагадіш Кумар, Найнару Таракараму
Факультет математики, школа вільних мистецтв і наук, Університет Мохана Бабу,
Срі Сайнат Нагар, Тірупаті-517102, Андрападеш, Індія

Існує широкий спектр застосувань, пов'язаних з ядерною промисловістю, промисловим виробництвом, наукою та інженерною обробкою, у яких гідромагнітний рух прикордонного шару рідин Кассона відіграє життєво важливу роль. Рідина Casson є корисною рідиною в атомній промисловості для оптимізації конструкції та роботи ядерних реакторів. Дослідники досліджували передачу тепла в русі рідини з лінійною стратифікацією, яка є явищем, коли температура змінюється лінійно з висотою, впливаючи на різні галузі, такі як медичне обладнання, виробництво скловолокна, електронні пристрої, полімерні листи, виробництво паперу, ниток і медицина . Проте найбільше обговорення проблем теплообміну полягає в тому, щоб отримати чисельні рішення комплексної рідинної моделі Кассона з утворенням тепла, описаним BVP4 за допомогою методу зйомки. У цьому дослідженні нова гранична умова швидкісного ковзання застосована на поверхні розтягування або звуження. Ці умови ґрунтуються на раніше встановленій моделі Буонгіорно, що забезпечує більш практичний і реалістичний підхід порівняно з попереднім дослідженням. Незалежне від часу Gov. Eqs. змінено на набір пари нелінійних ODE за допомогою відповідних перетворень подібності. Рівняння оцінюються через R-K-F за допомогою програмного забезпечення MATLAB.
Ключові слова: *магнітогідродинаміка; поверхня, що скорочується/розтягується; швидкісне ковзання; генерація/поглинання тепла; Кассонова рідина; 3D*

UNDERSTANDING THE PROJECTILE BREAKUP MECHANISM USING MONTE CARLO SIMULATION TECHNIQUE

M. Swain[a], Prasanta Kumar Rath[a,b]*, Balaji Padhy[a], Aditya Kumar Pati[a], Vaishali R. Patel[c], Nirali Gondaliya[c], Ami N. Deshmukh[c], Ravindra Prajapati[c], N.N. Deshmukh[c]

[a]*Centurion University of Technology and Management, Paralakhemundi, Odisha, 76121l - India*
[b]*Department of Physics, University of Naples "Federico II" and INFN, I-80125, Naples, Italy*
[c]*P.P. Savani University, Dhamdod, Kosamba, Surat, Gujarat, India*
*Corresponding Author email: prasanta.rath@cutm.ac.in

The breakup of projectile has been understood using a Montecarlo simulation at low energy, which indicates a wider breakup cone is present for near target breakup whereas at far target breakup there are well localized breakup cone is present. The simulations indicate the requirement of wider solid angle in experiment and localized kinematic solid angle to study the breakup phenomena. The case study of ^{7}Li+^{208}Pb has been considered and found well agreement of simulated results with experimental data.
Keywords: *ES (Elastic scattering); CF (Complete Fusion); ICF (Incomplete fusion); CN (Compound Nucleus); BU (Break up)*
PACS: 25.60.Dz, 25.10.+s, 25.40.Hs, 25.60.Gc, 25.60.Pj, 25.60.Je, 25.70.Gh

INTRODUCTION

Study of nuclear reaction involving loosely bound projectile is a subject of current study and interest in specific [1-5]. This is because when one can use a loosely bound projectile there is a possibility that the projectile can fuse with the target or it can break before the fusion leads to an incomplete fusion (ICF) process. Including ICF there can be a break up escape, transfer and pickup can also possible [6]. Many experimental studies [7-9] has been done and found that using loosely bound projectiles if complete fusion can be measured there is a fusion suppression of complete fusion above the barrier and enhancement bellow the barrier has been reported compared to the Single barrier penetration model calculation. The exact reason is still far from understanding. Not only the enhancement and suppression has observed but there can be proton transfer and n pickup has also been observed including main breakup channel [10]. All the above-mentioned feature has been observed only by using the projectile a loosely bound projectile (^{7}Li→α+t,^{6}Li→α+d,^{9}Be→α+α+n…etc). Recently there are reports which indicates the breakup from the resonant states including the excited states of projectiles are important [20]. In addition, with the breakup the location (near/far) where the breakup occurs also effects the crossection and it is difficult to measure experimentally all the times as it requires higher solid angle coverage experiment [16-19]. To understand these phenomena presently limited theoretical models are available for example CDCC, FRESCO, CCFULL [11-12]. All the models are complex quantum mechanical models. People are trying to develop simplified model which can explain all the phenomena simultaneously.

Our work is also on the same way. In the present paper we tried to understand the reaction specially the breakup of the projectile around the coulomb barrier using a classical approach and Monte Carlo modeling.

The present approach will be helpful to understand near /far breakup mechanism. Since experimentally it is always difficult to get the data in all 4π, So a model has been adopted (using classical trajectory under Monte Carlo modeling) to understand the breakup mechanism.

Specially we tried to understand the mechanism around the coulomb barrier regions. Because around the barrier, (below the barrier) the fusion will not possible, the nuclear reaction can happen because of tunneling phenomena. So, it is interesting to see a classical approach bellow the barrier to understand the breakup mechanism.

The paper has been organized as follows in the Section 1 experimental detail has been provided, Section 2 contains the modeling (classical trajectory approach using Montecarlo modeling) with results. The Summary with future outlook has been explained in Section 3.

EXPERIMENTAL DETAIL

The experiment was performed long time back with the projectile ^{7}Li and a target of ^{208}Pb of thickness 200 μg/cm^2. It was a self-supporting target. The experiment was done at 8PLP set up [13]. The projectile energies vary from 31 to 39 MeV. The beam intensity was around 10 nA. The Coulomb barrier is ~31 MeV with fusion radius R$_B$~10.69fm provided by Proximity potential [14]. In the present paper we have focused only on one energy, that is 31 MeV which is around the barrier. The other energies are above the barrier so it has not considered presently. The detail experimental approach has been reported in [14]. There are ΔE vs Time and E vs ΔE graph has been generated to identify the particles ejected during the reaction.

A typical experimental spectrum has been shown in Fig. 1 for 31 MeV. It can be observed from Fig. 1 that there are different particles (alpha, triton, deuteron, proton) are present which come out from the reaction because of many reactions' mechanism. The particles have been identified very clearly.
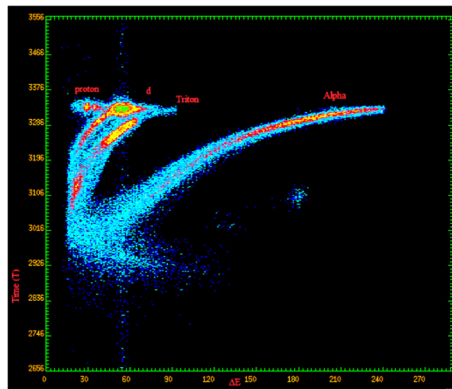

Figure 1. Typical raw spectra of particles detected during the experiment for 31MeV of ^{7}Li. All the particles are clearly visible

CALCULATION AND MODEL SIMULATIONS

A theoretical calculation including a Montecarlo modeling has been performed to understand the breakup mechanism. As a first work we have generated the coulomb barrier which is the addition of nuclear plus coulomb potential as shown in Fig. 2. The proximity potential [14] has been chosen for nuclear one which is a Wood-Saxon type in nature. The form of the wood Saxon potential is $V(r) = -V_0/(1+\exp(r-r_0)/a)$, where V_0 is the depth of the nuclear potential, a_0 is the diffuseness parameter which has taken as 0.63 fm for the present case, r is the radial distance between the interacting nuclei and r_0 is 1.02fm.

For our simulation and modeling the breakup fragments of projectile (^{7}Li→ α+t) has been detected in coincidence mode and the coincidence spectrum of alpha and triton for a beam energy of 31 MeV has been shown in Fig. 3.
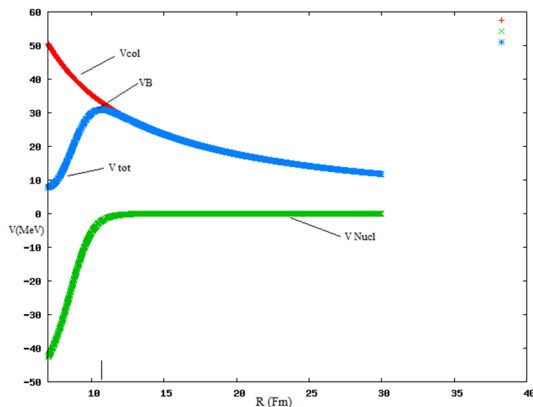

Figure 2. The effective potential for ^{7}Li+^{208}Pb using proximity potential. The barrier radius R_B and different contribution has been shown. (Vcol is the Coloumb potential; Vnucl is the nuclear potential, Vtot is the addition of Coloumb+ nuclear potential. VB – the barrier height which will be taken as the barrier of the system)
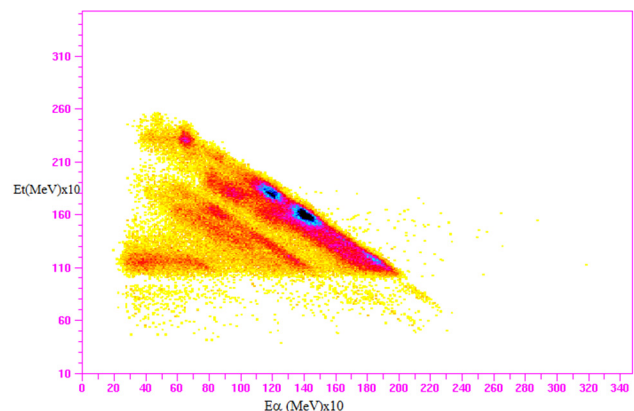
Figure 3. Coincidence experimental data of alpha and triton for 31 MeV projectile energy

From Fig. 3 one can see that there are different bands and the different bands results from the different break up process. (breakup from GS, breakup from excited state, breakup from resonant state, Ex: Ex = 4.630 MeV, 7/2$^-$ for ^{7}Li …etc). The same structure of the band in coincidence mode keeping the detector geometry in mind has been simulated using Montecarlo technique and shown in Fig. 4.

In the simulation the target excitation has not included as our aim is to see the effect of projectile breakup only. If we see the value of the loci of the 2d spectra (Fig. 4) and compare with the loci of Fig. 3 for the projectile breakup we will see the patches matches at the same values which indicates the reproduction of the experimental data for the projectile breakup. No contribution of the target excited states has considered as it makes the situation complex. The same can be tried later.

In the present case to understand the interaction/breakup mechanism of the projectile we have considered only around the barrier points i.e 31 MeV data only. From Fig. 2 one can see that the barrier radius (R_B) ~ 10.6 Fm. This indicates that if the projectile wants to fuse with the target it has to cross that barrier radius and below the barrier energy it is difficult for the projectile to reach that barrier radius. So, it has assumed that the maximum break up point after which the particle can fuse

with the target is the barrier radius (R_B). In the below barrier energy in addition with tunneling the projectile can scattered to different direction. For each scattering the scattered angle has been randomly samples between the angle $0°$ to 180^0. For a given randomly generated scattering angle the distance of closest approach has been calculated as prescribe in [15]. The randomly generated scattering angle with the distance of closet approach has been shown in Fig. 5.
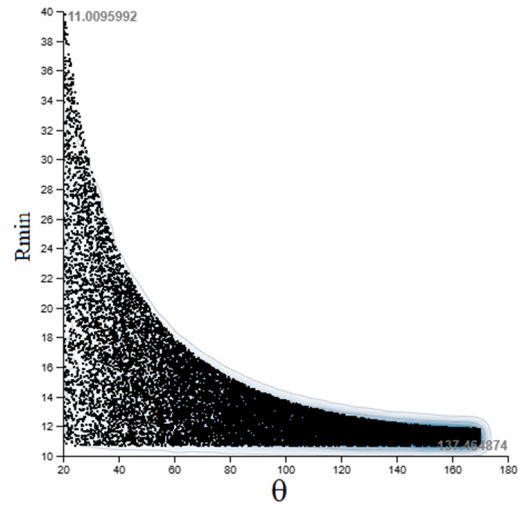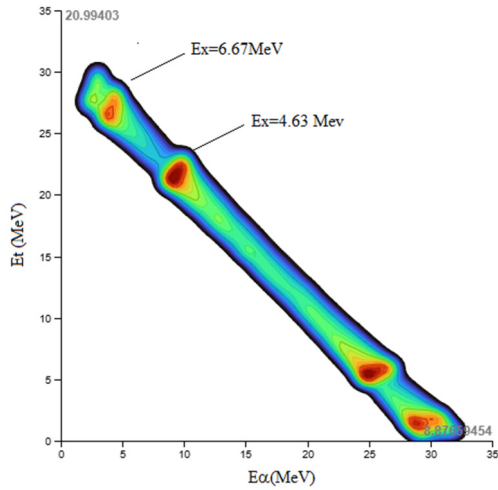

Figure 4. Montecarlo simulation keeping the geometry in mind. The coincidence of alpha and triton has been considered only. The different patch leads to the different excited states of the projectile

Figure 5. Randomly generated R_{min} w.r.t. the scattering angle for a given energy

After determining the distance of closest approach, a breakup point has been chosen randomly between the distance of closest approach and the barrier radius by doing a random sampling with a probability of breakup exponential decaying in nature ($P_{bu} \alpha e^{Rand(R_{min}-R_{BU})}$). Once the breakup point has been identified then the particle can be scattered and two break up fragments can be detected in coincidence. Here two types of break up has been considered 1) near target breakup 2) far or asymptotic breakup. In the above expression α is the proportionality constant, P_{bu}- breakup probability, Rand (R_{BU} - R_{min}) is the randomly generated point between breakup radius (R_{BU}) and R_{min}. R_{min} is the distance of closest approach for a given energy and angle.

In case of near target breakup, the influence of the coulomb potential may provide a wider breakup cone which translates to a wider $\Delta\theta$, where as in case of asymptotic breakup the influence of the coulomb potential will be negligible and the breakup may have a narrow breakup cone as shown in Fig. 6.
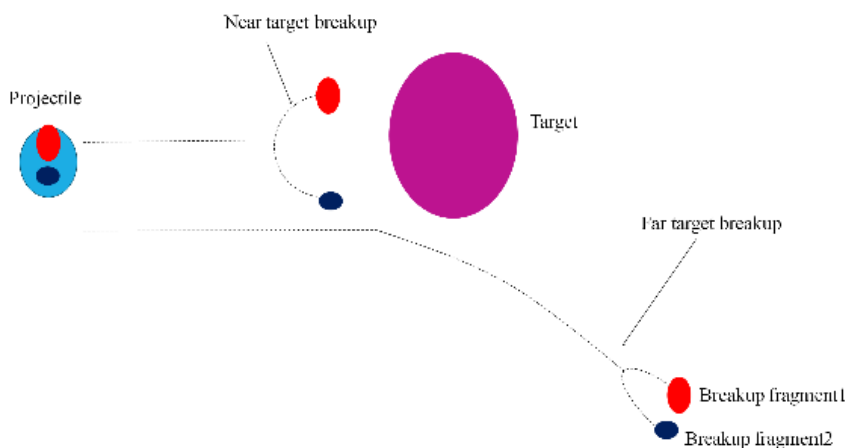

Figure 6. Pictorial diagram of the breakup of the projectile near target and far away from the target

When the projectile breaks near the target it has assumed that it breaks instantly from the breakup point. where as when breakup happens asymptotically, far from target, its breakup happens from the excited state of a specific energy and time. So, when the projectile breaks from the excited states or resonance states (For ^7Li the resonance state considered for simulation are 4.652 MeV, $7/2^-$, & 6.67 MeV, $5/2^-$). The $\Delta\theta$ with the breakup angle (β) has been shown schematically in Fig. 7.
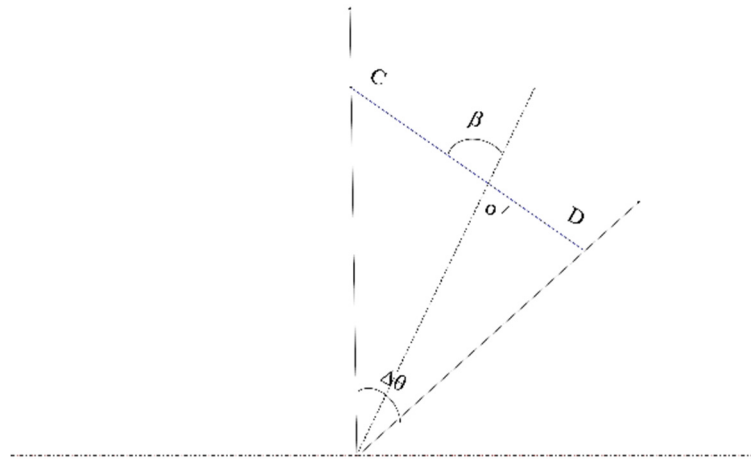
Figure 7. Schematic diagram to represent the Dq and b (b). The ejectile can break in to two fragment C, D and the fragments move in opposite direction in their c.m. frame of projectile from the point o$^{/}$

The breakup fragments have been detected coincidently for both the case near target and far away from the target. The full simulation has been done using the present geometry in consideration and the result has been shown in Fig. 8.
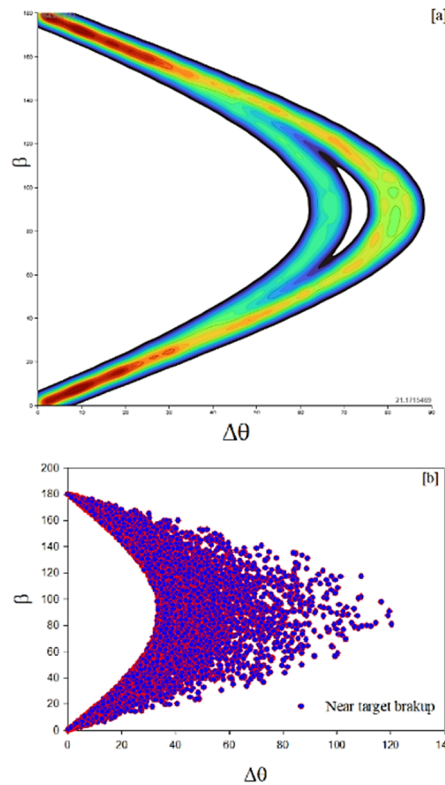

Figure 8. [a] – the result of Montecarlo simulation for the two resonant states of ^{7}Li. i.e. the breakup has happened far away from the target and one can see a well-defined localized distribution of the fragments with narrow detection cone; [b] - The breakup near the target which indicates wider angle of detection cone w.r.t β breakup angle).

One can see from the Fig. 8 that if we consider the near target breakup then there is a wider distribution of the Δθ with respect to β. In case of a far or asymptotic breakup the breakup fragments have a narrow angle of detection that means the Δθ will be more localized whereas the near target breakup the distribution is wider as shown from Fig. 8.

SUMMARY & FUTURE WORK

A Montecarlo simulation has been performed to understand the breakup at low energy and it has found that there are wider cones for near target breakup compared to asymptotic breakup. This provides an important input to experimentalist to setup their experimental apparatus for experiment to catch the breakup fragments. In addition, a coincidence energy spectrum has also simulated and presented. In future the time evolution of the trajectory will be simulated under the potential surface.

ORCID
Prasanta Kumar Rath, https://orcid.org/0000-0002-3869-9705, **Balaji Padhy**, https://orcid.org/0000-0002-3447-2917
Aditya Kumar Pati, https://orcid.org/0000-0003-0966-5773

REFERENCES
[1] L.F. Canto, P.R.S. Gomes, R. Donangelo, and M.S. Hussein, Phys. Rep. **424**, 1 (2006). https://doi.org/10.1016/j.physrep.2005.10.006
[2] P.K. Rath, *et al*., Phys. Rev. C, **79**, R051601 (2009). https://doi.org/10.1103/PhysRevC.79.051601
[3] P.K. Rath, *et. al*., Phys. Rev. C, **88**, 044617 (2013). https://doi.org/10.1103/PhysRevC.88.044617
[4] P.K. Rath, *et al*., Nuclear Physics A, **874**, 14 (2012). https://doi.org/10.1016/j.nuclphysa.2011.10.004
[5] C.S. Palshetka, *et al*., Phys. Rev. C, **82**, 044608 (2010). https://doi.org/10.1103/PhysRevC.82.044608
[6] L Morelli, J. Phys. G: Nucl. Part. Phys. **43**, 045110 (2016). https://doi.org/10.1088/0954-3899/43/4/045110
[7] V.V. Parkar, *et al*., Phys. Rev. C, **82**, 054601 (2010). https://doi.org/10.1103/PhysRevC.82.054601
[8] S. Santra, Phys. Lett. B, **677**, 139 (2009). https://doi.org/10.1016/j.physletb.2009.05.016
[9] R. Rafiei, Phys. Rev. C, **81**, 024601 (2010). https://doi.org/10.1103/PhysRevC.81.024601
[10] D.H. Luong, Phys. Lett. B, **695**, 105 (2011). https://doi.org/10.1016/j.physletb.2010.11.007
[11] K. Hagino, *et al*., Comput. Phys. Commun. **123**, 143 (1999). https://doi.org/10.1016/S0010-4655(99)00243-X
[12] I.J. Thompson, Comput. Phys. Rep. **7**, 167 (1988). https://doi.org/10.1016/0167-7977(88)90005-6
[13] E. Vardaci, *et al*., Eur. Phys. J. A, **57**, 95 (2021). https://doi.org/10.1140/epja/s10050-021-00400-3
[14] W. Reisdorf, J. Phys. G: Nucl. Part. Phys. **20**, 1297 (1994). https://doi.org/10.1088/0954-3899/20/9/004
[15] A. Diaz-Torres Com. Phy. Comm, **182**, 1100 (2011). https://doi.org/10.1016/j.cpc.2010.12.053
[16] K.J. Cook, *et.al*., Nature Communications, **14**,7988 (2023). https://doi.org/10.1038/s41467-023-43817-8
[17] E.C. Simpson, *et al*., EPJ Web of Conferences, **163**, 00056 (2017). https://doi.org/10.1051/epjconf/201716300056
[18] S. Kalkal, *et.al*., Phys. Rev. C, **93**, 044605 (2016). https://doi.org/10.1103/PhysRevC.93.044605
[19] L. Yang, *et al*., Fundamental research, (2023). https://doi.org/10.1016/j.fmre.2023.10.006
[20] D. Chattopadhyay, *et al*., Nuclear Physics A, **1053**, 122296 (2025). https://doi.org/10.1016/j.nuclphysa.2024.122965

РОЗУМІННЯ МЕХАНІЗМУ РОЗПАДУ ЯДРА ЗА ДОПОМОГОЮ МЕТОДИКИ МОДЕЛЮВАННЯ МОНТЕ-КАРЛО

М. Суейн[a], Прасанта Кумар Рат[a,b], Баладжі Падхі[a], Адітья Кумар Паті[a], Вайшалі Р. Патель[c], Ніралі Гондалія[c], Амі Н. Дешмук[c], Равіндра Праджапаті[c], Н.Н. Дешмух[c]
[a]Університет технології та менеджменту Центуріон, Паралахемунді, Одіша, 761211 - Індія
[b]Факультет фізики Неапольського університету «Федеріко II» та INFN, I-80125, Неаполь, Італія
[c]П.П. Університет Савані, Дхамдод, Косамба, Сурат, Гуджарат, Індія

Розпад ядра був з'ясований за допомогою моделювання Монте-Карло при низькій енергії, що вказує на наявність ширшого конуса розпаду для розпаду поблизу цілі, тоді як при розпаді далекої цілі присутній добре локалізований конус розпаду. Симуляції вказують на необхідність ширшого тілесного кута в експерименті та локалізованого кінематичного тілесного кута для вивчення явищ розпаду. Було розглянуто приклад $^{7}Li+^{208}Pb$ і виявлено добре узгодження результатів моделювання з експериментальними даними.
Ключові слова: *ES (пружне розсіювання); CF (повний синтез); ICF (неповний синтез); CN (складне ядро); BU (розпад)*